Trinity College Dublin
Coláiste na Tríonóide, Baile Átha Cliath
The University of Dublin

The Production, Characterisation, Stabilization and Isolation of Azole Anti-Fungal Nanoparticles

A dissertation submitted for the degree of
Doctor of Philosophy
at the School of Pharmacy & Pharmaceutical Sciences,
Trinity College Dublin,
the University of Dublin, Ireland
by

Kate P.M. McComiskey

Under the supervision of Dr. Lidia Tajber

2019

Declaration

I declare that this thesis has not been submitted as an exercise for a degree at this or any other university. A small proportion of the work described in this thesis was carried out by others, and this is duly acknowledged in the text wherever relevant. I declare that all other work is entirely my own.

I agree to deposit this thesis in the University's open access institutional repository or allow the Library to do so on my behalf, subject to Irish Copyright Legislation and Trinity College Library conditions of use and acknowledgement.

Kate P.M. McComiskey

Summary

The work carried out in this thesis incorporated all aspects of the pharmaceutical drug development process. APIs were formulated as nanoparticles (NPs), with initial work beginning with developing a robust and reproducible NP production method tailored to each API. Stabilization of NPs was explored in great detail. The impact of small differences in both API and stabilizer structure was explored, with a diverse range of behaviour displayed by the various API/polymer combinations explored. In particular, the effect of stabilizer choice and concentration was investigated on nanoparticle (NP) stability over time. Three different BCS class II active pharmaceutical ingredient (APIs): itraconazole (ITR), ketoconazole (KETO) and posaconazole (POS) were chosen due to their poor aqueous solubility and closely related chemical structures. Polyethylene glycol (PEG), polyethylene glycol methyl ether (MPEG) and polyethylene glycol dimethyl ether (DMPEG) with a molecular weight of 2,000 Dalton were included as stabilizers. NP formation *in situ* using an anti-solvent addition, bottom up method at 25 °C was explored. Colloidal stability was monitored using dynamic light scattering (DLS), accompanied by morphological examination of the NPs using scanning electron microscopy (SEM). Kinetic modelling indicated nanoparticle growth is driven by Ostwald ripening (OR). The presence of DMPEG caused OR growth to become an interface controlled process following a parabola trend. DMPEG encouraged OR for POS NPs whilst driving the crystallisation process. Crystallisation mechanisms were API, stabilizer type and concentration dependent.

Evidence from DLS studies, along with powder X-ray diffraction (PXRD) and scanning electron microscopy (SEM) suggested possible crystallisation of POS nano-dispersions during the time scale of the study. This information presented an interesting potential research area. In addition, the execution of particle sizing via more than one technique is critical to the success of the formulation process therefore it seemed logical to move forward by comparing results from DLS and nanoparticle tracking analysis (NTA), two techniques that size particles based on their Brownian motion in liquid medium. The impact of PEG, MPEG and DMPEG as stabilizers, were assessed using these two particle sizing techniques. Mie light scattering theory was successfully used to explain the relationship between material composition and particle scattering power. A change in material refractive index, associated with an amorphous to crystalline solid state transformation, was predominantly responsible for the observed change in the light scattering power of POS nano-dispersions. The innovative application of NTA for the live tracking of these physical processes was explored for the first time. This novel finding provided further confirmation of POS nano-dispersion crystallisation during the time scale of

the study and emphasised the different behaviour exhibited by the various API/polymer systems.

Numerous techniques were coupled in an attempt to deduce the exact location of the polymers in relation to NP structure. The assembly of polymer molecules onto ITR particle surfaces via coating layer formation was described. The thermodynamics of mixing can provide important information regarding the level of interaction between the components of a system, in other words their miscibility. The miscibility of these systems along with the solid state characteristics of the APIs can be a useful indicator of polymer adsorption and/or integration within NPs. For this reason, phase diagrams were constructed for KETO and ITR/polymer systems. Eutectic compositions and temperatures were calculated for KETO and ITR/polymer systems. High ITR to polymer ratio led to the existence of liquid crystalline ITR phases. The findings of this work revealed key information in relation to NP stabilization and drug polymer interactions. DMPEG was proven to be the most effective stabilizer in terms of achieving colloidal stability for all API NPs. In the case of ITR, quantification of drug polymer miscibility confirmed that low miscibility and solubility between components is a good predictor for effective NP stabilization. In the case of KETO NPs, low miscibility between components was a good predictor for effective NP stabilization. However, some degree of miscibility may be necessary for sufficient physio-sorption of polymer chains onto API surfaces. DLS was utilised to investigate the formation of polymer coating layers onto ITR particle surfaces. DMPEG formed this coating layer more readily than PEG and MPEG. Layer formation readiness corresponded with effective NP stabilization.

In the final chapter of this thesis, ITR was selected as a model API for the production of solidified nanostructured microparticles (NMPs) via spray drying. In this way, the pharmaceutical drug development process was completed, with the end product being a convenient solid oral dosage form. Soluble sugars and one sugar alcohol exhibiting a variety of physical properties were explored for inclusion as potential matrix formers, aiding the redispersibility of solidified nano-dispersions. Sugars were added to aqueous nano-dispersions prior to spray drying. ITR NMPs were characterised in terms of their solid state, particle morphology and redispersibility. A subset of these formulations were selected for further tabletting studies. Resulting tablets were examined using a number of standard or modified pharmacopeia tests. The impact of the presence of ITR NMPs upon the processability and tabletability of spray dried sugars was assessed. Trehalose proved to be a better matrix former

for ITR NPs boasting superior performance in numerous aspects when compared with mannitol. Namely, compressed ITR NMPs made with trehalose redispersed to smaller average particle sizes upon hydration compared with uncompressed equivalents, confirmed by both NTA and DLS. In addition, trehalose NMPs compressed into tablets exhibited increased tensile strength, compared with mannitol compressed NMPs, with adequate disintegration time maintained. Furthermore, trehalose was capable of solubilising a greater amount of ITR in gastric conditions (0.1M HCl) when compared with mannitol. Solid state effects dominated in determining tablet properties, with amorphous trehalose exhibiting favourable mechanical and disintegrant properties. The matrix former type had a profound impact upon end product performance. All aspects of the development process were explored in detail with the value of a rational approach demonstrated throughout the thesis.

Acknowledgements

I would like to express my sincere thanks to my supervisor, Dr. Lidia Tajber, for her endless support and mentorship throughout my PhD studies. I feel lucky to have had an enthusiastic and approachable supervisor who was so easy to work with. I would like to thank past and current members of the research group and lab in the School of Pharmacy for their friendship and entertainment during my PhD, in particular Naila, Hanah, Agnieszka, Svenja, David, Alan, Ricardo, Emer, James, Jeremiah, Karl, Peter, Zelalem, Mai, Kieran and Clare. I would also like to thank the technical staff in the school of Pharmacy, Trevor, Brian, Ray and Conan.

I would also like to acknowledge the undergraduate students Jack Stapleton and Mark Lynch, who helped me with my experimental work as part of their research projects. The research carried out in this thesis would not have been possible without the funding provided by Science Foundation Ireland, under the Synthesis and Solid State Pharmaceutical Centre (SSPC). I am grateful to the other SSPC researchers and academics, in particular those in LT2, who listened to many presentations regarding my work and provided valuable feedback.

Finally, I would like to thank my family for their support throughout, in particular my parents. A special thank you to my husband Neill for his constant encouragement and support throughout my studies, and without whose support I would not have completed this PhD.

Publications and Presentations

Publications Associated with the Thesis:

- McComiskey, K.P.M., Mugheirbi, N., Stapleton, J., Tajber, L., *In situ* monitoring of nanoparticle formation: Antisolvent precipitation of azole anti-fungal drugs. *International Journal of Pharmaceutics.* **2018,** 543, 201-213.
- McComiskey, K.P.M., Tajber, L., Comparison of particle size methodology and assessment of Nanoparticle Tracking Analysis (NTA) as a tool for live monitoring of crystallisation pathways. *European Journal of Pharmaceutics and Biopharmaceutics*. **2018,** 130, 314-326.
- McComiskey, K.P.M., Cruz, R., Tajber, L., Quantification of Drug Polymer Interaction and its Impact upon Nanoparticle Stabilization. In preparation.
- McComiskey, K.P.M., McDonagh, A., Tajber, L., Isolation and Characterisation of Itraconazole Nanostructured Microparticles (NMPs) via Spray Drying with Rational Selection of Optimum Sugar Base for Tabletting. In preparation.

Other Publications:

- Sladek, S., McComiskey, K., Healy, A.M., Tajber, L., Nanoparticle Tracking Analysis to examine the temperature-induced aggregation of proteins. Methods in Molecular Biology, **2018**

Poster Presentations:

- McComiskey, K.P.M., Mugheirbi, N., Tajber, L., *In Situ* Monitoring of Kinetics of Nanoparticle Formation. 37th All Ireland Schools of Pharmacy Conference, Queen's University Belfast, UK. **2015** Mar 30-31.
- McComiskey, K.P.M., Mugheirbi, N., Tajber, L., *In Situ* Monitoring of Kinetics of Nanoparticle Formation. Summer School - Crystal Shape Engineering, ETH Zurich, Switzerland. **2015** July 6 – 10.
- McComiskey, K.P.M., Mugheirbi, N., Stapleton, J., Tajber, L., *In situ* monitoring of nanoparticle formation: Antisolvent precipitation of azole anti-fungal drugs. 2015 AAPS Annual Meeting and Exposition, Orlando, FL, USA, **2015** Oct 25-29; M1127.
- McComiskey, K.P.M., Mugheirbi, N., Tajber, L., *In Situ* Monitoring of Kinetics of Nanoparticle Formation. 38th All Ireland Schools of Pharmacy Conference, RCSI, Dublin, Ireland. **2016** Mar 21-22.

- McComiskey, K.P.M., Mugheirbi, N., Stapleton, J., Tajber, L., *In Situ* Monitoring of Azole Anti-fungal Nanoparticle Formation. 2017 AAPS Annual Meeting and Exposition, San Diego, CA, USA, **2017** Nov 12 -15; AM-17-1091.
- McComiskey, Tajber, L., Critical Comparison of Dynamic Light Scattering versus Nanoparticle Tracking Analysis as Particle Sizing Techniques and Solid State Monitoring for Azole Anti-Fungal Nano-dispersions. 2017 AAPS Annual Meeting and Exposition, San Diego, CA, USA, **2017** Nov 12 -15; AM-17-1442.

List of Abbreviations

AFM = Atomic force microscopy

AM = Amorphous

ANOVA = Analysis of variance

API = Active pharmaceutical ingredient

a.u. = Arbitrary unit

AUC = Analytical ultracentrifugation

BCS = Biopharmaceutical classification system

CARS = Coherent anti-Stokes Raman scattering

CE = Capillary electrophoresis

CR = Crystalline

Da = Dalton

DC = Direct compression

DCS = Developability classification system

DLS = Dynamic light scattering

DLVO = Derjaguin-Landau-Verwey-Overbeek

DMPEG = Polyethylene glycol dimethyl ether

DSC = Differential scanning calorimetry

DVS = Dynamic vapour sorption

endo^ = Endothermic direction

ESD = Equivalent spherical diameter

^exo = Exothermic direction

F-H = Flory-Huggins

FL = Flocculation

HDC = Hydrodynamic chromatography

HPC = Hydroxypropylcellulose

HPLC = High performance liquid chromatography

HSP = Hansen Solubility Parameter

ICP-MS = Inductively coupled plasma mass spectrometry

ISO = International Organization for Standardization

ITR = Itraconazole

KETO = Ketoconazole

LC = Liquid crystal

LLPS = Liquid-liquid phase separation

MALS = Multi-angle light scattering

MPEG = Polyethylene glycol methyl ether

MP = Microparticle

M-S-M = Maier-Saupe-McMillan

NMP = Nanostructured microparticle

NP = Nanoparticle

NTA = Nanoparticle tracking analysis

OA = Orientated attachment

OR = Ostwald ripening

PCS = Photon correlation spectroscopy

PDI = Polydispersity index

PEG = Polyethylene glycol

PIXE = Particle induced X-ray emission

POL = Polymer

POS = Posaconazole

PSD = Particle size distribution

PTFE = Polytetrafluoroethylene

PVA = Polyvinyl alcohol

PVP = Polyvinylpyrrolidone

PXRD = Powder X-ray diffraction

Redisp = Redispersed

RES = Reticuloendothelial system

RH = Relative humidity

RI = Refractive index

RSD = Relative standard deviation

S = Supersaturation ratio

SEC = Size exclusion chromatography

SD = Spray dried

SD = Standard deviation

SEM = Scanning electron microscopy

SIOS = Scanning ion occlusion sensing

SLS = Sodium lauryl sulfate

SOP = Standard operating procedure

SPR = Surface plasmon resonance

TEM = Transmission electron microscopy

TGA = Thermogravimetric analysis

USP = United States pharmacopoeia

UV-vis = Ultraviolet visible spectroscopy

TABLE OF CONTENTS

1.1 BIOPHARMACEUTICAL CLASSIFICATION SYSTEM (BCS)

Generation of new chemical compounds resulting from advances in drug development has led to the discovery of an increasing number of drugs with poor aqueous solubility and reduced bioavailability (Lipinski, 2002). For this reason, formulation scientists have been forced to develop delivery platforms ensuring the delivery of promising poorly soluble new chemical entities.

Many formulation strategies are based on the Biopharmaceutical Classification System (BCS). BCS has emerged as an invaluable tool in guiding the decision-making process involved in formulation development from a biopharmaceutical perspective (Shah and Amidon, 2014). The system categorizes substances based on their solubility and intestinal permeability. Class I have high solubility and permeability, class II have low solubility and high permeability, class III have high solubility and poor permeability, while class IV have poor solubility and permeability. Compounds with aqueous solubility below 100 µg/ml often present with dissolution limited bioavailability (Hörter and Dressman, 2001). The FDA have defined a substance as being "highly permeable", when the systemic bioavailability or extent of absorption in humans is 85% or more of an administered dose (FDA, 2017). This thesis will focus on formulation strategies concerning the BCS class II compounds: itraconazole (ITR), ketoconazole (KETO) and posaconazole (POS). Examples of technologies commonly utilised for these compounds include: salt and cocrystal formation, particle size reduction including microparticles (MPs) and nanoparticles (NPs), amorphisation, cyclodextrin complexation, lipid formulations and pH modification.

Butler et al. (2010), have recently proposed a revised classification system, the developability classification system (DCS). This system addresses drug developability for oral immediate release formulations in an attempt to aid the formulator in design. It divides BCS Class II compounds into IIa and IIb, where IIa compounds are said to be dissolution rate limited, whereby drug particles cannot dissolve in the time it takes to pass their absorption site. On the other hand, IIb compounds are solubility limited, whereby there is an inadequate volume of fluid available in the gastrointestinal (GI) tract to dissolve the administered dose (Butler and Dressman, 2010). ITR has an aqueous solubility below 1 µg/ml (Matteucci et al., 2009) while, POS and KETO are both poorly soluble in water (Dressman and Reppas, 2000; Evans et al., 2006; FDA, 2013). For this reason, it is likely that ITR is solubility limited, responsible for its limited dissolution while POS and KETO are dissolution rate limited. Therefore, these APIs are ideal candidates for dissolution rate enhancement technologies. These characteristics, along

with their closely related chemical structures made formulation of these APIs as NPs an interesting area of research.

ITR is currently commercially available in the form of a gelatin capsule, known as Sporanox®. Sporanox® capsules contain 100 mg of ITR coated onto sugar spheres consisting of sugar, maize starch and purified water. PEG 20,000 is currently included in this formulation as an excipient, this reaffirms its exploration as a stabilizer in this thesis (Namburi et al., 2002). ITR is a common model drug used in the study of solubility and dissolution issues. Previous approaches have employed nanosization, co-crystal formation and amorphous solid dispersions (Mugheirbi et al., 2014; Mugheirbi et al., 2015b). ITR is known to exhibit polymorphic character, with up to four different polymorphic forms having been observed in the literature (Zhang et al., 2016). In addition, ITR has the ability to form stable liquid crystalline phases when formulated as a NP (Mugheirbi and Tajber 2015). KETO is commercially available in tablet form containing 200 mg of KETO. Numerous techniques have been employed in an attempt to enhance the dissolution rate of KETO. Rasenack and Muller (2002) produced micronized KETO powder in crystalline form using an anti-solvent precipitation technique followed by spray drying (Rasenack and Muller 2002). Whilst others have produced KETO salts and co-crystals using fumaric, adipic and succinic acid, exhibiting enhanced dissolution rates (Martin et al., 2013). POS is available in solid oral dosage form, marketed under the brand name Noxafil®. This formulation consists of an amorphous solid dispersion of POS with hydroxypropylmethylcellulose acetate succinate (HPMCAS) (Percival and Bergman 2014). POS has been formulated as a stable nano-particulate intended for use in a parenteral dosage form, with particle sizes below 2000 nm (Wichmann et al., 2007). POS exhibits rich solid state polymorphism (Andrews et al., 2004; Wieser et al., 2012 and 2013). The diverse solid state properties of these APIs, makes them interesting candidates for further exploration in terms of their nanosization.

1.2 NANOSCIENCE

The production of NPs has emerged as a viable strategy for overcoming the limitations faced by BCS class II compounds. NPs are defined as having a particle size below 1 µm (Müller et al., 2006). Reduction of particle size results in an increased dissolution rate due to an increased surface area. According to the Noyes-Whitney model for dissolution (Eq. 1.1):

$$\frac{dW}{dt} = \frac{D\,A\,(Cs-C)}{L} \qquad \text{(Eq. 1.1)}$$

Where dW/dt = dissolution rate, D = diffusion coefficient, A = surface area, L = thickness of the boundary layer, C = is the concentration of the solid in the bulk dissolution medium, C_s = is the concentration of the solid in the diffusion layer surrounding the solid, surface area is therefore directly proportional to dissolution rate (Noyes and Whitney, 1897). In addition, the high surface curvature of NPs results in an increase in saturation solubility which can be explained by the Ostwald-Freundlich equation (Ostwald, 1900; Freundlich, 1909) (Eq. 1.2):

$$X_{A(\beta)} = X^{O}_{A(\beta)}.\exp\frac{(2.V^{O}_{A(\alpha)}.\sigma^{O}_{\frac{\alpha}{\beta}})}{R.T.r_x} \qquad \text{(Eq. 1.2)}$$

where $x_{A(\beta)}$ = is the solubility of component A (mole fraction) in the form of a spherical, pure phase α, r_m = radius, β = solution, T (K) = temperature, $x^{O}_{A(\beta)}$ = solubility of component A for an infinitely large phase α, $\sigma^{O}_{\alpha/\beta}$ = the interfacial energy (J/m^2) between the two phases, $V^{O}_{A(\alpha)}$= the molar volume (m^3/mol) of the pure phase A (α), and R = universal gas constant (8.3145 J/mol K). When particles are suspended in liquid medium and have a mean particle size below 1 micron, they are referred to as nano-suspensions. Whereas, nano-dispersion is a more general term, describing a dispersion of nano-sized particles. The term nanocrystal is employed when those particles are partially or fully crystalline (Möschwitzer and Müller, 2007).

1.3 NANOPARTICLE (NP) CHARACTERISATION

Analytical techniques employed for NP sizing can be categorised into counting, fractionation, ensemble and single particle. Counting methods encompass microscopy techniques including scanning electron microscopy (SEM), transmission electron microscopy (TEM), atomic force microscopy (AFM) and confocal microscopy. Fractionation methods include AF4 coupled with multi-angle light scattering (MALS) and inductively coupled plasma mass spectrometry (ICP-MS) (Contado, 2017). Other techniques in this category include size exclusion chromatography (SEC), hydrodynamic chromatography (HDC) and capillary electrophoresis (CE). Separation techniques such as these can be combined with ultraviolet visible spectroscopy (UV-vis) and ICP-MS. The remaining techniques encompass a wide range of methods that measure many particles simultaneously. Examples include dynamic light scattering (DLS), surface plasmon resonance (SPR), coherent anti-Stokes Raman scattering (CARS) and particle induced X-ray emission (PIXE) (Soriano et al., 2018). Examples of single particle sizing techniques include nanoparticle tracking analysis (NTA) and scanning ion occlusion sensing (SIOS). The above mentioned techniques have the capability to provide information on particle morphology,

surface area properties, particle composition, particle size, size distribution, concentration, porosity and aggregation trends. In order for the field of nanotechnology to fulfil its potential, precise, reproducible, synthesis and manufacture is needed. As a pre-requisite for this, a standardized framework must exist. In recent years advances have been made in this area, with the introduction of best practice guidelines (Mingard et al., 2009), inter-laboratory studies (Wang et al., 2009) and ISO documents (International Organization for Standardization, 2008).

This thesis will primarily focus on DLS and NTA as NP characterisation tools. DLS is also known as photon correlation spectroscopy (PCS) or quasi-elastic light scattering. If we consider the basic principles of a light scattering experiment, a sample is exposed to a monochromatic wave of light, followed by detection of a signal by a suitable detector. John Tyndall first described the Tyndall effect in 1868, in relation to light scattering by colloidal suspensions, he concluded that the particles were larger than the wavelength of incident light (Tyndall, 1868). Rayleigh scattering describes the light scattering from particles that are smaller than the wavelength of light (Strutt, 1871). Gustav Mie described Mie theory, whereby the light scattered by absorbing and non-absorbing particles is larger than the wavelength of light. Mie scattering is determined by the particle shape and refractive index (Mie, 1908). Brownian motion of particles forms the basis of DLS measurements. This refers to the random molecular motion of particles (Einstein, 1905). DLS looks at light intensity fluctuations caused by the Brownian motion of particles in a liquid medium. DLS determines the hydrodynamic radius based on the diffusion coefficient (D_τ) of the particles. D_τ is determined by the size, temperature and solvent viscosity (Harding et al., 1998). Accurate temperature control is imperative during analysis as solvent viscosity is also determined by this parameter. If we consider particle movement over time, large particles will diffuse more slowly than their smaller counterparts. During the DLS measurement process, incident light will encounter particles in solution which will scatter light of a particular intensity, scattering intensity is then detected by a detector. A digital autocorrelator will correlate intensity fluctuations in light scattering with time, and determine the rate of those fluctuations based on the diffusion behaviour of the particles. Numerous other parameters can be derived using DLS. An intensity based distribution will be produced which is susceptible to bias from larger particles present within the sample. This can be converted to a volume weighted distribution representing the relative proportion of multiple sizes within the sample based on volume, and not intensity. Volume distribution assumes that all particles within the sample are spherical and homogeneous. Number weighted

distributions can also be derived from DLS, whereby all particles within the distribution are given equal weighting irrespective of their size (Stetefeld et al., 2016).

NTA is a light scattering technique capable of providing particle size and concentration measurements. The software employed has the capability to track the Brownian motion of individual particles and relate that movement to their particle size via the Stokes-Einstein equation (Eq. 1.3):

$$d_H = \frac{k_B T}{6 \pi n D} \quad \text{(Eq. 1.3)}$$

Where d_h is the hydrodynamic diameter, k_B is the Boltzmann constant, T is the temperature, η is the solvent viscosity and D is the diffusion coefficient. NTA has the unique capability of real time visualisation of particles suspended in a liquid. A laser beam is passed into the sample chamber where the particles scatter light from the incident beam (Dragovic et al., 2011). This scattering behaviour is viewed via a microscope which records a video file of the Brownian motion of the particles within the viewing field. Particle concentration information is obtained by averaging the particle count and dividing it by the interrogated volume in which the particle number is determined. In order to obtain statistically reliable data, a sufficient number of particles must be analysed in a video frame. Furthermore, to avoid neighbouring particles obscuring one another, a sufficiently low sample concentration must be analysed. The typical concentration range employed is 10^6 to 10^9 particles/ml. Another unique aspect of NTA involves its ability to characterise the amount of light scattered by particles. Light scattering properties of materials are determined by both particle size and composition. Thereby making it possible to distinguish between particles of a similar size based on their refractive indices (Gallego-Urrea et al., 2011).

1.4 Current Applications of NPs

There are numerous commercial nanocrystal products available on the market. The majority of these are designed for oral administration. The first nanocrystal product was Rapamune® (sirolimus), an immunosuppressant, was brought to market by Wyeth in 2000. Prior to this, rapamycin was marketed as an oral solution. The Rapamune® tablet contains 2 mg sirolimus, of a total tablet weight 370 mg. This low drug loading meant problems such as nanocrystal aggregation were avoided. Aggregation can reduce dissolution velocity, and therefore bioavailability. A NP load of 1%, is below what is considered critical (Bushrab 2005). Tablet performance exceeded that of the solution, with an increased bioavailability of 21% over the oral solution (Junghanns and Müller, 2008). This tablet formulation benefitted from being

more user friendly and having greater bioavailability over the oral solution (Shegokar and Müller, 2010). Emend® (aprepitant) manufactured by Merck reached the market in 2001. This anti-emetic is available as a single dose (80 or 125 mg), and has a narrow absorption window as it is only absorbed in the upper GI tract. NPs make rapid dissolution and enhanced bioavailability possible. Emend® consists of nanocrystals incorporated into pellets and filled into a hard gelatin capsule (Junghanns and Müller, 2008). Tricor® (fenofibrate) for the treatment of hypercholesterolemia, was developed by Abbott Laboratories. Another fenofibrate tablet, Triglide® was produced by SkyePharma using IDD-P® technology. Tricor® exhibited enhanced product performance over conventional fenofibrate products. Absorption was increased by 35% in the fed state. Nanocrystals reduce food effects, given their adhesive properties which are effective regardless of patient nutritional state. Megace ES® (megestrol acetate) is an anti-anorexic drug produced by Par Pharmaceutical Companies Inc. Notably, this product is a nano-dispersion resistant to bioavailability changes induced by the fasted/fed state. It has preferable properties over other available liquid formulations of megestrol acetate, including reduced viscosity and administration volumes.

1.5 Oral Administration for NPs

NPs can be tailored for administration via a number of routes. The route selected will depend on the disease, desired clinical outcome and API properties. Ultimately, optimum therapeutic response is the end goal. Oral administration can result in increased bioavailability, resistance to fed/fast variations, increased absorption rate, as well as greater patient acceptability (Shah et al., 2016).

Subsequent to ingestion of an oral formulation, disintegration takes place followed by dissolution. The increased surface area of nanocrystals results in enhanced dissolution rate, in turn increasing absorption and bioavailability. NPs also have a tendency to adhere to the gut wall (Ponchel et al., 1997). Generally, drug bioavailability is increased in the presence of food as a result of increased bile acid secretion and delayed gastric emptying. Persistent improvements in bioavailability can only be available by removing these food effects (Prajapati et al., 2012). Dissolution rate enhancement imparted by NPs exists regardless of fasted or fed state. Patient to patient variability is also a major issue with NPs.

NP properties can be manipulated to achieve highly specific site delivery. Nano-sization can reduce drug effects elsewhere in the body, whilst maintaining therapeutic effect in the desired target site. This property is particularly beneficial for anti-cancer drugs which can be toxic to both healthy and cancerous cells. NPs have the ability to transverse different biological

barriers through small capillaries and into cells. NP design can be optimised to bind or encapsulate molecules thereby improving API solubility, absorption and stability. In this way NPs are capable of avoiding the reticuloendothelial system, safe guarding drug molecules from early inactivation on their journey within the body (Medina et al., 2009). In addition, polymer-based NPs are a popular drug delivery system, as they are biodegradable, removing the danger of accumulation within the body (Sapra et al., 2005).

1.6 Nano-structured Microparticles (NMPs)

Nano-structured microparticles (NMPs) are also known as "Trojan" microparticles. Manufacture of these systems involves first fabricating a nano-dispersion, followed by encapsulation of these NPs within MPs. Microencapsulation of NPs should preserve their nano-size and particle morphology. This process should also not induce premature drug release. Particle size within the nano-metre range is beneficial from a biopharmaceutical perspective. However, micron sized particles are preferred from a manufacturing and processing point of view, having better flow and handling properties. Therefore, a hybrid approach whereby NPs are encapsulated within MPs offers an attractive solution.

NMPs have a profound impact upon NP release profiles. Namely, a reduction in burst effect is seen with a slowing down in release kinetics (Thote and Gupta, 2005). NMPs are normally produced via spray drying. Resulting spray dried powders tend to be amorphous, exhibiting an array of particle morphologies, including matricial or hollowed (Benoit, 2000). Processing and formulation variables dictate particle characteristics to a large extent. Precipitation kinetics and crystallisation will determine evaporation rate and drying temperature within the spray dryer (Raula et al., 2004). NMPs have the remarkable ability to reduce the burst release effect of drugs with a decrease in release kinetics. Gomez-Gaete et al. (2008) compared drug release profiles for dexamethasone encapsulated within MPs, with dexamethasone NPs encapsulated within PLGA MPs. A reduced burst effect was observed accompanied by a reduction in drug release kinetics. Authors concluded that polymer erosion was responsible for this release profile (Gómez-Gaete et al., 2008). However, there is a lack of solid understanding surrounding drug release from NMPs. Drug release is dictated by processing and formulation parameters (Anton et al., 2012).

1.6.1 Biopharmaceutical Applications of Nano-Structured Microparticles (NMPs)

In order to achieve optimum pharmacological and therapeutic activity of drugs, dosage form design is a critical part of the biopharmaceutical design process. Therapeutic activity is

determined by drug availability. Furthermore, kinetics have a part to play in the rate and amount of drug penetrating different membrane barriers and reaching target sites within the body. Dosage form design should enable on-demand drug release in the desired target site. Drugs such as those studied in this thesis, serve to benefit from the biopharmaceutical development process, suffering from poor stability, permeability and solubility. One approach for overcoming these problems, includes modification of the chemical structure of the active compounds. However, this results in a new chemical entity with a different physicochemical profile. Therefore, alternative approaches involving the development of new products provide a viable solution. Formulation of an existing API within a new dosage form offers a more convenient option. Such technology, provides the opportunity to bring existing APIs in the form of a new product with improved bioavailability, to the market at a lower cost (Anton et al., 2012).

Re-formulation of drugs using NMPs alters their pharmacokinetic/dynamic profiles, with improved absorption and distribution. NMPs have a number of biopharmaceutical advantages including improved bioavailability, prolonged drug action, reduced administered dose, and reduced toxicity, use of non-invasive administration routes and better patient compliance. Oral administration of NMPs provides a means of achieving a sustained drug release profile (Anton et al., 2012).

1.7 NP PRODUCTION

Production of NPs is generally categorised into four subsets: top down, bottom up, chemical synthesis and combination approaches (Moeschwitzer, 2010). Top down methods begin with larger particles, which are broken down into NPs (Keck and Müller, 2006). Top down approaches include high pressure homogenisation (HPH) and wet media milling. HPH can employ micro-fluidiser technology (IDD-P™ technology), piston gap homogenisation in either aqueous media (Dissocubes® technology, SkyePharma) or non-aqueous (Nanopure® technology, Abbott Laboratories). Examples of commercialised milling techniques include Nanocrystal® technology by Elan Corporation. It can be difficult to achieve particle sizes below 100 nm using these methods (Shah, 2006). Such methods are energy intensive, which can be costly from an industrial perspective. They also have a tendency to produce amorphous particles. The input of mechanical energy during the milling process increases lattice vibrations, in turning destabilizing the order of the crystal lattice. This results in an increase in the number of crystal defects and the generation of localised amorphous regions (Crowley K.J., 2002). Propensity for amorphisation is dependent upon both API and stabilizer properties,

and the interactions present between them. Process parameters also have a part to play. The presence of water during wet milling of crystalline drugs can inhibit the formation of an amorphous phase, caused by a reduction in glass transition temperature (Peltonen and Hirvonen, 2010).

Nanoedge™ technology (Baxter) is a combination method using a precipitation step, followed by HPH. SmartCrystal® (Abbott Laboratories) is an example of another combination approach also using HPH (Muller et al., 2011). Bottom up methods produce particles starting at the atomic level. Examples of bottom up approaches include anti-solvent precipitation, evaporative precipitation techniques (EPAS) and precipitation in supercritical fluid (SCF). Nanomorph technology is an example of a bottom up approach (Auweter et al., 1998). Bottom up approaches offer the advantage of being low in cost and relatively simple to perform. They also allow for greater manipulation of process parameters enabling fine-tuning of particle characteristics such as size, crystallinity and morphology (Zhang et al., 2016). Nevertheless, these methods can also lead to the formation of unstable polymorphs and solvates. They normally involve the use of a solvent which can be difficult to completely eliminate leading to possible instability upon storage (Patravale et al., 2010). Particles formed via these methods have a tendency to take on a needle shaped morphology caused by rapid growth in one particular direction, this can contribute to instability (Rabinow, 2004). This thesis focuses on the production of NPs via liquid anti-solvent (LAS) precipitation.

LAS precipitation involves a number of steps. Initial mixing of solvent and anti-solvent results in supersaturation, followed by nucleation and growth, and finally agglomeration. The generation of high supersaturation in a rapid manner, is fundamental in determining particle properties, such as size and crystallinity (Mullin and Nývlt, 1971). Supersaturated solutions generated in this thesis, are done so in a mixture of water and acetone. Supersaturation (S) is defined as (Eq. 1.4):

$$S = \frac{C}{C*} \qquad \text{(Eq. 1.4)}$$

Where c = concentration of API in the mixture of water and acetone (mol/L) and c* = equilibrium solubility (mol/L) of API in water (Kuentz, 2018). Critical parameters in the process include; temperature, stirring rate, selection of solvent and anti-solvent phase, as well as volume ratio (Sinha et al., 2013). LAS can be performed at ambient temperature and atmospheric pressure, removing the need for expensive equipment. In addition, LAS allows for close control of process parameters and manipulation of the desired product.

1.8 NP STABILITY ISSUES

Reduction in particle size results in particles having a large surface area and hence high total surface energy, which is thermodynamically unstable. For this reason, addressing the physical stability issues remains a challenging aspect of successful nano-dispersion product development. Flocculation is a reversible process whereby particles aggregate but remain as individual particles. Flocculation can lead to coalescence. Coalescence is the process by which two or more particles merge during contact, resulting in the formation of a single particle. Once in contact a pair or group of NPs will coalesce to reduce their surface energy. Surface processes control coalescence. Coalescence is an irreversible process (Ingham et al., 2011). Particles have a tendency to agglomerate to reduce their high surface energy as a result of their reduction in particle size (Van Eerdenbrugh et al., 2008). The terms agglomerate and aggregate are often used interchangeably resulting in widespread confusion surrounding their definition. The United States Pharmacopoeia (USP) defines aggregates as a mass of adhered particles, whilst agglomerates are fused or cemented particles (USP, 2000). In 1966 Gerstner et al., provided the following definitions: an agglomerate is a loose arrangement of primary particles or aggregates or a mixture of the two attached, for instance, at the corners and edges. The total surface is identical with the sum of the surfaces of the individual particles. Whereas, an aggregate consists of primary particles attached at their surfaces. The surface of such an aggregate is smaller than that of the sum of the surfaces of the primary particles or, in other words, the inner surface of an aggregate is either completely inaccessible or only partially accessible (Gerstner, 1966). Nichols et al. (2002), have proposed universal definitions for both: agglomerate, which should be used to describe an assemblage of particles in a powder and that the term aggregate, should be confined to pre-nucleation structures (Nichols et al., 2002). All of the above processes can contribute to problems in downstream processing of nano-dispersions, including batch to batch variability, as well as inconsistent dosing in the final formulation.

Physical stability issues associated with nano-dispersions include sedimentation, agglomeration, Ostwald ripening (OR) and change in crystallinity. Sedimentation relates to the settling down of particles within a formulation which is determined by particle density relative to the medium itself (Kim, 2004). NPs have a tendency to agglomerate to reduce their surface energy. Addition of stabilizers can counteract this problem.

OR is often responsible for changes in particle size. OR occurs due to saturation solubility differences existing between large and small particles, high saturation solubility exists at the

surface of smaller particles, for this reason particles diffuse through the bulk medium towards the surface of larger particles where a lower saturation solubility exists (Carstensen, 2001). A process involving diffusion and dissolution of smaller particles ensues, followed by deposition onto the surface of larger particles. The presence of stabilizers can reduce interfacial tension present between solid particles and liquid medium, thereby preventing OR (Kim, 2004). A narrow particle size distribution can decrease the saturation solubility difference within the medium, thereby inhibiting OR (Rabinow, 2004). OR growth is dependent upon material properties, particle surfaces and the nature of the solution itself (Yin et al., 2011). Kinetic growth models have been applied in the hope of gaining knowledge surrounding the kinetics of the OR process (Wagner, 1961; Speight, 1968; Kirchner, 1971). The application of these models provides the necessary means for achieving optimal NP properties. If we can determine the critical factors driving the OR process, we can manipulate these to our advantage. By fitting experimental data using these models, we can gain more understanding with regards the role of stabilizers within the crystal growth process.

Crystal growth can occur during the production and shelf life of nano-dispersions, which can adversely affect their dissolution behaviour and *in vivo* performance (Ghosh et al., 2012). Nano-dispersions are thermodynamically unstable, therefore they have a tendency to agglomerate in an effort to reduce their total energy (Gonzáles-Caballero and de Dios Garciá López-Durán, 2000). Agglomeration is determined by activation energy, from a kinetic perspective. Addition of a stabilizer can increase the activation energy of the process. Effective stabilization is dependent upon how the stabilizer interacts with the drug compound (Patravale et al., 2010). Amorphisation during NP fabrication is undesirable as it can induce instability. Accurate and reproducible control over the quantity and location of amorphous regions can be difficult. However, stabilization of amorphous regions is possible by entrapping API molecules within polymeric networks. Furthermore, stabilizer selection to date has remained a challenge due to the lack of fundamental understanding surrounding interactions within colloidal systems (Shete et al., 2014).

1.9 NP STABILIZATION

Stabilization of nano-dispersions can be achieved via tailoring of particle surfaces. Without stabilization particles may coagulate due to high particle mobility caused by surface forces. Stabilizers act to inhibit aggregation within nano-dispersions via two methods, electrostatic repulsion or steric stabilization. Electrostatic stabilization involves the adsorption of ionic charges onto particle surfaces which results in mutual repulsive forces acting between

particles (Peltonen and Hirvonen, 2010). Stabilizers can be used alone or in combination. Common stabilizers used include polymers and surfactants (ionic and non-ionic). Common examples of non-ionic surfactants include Tween 80 and Poloxamers (Quintanar-Guerrero et al., 1998). Sodium lauryl sulfate (SLS) is the ionic surfactant of choice (Qiao et al., 2017). Examples of polymers used as stabilizers include polyvinyl alcohol (PVA), polyvinylpyrrolidone (PVP), and polyethylene glycol (PEG) (Maged et al., 2016). Drug to stabilizer ratios employed throughout the literature range from 1:3 to 1:50 (Van Eerdenbrugh et al., 2008).

Ionic surfactants are capable of creating sufficient surface charge for stabilization. However, whilst effective in an aqueous environment, the ionized state is lost during the drying process (Farrokhpay, 2009). Ionic stabilizers are also sensitive to changes in pH and ionic strength. Electrostatic stabilization requires a zeta potential value of at least 30 mV to be effective (Peltonen and Hirvonen, 2010). Polymers work via steric stabilization, whereby, adsorption of stabilizer molecules onto particle surfaces creates physical barriers which hinder van der Waals attractive forces between neighbouring particles (Palla and Shah, 2002). Polymeric stabilizers can have numerous sites in their chains with affinity for API surfaces, therefore polymer chain morphology determines conformation of adsorption. Their structure consists of an anchoring segment attached to the drug particle surface with a stabilizing moiety protruding into the dispersion medium (Liz-Marzan et al., 1996). With stabilizers adsorbed onto the particle surface through the anchor segment, good solvation between the solvent and the stabilizing segment of the stabilizer is required to achieve steric stabilization and prevent particles from agglomerating within the dispersion medium (Kim, 2004). In addition, molecular weight of polymer chains requires careful consideration in steric stabilization. The stabilizing moiety needs to be of sufficient length to maintain a steric barrier capable of minimising particle–particle interactions such that the van der Waals forces are less than the repulsive steric forces present (Choi et al., 2005). Short chains can result in a barrier that is too thin, while longer chains can promote particle bridging. Steric stabilization is effective in both aqueous and non-aqueous environments, whilst also being resistant to electrolyte addition (Peltonen and Hirvonen, 2010). Steric stabilization achieved via polymers does not normally result in destruction of the crystal structure of API particles. In addition, steric stabilization is more receptive to temperature fluctuations in the surrounding environment (Lee et al., 2008).

1.10 Stabilizer Selection

Different APIs require different stabilizers. However, stabilizer selection remains a challenge. The main drawback associated with steric stabilization is the constant need to tailor the

anchoring segment according to the particular drug of interest. Stabilizer molecules need to adsorb strongly enough onto particle surfaces and for a sufficient period of time. Stabilizer adsorption can occur in a number of ways: van der Waals forces, ion-dipole interaction, ionic interaction, hydrogen bonding, or by hydrophobic effect (Verma et al., 2009). There are numerous factors to be considered when assessing stabilizer selection. Namely, dispersion medium pH and viscosity, API solubility in stabilizer solutions, hydrophobicity, concentration of stabilizer, temperature of dispersion medium and surface energies. Ultimately, the mechanism of stabilization depends on the physicochemical nature of the stabilizer. Different surface characteristics of APIs require different stabilizer properties.

Viscosity is particularly important during milling. High viscosity media extends processing time. Van Eerdenburgh et al. (2009) assessed stabilization of 9 drugs and 13 stabilizers. Surfactants proved to be the best with low viscosity and high surface activity deemed to be critical (Van Eerdenbrugh et al., 2009). Measurements of surface free energies, has been reported as useful in stabilizer selection. In the case of polymeric stabilizers, similar surface free energies for drug and stabilizer result in effective stabilization. Including a surfactant appears to be helpful when there is a great difference between the surface free energies of the drug and polymer (Gupta and Wells, 2004). Choi et al. (2005) assessed the effective stabilization of 7 model compounds by polyvinylpyrrolidone (PVP) and hydroxypropylcellulose (HPC) by wet milling. The author attempted to relate particle sizes achieved with surface energy values of drugs and stabilizers determined by contact angle measurements. When PVP was used, better stabilization was achieved when the drug and stabilizer had similar surface energy values. Yet, when HPC was used, surface energy seemed to play no role in the level of stabilization achieved (Choi et al., 2005).

Solubility of the API in aqueous stabilizer solutions has also been deemed important. OR can be directly correlated to concentration of the dispersed phase, via Lifshitz-Slyozov-Wagner theory (Shete et al., 2014). Verma et al. (2009) found that the increased solubility of ibuprofen in the presence of stabilizer resulted in an increased rate of OR, and overall increase in particle size (Verma et al., 2009). Surfactant solutions increase the solubility of APIs via the formation of micelles, which in turn destroys crystallinity resulting in stability issues (Peltonen and Hirvonen, 2010). Hydrophobicity of stabilizers is key in determining the degree of adsorption of stabilizers onto hydrophobic API particle surfaces (Van Eerdenbrugh et al., 2009). Stabilizer concentration is also important. Polymer molecules will only adsorb onto API particle surfaces when reduction in free energy caused by adsorption, is sufficient to compensate for entropy

loss (Ploehn and Russel, 1990). Steric stabilization involves a dynamic equilibrium between sorption/desorption processes. Notably, a stabilizer concentration that may be sufficient in aqueous media may not have the same effect when in the dry form (Peltonen and Hirvonen, 2010). Temperature of the dispersion medium should not be overlooked, with changes in temperature altering viscosity and diffusion coefficients (Kholodenko and Douglas, 1995). The physical process involved in the destabilization of nano-dispersions, can occur more rapidly, benefitting from the surplus energy supplied at higher temperatures.

Lee et al. (2008) carried out a comprehensive screening study including 11 different APIs and 5 different polymers. Polymers included were HPC, PVP, PEG and Poloxamer 47 and 188. The addition of ionic surfactants and their effect on stabilization was also investigated. Poor stabilization achieved by PEG was attributed to a lack of hydrophobic units present in the polymer, needed for adequate adsorption onto particle surfaces. The remaining polymers investigated exhibited successful stabilization attributed to similar surface energies between drug and stabilizers. Poloxamer 188 outperformed Poloxamer 407, and this was explained by its lower molecular weight. Despite less physical adsorption by the lower molecular weight polymer, the adsorption process is less kinetically restricted. The addition of ionic surfactants to polymers produced variable results. Upon analysis of drug properties, those having higher molecular weight, poor aqueous solubility and high melting point were better candidates for stabilization (Lee et al., 2008). NP stabilization is a complex process which may be dictated by numerous factors. Notably, the potential for interaction between different parameters should not be overlooked.

1.11 PEG Coated Particle based Drug Delivery

This thesis focuses on the use of PEG and its derivatives, methyl ether PEG (MPEG) and dimethyl ether PEG (DMPEG) as stabilizers. PEG exhibits favourable biocompatibility, making it an attractive stabilizer for inclusion in the nano-formulations produced in this thesis. In addition, elsewhere in the literature PEG and MPEG 2000 have been successfully utilized as stabilizers in the formulation of ITR as a NP, using a similar bottom up anti-solvent precipitation approach, to that employed in this thesis (Mugheirbi et al., 2014). Hydrophilic PEG reduces non-specific interactions of hydrophobic NPs with opsonin, which specifically targets hydrophobic molecules (Otsuka et al., 2003). In this way, removal via the reticuloendothelial system (RES) is avoided, prolonging *in vivo* circulation, ultimately resulting in enhanced bioavailability (Owens and Peppas, 2006). Santos-Martinez et al. (2014) showed PEGylation of gold NPs to increase platelet and endothelium compatibility (Santos-Martinez et al., 2014).

The addition of PEG to drug delivery systems has the propensity for the formation of a superficial hydrophilic corona, with favourable impact on pharmacokinetic properties. PEG and MPEG have received FDA approval, making the development of new formulations a simpler process (United States Pharmacopeia and National Formulary, 2013a and b). DMPEG was included for its closely related chemical structure. Despite this, few PEG based products have reached the market. A lack of knowledge regarding the exact coverage density, conformation or thickness of the adsorbed PEG layer can result in failure to maximise these advantages. PEG can act as a hydrophilic corona providing coverage of the particle surface, designated with the difficult task of specific targeting at biological sites, with avoidance of recognition resulting in clearance.

1.11.1 Formation of PEG Coating Layer

Formation of PEG coating on particle surfaces can occur via a number of processes inherent of the NP fabrication procedure. Segregation of a hydrophilic segment of the core matrix polymer at the surface or segregation of additives, which are amphiphilic is possible. Additionally, in the case of preformed particles polymers can adsorb via physiosorption, electrostatic interactions, covalent bonding or copolymerisation (Gref et al., 1995; Owens and Peppas, 2006). In nanoprecipitation, PEG segments have the propensity to segregate with their hydrophilic parts interfacing with water and their hydrophobic parts being retained within the particle core. Alternatively, they can remain entirely within the particle core itself (Vila et al., 2004). A number of factors determine the exact location of the polymer chains within NPs. Processes inherent of the fabrication procedure include polymer interactions, viscosity and diffusion of solvent and anti-solvent phases. Entanglements, solidification processes and aqueous cavities can all determine PEG distribution in NPs (Rabanel et al., 2014). Physiosorption of PEG chains via hydrophobic interactions, onto preformed particles surfaces has the added advantage of PEG coverage being confined to particle surfaces alone, however anchorage of chains can be unstable with coverage density restricted due to steric hindrance (Stolnik et al., 1994). Optimal PEG coverage density of particle surfaces remains a debated topic. Resistance to protein binding *in vivo* has been reported at high coverage density and brush regime conformation (Vonarbourg et al., 2006). Meanwhile Perry et al. (2012) reported resistance to protein adsorption even at low coverage density (Perry et al., 2012). PEG surface coverage dictates NP diffusion through biological media. Layer density and thickness also determine docking of ligands onto molecules and target recognition (Sawant et al., 2008). In turn, these affect circulation times and active targeting.

The accurate and reproducible assessment of PEG surface coverage density is a key element of the drug development process. When approaching the challenging task of determining PEG surface content difficulties arise due to the lack of method standardisation present within the field. A number of techniques have been explored in the literature for the characterisation of the PEG layer (Rabanel et al., 2014). Techniques included are both qualitative and quantitative. A key issue remains with the inability to directly quantify surface bound PEG chains via spectroscopic techniques. Such techniques require coupling of PEG chains to a chromophore. Difficulties can also arise in differentiating between PEG present within the carrier and bound to particle surfaces. Complete segregation between the two is often assumed leading to overestimation of PEG coverage density. The presence of free PEG must not interfere with PEG quantification techniques (Rabanel et al., 2014). The NP fabrication procedure employed in this work involves nanoprecipitation whereby PEG is present in the anti-solvent phase prior to NP formation, therefore we cannot assume PEG chains are exclusively bound onto particle surfaces but may also be incorporated throughout the particle matrix.

Indirect assessment of PEG present on particle surfaces includes comparative measurements of chemical or physical properties caused by the introduction of PEG. DLS can be utilised to measure particle size changes before and after PEG addition. The "hydrodynamic radius" generated via DLS will encompass NP core size as well as polymer bound onto particle surfaces. Grafting of PEG layers onto NP surfaces is confirmed by NP size increase of twice the thickness of the PEG layer (Thierry and Griesser, 2012). Physiosorption of PEG chains onto NP surfaces is often associated with lower increase in particle size, equating to a layer thickness of 4-6 nm (Redhead et al., 2001). Quantitative assessment of such parameters via DLS is limited by a number of factors. The technique is suitable for uniform spherical NPs. PEG layer thickness is determined by PEG molecular weight and coverage density, which is normally between 1 and 10 nm. The small size of the layer can go undetected or may not appear significant when measuring NPs above 100 nm. Comparison of different batches can be helpful in overcoming these limitations (Thierry and Griesser, 2012). A number of other parameters must be controlled to avoid their interference with obtaining accurate measurements, these include: viscosity, temperature and pH (Hackey and Clogston, 2010).

Microscopy techniques are limited in their use in characterising PEG layers. SEM and TEM require a substantial number of particles to be analysed to achieve statistical significance (Bonevich and Haller, 2010). Polymeric layers have the potential to collapse under vacuum,

undermining PEG layer assessment. Atomic force microscopy (AFM) is limited by the same factor. For this reason, microscopy is limited to measuring NP core size (Sitterberg et al., 2010).

Zeta potential (ζ) is the electrostatic potential of a NP at the interface of the bound layer of solvent molecules, ions and bulk liquid (Rabanel et al., 2014). A change in zeta potential following adsorption of PEGylated macromolecules has been observed (Redhead et al., 2001). A decrease in zeta potential can be attributed to increased surface coverage density of PEG chains leading to an increase in PEG layer thickness (Fenghua et al., 2004). Limitations exist in the application of zeta potential for assessing PEG layer thickness. Zeta potential is affected by pH, buffer type and salt concentration which can affect PEG layer (Ebbesen et al., 2013). Protein binding is controlled by PEG conformation and coverage density. Therefore, protein binding can be used as an indicator of PEG layer presence (Vonarbourg et al., 2006). Indirect methods can be a useful indicator of the presence of a PEG layer however, the lack of quantitative data provided remains a drawback.

1.12 Secondary Processing of Nano-dispersions

Isolation of nano-dispersions in their dried form is usually performed via spray drying or freeze drying. Liquid nano-dispersions have stability issues associated with their use, as mentioned above. This fact makes ensuring exact particle size upon storage difficult. In addition, the liquid media of nano-dispersions has a propensity to harvest microbial growth upon storage. The addition of antimicrobial preservatives within formulations has been reported to cause destabilization of nano-dispersions (Kobierski et al., 2011). For these reasons, solidification of nano-dispersions offers a means for advancing the commercial aspect of nano-formulations. The drying process should preserve redispersibility upon hydration. For this reason, redispersants are normally added such as sugars like sucrose, mannitol and lactose. During the development process a limited supply of material is a normal challenge, therefore streamlining and rationalising the selection process seems logical. Redispersibility should be assessed in both aqueous and acidic media (Kesisoglou et al., 2007).

1.12.1 Freeze Drying Nano-dispersions

Freeze drying is also known as lyophilisation, involves the removal of water from products without inflicting damage whilst enhancing redispersibility on storage (Tang and Pikal, 2004). A liquid suspension is cooled and ice crystals of pure water form. As freezing proceeds, an increasing amount of water freezes. This increases the concentration of any remaining liquid.

Increased concentration results in increased viscosity of the liquid which inhibits any further crystallisation. Any water that remains as a liquid and does not freeze is called bound water. The subsequent drying stage involves sublimation of ice from the frozen product. This results in the formation of a porous plug, where any remaining pores were previously occupied by ice crystals (Williams and Polli, 1984). The secondary drying step involves removal of absorbed water from the product. Freeze drying has the potential to induce change caused by the stress of freezing and dehydration, resulting in destabilization of nano-dispersions. Therefore, excipients are normally added to protect from freezing and drying stresses, increasing storage stability. Popular cryoprotectants added to nano-dispersions during freeze-drying include: mannitol, glucose, trehalose and sucrose.

1.12.2 Spray Drying of Nano-dispersions

Spray drying follows four stages: initial atomization of the liquid feed, mixing of the liquid with a hot drying gas, evaporation of the liquid followed by separation of dried particles from the drying gas. Particle characteristics can be manipulated via careful adjustment of process parameters. Parameters of interest include feed rate, inlet and outlet temperature, and feed composition. Spray drying is a robust process, lending itself to early small lab scale development. Zuo et al. (2013) produced fenofibrate nano-dispersions via wet milling followed by spray drying. Mannitol was employed as a matrix former. Their findings confirmed that irreversible aggregation could be minimised by using a low drug to mannitol ratio and an inlet temperature lower than the API melting point. However, comparison of the existing nano-crystalline commercial formulation with their spray dried nano-crystalline product, showed no difference in the *in vitro* and *in vivo* performance of the two (Zuo et al., 2013). Freag et al. (2013) developed diosmin nano-dispersions via an acid-base neutralisation technique. The addition of mannitol in the spray drying process as a matrix former was investigated. Using the *ex vivo* technique of the non everted sac, the diosmin liquid nano-dispersion showed improved permeation, whilst the spray dried nano-dispersion permeability was reliant upon the presence of mannitol. Those powders spray dried without mannitol exhibited inferior permeability to liquid nano-dispersions. However, those spray dried with mannitol had a performance comparable with that of the liquid nano-dispersions. Improved performance was attributed to the presence of mannitol and its ability to enhance redispersibility (Freag et al., 2013). Formulation of ITR NPs embedded within MPs for dry powders for inhalation was performed by Duret et al. (2012). Nano-dispersions were produced via HPH, followed by their solidification using spray drying with or without mannitol. Those ITR NPs spray dried with

mannitol had favourable aerodynamic properties and significantly improved ITR solubility (Duret et al., 2012).

MPs produced via spray drying tend to exist in an energetically unfavourable state as a result of their large surface area. Amorphous MPs will convert to a more energetically favourable state via crystallisation (Hak Kim and Igor, 2000) or polymorphic transition (Chan et al., 2004). Generation of a fully crystalline or amorphous material with high viscosity can overcome these issues (Gupta and Bansal, 2005). Incorporating molecules within a rigid amorphous matrix delays degradation by hindering translational motion. A water replacement strategy can also address stability issues (Maury et al., 2005). Partially crystalline systems are not desirable, as the more stable form has already been nucleated, with the remaining less stable fraction having an increased tendency to convert during storage, compromising stability. Crystallisation of the amorphous fraction expels water contained within the material, increasing the mobility of the remaining amorphous fraction and causing plasticisation, ultimately ending in crystallisation (Davidson et al., 2003). On scale up, materials which are sensitive to drying times may be susceptible to physical changes and hence instability, with increased drying times associated with larger dryers (Langrish, 2007).

1.13 Solid Dosage Forms

The term solid dosage form refers to tablets and capsules. Solid dosage forms represent 90% of all dosage forms used as delivery platforms for medicines. Tablets represent a diverse and convenient means for achieving therapeutic outcomes. Tablet types include: conventional compressed tablets, effervescent tablets, chewable tablets, vaginal tablets, enteric coated tablets, sugar coated tablets, film coated tablets, buccal and sublingual tablets, and multiple compressed tablets (Nagashree, 2015). There are three methods by which tablets are manufactured: wet granulation, dry granulation and direct compression (Qui et al., 2017). Numerous excipients are included in tablet formulation to optimise processing or tailor *in vivo* performance. Excipients commonly used in the manufacture of tablets include diluents or fillers such as lactose monohydrate, binders e.g. sucrose, disintegrants such as starch, lubricants e.g. magnesium stearate and PEG, and glidants such as colloidal silicon dioxide (Nagashree 2015).

Conventional compressed tablets offer rapid disintegration making them a popular choice for therapeutic medicines. Following ingestion, they disintegrate in the gastric media of the stomach and are absorbed systemically. Effervescent tablets are added to water prior to

administration, where they rapidly disintegrate generating a suspension or solution. A chemical reaction takes place when they are added to water whereby evolution of carbon dioxide occurs. The ingestion of this suspension or solution results in rapid absorption of the therapeutic compound. On the other hand, these tablets require higher grade packaging due to their moisture sensitivity (Jacob et al., 2009). Chewable tablets are chewed inside the mouth before being swallowed. They are often used for patients who have swallowing difficulties including children and the elderly. These dosage forms are not ideal for formulations whereby taste acceptability is an issue (Suzuki et al., 2003). Vaginal tablets are designed for direct insertion into the vagina. After they are inserted, they are retained and slow dissolution of the drug follows at the target site of a local bacterial or fungal infection (Wang and Tang, 2008). Enteric coated tablets have a polymer coating preventing their dissolution in acidic conditions (stomach), enabling their dissolution to take place in alkaline conditions of the intestine. In this way, APIs are protected from degradation and irritating the gastric mucosa. Examples of polymers used for this purpose include cellulose acetate phthalate and methacrylic acid co-polymers (Eudragit®) (Nykanen et al., 2001). Sugar coated tablets are coated in a concentrated sugar solution which helps to improve their palatability (Sohi et al., 2004). Film coated tablets are those which have been coated in a polymer or mixture of polymers. Film coatings have superior mechanical properties compared with sugar coated equivalents. Polymers typically used for this application include hydroxypropylmethylcellulose and Eudragit E100. Film coatings offer the advantage of targeted drug release in the GI tract, as well as tailored duration and rate of release (Lee et al., 1999; Cerea et al., 2004). Buccal and sublingual tablets are those which are retained within the mouth followed by slow dissolution. Systemic absorption is achieved via absorption through the buccal mucosa. Buccal tablets are normally held between the cheek and gingiva, whereas sublingual tablets are intended to be held under the tongue. These tablets are ideal for situations where oral drug delivery is not suitable, such as in the treatment of nausea. Drug absorption across the buccal mucosa avoids first pass metabolism (Andrews et al., 2009). Multiple compressed tablets consist of at least two layers. They are often used in cases where drugs have to be separated if they are incompatible when formulated as a single layer. They can also be used to deliver drugs to different sites within the GI tract or at different release rates (Vaithiyalingam and Sayeed, 2010).

1.13.1 Advantages of Tablets

Tablets as dosage forms have a number of advantages associated with their use. Namely, they are extremely convenient to use leading to greater patient acceptability and compliance.

Tablet design can be tailored to achieve the desired rate and duration of drug release. With controlled drug release this can lead to dose reduction and therefore better patient compliance. Tablets provide a means for targeted release within the GI tract. This can achieve local action at the target site, reduce side effects and promote optimal absorption (Aulton and Taylor, 2017). More than one therapeutic active can be formulated into a single tablet, also known as fixed dosed combination products. In this way, polypharmacy is reduced and patients with multiple co-morbidities are more likely to remain adherent with treatment regimens (Agrawal et al., 2002). Tablets are a convenient means for masking the unpleasant taste of medicines via coating. Tablets are an inexpensive dosage form to manufacture, with lower costs being passed onto the consumer. Tablets exhibit superior, chemical and physical stability compared to other dosage forms (Aulton and Taylor, 2017). However, there are also a number of drawbacks associated with tablets. The tablet manufacturing process is often made up of a number of steps, with product being lost during each step. Absorption from tablets is subject to inter patient variation and other physiological factors. Not all materials have good compression properties. Swallowing difficulties in certain patient groups means administration of tablets is not always possible (Jones, 2008).

1.13.2 METHODS OF TABLET MANUFACTURE

The method of tablet manufacture is dependent upon the excipients to be included in the formulation, cost of the process, stability of the API during the process and available resources (Jones, 2008). This thesis focuses on the production of tablets via direct compression (DC). DC is generally preferred over wet or dry granulation as the increased number of unit operations associated with the latter, can be costly from a time and money perspective (Shangraw, 1989). On a large scale, DC involves mixing of powder followed by compression of the powder bed. The process is comprised of four main stages. The different components of the formulation are normally milled. Particle size distribution is an important determinant for the compression properties of the material. Particle reduction is performed by rotation of blades, with particle size distribution manipulation achieved via alteration of rotary speed and blade morphology. The next step involves mixing the API with the remaining formulation excipients in a mixing chamber. Examples of commonly used mixers include a planetary bowl mixer or a rotating drum mixer. The final step of the process involves compression of the powder bed forming the tablets. Compression itself begins with the powder being fed into the die from a hopper. Subsequently, repositioning of the lower and upper punch modifies the volume of space occupied by the powder. The upper punch is descended towards the powder bed, a stress is

applied and tablet is formed. Tablet hardness can be modified by altering the stress applied. The final stage of tablet ejection occurs by elevating the upper punch. The lower punch is raised until it is flush with the die plate of the tablet press (Aulton and Taylor, 2017). There are two types of tablet press: a single punch press and a rotary press. A single punch press is ideal for small lab scale studies and was used to carry out the work detailed in this thesis. Rotary press can produce up to 10,000 tablets per minute, compared to 200 per minute for a single punch press. For this reason, rotary press is the gold standard for large scale manufacture of tablets. This type of press operates by a slight different mechanism whereby a series of upper and lower punches are held within a circular die table that rotates in a circular way. Upper and lower punches are lowered and raised by rollers (Charlton and Newton, 1984).

Compression of powder results in cohesion. Following the application of stress particles will undergo elastic deformation. Deformation of the crystalline and amorphous structure of particles occurs. If the stress is released at this stage, the structure will return to its equilibrium position. If the material is elastic in nature, delamination and tablet failure will result. Therefore, the stress applied must exceed that required to achieve elastic deformation. Plastic deformation follows caused by the movement of molecules in the direction of stress. This irreversible deformation results in good cohesion between particles and limited structural recovery. Fragmentation will destroy intra-particle bonds resulting in many smaller particles. The more stress that is applied, the more fragmentation that will occur. Tablets formed via fragmentation are resistant to the effects of other excipients (Jones, 2008). When a powder bed undergoes compression, the application of stress causes rearrangement of the powder bed to reduce free space between particles. The degree of rearrangement that takes place is determined by particle size and frictional forces. Subsequently, particles undergo deformation with the materials' physicochemical properties dictating the predominant deformation mechanism (Jivraj et al., 2000). When the required stress is applied, inter-particle bonding will occur resulting in the formation of a tablet. Bonding can occur via adsorption or diffusion. When bonding via adsorption occurs, the repulsive forces between neighbouring particles is overcome bringing the particles into close contact. Van der Waals forces are the predominant force at play. This is the most common type of bonding involved in tablet formation. Bonding by diffusion will occur when sufficient molecular mobility exists at the particle surface, as a result of melting or rubbery properties of the material when compressed. Increased mobility allows for interaction between particles (Jones, 2008).

1.13.3 Potential Issues during the Tabletting Process

Pitting, lamination and capping are all defects that can arise during the tableting process. Pitting refers to the presence of pit marks on the tablet surface. This can result due to insufficient lubricant or damage to the punch itself. Punches should be polished regularly to avoid this issue. Capping involves tablet fracture from the top of the tablet, whereas lamination is when fracture occurs within the main body of the tablet. Capping and lamination tend to occur during ejection and are normally stress induced. Increasing compression pressure can lead to production of a tablet with greater mechanical strength, however the application of excessive pressure can cause capping and lamination (Naito et al., 1977). Storage and packaging of tablets requires careful consideration. Water adsorption within the porous structure of a tablet can cause dissolution and recrystallisation of formulation components. Crystallisation can increase interaction within the powder, and hence act as solid bridges. The presence of moisture can also cause crystallisation of amorphous regions within the tablet or alter the polymorphic state of its constituents. Moisture can also compromise tablet strength due to disruption of interactions between particles and dissolution. Water can also cause stress relaxation of viscoelastic formulation components (Amidon and Houghton, 1995). Polymers are a classic example of viscoelastic materials that will undergo structural relaxation over time following removal of the stress. Polymer chains are capable of rearranging which can decrease the structural integrity of the tablet (Jones, 2008).

1.14 Tabletting of Nano-dispersions

To date, there has been little research into the solidification and development of oral dosage forms for nano-dispersions (Vergote et al., 2001; Basa et al., 2008; Mauludin et al., 2009; Parmentier et al., 2017). There are a number of factors influencing tabletability of a material that need careful consideration. These include particle size, excipient type and amount, type and amount of coating agent, as well as speed and magnitude of applied compaction pressure (Celik, 1994). The ideal oral dosage form should have adequate tensile strength accompanied by a fast disintegration rate. Particle size has a profound impact upon tablet properties. Generally, a material with smaller particle size leads to the production of tablets with increased tensile strength. This property is inherent of increased bonding due to a greater number of contact points between particles of smaller size (He, 2009). During consolidation of a powder bed, tensile strength will increase to a limit, beyond which any further increase in compaction pressure will lead to over compaction and decline in tensile strength (Tye et al., 2005). Disintegration should increase as tensile strength increases, however a certain level of

tensile strength will eventually result in a slower disintegration rate. The application of pressure during compaction can result in structural change of the material. With nano-dispersions, coalescence of nanocrystals can occur, in addition to agglomeration. In turn, any particle growth can have a negative effect on disintegration rate. Addition of an appropriate stabilizer can overcome this issue. Compactability profiles do not follow a linear relationship over a range of compaction pressures. A delicate balance must be achieved where a tablet of adequate tensile strength continues to deliver enhanced dissolution (Tan et al., 2017). Each step of the manufacturing process has the opportunity to alter the properties of the final dosage form. The enhanced dissolution rate offered by nano-dispersions should be preserved throughout this process.

Tan et al. (2017) formed compressed tablets via layering of ITR nano-suspensions onto sugar beads using different ratios of cushioning and disintegration agents. Screening resulted in the production of compacts of adequate tensile strength and drug release of 99% within 10 minutes (Tan et al., 2017). Tuomela at al. (2015) demonstrated the up-scaling of nano-crystallisation batch size. They employed wet milling, freeze drying followed by direct compression and granulation of tablet masses for the manufacture of ITR and indomethacin tablets. They concluded that the amount of the nanocrystals in the final solid tablet formulation was critical to fully utilize the fast dissolution of those nanocrystals. Those formulations which were produced via the DC method outperformed those which where granulated. This research demonstrates the industrial feasibility of nanocrystal up-scale (Tuomela et al., 2015). Dolenc et al. (2009) developed celecoxib nano-dispersions using an emulsion-diffusion method, followed by their transformation into powders for tableting via spray drying. Results confirmed that solvent and stabilizer selection dictate the crystallisation process and wettability of the API. Transformation of celecoxib into the nano-metre size range translated into an increase in dissolution rate compared with micron-sized equivalents. Furthermore, lower compaction forces were required to produce tablets of equal tensile strength for nano-sized celecoxib compared to micron-sized celecoxib (Dolenc and Kristl, 2009). Mauludin et al. (2008) produced rutin nanocrystals for tabletting via lyophilisation. Tablets were formed using DC. Rutin nanocrystal loaded tablets released and fully dissolved within 30 minutes, compared to 71 and 55% of total rutin amount for microcrystal loaded and marketed tablets. Once again, downstream processing of nano-dispersions into solid oral dosage forms proved to be a viable approach for enhancing the bioavailability of a poorly soluble compound (Mauludin et al., 2009). Vergote et al. (2001) transformed aqueous nanocrystal colloidal dispersions of ketoprofen into solid dosage forms using spray drying.

Nano-crystalline ketoprofen was loaded onto wax based pellets produced using a melt pelletisation technique. The end product was an oral dosage form capable of delivering complete and controlled release of ketoprofen (Vergote et al., 2001). TriCor® and Triglide® (fenofibrate) are commercially available examples of nano-crystalline tablet products.

1.15 Issues Associated with NP Use

The pharmacological advantages associated with NP use are accompanied by potential toxicological side effects. Increased surface area makes NPs reactive species within the cellular environment (Donaldson et al., 2006). NPs are capable of entering the human body via a number of sites including the skin, lungs and GI tract. This thesis focuses on the issues associated with GI tract entry, as the others remain outside the scope of this work. NPs also have the potential to deposit and accumulate in specific organs and sites within the body. Hence, adverse biological adverse reactions can follow (Oberdörster et al., 2005). NP toxicity will be determined by their clearance rate from organs and the host response mounted in dealing with their presence (Medina et al., 2009).

Entry into the GI tract is possible via direct ingestion of drugs or from their clearance from the respiratory tract (Hoet et al, 2004). Uptake in the GI tract is a kinetic process, whereby a number of events take place. Namely, diffusion and accessibility through mucus, contact with enterocytes, cellular trafficking and post-translocation events (Medina et al., 2009). Reduction in particle size increases the rate of diffusion from GI secretions through to colonic enterocytes (Szentkuti, 1997). This is followed by translocation to the blood stream and distribution throughout the body (Jani et al., 1990). Chen et al. (2006) have reported heavy assault to the kidney, liver and spleen of mice. As well as adverse effects caused by oral ingestion of copper NPs (Chen et al., 2006).

Despite the initial promise of nanotechnology, few commercially available nano-formulations have reached the market. Examples have been discussed in Section 1.4. There are a number of reasons for this, including growing concerns regarding toxicity and safety associated with NP application. In response to this, there has been a co-ordinated effort to address these issues. The US federal government published a research plan for nano-safety research in 2008 (Initiative, 2008). Meanwhile in Europe, there are intense research efforts under Horizon 2020. This framework outlines nano-safety topics as being a critical part of its Nanotechnologies, Materials and Production Technologies (NMP) programme (Maynard and Aitken, 2016). In addition, in 2004 the National Cancer Institute (NCI), along with the FDA and National Institute

of Standards and Technology (NIST), established the Nanotechnology Characterization Laboratory (NCL). The goal of this organisation is to standardise preclinical characterisation of nano-medicines, as well as identifying key parameters of NP toxicological behaviour (Tinkle et al., 2014). NP fabrication can also be associated with batch to batch variability during the manufacturing process, making scale up and commercialisation difficult from an industrial perspective (Landesman-Milo and Peer, 2016).

References

Agrawal, S., Kaur, K.J., Singh, I., Bhade, S.R., Kaul, C.L., Panchagnula, R., 2002. Assessment of bioequivalence of rifampicin, isoniazid, pyrazinamide in a four drug fixed dose combination with separate formulations at the same dose levels. Int. J. Pharm. 233, 169-177.

Amidon, G.E., Houghton, M.E., 1995. The effect of moisture on the mechanical and powder flow properties of microcrystalline cellulose. Pharm. Res. 12, 923-929.

Andrews, D.R., Leong, W., Sudhakar, A., 2004. United States Patent US006958337B2. Andrews, G.P., Laverty, T.P., Jones, D.S., 2009. Mucoadhesive polymeric platforms for controlled drug delivery. Eur. J. Pharm. Biopharm. 71, 505-518.

Aulton, M.E., Taylor, K.M.G., 2017. Chapter 1 – Design of dosage forms, in: Aulton's Pharmaceutics, International Edition: The Design and Manufacture of Medicines. pp. 9-10.

Anton, N., Jakhmola, A., Vandamme, T.F., 2012. Trojan microparticles for drug delivery. Pharmaceutics. 4, 1–25.

Auweter, H., André, V., Horn, D., Lüddecke, E., 1998. The function of gelatin in controlled precipitation processes of nanosize particles. J. Dispers. Sci. Technol. 19, 163–184.

Basa, S., Muniyappan, T., Karatgi, P., Prabhu, R., Pillai, R., 2008. Production and *in vitro* characterization of solid dosage form incorporating drug nanoparticles. Drug Dev. Ind. Pharm. 34, 1209–1218.

Bonevich, J.E., Haller, W.K., 2010. Measuring the size of nanoparticles using transmission electron microscopy (TEM). NSIT-NCL Jt. Assay Protoc. PCC-7, ver 1.1.

Bushrab, N.F., 2005. Pharmazeutische Technologie. Berlin: Freie Universität; PhD Thesis (in preparation)

Butler, J.M., Dressman, J.B., 2010. The Developability Classification System: Application of Biopharmaceutics Concepts to Formulation Development. J. Pharm. Sci. 99, 4940–4954.

Carstensen, J.T., 2001. Solubility Advanced pharmaceutical solids: Marcel Dekker.

Celik, M., 1994. Compaction of Multiparticulate Oral Dosage Forms, Multiparticulate Oral Drug Delivery., in: CRC Press. pp. 181–215.

Cerea, M., Zheng, W., Young, C.R., McGinity, J.W., 2004. A novel powder coating process for attaining taste masking and moisture protective films applied to tablets. Int. J. Pharm. 279, 127-139.

Chan, H.K., Clark, A.R., Feeley, J.C., Kuo, M.C., Russ Lehrman, S., Pikal-Cleland, K., Miller, D.P., Vehring, R., Lechuga-Ballesteros, D., 2004. Physical Stability of Salmon Calcitonin Spray-Dried Powders for Inhalation. J. Pharm. Sci. 93, 792–804.

Charlton, B., Newton, J.M., 1984. Theoretical estimation of punch velocities and displacements of single puch and rotary tablet machines. J. Pharm. Pharmacol. 36, 645-651.

Chen, Z., Meng, H., Xing, G., Chen, C., Zhao, Y., Jia, G., et al., 2006. Acute toxicological effects of copper nanoparticles in vivo. Toxicol Lett. 163, 109–120.

Choi, J., Youn, J., Kwak, H., Uk, B., Lee, J., 2005. Role of polymeric stabilizers for drug nanocrystal dispersions. Curr. Appl. Phys. 5, 472–474.

Contado, C., 2017. Field flow fractionation techniques to explore the “nano-world.” Anal. Bioanal. Chem. 2501–2518.

Crowley K.J., Z.G., 2002. Cryogenic grinding of indomethacin polymorphs and solvates: assessment of amorphous phase formation and amorphous phase physical stability. J Pharm. Sci. 91, 492–507.

Davidson, I.G., Langner, E.J., Plowman, S. V, Blair, J.A., 2003. Release mechanism of insulin encapsulated in trehalose ester derivative microparticles delivered via inhalation. Int. J. Pharm. 254, 211–222.

Dolenc, A., Kristl, J., 2009. Advantages of celecoxib nanosuspension formulation and transformation into tablets. Pharm. Nanotechnol. 376, 204–212.

Donaldson, K., Aitken, R., Tran, L., Stone, V., Duffin, R., Forrest, G., et al., 2006. Carbon nanotubes: a review of their properties in relation to pulmonary toxicology and workplace safety. Toxicol. Sci. 1, 5–22.

Dragovic, R.A., Gardiner, C., Brooks, A.S., Tannetta, D.S., Ferguson, D.J.P., Hole, P., Carr, B., Redman, C.W.G., Harris, A.L., Dobson, P.J., Harrison, P., Sargent, I.L., 2011. Sizing and phenotyping of cellular vesicles using Nanoparticle Tracking Analysis. Nanomedicine Nanotechnology, Biol. Med. 7, 780–788.

Dressman, J.B., Reppas, C., 2000. In vitro-in vivo correlations for lipophilic, poorly water-

soluble drugs. Eur. J. Pharm. Sci. 11, 73–80.

Duret, C., Wauthoz, N., Sebti, T., Vanderbist, F., Amighi, K., 2012. New inhalation-optimized itraconazole nanoparticle-based dry powders for the treatment of invasive pulmonary aspergillosis. Int. J. Nanomedicine 7, 5475–5489.

Ebbesen, M.F., Whitehead, B., Ballarin-Gonzalez, ., B., Kingshott, P., Howard, K.A., 2013. Surface analysis of PEGylated nano-shields on nanoparticles installed by hydrophobic anchors. Pharm. Res. 1–10.

Einstein, A., 1905. Über einen die Erzeugung und Verwandlung des Lichtes betreffenden heuristischen Gesichtspunkt. Ann. Der. Phys. 322, 132–148.

El-Sherbiny, I.M., Abdel-Mogib, M., Dawidar, A.A.M., Elsayed, A., Smyth, H.D.C., 2011. Biodegradable pH-responsive alginate-poly (lactic-co-glycolic acid) nano/micro hydrogel matrices for oral delivery of silymarin. Carbohydr. Polym. 83, 1345–1354.

Evans, J.C., Scherzer, B.D., Tocco, C.D., Kupperblatt, G.B., Becker, J.N., Wilson, D.L., Saghir, S., Elder, E.J., 2006. Preparation of Nanostructured Particles of Poorly Water Soluble Drugs via a Novel Ultrarapid Freezing Technology. ACS Symposium Series. 924, 320-328.

Farrokhpay, S., 2009. A review of polymeric dispersant stabilisation of titania pigment. Adv. Colloid Interface Sci. 151, 24–32.

FDA, 2013. Clinical Pharmacology and Biopharmaceutics Review. Application Number: 205053Orig1s000.

FDA, 2017. Waiver of In Vivo Bioavailability and Bioequivalence Studies for Immediate-Release Solid Oral Dosage Forms Based on a Biopharmaceutics Classification System: Guidance for Industry.

Fenghua, M., M., E.G.H., Jan, F., 2004. Polyethylene glycol–grafted polystyrene particles. J. Biomed. Mater. Res. Part A 70A, 49–58.

Freag, M.S., Elnaggar, Y.S.R., Abdallah, O.Y., 2013. Development of novel polymer-stabilized diosmin nanosuspensions: In vitro appraisal and ex vivo permeation. Int. J. Pharm. 454, 462–471.

Freundlich, H., 1909. Kolloidchemie. Akad. Verlag, Leipzig.

Gallego-Urrea, J.A., Tuoriniemi, J., Hassellöv, M., 2011. Applications of particle-tracking analysis to the determination of size distributions and concentrations of nanoparticles in

environmental, biological and food samples. TrAC - Trends Anal. Chem. 30, 473–483.

Gerstner, W., 1966. Crystal form and particle size of organc pigments in printing inks and paints. J. Oil. Col. Chem. Assoc., 49, 954–973.

Ghosh, I., Schenck, D., Bose, S., Ruegger, C., 2012. Optimization of formulation and process parameters for the production of nanosuspension by wet media milling technique: Effect of Vitamin E TPGS and nanocrystal particle size on oral absorption. Eur. J. Pharm. Sci. 47, 718–728.

Gómez-Gaete, C., Fattal, E., Silva, L., Besnard, M., Tsapis, N., 2008. Dexamethasone acetate encapsulation into Trojan particles. J. Control. Release 128, 41–49.

Gonzáles-Caballero, F., de Dios Garciá López-Durán, J., 2000. Suspension formulation, in: Nielloud, F., Marti-Mestres, G. (Eds.), Pharmaceutical Emulsions and Suspensions, Drugs and the Pharmaceutical Sciences. pp, 127–190.

Gref, R., Domb, A., Quellec, P., Blunk, P.T., Müller, R.H., Verbavatz, J.M., Langer, R., 1995. The controlled intravenous delivery of drugs using PEG-coated sterically stabilized nanospheres. Adv. Drug Deliv. Rev. 16, 215–233.

Gupta, A.K., Wells, S., 2004. Surface-modified superparamagnetic nanoparticles for drug delivery: preparation, characterization, and cytotoxicity studies. 194. IEEE Trans Nanobioscience 3, 66–73.

Gupta, P., Bansal, A.K., 2005. Spray Drying for Generation of a Ternary Amorphous System of Celecoxib, PVP, and Meglumine. Pharm. Dev. Technol. 10, 273–281.

Hackey, V.A., Clogston, J.D., 2010. Measuring the size of nanoparticles in aqueous media using batch-mode dynamic light scattering. NIST-NCL Jt. Assay Protoc. PCC-1, version 1.2.

Hak-Kim, C., Igor, G., 2000. Solid state characterization of spray-dried powders of recombinant human deoxyribonuclease (RhDNase). J. Pharm. Sci. 87, 647–654.

Harding, S.E., Jumel, K., 1998. Light scattering. In: Coligan JE, Dunn BM, Ploegh HL, Speicher DW, Wingfield PT, editors. Current protocols in protein science. New York: John Wiley & Sons, I..

He, X., 2009. Integration of Physical, Chemical, Mechanical, and Biopharmaceutical Properties in Solid Oral Dosage Form Development, in: Qiu, Y., Chen, Y., Zhang, G.G.Z., Liu, L., Porter, W.R. (Eds.), Developing Solid Oral Dosage Forms. Academic Press, San Diego, pp. 407–

441.

Hoet, P.H., Bruske-Hohlfeld, I., Salata, O.V., 2004. Nanoparticles – known and unknown health risks. J. Nanobiotechnol. 2, 12.

Hörter, D., Dressman, J.B., 2001. Influence of physicochemical properties on dissolution of drugs in the gastrointestinal tract. Adv. Drug Deliv. Rev. 46, 75–87.

Ingham, B., Lim, T.H., Dotzler, C.J., Henning, A., Toney, M.F., Tilley, R.D., 2011. How Nanoparticles Coalesce : An in Situ Study of Au Nanoparticle Aggregation and Grain Growth. Chem. Mater. 23, 3312–3317.

Initiative, N.N., 2008. Strategy for Nanotechnology-Related Environmental, Health and Safety Research.

International Organization for Standardization, 2008. Nanotechnologies: Terminology and Definitions for Nano-objects. Nanoparticle Nanofibre and Nanoplate; ISO/TS 27687. Geneva, Switzerland.

Jacob, S., Shirwaikar, A., Nair, A., 2009. Preparation and evaluation of fast disintegrating effervescent tablets of glibenclamide. Drug Development and Industrial Pharmacy. 35, 321-328.

Jani, P., Halbert, G.W., Langridge, J., Florence, A.T., 1990. Nanoparticle uptake by the rat gastrointestinal mucosa: quantitation and particle size dependency. J Pharm Pharmacol. 42, 821–82.

Jivraj, M., Martini, L.G., Thomson, C.M., 2000. An overview of the different excipients useful for the direct compression of tablets. Pharmaceutical Science and Technology Today. 3, 58-63.

Jones, D., 2008. Chapter 9 - Solid dosage forms 1: tablets, in: Pharmaceutics - Dosage Form and Design. pp. 203–253.

Junghanns, J.U., Müller, R.H., 2008. Nanocrystal technology, drug delivery and clinical applications. Int. J. Nanomedicine 3, 295–310.

Keck, C.M., Müller, R.H., 2006. Drug nanocrystals of poorly soluble drugs produced by high pressure homogenisation. Eur. J. Pharm. Biopharm. 62, 3–16.

Kesisoglou, F., Panmai, S., Wu, Y., 2007. Nanosizing - Oral formulation development and biopharmaceutical evaluation. Adv. Drug Deliv. Rev. 59, 631–644.

Kholodenko, A.L., Douglas, J.F., 1995. Generalized Stokes-Einstein equation for spherical particle suspensions. Phys. Rev. E 51, 1081–1090.

Kim. C.J., 2004. Surface chemistry and colloids, Advanced pharmaceutics: physicochemical principles, in: CRC Press. CRC Press, pp. 193–256.

Kirchner, H.O., 1971. Coarsening of grain-boundary precipitates. Metall. Trans. 2, 2861–2864.

Kobierski, S., Ofori-Kwakye, K., Muller, R.H., Keck, C.M., 2011. Reserveratrol nanosuspensions: interaction of peservatives with nanocrystal production. Pharmazie 66, 942–947.

Kuentz, M., 2018. Drug Supersaturation during drug formulation digestion, including real time analytical approaches. Advanced Drug Delivery Reviews, In Press.

Landesman-Milo, D., Peer, D., 2016. Transforming Nanomedicines From Lab Scale Production to Novel Clinical Modality. Bioconjug. Chem. 27, 855–862.

Langrish, T.A.G., 2007. New Engineered Particles from Spray Dryers: Research Needs in Spray Drying. Dry. Technol. 25, 971–983.

Lee, B.J., Ryu, S.G., Cui, J.H., 1999. Controlled release of dual drug loaded hydroxypropyl methylcellulose matrix tablet using drug containing polymeric coatings. Int. J. Pharm. 188, 71-80.

Lee, J., Choi, J.Y., Park, C.H., 2008. Characteristics of polymers enabling nano-comminution of water-insoluble drugs. Int. J. Pharm. 355, 328–336.

Lipinski, C., 2002. Poor aqueous solubility - An industry wide problem in drug discovery, American Pharmaceutical Review. 5, 82-85.

Liz-marza, L.M., Giersig, M., Mulvaney, P., 1996. Synthesis of Nanosized Gold - Silica Core - Shell Particles. 7463, 4329–4335.

LVIII., S.J., 1871. On the scattering of light by small particles. Philos. Mag. Ser. 4, 447–454.

Maged, A., Mahmoud, A.A., Ghorab, M.M., 2016. Nano spray drying technique as a novel approach to formulate stable econazole nitrate nanosuspension formulations for ocular use. Mol. Pharm. 13, 2951–2965.

Martin, F.A., Mihaela, M.P., Borodi, G., Filip, X., Kacso, I., 2013. Ketoconazole salt and co-crystals with enhanced aqueous solubility. Cryst. Growth Desgin. 10, 4295-4304.

Mauludin, R., Müller, R.H., Keck, C.M., 2009. Development of an oral rutin nanocrystal

formulation. Int. J. Pharm. 370, 202–209.

Maury, M., Murphy, K., Kumar, S., Mauerer, A., Lee, G., 2005. Spray-drying of proteins: effects of sorbitol and trehalose on aggregation and FT-IR amide I spectrum of an immunoglobulin G. Eur. J. Pharm. Biopharm. 59, 251–261.

Maynard, A.D., Aitken, R.J., 2016. "Safe handling of nanotechnology" ten years on. Nat. Nanotechnol. 11, 998–1000.

Medina, C., Santos-Martinez, M.J., Radomski, A., Corrigan, O.I., Radomski, M.W., 2009. Nanoparticles: pharmacological and toxicological significance. Br. J. Pharmacol. 150, 552–558.

Mie, G., 1908. Beiträge zur Optik trüber Medien, speziell kolloidaler Metallösungen. Ann Phys. 330, 377–445.

Mingard, K., Morrell, R., Jackson, P., Lawson, S., Patel, S., Buxton, R., 2009. Good Practice Guide for Improving the Consistency of Particle Size Measurement. Natl. Phys. Lab. Washington, DC., 66.

Moeschwitzer, J., 2010. Nanotechnology: particle size reduction technologies in the pharmaceutical development process. Am. Pharm. Rev. 54–59.

Möschwitzer, J., Müller, R., 2007. Drug nanocrystals—the universal formulation approach for poorly soluble drugs., in: Nanoparticulate Drug Delivery Systems. Informa Healthcare. pp. 71–88.

Mugheirbi, N.A., Paluch, K.J., Tajber, L., 2014. Heat induced evaporative antisolvent nanoprecipitation (HIEAN) of itraconazole. Int. J. Pharm. 471, 400-411.

Mugheirbi, N.A., Tajber, L., 2015a. Mesophase and size manipulation of itraconazole liquid crystalline nanoparticles produced via a quasi nanoemulsion precipitation. Eur. J. Pharm. Biopharm. 96, 226-236.

Mugheirbi, N.A., Tajber, L., 2015b. Crystal habits of itraconazole microcrytsals: Unusual isomorphic intergrowths induced via tuning recrystallisation conditions. Mol. Pharm. 12, 3468-3478.

Müller, R.H., Möschwitzer, J., Bushrab, F.N., 2006. Manufacturing of nanoparticles by milling and homogenization techniques., in: Nanoparticle Technology for Drug Delivery, Drugs and the Pharmaceutical Sciences. pp. 21–51.

Müller, R.H., Gohla, S., Keck, C.M., 2011. State of the art of nanocrystals - Special features, production, nanotoxicology aspects and intracellular delivery. Eur. J. Pharm. Biopharm. 78, 1–9.

Mullin, J.W., Nývlt, J., 1971. Programmed cooling of batch crystallizers. Chem. Eng. Sci. 26, 369–377.

Naito, S.I., Masui, K., Shiraki, T., 1977. Predicition of tableting problems such as capping and sticking: theoretical calculations. J. Pharm. Sci. 66, 254-259.

Nagashree, K., 2015. Solid dosage forms: tablets. Research and Reviews: Journal of Pharmaceutical Analysis. 4, 60-71.

Namburi, R.R., Kerr, J.E., 2002. United States Patent WO2002062318A2.

Nichols, G., Byard, S., Bloxham, M.J., Botterill, J., Dawson, N.J., Dennis, A., Diart, V., North, N.C., Sherwood, J.D., 2002. A review of the terms agglomerate and aggregate with a recommendation for nomenclature used in powder and particle characterisation. J. Pharm. Sci. 91, 2103–2109.

Noyes, A.A., Whitney, R., 1897. The rate of solution of solid substances in their own solutions. J. Am. Chem. Soc. 19, 930–934.

Nykanen, P., Lempaa, S., Aaltonen, M.L., Jurjenson, H., Veski, P., Marvola, M., 2001. Citric acid as an excipient in muliple unit enteric coated tablets for targeting drugs on the colon. Int. J. Pharm. 229, 155-162.

Oberdörster, G., Maynard, A., Donaldson, K., Castranova, V., Fitzpatrick, J., Ausman, K., et al., 2005. Principles for characterizing the potential human health effects from exposure to nanomaterials: elements of a screening strategy. Part. Fibre. Toxicol. 2, 8.

Ostwald, W., 1900. Über die vermeintliche Isomerie des roten und gelben Quesck-silberoxyds und die Oberflachenspannung fester Körper. Z.Phys. Chem. 34, 495–503.

Otsuka, H., Nagasaki, Y., Kataoka, K., 2003. PEGylated nanoparticles for biological and pharmaceutical applications. Adv. Drug Deliv. Rev. 55, 403–419.

Owens D.E., Peppas, N.A., 2006. Opsonization, biodistribution,and pharmacokinetics of polymeric nanoparticles. Int. J. Pharm. 307, 93–102.

Palla, B.J., Shah, D.O., 2002. Stabilization of High Ionic Strength Slurries Using Surfactant Mixtures: Molecular Factors That Determine Optimal Stability. J. Colloid Interface Sci.

256, 143–152.

Parmentier, J., Tan, E.H., Low, A., Moeschwitzer, J.P., 2017. Down-stream drug product processing of itraconazole nanosuspension: Factors influencing drug particle size and dissolution from nanosuspension-layered beads. Int. J. Pharm. 524, 443–453.

Patravale, V. B., Date Abhijit, A., Kulkarni, R.M., 2010. Nanosuspensions: a promising drug delivery strategy. J. Pharm. Pharmacol. 56, 827–840.

Peltonen, L., Hirvonen, J., 2010. Pharmaceutical nanocrystals by nanomilling: critical process parameters , particle fracturing and stabilization methods. J. Pharm. Pharmacol. 56, 1569–1579.

Percival, K.M., Bergman, S.J., 2014. Update on posaconazole pharmacokinetics: Comparsion of old and new formulations. Curr. Fungal Infect. Rep. 8, 139-145.

Perry, J.L., Reuter, K.G., Kai, M.P., Herlihy, K.P., Jones, S.W., Luft, J.C., Napier, M., Bear, J.E., DeSimone, J.M., 2012. PEGylated PRINT Nanoparticles: The Impact of PEG Density on Protein Binding, Macrophage Association, Biodistribution, and Pharmacokinetics. Nano Lett. 12, 5304–5310.

Ploehn, H.J., Russel, W.B., 1990. Interactions Between Colloidal Particles and Soluble Polymers, in: Wei, J.B.T.-A. in C.E. (Ed.), . Academic Press, pp. 137–228.

Ponchel, G., Montisci, M.J., Dembri, A., Durrer, C., Duchêne, D., 1997. Mucoadhesion of colloidal particulate systems in the gastro-intestinal tract. Eur. J. Pharm. Biopharm. 44, 25–31.

Prajapati, H.N., Dalrymple, D.M., Serajuddin, A.T.M., 2012. A Comparative Evaluation of Mono, Di and Triglyceride of Medium Chain Fatty Acids by Lipid/Surfactant/Water Phase Diagram, Solubility Determination and Dispersion Testing for Application in Pharmaceutical Dosage Form Development. Pharm. Res. 29, 285–305.

Qiao, H., Chen, L., Rui, T., Wang, J., Chen, T., Fu, T., Li, J., Di, L., 2017. Fabrication and in vitro/in vivo evaluation of amorphous andrographolide nanosuspensions stabilized by d-α-tocopheryl polyethylene glycol 1000 succinate/sodium lauryl sulfate. Int. J. Nanomedicine 12, 1033–1046.

Qui, Y., Chen, Y., Zhang, G.G.Z., Yu, L., Mantri, R.V., 2017. Developing solid oral dosage forms. Pharmcaeutical Theory and Practice. Part III.

Quintanar-Guerrero, D., Ganem-Quintanar, A., Allémann, E., Fessi, H., Doelker, E., 1998. Influence of the stabilizer coating layer on the purification and freeze-drying of poly(D, L-lactic acid) nanoparticles prepared by an emulsion-diffusion technique. J. Microencapsul. 15, 107–119.

Rabanel, J.M., Hildgen, P., Banquy, X., 2014. Assessment of PEG on polymeric particles surface, a key step in drug carrier translation. J. Control. Release 185, 71–87.

Rabinow, B.E., 2004. Nanosuspensions in drug delivery. Nat. Rev. Drug Discov. 3, 785.

Rasenack, N., Muller, B.W., 2002. Dissolution rate enhancement by *in situ* micronization of poorly water soluble drugs. Pharmaceutical Research 19, 1894-1900.

Raula, J., Eerikäinen, H., Kauppinen, E.I., 2004. Influence of the solvent composition on the aerosol synthesis of pharmaceutical polymer nanoparticles. Int. J. Pharm. 284, 13–21.

Redhead, H.M., Davis, S.S., Illum, L., 2001. Drug delivery in poly(lactide-co-glycolide) nanoparticles surface modified with poloxamer 407 and poloxamine 908: in vitro characterisation and in vivo evaluation. J. Control. Release 70, 353–363.

Richard, J., Benoit, J.P., 2000. Microencapsulation, in: Tech. l'ingénieur. pp. 1–20.

Santos-Martinez, M.J., Rahme, K., Corbalan, J.J., Faulkner, C., Holmes, J.D., Tajber, L., Medina, C., Radomski, M.W., 2014. Pegylation increases platelet biocompatibility of gold nanoparticles. J. Biomed. Nanotechnol. 10, 1004–15.

Sapra, P., Tyagi, P., Allen, T.M., 2005. Ligand-targeted liposomes for cancer treatment. Curr. Drug. Deliv. 2, 369–381.

Sawant, R.R., Sawant, R.M., Kale, A.A., Torchilin, V.P., 2008. The architecture of ligandattachment to nanocarriers controls their specific interactionwith target cells. J. Drug. Target. 16, 596–600.

Shah, D.A., Murdande, S.B., Dave, R.H., 2016. A Review: Pharmaceutical and Pharmacokinetic Aspect of Nanocrystalline Suspensions. J. Pharm. Sci. 105, 10–24.

Shah, P., 2006. Use of Nanotechnologies for Drug Delivery. MRS Bull. 31, 894–899.

Shah, V.P., Amidon, G.L., 2014. G.L. Amidon, H. Lennernas, V.P. Shah, and J.R. Crison. A Theoretical Basis for a Biopharmaceutic Drug Classification: The Correlation of In Vitro Drug Product Dissolution and In Vivo Bioavailability. AAPS J. 16, 894–898.

Shangraw, R.F., 1989. Chapter 4 - Compressed tablets by direct compression, in: Pharmaceutical dosage forms:Tablets. pp. 198-199.

Shegokar, R., Müller, R.H., 2010. Nanocrystals: Industrially feasible multifunctional formulation technology for poorly soluble actives. Int. J. Pharm. 399, 129–139.

Shete, G., Jain, H., Punj, D., Prajapat, H., Akotiya, P., 2014. Stabilizers used in nano-crystal based drug delivery systems . J. Excipients Food Chem. 5, 184–210.

Sinha, B., Muller, R.H., Moschwitzer, J.P., 2013. Bottom-up approaches for preparing drug nanocrystals: Formulations and factors affecting particle size. Int. J. Pharm. 453, 126–141.

Sitterberg, J., Özcetin, A., Ehrhardt, C., Bakowsky, U., 2010. Utilising atomic force microscopy for the characterisation of nanoscale drug delivery systems. Eur. J. Pharm. Biopharm. 74, 2–13.

Soriano, L.M., Zougagh, M., Valcárcel, M., Ríos, Á., 2018. Analytical Nanoscience and Nanotechnology: Where we are and where we are heading. Talanta. 177, 104–121.

Speight, M.V., 1968. Growth kinetics of grain-boundary precipitates. Acta. Metall. 16, 133–135.

Stetefeld, J., McKenna, S.A., Patel, T.R., 2016. Dynamic light scattering: a practical guide and applications in biomedical sciences. Biophys. Rev. 8, 409–427.

Stolnik, S., Dunn, s., Garnett, M., Davies, M., Coombes, A.A., Taylor, D.C., Irving, M.P., Purkiss, S.C., Tadros, T.F., Davis, S., Illum, L., 1994. Surface modification of poly(lactide-co-glycolide) nanospheres by biodegradable poly(lactide)-poly(ethylene glycol) co-polymers. Pharm. Res. 11, 1800–1808.

Suzuki, H., Onishi, H., Takahashi, Y., Iwata, M., Machida, Y., 2003. Development of oral acetaminophen chewable tablets with inhibited bitter taste. Int. J. Pharm. 251, 123-132.

Szentkuti, L., 1997. Light microscopical observations on luminally administered dyes, dextrans, nanospheres and microspheres in the pre-epithelial mucus gel layer of the rat distal colon. J Control Release. 46, 233–242.

Tan, E.H., Parmentier, J., Low, A., Möschwitzer, J.P., 2017. Downstream drug product processing of itraconazole nanosuspension: Factors influencing tablet material properties and dissolution of compacted nanosuspension-layered sugar beads. Int. J.

Pharm. 532, 131–138.

Tang, X., Pikal, M.J., 2004. Design of freeze-drying processes for pharmaceuticals: practical advice. Pharm. Res. 21, 191–200.

Thierry, B., Griesser, H.J., 2012. Dense PEG layers for efficient immunotargeting of nanoparticles to cancer cells. J. Mater. Chem. 22, 8810–8819.

Thote, A.J., Gupta, R.B., 2005. Formation of nanoparticles of a hydrophilic drug using supercritical carbon dioxide and microencapsulation for sustained release. Nanomedicine Nanotechnology, Biol. Med. 1, 85–90.

Tinkle, S., Mcneil, S.E., Mühlebach, S., Bawa, R., Borchard, G., Barenholz, Y.C., Tamarkin, L., Desai, N., 2014. Nanomedicines: Addressing the scientific and regulatory gap. Ann. N. Y. Acad. Sci. 1313, 35-56.

Tuomela, A., Laaksonen, T., Laru, J., Antikainen, O., Kiesvaara, J., Ilkka, J., Oksala, O., Rönkkö, S., Järvinen, K., Hirvonen, J., Peltonen, L., 2015. Solid formulations by a nanocrystal approach: Critical process parameters regarding scale-ability of nanocrystals for tableting applications. Int. J. Pharm. 485, 77–86.

Tye, C.K., Sun, C., Amidon, G.E., 2005. Evaluation of the effects of tableting speed on the relationships between compaction pressure, tablet tensile strength, and tablet solid fraction. J. Pharm. Sci. 94, 465–472.

Tyndall, J., 1868. On the Blue Colour of the Sky, the Polarization of Skylight, and on the Polarization of Light by Cloudy Matter Generally. Proc. R. Soc. London. 17, 223–233.

United States Pharmacopeia and National Formulary (USP 36 NF 31), The United States Pharmacopeial Convention, Rockville, M.D., U., 2013. Polyethylene glycol.

United States Pharmacopeia and National Formulary (USP 36 NF 31), The United States Pharmacopeial Convention, Rockville, M.D., U., 2013. Polyethylene glycol monomethyl ether.

Vaithiyalingham, S.R., Sayeed, V.A., 2010. Critical factors in manufacturing multi-layer tablets – Assessing material attributes, in-process controls, manufacturing process and product performance. Int. J. Pharm. 398, 9-13.

Van Eerdenbrugh, B., Van den Mooter, G., Augustijns, P., 2008. Top-down production of drug nanocrystals: Nanosuspension stabilization, miniaturization and transformation into

solid products. Int. J. Pharm. 364, 64–75.

Van Eerdenbrugh, B., Vermant, J., Martens, J.A., Froyen, L., Van Humbeeck, J., Augustijns, P., Van Den Mooter, G., 2009. A screening study of surface stabilization during the production of drug nanocrystals. J. Pharm. Sci. 98, 2091-2103.

Vergote, G.J., Vervaet, C., Van Driessche, I., Hoste, S., De Smedt, S., Demeester, J., Jain, R.A., Ruddy, S., Remon, J.P., 2001. An oral controlled release matrix pellet formulation containing nanocrystalline ketoprofen. Int. J. Pharm. 219, 81–87.

Verma, S., Gokhale, R., Burgess, D.J., 2009. A comparative study of top-down and bottom-up approaches for the preparation of micro/ nanosuspensions. Int. J. Pharm. 380, 216–222.

Vila, A., Gill, H., McCallion, O., Alonso, M.J., 2004. Transport of PLA-PEG particles across the nasalmucosa: effect of particle size and PEG coating density. J. Control. Release 98, 231–24.

Vonarbourg, A., Passirani, C., Saulnier, P., Benoit, J.P., 2006. Parameters influencing the stealthiness of colloidal drug delivery systems. Biomaterials. 27, 4356–4373.

Wagner, C.Z., 1961. Theory of precipitate change by redissolution. Elektrochem. 65, 581–591.

Wang, Y.; Chen, L.; Yang, H.; Guo, Q.; Zhou, W.; Tao, M., 2009. Spherical antireflection coatings by large area convective assembly of monolayer silica microspheres. Sol. Energy Mater. Sol. C. 93, 85–91.

Wang, L., Tang, X., 2008. A novel ketoconazole bioadhesive effervescent tablet for vaginal delivery: Design, in vitro and 'in vivo' evaluation. Int. J. Pharm. 350, 181-187.

Wichmann, H., Wuesthoff, H., Schweigerstrasse, W., 2007. European Patent Number, EP 2,343,053,A1.

Wieser, J., Pichler, A., Hotter, A., Griesser, U., Langes, C., 2013. Patent Number US 8,563,555 B2.

Wieser, J., Pichler, A., Hotter, A., Griesser, U., Langes, C., 2012. Patent Number US 2012/0101277 A1.Williams, N.A., Polli, G.P., 1984. The lyophilization of pharmaceuticals: a literature review. J. Parenter. Sci. Technol. 38, 48–59.

Yin, S., Huang, F., Zhang, J., Zheng, J., Lin, Z., 2011. The Effects of Particle Concentration and Surface Charge on the Oriented Attachment Growth Kinetics of CdTe Nanocrystals in H2O. J. Phys. Chem. C. 115, 10357–10364.

Zhang, S., Lee, T.W.Y., Chow, A.H.L., 2016. Crystallization of Itraconazole Polymorphs from Melt. 16, 3791-3801.

Zuo, B., Sun, Y., Li, H., Liu, X., Zhai, Y., Sun, J., He, Z., 2013. Preparation and *in vitro/in vivo* evaluation of fenofibrate nanocrystals. Int. J. Pharm. 455, 267–275.

2.1 INTRODUCTION

It has been reported in literature that 40% of marketed drugs suffer from poor aqueous solubility thereby limiting their dissolution in biological fluids. As a result, we have new chemical entities with poor bioavailability and erratic absorption (Shegokar and Müller, 2010). Nano-sization i.e. production of NPs, has emerged as a promising strategy for optimizing bioavailability of hydrophobic drugs.

Reduction of particle size results in an increase in surface area available for dissolution (Noyes and Whitney, 1897). Small particles with a high surface curvature exhibit high saturation solubility (Ostwald, 1900). This gives rise to OR phenomenon, whereby particles which possess a degree of solubility in the dispersed phase are thermodynamically unstable. The system will move to reduce the interfacial energy via particle growth. Consequently, larger particles grow as the result of the re-dissolution of smaller more soluble particles (Voorhees, 1985). For this reason, physical stability of resultant nanoparticles remains a challenging aspect of successful nano-dispersion product development. NP production methods can be categorised as top down or bottom up. Wet milling is a common top down method avoiding organic solvent use and benefitting from easy scale-up. However common problems associated with this technique include degradation and stability. In contrast, bottom up approaches such as anti-solvent precipitation allow for fine tuning of product characteristics such as morphology and crystallinity, with simplicity and cost also being noted as advantages (Van Eerdenbrugh et al., 2009).

Other processes affecting the physical stability of nano-dispersions include flocculation, a reversible process whereby particles aggregate but remain as individual particles and coalescence is the process by which two or more particles merge during contact resulting in the formation of a single particle. Once in contact a pair or group of NPs will coalesce to reduce their surface energy. Surface processes control coalescence. Coalescence is an irreversible process (Ingham et al., 2011). In addition, the high surface area of drug nano-dispersions promotes nucleation and crystal growth resulting in instability (Dolenc and Kristl, 2009). Crystal growth can occur during the production and shelf life of nano-dispersions which can adversely affect their dissolution behaviour and *in vivo* performance (Ghosh et al., 2012). Inclusion of a suitable stabilizer can maintain colloidal stability, therefore avoiding aggregation and OR. However, stabilizer selection has remained a challenge due to the lack of fundamental understanding surrounding interactions within colloidal systems. For this reason, systematic stabilizer selection offers pharmaceutical companies attractive gains in terms of time and cost.

Stabilizers act to inhibit aggregation within nano-dispersions via two methods, electrostatic repulsion or steric stabilization. Polymers work via steric stabilization, whereby, adsorption of stabilizer molecules onto particle surfaces creates physical barriers which hinder van der Waals attractive forces between neighbouring particles (Palla and Shah, 2002). Polymeric stabilizers can have numerous sites in their chains with affinity for API surfaces therefore polymer chain morphology determines conformation of adsorption. With stabilizers adsorbed onto the particle surface through the anchor segment, good solvation between the solvent and the stabilizing segment of the stabilizer is required to achieve steric stabilization and prevent particles from agglomerating in the dispersion medium. Stabilizer adsorption can occur in a number of ways: van der Waals forces, ion-dipole interaction, ionic interaction, hydrogen bonding, or by hydrophobic effect (Mahesh et al., 2014). Current literature highlights the benefits offered by PEG as a stabilizer. Not only is PEG low in cost, it also possesses a good *in vivo* safety profile (Mugheirbi et al., 2014).

For efficient NP application, it is necessary to fully understand the crystallisation pathways and growth kinetics responsible for the evolution of those NPs. NP coarsening was first described using the OR mechanism mentioned above, whereby crystal growth is controlled by diffusion (Wagner, 1961; Speight, 1968; Kirchner, 1971). The unique kinetics of crystallisation pathways involving NPs have led to the exploration of alternative crystal growth models, namely oriented attachment (OA) based crystal growth. OA growth occurs when a secondary crystal is formed through the attachment of primary particles in an oriented, irreversible manner. Resulting particles are generally irregular in shape, in contrast to those arising from OR which tend to be spherical in shape (Huang et al., 2003a). In addition, OA tends to follow an asymptotic curve whilst OR growth generally follows a parabola trend (Wagner, 1961; Speight, 1968; Kirchner, 1971). Two-stage crystal growth has been observed whereby asymptotic growth described by the OA growth model, was followed by cubic parabola growth well described by the OR growth model (Huang et al., 2003a). Elsewhere in the literature, the phenomena of hybrid crystal growth has been described by a model accounting for both OA and OR physical processes occurring simultaneously in a competitive manner (Huang et al., 2003a; Yin et al., 2011). For this reason, it can be difficult to study the growth kinetics of such NPs. The role of surface adsorption in such processes has been explored, with strong surface adsorption being found to promote OA whilst delaying OR growth (Yin et al., 2011). It has been proposed that OA occurs via three steps; diffusion of NPs in solution followed by collision, then desorption of surface ligands and finally coalescence. Therefore, factors such as surface

properties of the NPs and particle-particle interactions can play a part in these events (Huang et al., 2003b).

ITR, POS and KETO are azole anti-fungal compounds which can be categorised as BCS class II drugs. For this reason, these APIs are ideal candidates for particle size reduction techniques.

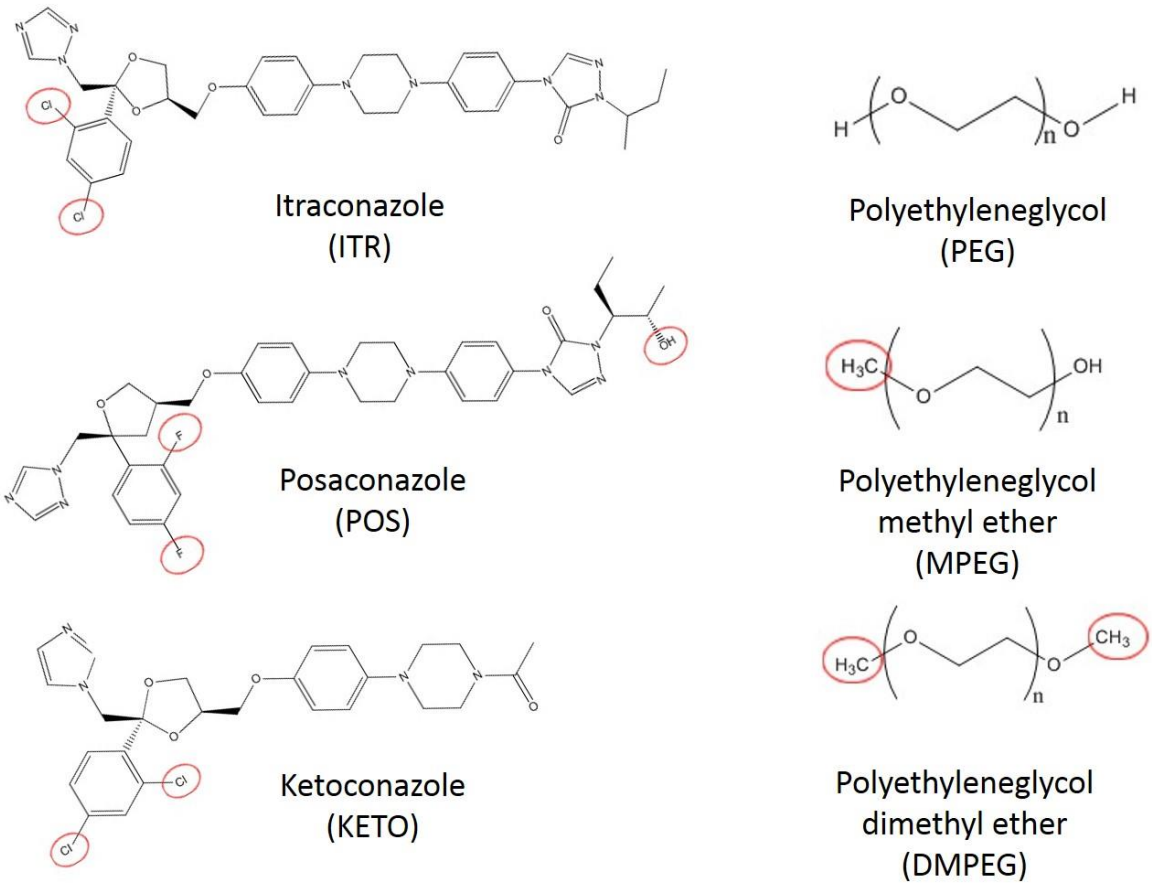

Fig. 2.1. Chemical structure of APIs and stabilizers. Red circles highlight important differences between structures.

Currently, the selection of optimum stabilizer for nano-dispersions is achieved via a trial and error approach. A systematic screening method for stabilizer selection should be simple to execute in a quick manner, whilst providing a wealth of information regarding the NPs under analysis. Attempts were made to utilize DLS as a means of aiding stabilizer selection for antifungal azole BCS class II drugs; ITR, KETO and POS (Fig. 2.1). PEG, MPEG and DMPEG with a molecular weight of 2,000 Dalton (Da) were investigated as stabilizers (Fig. 2.1). We report

the effect of stabilizer choice and its concentration on particle size, indicative of colloidal stability. In addition, derived mean count rate was noted. This is a measure of scattered light intensity which is proportional to particle concentration (Shang and Gao, 2014). Morphological examination of NPs was performed via SEM, and solid state transformations were monitored via PXRD. Kinetic modelling was utilised as a tool for strengthening our understanding surrounding the effect of stabilizer choice and concentration on the OR process (Ostwald, 1900; Voorhees, 1985).

2.2 MATERIALS AND METHODS

2.2.1 MATERIALS

Itraconazole (ITR) was a gift from Welding GmbH (Hamburg, Germany). Ketoconazole (KETO) and posaconazole (POS) were purchased from Glentham Life Sciences Ltd. (Wiltshire, UK). Potassium dihydrogen phosphate reagent, poly(ethlyene glycol) (PEG), poly(ethylene glycol) methyl ether (MPEG) and its dimethoxylated derivative (DMPEG) with average molecular weights of 2,000 Da were purchased from Aldrich Chemical Co., Ltd. (Dorset, UK). Methanol HPLC grade was purchased from Fisher Scientific (Loughborough, UK). Acetone and acetonitrile Chromasolv® HPLC grade was obtained from Sigma Aldrich (Dorset, UK). MilliQ water was used in all instances. Potassium hydroxide pellets were purchased from Merck KGaA (Darmstadt, Germany).

2.2.2 METHODS

2.2.2.1 Anti-Solvent Formation of ITR, POS and KETO Nanoparticles

Solutions of drugs dissolved in acetone (solvent phase) and water or a polymer/stabilizer solution (anti-solvent phase) were maintained at 25 °C and filtered using 0.45 µm syringe polytetrafluoroethylene (PTFE) filter (VWR, Ireland) prior to NP formation. Stabilizers were included at the following concentrations: 0.5 (0.05 % w/v), 1 (0.1 % w/v) and 1.5 mg/ml (0.15 % w/v).

NPs were formed in a 12 o.d. mm square glass cuvette (part number PCS8501) with anti-solvent added first, followed by rapid addition of a solvent phase forming NP dispersions at 25 °C. Solvent phase consisted of 70-80% saturated solution of API in acetone. The exact conditions of NP formation were dependent on the drug used. ITR NPs were formed using a solvent phase (2.0 mg/ml ITR in acetone = 80% saturated solution) into an anti-solvent phase, using a 1:10 solvent to anti-solvent (v/v) ratio (0.1 ml solvent phase added to 0.9 ml anti-

solvent phase). POS NPs were formed by rapid mixing of a solvent phase (14.8 mg/ml POS in acetone = 75% saturated solution) into an anti-solvent phase, using a 1:12.5 solvent to anti-solvent (v/v) ratio (0.08 ml solvent phase added to 0.92 ml anti-solvent phase). KETO NPs were formed by rapid mixing of a solvent phase (3.75 mg/ml KETO in acetone = 70% saturated solution) into an anti-solvent phase, using a 1:10 solvent to anti-solvent (v/v) ratio (0.1 ml solvent phase added to 0.9 ml anti-solvent phase).

2.2.2.2 Dynamic Light Scattering (DLS)

The mean particle size and polydispersity indices of NPs formed as per Section 2.2.2.1 were measured using the Zetasizer Nano ZS series (Malvern Instruments, UK) as described by (Mugheirbi et al., 2014) without further dilutions. Measurement position and attenuator factor were automatically optimised by the software. All measurements were carried out at 25 °C in a 1 ml glass cuvette (part number PCS8501). The analysis was performed in triplicate for each sample. Viscosity of the continuous phase was measured using a Vibro Viscometer SV-10 (A&D, Japan) and the size values corrected for the actual viscosity of the dispersion medium.

2.2.2.3 Determination of Solubility of APIs in Acetone and Deionised Water

Solubility of APIs in acetone and deionised water were obtained as follows. Excess API was added to the solvent of interest in a closed glass vial and allowed to equilibrate overnight with continuous stirring at 1000 rpm with temperature maintained at 25 °C. Samples in acetone were filtered through a 0.45 µm PTFE syringe filter (VWR, Ireland). Whereas, samples in water were centrifuged for 1 hour at 25 °C, 13,000 rpm using a Thermo Scientific Heraeus Fresco 17 centrifuge. All samples were diluted appropriately and concentrations determined via HPLC (as described in Section 2.2.2.4). It should be noted that ITR solubility in water at 25 °C was obtained from literature (Matteucci et al., 2009). The solubility values are presented in Table 2.1.

2.2.2.4 High Performance Liquid Chromatography (HPLC)

The concentrations of ITR, POS and KETO in acetone and deionised water were measured using a Waters Symmetry® C_{18} 5 µm (4.6 mm x 150 mm) column attached to a Waters HPLC system equipped with a Waters 2695 separations module and a 2996 photodiode array detector (ITR λ = 260 nm, POS λ = 260 nm, KETO = 240 nm).

ITR mobile phase used consisted of acetonitrile: buffer pH 6.8 (60:40) (v/v). A 0.1M phosphate buffer solution was prepared by dissolving 6.8 mg of potassium dihydrogen phosphate in 1L of deionised water. 1M potassium hydroxide solution was prepared by dissolving 5.6 g of

potassium hydroxide in 0.1L of deionised water, this solution was used to adjust the phosphate buffer pH to 6.8. For POS and KETO, mobile phase used consisted of methanol: water (75:25) (v/v). A flow rate of 1 ml/min and run time of 14 minutes was used in all cases. For the solubility of all APIs in deionised water, a 100 µl injection volume was used due to low solubility. For solubility studies of ITR in acetone, a 50 µl injection volume was used. For solubility studies of POS and KETO in acetone, a 20 µl injection volume was used. For the aqueous solubility determination, calibration curves used were in the concentration range of 0.05 to 1 mg/ml. For solubility in acetone determination calibration curves were used in the range 2 to 20 mg/ml. Column temperature was maintained at 25 °C for the duration of separation using a column heater.

2.2.2.5 Scanning Electron Microscopy (SEM)

A Zeiss Ultra variable pressure field emission scanning electron microscope (Germany) equipped with a secondary electron detector and accelerating voltage of 5 kV was used for morphological examination of ITR NPs. NP formulations were centrifuged at 4 °C for 10 min at 12,000 rpm using an Eppendorf 5810R centrifuge (Hamburg, Germany). The supernatant was removed and the remaining material was washed using deionised water. Aliquots of nano-dispersions were directly placed on aluminium stubs and dried using nitrogen purge. Prior to examination samples were sputter coated with gold palladium under vacuum.

2.2.2.6 Powder X-ray Diffraction (PXRD)

NPs were formed, centrifuged at 4 °C for 1 minute at 13,000 rpm using a Thermo Scientific Heraeus Fresco 17 centrifuge. The supernatant was discarded and pellet examined using a Rigaku Miniflex II, desktop X-ray diffractometer (Japan) equipped with a Cu Kαradiation X-ray source. The samples were mounted on a low background silicon sample holder and scanned over a 2θ range 2-40°.

2.3 Results and Discussion

2.3.1 Particle Formation and Size Evolution

2.3.1.1 Stabilizer-free NPs

It should be noted that the theoretical supersaturation ratio presented in Table 2.1 is not a true supersaturation ratio, such as that denoted in Chapter I. The theoretical supersaturation values presented in Table 2.1 are an overestimation of the true supersaturation values. Table 2.1 demonstrates that POS possesses the greatest solubility in both acetone and water, in

contrast with ITR having the lowest. In addition, it should be noted that POS aqueous solubility is 2-fold greater than that of KETO and 200-fold greater than that of ITR.

Table 2.1. Solubility of APIs in acetone and water along with theoretical supersaturation ratio (S) at 25 °C.

API	Solubility in acetone (mg/ml)	Solubility in water (mg/ml)	Theoretical Supersaturation ratio (S) (API solubility in acetone/API Solubility in water)
ITR	2.5 ± 0.4	0.001*	2500
POS	19.7 ± 2.3	0.2 ± 0.006	98.5
KETO	5.2 ± 0.03	0.1 ± 0.03	52

* value taken from Matteucci et al., (2009)

Table 2.2 shows that upon initial NP formation stabilizer free ITR NPs are the smallest in size (155 ± 14 nm) with great reproducibility indicated by low standard deviation (SD) and relative standard deviation (RSD) of 14 and 9%, respectively. In contrast, POS NPs are the largest in size (308 ± 66 nm), with large variability in size (RSD of 21%). Therefore, even very small changes within the API structure can lead to NPs with entirely different sizes.

Table 2.2. Initial mean particle size (nm) for ITR, POS and KETO NPs measured immediately after particle formation, with 0.5 mg/ml stabilizer and without stabilizer included.

	ITR mean particle size ± SD (nm)	ITR PDI ± SD	POS mean particle size ± SD (nm)	POS PDI ± SD	KETO mean particle size ± SD (nm)	KETO PDI ± SD
Stabilizer free	155 ± 14	0.07 ± 0.05	308 ± 66	0.03 ± 0.03	200 ± 34	0.06 ± 0.03
PEG 0.5 mg/ml	197 ± 74	0.09 ± 0.04	262 ± 23	0.06 ± 0.03	507 ± 130	0.10 ± 0.01
MPEG 0.5 mg/ml	152 ± 13	0.08 ± 0.04	318 ± 28	0.07 ± 0.03	310 ± 85	0.12 ± 0.05
DMPEG 0.5 mg/ml	237 ± 32	0.10 ± 0.04	243 ± 13	0.07 ± 0.04	221 ± 17	0.07 ± 0.05

*SD: standard deviation, PDI: polydispersity index

Fig. 2.2 presents an intensity based particle size distribution (PSD) obtained using DLS for stabilizer free ITR NPs. Three distinct NP size populations exist over the 30 minutes (labelled a, b and c), of subsequent increasing particle size. In addition, slight peak broadening between 0 and 30 minutes would suggest increasing polydispersity between these particle populations (Fig. 2.2). The presence of polymers during the NP formation process will have an impact upon the true supersaturation value, with an increase in supersaturation anticipated.

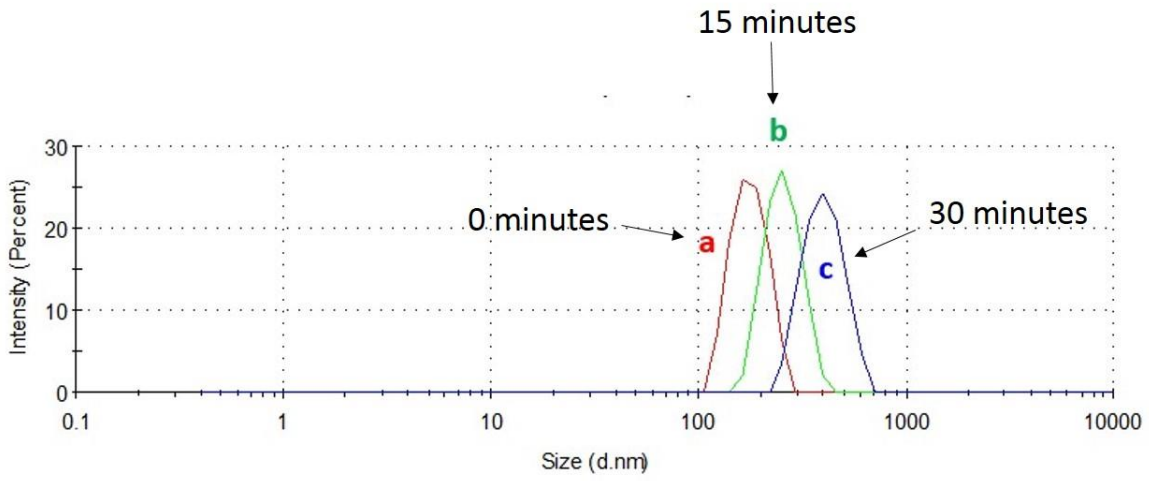

Fig. 2.2. DLS intensity based particle size distribution at (a) 0 (b) 15 and (c) 30 minutes for ITR stabilizer free NPs.

Fig. 2.3 shows that stabilizer free ITR NPs have the greatest colloidal stability over time, while stabilizer free KETO NPs are the least stable, as indicated by the large error bars for the size values present beyond 15 minutes. While ITR NPs doubled their size by 30 minutes of the experiment and POS NPs grew by 200%, KETO particles displayed very erratic and non-reproducible behaviour in terms of size. When we consider the supersaturation values for the APIs (Table 2.1), KETO and POS have relatively low S values (52 and 98.5, respectively), when compared with ITR (Table 2.1). ITR NP formation can be related to its limited miscibility in water, as its hydrophobic molecules are unable to form energetically favourable interactions with water, leading to aggregation of the molecules and the formation of a drug-rich phase i.e. ITR NPs dispersed within a continuous liquid phase (Ilevbare and Taylor, 2013). Nanocrystal growth in solution follows three steps: supersaturation and nucleation, followed by crystal growth. It appears that a high theoretical S ratio might be necessary for the formation of stable NPs composed of the APIs studied (Table 2.1 and Fig. 2.3a and b).

Sample scattering intensity is represented by count rates, here shown as derived count rates accounting for different signal attenuation levels, which are dependent upon both particle size and particle concentration (Shang and Gao, 2014). Fig. 2.3c shows a decreasing count rate trend for all stabilizer free NPs, this is indicative of particle instability, most likely caused by aggregation. Such instability of NPs may be addressed via the addition of a stabilizer to the system (Van Eerdenbrugh et al., 2009).

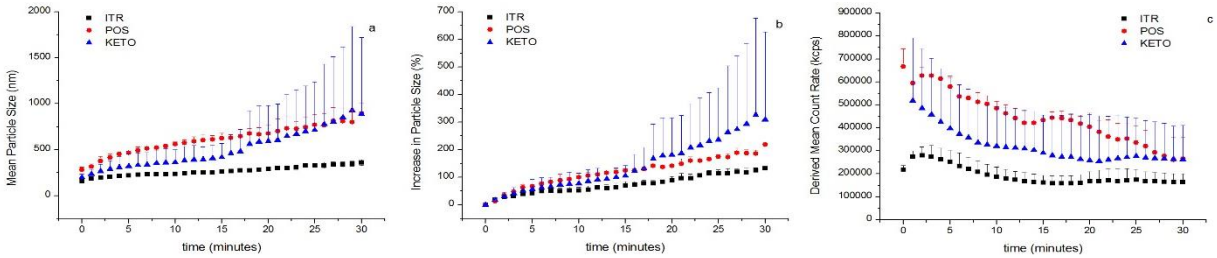

Fig. 2.3. Plots showing (a) mean particle size (nm) (b) increase in particle size (%) (c) derived mean count rate (kcps), for stabilizer free NPs.

2.3.1.2 Polymer-stabilized NPs

Initial experiments with polymers as NP stabilizers were carried out using 0.5 mg/ml of PEG, MPEG and DMPEG, results of which indicated variable success in achieving stable formulations. ITR NPs remained the smallest in size when stabilized with PEG and MPEG 0.5 mg/ml concentration (< 200 nm, Table 2.2). Interestingly, when DMPEG at 0.5 mg/ml is used as a stabilizer, KETO NPs are the smallest in size upon initial formation compared with ITR and POS NPs. All nano-dispersions in this case can be described as having low polydispersity, however stabilizer free nano-dispersions had lower polydispersity than those including a stabilizer (Rane et al. 2005). Examples of particle size distributions for nano-dispersions stabilized by polymers can be found within Fig. A.1.1-3. Based on these initial results, a wider range of polymer concentration was explored. It is evident from the literature that common stabilizer concentrations range between 0.0125 % (w/v) and 5 % (w/v) (Mugheirbi et al., 2014).

While ITR NPs presented relatively good stability even when no stabilizer was used, tests with polymers were conducted to explore if superior colloidal stability could be achieved. Fig. 2.4 presents a stabilizer type and concentration comparison for ITR NPs, including mean particle size (nm) and increase in particle size (%) data. Fig. 2.4b demonstrates PEG to be an effective stabilizer for ITR NPs when used at 1 mg/ml, as demonstrated by the low increase in particle size over 30 minutes. In Fig. 2.4d we can see that all ITR NPs stabilized with MPEG exhibit more than a 50% increase in particle size. Fig. 2.4e and f highlights DMPEG to be an ineffective stabilizer for ITR NPs when used at 1.5 mg/ml, however NP stabilization is favourable when concentrations below this are employed (Fig. A.1.4). In general, biphasic NP growth was observed consistently across all concentrations, with an initial rapid increase in particle size followed by a slower particle growth phase (Fig. 2.4b, d, f). In general, an initial burst/increase in count rate was seen upon ITR NP formation at 0 minutes, followed by a decline and eventual

plateau in count rate (Fig. A.1.5). These events are likely to accompany rapid nucleation followed by a slower particle growth phase.

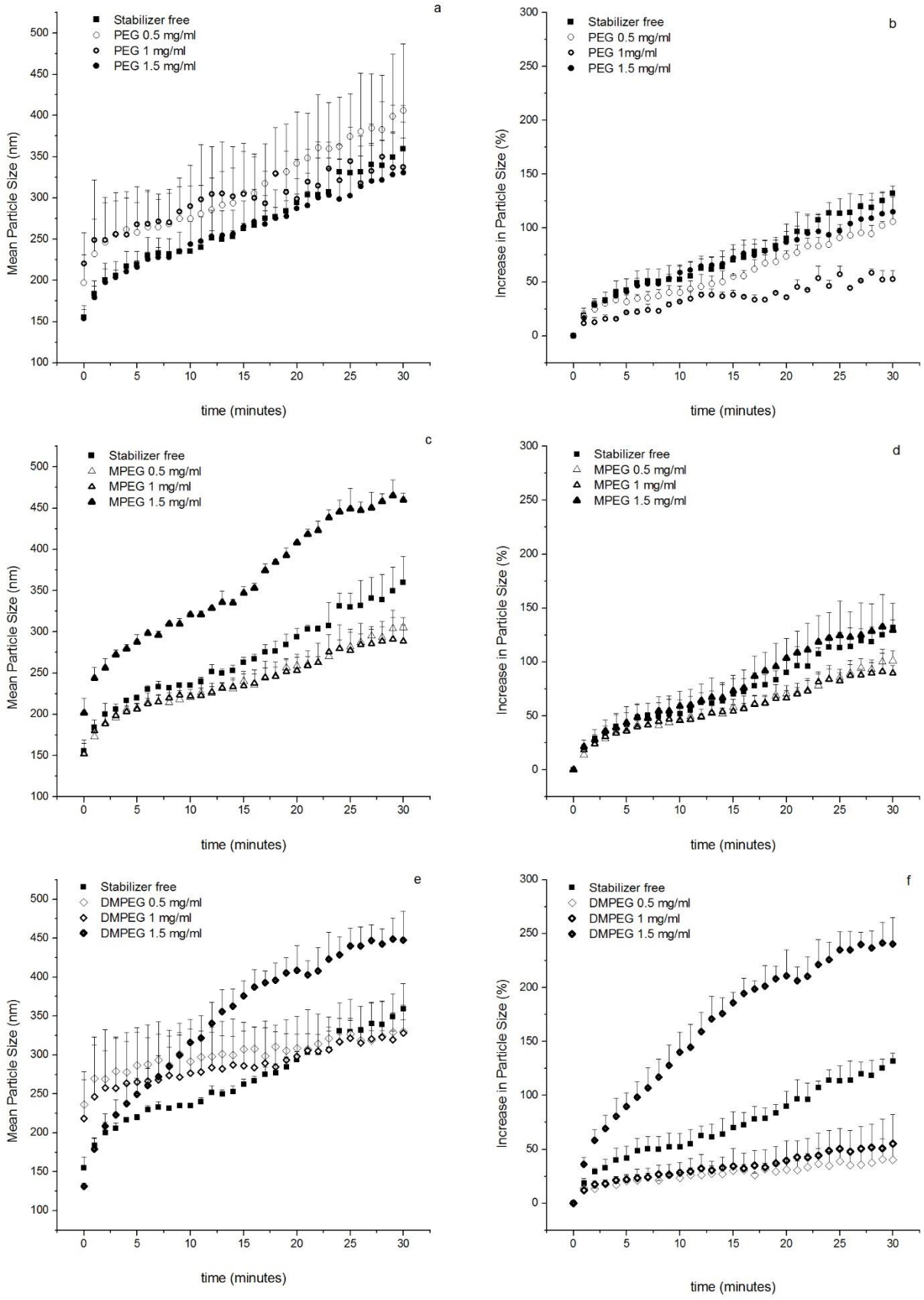

Fig. 2.4. Mean particle size (nm) and increase in particle size (%) versus time (minutes) for ITR NPs stabilized with (a and b) PEG (c and d) MPEG and (e and f) DMPEG.

Fig. 2.5 presents mean particle size (nm) and increase particle size (%) data for POS NPs. The most stable systems were observed when DMPEG was included as a stabilizer or in the absence of a stabilizer (Fig. 2.5e and f). This was confirmed by a smaller increase in particle size (%) observed in these circumstances. POS NPs initially form around 200 nm (Fig. 2.5e). After 30 minutes NPs were generally above 1 micron in size as Fig. 2.5 shows. Extremely large particle sizes were observed after 30 minutes when PEG and MPEG were utilised as stabilizers (Fig. 2.5a and c) with POS NPs visibly precipitating at ~ 15 minutes. DMPEG was the most effective stabilizer for POS NPs, with particle size remaining ~ 1 micron at 30 minutes (Fig. 2.5e and f). Count rate trends for POS NPs also reflect the great variability as shown in Fig. A.1.6.

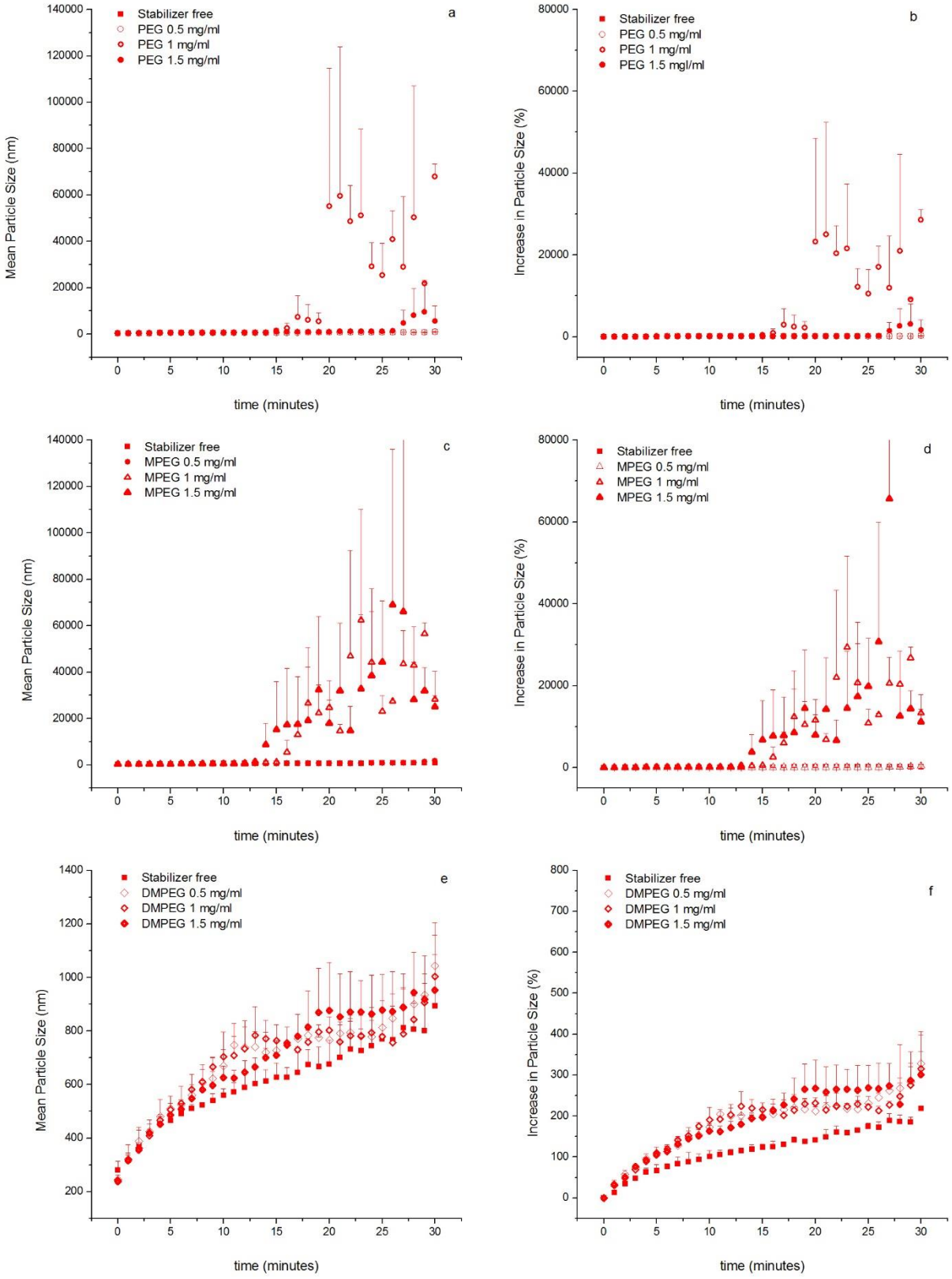

Fig. 2.5. Mean particle size (nm) and increase in particle size (%) versus time (minutes) for POS NPs stabilized with (a and b) PEG (c and d) MPEG and (e and f) DMPEG.

Fig. 2.6 presents mean particle size (nm) and increase particle size (%) data for KETO NPs. When PEG and MPEG were used as stabilizers, upon initial formation KETO NPs form ~ 250 - 500 nm. At 30 minutes NPs are > 1500 nm (Fig. 2.6a and c). In contrast, when DMPEG was used as a stabilizer initial NPs form ~ 207 – 221 nm as shown by Fig. 2.7e. At 30 minutes DMPEG stabilized NPs are < 1 micron (Fig. 2.6e). We can conclude from mean particle size data that DMPEG is the most effective stabilizer at maintaining colloidal stability of KETO NPs, with 1.5 mg/ml being the most effective concentration (Figure 2.6c). Fig. A.1.7 reiterates the general trend of falling count rates observed across all KETO NPs systems. Colloidal stability is shown to be concentration dependent when PEG is used as a stabilizer for KETO NPs. This is confirmed by increasing particle size (%) observed when PEG concentration is increased (Fig. 2.6b). Again, biphasic NP growth was seen across all KETO systems with an initial burst in size followed by a slower growth phase (Fig. 2.6b, d and f). As shown by Fig. 2.6f, DMPEG is the most effective stabilizer for KETO NPs in terms of maintaining colloidal stability over 30 minutes, with increase in size remaining ~ 200 %.

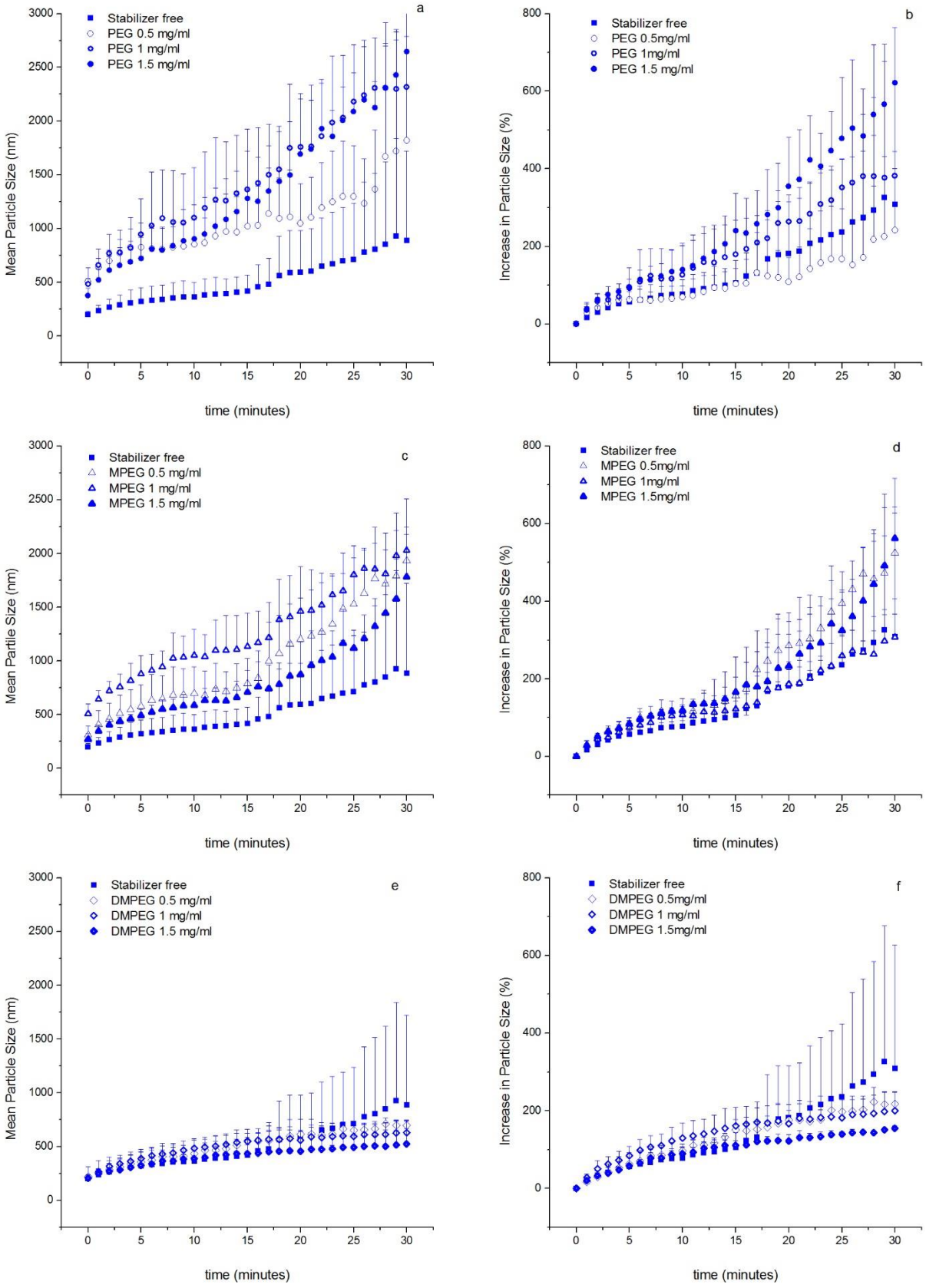

Fig. 2.6. Mean particle size (nm) and increase in particle size (%) versus time (minutes) for KETO NPs stabilized with (a and b) PEG (c and d) MPEG and (e and f) DMPEG.

In summary, the most effective stabilizer for all the APIs investigated, although marginally for KETO, was DMPEG. In all cases, stabilization was polymer concentration dependent as seen in Fig. A.1.4. Wang et al., (2011) have previously shown this to be the case, suggesting polymer (acting as steric stabilizer) concentration affects efficacy of stabilization. More importantly that, an optimum concentration of stabilizer is required as an inadequate amount of stabilizer can result in incomplete coverage of API particle surfaces. It seems logical, in some instances that beyond the optimum stabilizer concentration, all API particle surface adsorption sites are occupied and a further increase in stabilizer concentration is of no benefit in terms of stabilization. We have observed that effective stabilizer concentration is dependent upon both API and stabilizer structure, similar to the findings of Wang et al., (2011). As the three structurally similar APIs (Fig. 2.1) studied in this work were all effectively stabilized by the same polymer, DMPEG, we can conclude that a structural component common to all three APIs is responsible for this stabilization. Choi et al. (2005) concluded that polymers with higher hydrophobicity successfully produced stable nanocrystals of hydrophobic drugs in comparison to those with lower hydrophobicity. This was attributed to the strong polymer adsorption onto the hydrophobic drug surfaces (Choi et al., 2005). DMPEG possesses greater hydrophobic character in comparison to PEG and MPEG. Hence, it is possible that improved surface coverage owing to DMPEG's stronger interaction with the API particle surfaces, resulted in greater stabilization of the resultant NPs.

Fig. A.1.5 reveals an initial increase in ITR derived count rate, followed by a decrease and eventual plateau in mean count rate (Hassan et al., 2015). This initial increase in mean count rate correlates with a precipitation burst in ITR NP growth, beyond this point sufficient ITR growth site coverage by the stabilizer inhibits NP aggregation and slower NP growth can be seen. Fig. A.1.6 and 7 also reveal a general trend of falling and eventual plateau in count rates for POS and KETO NPs. This provides suggestion that, OR, whereby particle solubility increases as the radius decreases via the Gibbs-Thomson effect, might be at play. Falling count rates may represent larger particles growing at the expense of their smaller counterparts.

2.3.2 Solid State Characterisation of NPs

All starting components (APIs and polymers) were crystalline in nature (Fig. 2.7 and A.1.8). ITR NPs stabilized by 0.5 mg/ml DMPEG appear amorphous from PXRD data shown in Fig. 2.7b, however work carried out by Mugheirbi and Tajber (2015a) has proven ITR NPs form stable liquid crystal (LC) structures with a nematic phase. POS has been reported to exhibit rich solid state polymorphism (Andrews et al., 2004; Wieser et al., 2012 and 2013). Crystalline POS

polymorph form III is denoted in Fig. 2.7c (Andrews et al., 2004). In this study, the POS polymorphic form used to formulate these NPs, was the more stable POS polymorph crystalline form I, denoted in Fig. 2.7d (Andrews et al., 2004). Within approximately 5 minutes of formation, POS NPs can be isolated in an amorphous phase, as confirmed by the diffractogram shown in Fig. 2.7f, which crystallises to form I within 30 minutes (Fig. 2.7e). Crystallisation of amorphous POS was also seen in studies by Mugheirbi et al. (2017) on spheres coated with solid dispersions containing either ITR or POS, which led to a decrease in the release rate of POS. It was not possible to isolate KETO NPs immediately upon formation for PXRD studies, however these NPs were confirmed as PXRD crystalline at 30 minutes as seen in Fig. 2.7h.

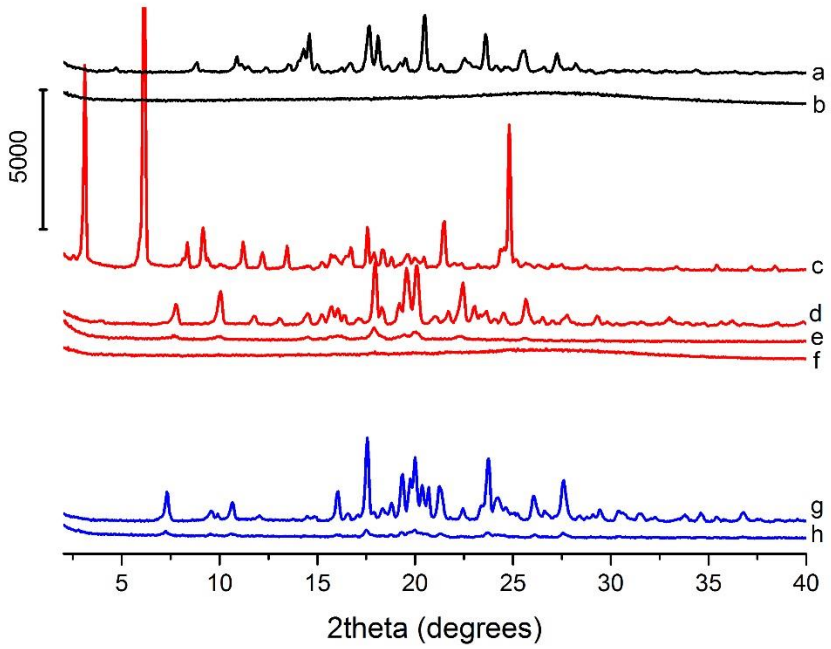

Fig. 2.7. PXRD diffraction patterns of (a) crystalline ITR (b) ITR NPs stabilized by 0.5 mg/ml DMPEG at 0 minutes (c) crystalline POS polymorph form III (d) crystalline POS polymorph form I (e) POS polymorph form I stabilizer free NPs at 30 minutes (f) amorphous POS stabilizer free NPs at 0 minutes (g) crystalline KETO (h) KETO – MPEG 0.5 mg/ml NPs at 30 minutes.

2.3.3 Particle Morphology

SEM images displayed in Fig. 2.8 confirm that the NPs were in the nanometre-size range. Fig. 2.8a reveals ITR NPs with porous nature when DMPEG 1 mg/ml was used, at 30 minutes. Pin prick "blowholes" present on NP surfaces provide evidence of the hollow structure of the NPs (Fig. 2.8b and c). This supports the theory proposed by Mugheirbi et al., (2014) whereby

particles are formed via solidification of droplets through counter diffusion of solvent and anti-solvent (Mugheirbi and Tajber, 2015a).

POS crystal structures can be seen in Fig. 2.8d, these are plate-like in structure with dendritic ends and particle size above 2 micron. The red circle in this image also shows amorphous POS NPs present alongside these crystalline structures. This, in conjunction with increase in particle size data (Fig. 2.5) and PXRD analysis (Fig. 2.7e and f), suggests that POS NPs underwent a solid state transformation over the 30 minutes. Saturation solubility differences between amorphous and crystalline POS NPs initiated a process similar to OR, leading to a rapid conversion of amorphous NPs into the crystalline state. Fig. 2.8c reveals peanut shaped POS NPs. This confirms that a number of stages exist during NP formation and growth including a "break-up" stage, with two daughter particles originating from an original mother particle.

Fig. 2.8e confirms the spherical nature of KETO NPs when no stabilizer is included in the system, as well as a particle size below 1 micron. Fig. 2.8f shows a rougher texture present on the KETO NP surface when PEG 0.5 mg/ml was included as a stabilizer in the system. The rough texture that can be observed on the surface of the NPs in Fig. 2.8a, g, h can be attributed to complete stabilizer coverage of API particle surfaces, which in turn results in colloidal stability.

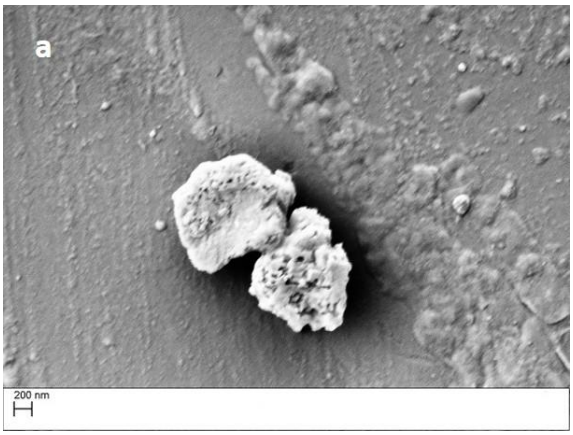
a
200 nm

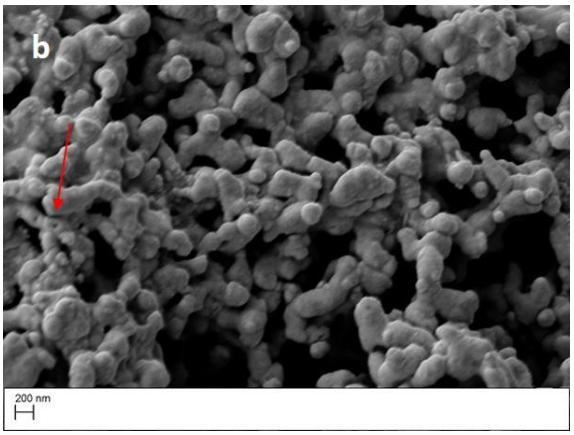
b
200 nm

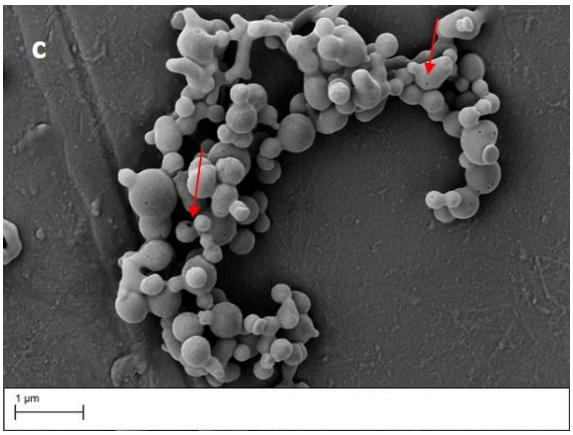
c
1 µm

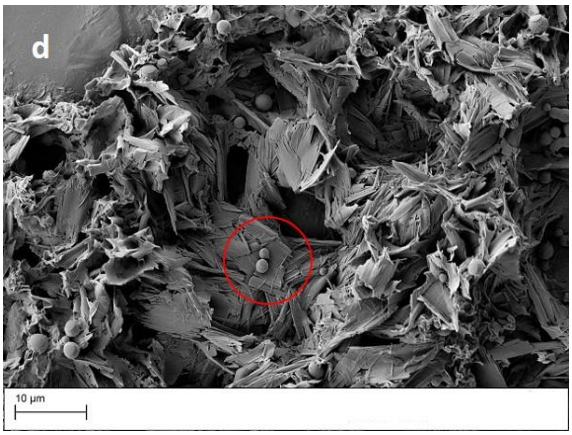
d
10 µm

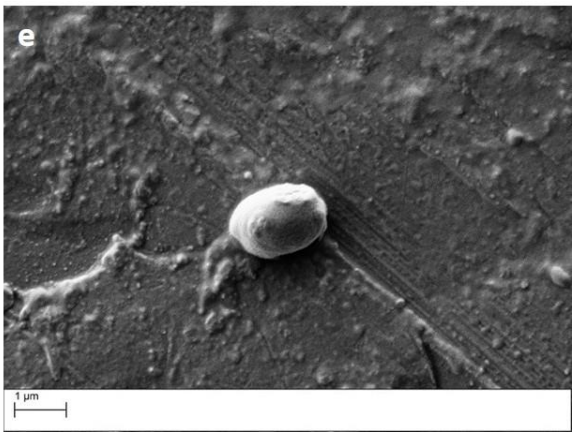
e
1 µm

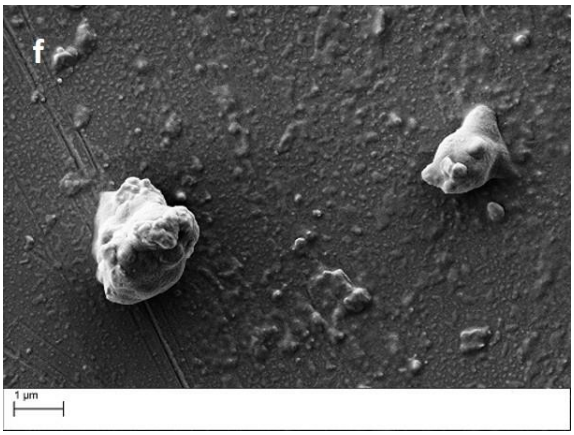
f
1 µm

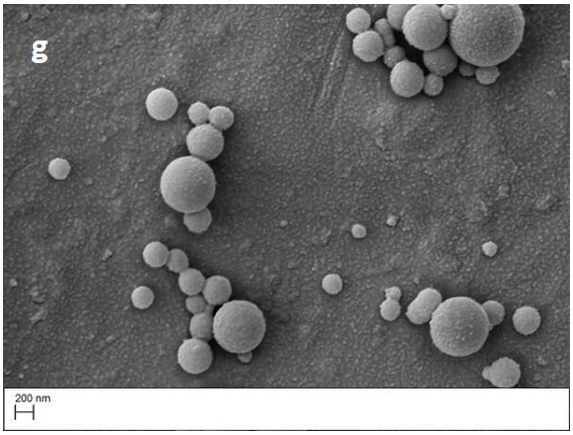
g
200 nm

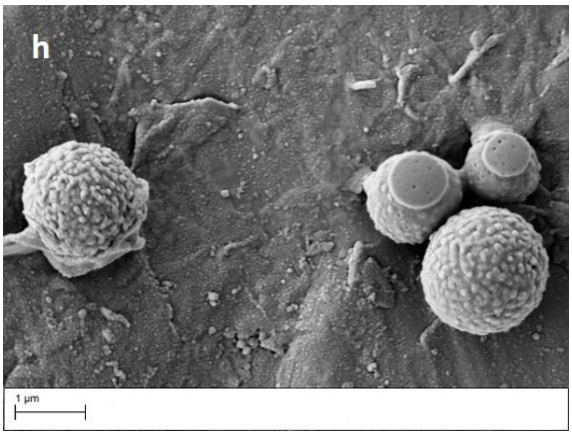
h
1 µm

Fig. 2.8. Scanning electron micrograph of (a) ITR NPs with DMPEG 1 mg/ml at 30 minutes (b) ITR NPs with DMPEG 0.5 mg/ml at 30 minutes (c) POS NPs with MPEG 0.5 mg/ml at 0 minutes (d) POS NPs with DMPEG 0.5 mg/ml at 30 minutes (e) KETO NPs with no stabilizer at 30 minutes (f) KETO NPs with PEG 0.5 mg/ml at 0 minutes (g) POS NPs with PEG 1 mg/ml at 0 minutes and (h) POS NPs with DMPEG 0.5 mg/ml at 30 minutes. (Hollow particle indicated by red arrow).

2.3.4 Mechanism of Particle Growth/Size Increase

Attempts were made to fit mean particle size data using a kinetic growth model. The hybrid crystal growth model described in Eq. 2.1 was employed to gain knowledge surrounding the mechanisms involved in particle growth. Understanding the factors that affect the kinetics of crystal growth provides key information necessary for the fine-tuning of NP properties. Elsewhere in the literature the process of OR has been described using kinetic models (Wagner, 1961; Speight, 1968; Kirchner, 1971). Kinetic modelling of DLS data focused on DMPEG (Fig. 2.8d), as it proved to be the most effective stabilizer for all API nano-dispersions according to DLS data. In addition, all other polymers encouraged crystallisation of POS NPs, therefore fitting of this data was simply not possible. This hybrid crystal growth considers the particle size at any time being the result of two processes, oriented attachment (OA) and Ostwald ripening (OR), occurring simultaneously (Eq. 2.1):

$$\boldsymbol{D} = \frac{\boldsymbol{D_0}\left(\sqrt[3]{\boldsymbol{2k_1 t}}+\boldsymbol{1}\right)}{(\boldsymbol{k_1 t}+\boldsymbol{1})} + \boldsymbol{k_2}\,\boldsymbol{t^{1/n}} \qquad \text{(Eq. 2.1)}$$

where D is the particle diameter at any time, D_0 is the initial particle diameter, k_1 is the rate constant for the OA process, k_2 is the rate constant for the OR process, t is time in hours and n is an exponent describing the relevant coarsening mechanism (Huang et al., 2003a; Yin et al., 2011). When the exponent n = 2, NP growth is said to be interface controlled and when n = 3, growth is diffusion controlled (Wagner, 1961; Speight, 1968; Kirchner, 1971). Parabolic growth has been associated with interface controlled growth, whereas cubic growth is characteristic of diffusion controlled coarsening (Wagner, 1961). Fig. A.1.9 provides evidence of growth following a parabola trend for KETO NPs stabilized with DMPEG 1.5 mg/ml. This trend was present for all APIs stabilized with DMPEG at a concentration of 1.5 mg/ml. These growth curves should be best fitted as a full data set hybrid crystal growth kinetic model (see Tables 2.3 to 2.5). This would be characteristic of interface controlled growth kinetics. In contrast, Fig. A.1.10 and 11 provides evidence of cubic growth kinetics. This trend was evident for all nano-dispersions, aside from those stabilized by DMPEG 1.5 mg/ml, for this reason such datasets

were fitted in two separate stages (Huang et al., 2003b). This cubic growth tends to be associated with diffusion controlled particle coarsening.

Growth curves were either fitted as a single phase of growth indicated by asterisks (*) in Table 2.3 to 2.5 and Fig. A.1.9, or as two separate stages of growth (Table 2.3 to 2.5 and Fig. A.1.10 and 11). Fitting parameters are presented in Table 2.3 with results supporting growth via Eq. 2.1 growth model. Initially, the data was fitted with the full model including OA and OR mechanisms, however it was not possible to achieve a good fit doing so. Thus, it was concluded that the particle size growth of azole antifungal NPs described in this work cannot be explained by the OA process. For this reason, it was necessary to fix the k_1 constant to zero, therefore one can assume that particle coarsening is driven solely by the OR process. In addition, D_0 values were fixed according to particle size. Also, when fitted as two separate stages of growth, D_0 for part B was fixed to the particle size at the beginning of part B.

Table 2.3. Summary of parameters obtained by fitting Eq. 2.1 to experimental data of mean particle size of ITR NPs. The stabilizer used was DMPEG.

	Part A				Part B			
Sample	Time (h)	D_0 (nm)	$k_2 \pm SE$ ($nm^n \bullet h^{-1}$)	n ± SE	Time (h)	D_0 (nm)	$k_2 \pm SE$ ($nm^n \bullet h^{-1}$)	n ± SE
0 mg/ml	0 - 0.18	155	170 ± 11.5	2.5 ± 0.2	0.18-0.5	239	598 ± 68	0.4 ± 0.03
0.5 mg/ml	0 - 0.23	237	99 ± 6.5	3.4 ± 0.4	0.23-0.5	300	218 ± 78	0.4 ± 0.05
1 mg/ml	0 - 0.15	218	92 ± 6	3.7 ± 0.4	0.15-0.5	272	239 ± 32	0.5 ± 0.04
1.5 mg/ml	0 - 0.15	131	451 ± 123	4.3 ± 2.0	0.15-0.5	300	412 ± 47	0.8 ± 0.07
1.5 mg/ml*	0 – 0.5	131	787 ± 46	1.5 ± 0.04	N/A	N/A	N/A	N/A

* - full dataset was fitted

Table 2.4. Summary of parameters obtained by fitting Eq. 2.1 experimental data of mean particle size of POS NPs. The stabilizer used was DMPEG.

	Part A				Part B			
Sample	Time (h)	D_0 (nm)	$k_2 \pm SE$ ($nm^n \bullet h^{-1}$)	n ± SE	Time (h)	D_0 (nm)	$k_2 \pm SE$ ($nm^n \bullet h^{-1}$)	n ± SE
0 mg/ml	0 - 0.27	280	795 ± 36	1.69 ± 0.07	0.27 - 0.5	627	2744 ± 718	0.29 ± 0.03
0.5 mg/ml	0 - 0.42	245	911 ± 45	2.12 ± 0.15	0.42 - 0.5	813	$3.3 \bullet 10^6 \pm 4.3 \bullet 10^6$	0.07 ± 0.01
1 mg/ml	0 - 0.23	242	1644 ± 78	1.35 ± 0.05	0.23 - 0.5	785	$1.3 \bullet 10^9 \pm 4.2 \bullet 10^6$	0.04 ± 0.01
1.5 mg/ml	0 - 0.23	238	517 ± 220	980 ± 170128	0.23 - 0.5	785	2136 ± 1815	0.28 ± 0.08
1.5 mg/ml*	0 - 0.5	238	1103 ± 28	1.69 ± 0.06	N/A	N/A	N/A	N/A

* - full dataset was fitted

Table 2.5. Summary of parameters obtained by fitting Eq. 2.1 experimental data of mean particle size of KETO NPs. The stabilizer used was DMPEG.

	Part A				Part B			
Sample	Time (h)	D_0 (nm)	$k_2 \pm SE$ ($nm^n \bullet h^{-1}$)	n ± SE	Time (h)	D_0 (nm)	$k_2 \pm SE$ ($nm^n \bullet h^{-1}$)	n ± SE
0 mg/ml	0 - 0.25	190	469 ± 16	1.9 ± 0.06	0.25 – 0.5	418	3959 ± 694	0.3 ± 0.02
0 mg/ml*	0 - 0.5	190	462 ± 97	351 ± 14425	N/A	N/A	N/A	N/A
0.5 mg/ml*	0 - 0.5	220	815 ± 17	1.4 ± 0.03	N/A	N/A	N/A	N/A
1 mg/ml*	0 - 0.5	210	600 ± 13	2.2 ± 0.08	N/A	N/A	N/A	N/A
1.5 mg/ml*	0 - 0.5	200	466 ± 7	2.0 ± 0.05	N/A	N/A	N/A	N/A

* - full dataset was fitted

Fitting of the model presented in Eq. 2.1 to ITR NP datasets suggests that OR growth is controlled by bulk diffusion in the first stage of growth where n ~ 3 and above (Table 2.3). Interestingly, the second stage of growth is characterised by n < 1, this would suggest a change to interface controlled growth (Table 2.3). Logically, the adsorption of stabilizers onto ITR particle surfaces may be a time dependent process and therefore their role may be one of greater importance in the later stages of OR. The ITR k_2 OR rate constant is lower in the first stage of growth compared with the second stage, aside from DMPEG 1.5 mg/ml. This suggests the rate of OR increases as time proceeds.

According to Table 2.4, in the first stage of growth for POS NPs, the k_2 OR rate constant increases with increasing stabilizer concentration. In this instance, DMPEG may achieve the opposite of stabilization, encouraging OR for POS NPs, as well as providing a driving force for the crystallisation process. This may also explain the large and meaningless *n* exponent obtained for POS DMPEG 1.5 mg/ml during the first stage of growth. During the second phase of growth, k_2 OR rate constant values become extremely large and meaningless, this may be caused by the rapid crystallisation taking place as confirmed by PXRD and SEM.

Stabilizer free KETO NPs exhibited cubic growth associated with bulk diffusion controlled growth, causing the *n* exponent to be meaningless when this data was fitted as a single (FULL) phase (Table 2.5). Introducing a stabilizer forces the OR process to transition to an interface controlled growth (n ~ 2) associated with parabolic growth seen in Fig. A.1.9. KETO NPs stabilized by polymers were therefore fitted as a single stage as denoted by an asterisk in Table 2.5. Increasing DMPEG concentration causes the KETO k_2 OR rate constant to decrease, suggesting the stabilizer in this instance is effectively hindering the OR process in a concentration dependent manner (Fig. 2.6f).

Furthermore, all NPs stabilized by DMPEG 1.5 mg/ml exhibit parabolic growth, characteristic of interface controlled growth, confirmed by n exponent values ~ 2. It should be noted, that ITR k_2 OR rate constant values are the lowest of all APIs, suggesting OR is slowest for these NPs (Table 2.3) thereby granting them greatest colloidal stability.

The role of surface adsorption in growth kinetics remains a complicated one. It is possible that the stabilizers employed in this study have multiple, conflicting roles. It seems likely that the presence of stabilizers has a steric hindrance effect achieved via long flexible polymer carbon chains. These chains provide an energy barrier to the bulk diffusion process forcing OR to become interface controlled. In the case of ITR, addition of a stabilizer appears to decrease the rate of the OR growth (Table 2.3). However, stabilizer concentration appears to be of great importance, with a concentration threshold existing whereby below this, inhibition of OR exists and above it, OR is promoted. For KETO NPs, increasing stabilizer concentration appears to exclusively inhibit OR growth confirmed by the decreasing k_2 OR rate constants in Table 2.5. Stabilizers appear to promote OR growth in the case of POS NPs, shown by k_2 OR rate constants in Table 2.3.

2.3.5 Solid state Transformation of NP in Dispersions over time

The three APIs formulated into NPs and investigated in this work undergo different crystallisation pathways. Particles existing in solution that interact through Brownian motion are capable of aggregating to form larger structures via numerous pathways.

ITR NPs possess liquid crystalline structures, with a nematic phase upon initial formation as shown previously (Mugheirbi and Tajber, 2015a). The conditions employed for ITR NP formation in the above mentioned studies have been replicated here. Molecules that induce liquid crystallinity are referred to as mesogens, they tend to be needle like or disk like in structure, making ITR an ideal candidate. As Mugheirbi and Tajber (2015a) have shown, the absence of H-bond donor groups within the ITR structure means that π - π stacking is likely to be responsible for stabilizing ITRs liquid crystalline structure (Fig. 2.1). The ability to form these LC phases may contribute to very good ITR NP colloidal stability and delayed crystallisation seen beyond 30 minutes. However, the LC phase of ITR has a higher solubility than the crystalline phase and, as observed by Mugheirbi and Tajber (2015b), can lead to crystallisation of the drug, via the OR mechanism to microcrystals. NP production via wet media milling has been shown to preserve the crystalline nature of ITR NPs (Liu et al., 2011). The method of production has a profound impact upon the crystallisation pathways taken by ITR.

POS particles associate in an unstructured way and are therefore amorphous in nature, with a tendency to crystallize quickly within 30 minutes as confirmed by Fig. 2.7e and 2.8d. Amorphous-to-crystalline pathways have a thermodynamic origin, with aggregation of metastable amorphous particles followed by transformation to a final thermodynamically stable ordered crystalline polymorph form I (Wieser et al., 2012). This strong tendency to crystallize can be attributed to the presence of a hydroxyl group within the chemical structure of POS, therefore responsible for hydrogen bonding within its crystal lattice (Fig. 2.1). Strong hydrogen bonding between colliding NPs increases the likelihood that they will coalesce together.

Unfortunately, it was not possible to isolate KETO NPs upon initial formation however, it is possible that amorphous particles were generated at this stage. PXRD data shown in Fig. 2.7h confirm the crystalline nature of KETO NPs at 30 minutes, however the peak intensities are below those of the starting material powder. The amorphous character of KETO NPs produced via high pressure homogenisation has been noted elsewhere in the literature (Kakkara et al., 2015). Also, KETO has shown itself to be resistant to solid state changes, maintaining its crystallinity when milled for NP production (Liu et al., 2011). This reiterates the profound impact NP production method has upon crystallisation pathways.

ITR, POS and KETO NPs produced in this work crystallised over time, however a less ordered precursor, preceding the full crystallisation, was isolated in each case. These APIs proceed via "non-classical crystallisation" routes involving kinetically metastable precursor particles which can be amorphous, liquid or crystal phases (Niederberger and Cölfen, 2006). This presents limitations in terms of the application of Eq. 2.1. As it is therefore possible that alternative physical processes are competing alongside OR growth. Nevertheless, fitting parameters confirm that ITR NPs experience the slowest rate of OR. The rate of OR appears to be inherent of the crystallisation pathway by which these APIs proceed (Fig. 2.9).

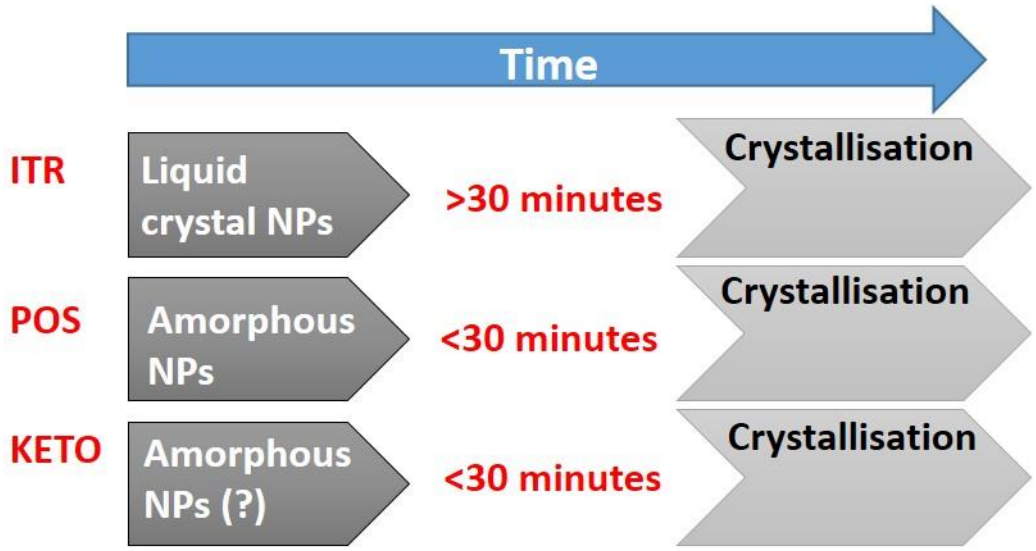

Fig. 2.9. Schematic representation of API crystallisation pathways. ITR = itraconazole, POS = posaconazole, KETO = ketoconazole, NPs = nanoparticles.

2.4 CONCLUSIONS

Nano-dispersions made of ITR, POS and KETO were formed by anti-solvent precipitation and characterised using a number of physical techniques. ITR NPs have the greatest colloidal stability when no stabilizer is included in the system, when compared with POS and KETO NP equivalents. It appears that the stabilizers employed in this study may have multiple, conflicting roles. DMPEG proved to be the most effective stabilizer for all APIs in these conditions. However, POS nano-dispersions had greater stability in the absence of any stabilizer. The greater hydrophobic content of DMPEG, in comparison to MPEG and PEG, appears to affect strength of stabilizer adsorption onto API particle surfaces and hence stabilization of NPs. In general, the presence of DMPEG causes OR growth to become an interface controlled process. Interestingly, DMPEG encourages OR for POS NPs and drives the crystallisation process. It cannot therefore be assumed the role of stabilizers is confined to stabilization alone. The rate of OR appears to be inherent of the crystallisation pathway by which these APIs proceed. Crystallisation mechanisms are API, stabilizer and stabilizer concentration dependent. These three structurally similar APIs undergo different crystallisation pathways. It appears that stabilization of NP system is dependent upon three factors: API chemical structure, crystallisation pathway and theoretical supersaturation ratio. Further work will look to improve our understanding behind the mechanism of stabilization for these NP systems and the role of stabilizers within these crystallisation pathways.

References

Andrews, D.R., Leong, W., Sudhakar, A., 2004. United States Patent US006958337B2.

Butler, J.M., Dressman, J.B., 2010. The Developability Classification System: Application of Biopharmaceutics Concepts to Formulation Development. J. Pharm. Sci. 99, 4940–4954.

Choi, J., Youn, J., Kwak, H., Uk, B., Lee, J., 2005. Role of polymeric stabilizers for drug nanocrystal dispersions. Curr. Appl. Phys. 5, 472–474.

Dolenc, A., Kristl, J., 2009. Advantages of celecoxib nanosuspension formulation and transformation into tablets. Pharm. Nanotechnol. 376, 204–212.

Dressman, J.B., Reppas, C., 2000. *In vitro-in vivo* correlations for lipophilic, poorly water-soluble drugs. Eur. J. Pharm. Sci. 11, 73–80.

Ghosh, I., Schenck, D., Bose, S., Ruegger, C., 2012. Optimization of formulation and process parameters for the production of nanosuspension by wet media milling technique: Effect of Vitamin E TPGS and nanocrystal particle size on oral absorption. Eur. J. Pharm. Sci. 47, 718–728.

Han, T.Y.J., Aizenberg, J., 2007. Calcium Carbonate Storage in Amorphous Form and Its Template-Induced Crystallization. Chem. Mater. 20, 1064–1068.

Hassan, P., Rana, S., Verma, G., 2015. Making sense of brownian motion: colloid characterization by dynamic light scattering. Langmuir. 31, 3–12.

Huang, F., Zhang, H., Banfield, J.F., 2003a. The Role of Oriented Attachment Crystal Growth in Hydrothermal Coarsening of Nanocrystalline ZnS. J. Phys. Chem. B. 107, 10470–10475.

Huang, F., Zhang, H., Banfield, J.F., 2003b. Two-stage crystal-growth kinetics observed during hydrothermal coarsening of nanocrystalline ZnS. Nano Lett. 3, 373–378.

Ilevbare, G., Taylor, L.S., 2013. Liquid-Liquid Phase Separation in Highly Supersaturated Aqueous Solutions of Poorly-Water Soluble Drugs – Implications for Solubility Enhancing Formulations. Cryst. Growth Des. 13, 1497–1509.

Ingham, B., Lim, T.H., Dotzler, C.J., Henning, A., Toney, M.F., Tilley, R.D., 2011. How Nanoparticles Coalesce: An in Situ Study of Au Nanoparticle Aggregation and Grain Growth. Chem. Mater. 23, 3312–3317.

Kakkara, S., Karuppayilb, S.M., Rauta, J.S., Giansantic, F., Papuccid, L., Schiavonee, N., Kaura, I.P., 2015. Lipid-polyethylene glycol based nano-ocular formulation of ketoconazole. Int.

J. Pharm. 495, 276-289.

Kirchner, H.O., 1971. Coarsening of grain-boundary precipitates. Metall. Trans. 2, 2861–2864.

Liu, P., Rong, X., Laru, J., Van Veen, B., Kiesvaara, J., Hirvonen, J., Laaksonen, T., Peltonen, L., 2011. Nanosuspensions of poorly soluble drugs: Preparation and development by wet milling. Int. J. Pharm. 411, 215–222.

Mahesh, K.V., Singh, S.K., Gulati, M., 2014. A comparative study of top-down and bottom-up approaches for the preparation of nanosuspensions of glipizide. Powder Technol. 256, 436–449.

Matteucci, M.E., Paguio, J.C., Miller, M.A., Williams, R.O., Johnston, K.P., 2009. Highly supersaturated solutions from dissolution of amorphous ltraconazole microparticles at pH 6.8. Mol. Pharm. 6, 375–385.

Mugheirbi, N.A., Paluch, K.J., Tajber, L., 2014. Heat induced evaporative antisolvent nanoprecipitation (HIEAN) of itraconazole. Int. J. Pharm. 471, 400–411.

Mugheirbi, N.A., Tajber, L., 2015a. Mesophase and size manipulation of itraconazole liquid crystalline nanoparticles produced via quasi nanoemulsion precipitation. Eur. J. Pharm. Biopharm. 96, 226–236.

Mugheirbi, N.A., Tajber, L., 2015b. Crystal habits of itraconazole microcrystals: unusual isomorphic intergrowths induced via tuning recrystallization conditions. Mol. Pharmaceutics. 12, 3468–3478.

Mugheirbi, N.A., O'Connell, P., Serrano, D.R., Healy, A.M., Taylor, L.S., Tajber L., 2017. A comparative study on the performance of inert and functionalized spheres coated with solid dispersions made of two structurally related antifungal drugs. Mol. Pharmaceutics, 14, 3718–3728.

Niederberger, M., Cölfen, H., 2006. Oriented attachment and mesocrystals: non-classical crystallization mechanisms based on nanoparticle assembly. Phys. Chem. Chem. Phys. 8, 3271–3287.

Noyes, A.A., Whitney, R., 1897. The rate of solution of solid substances in their own soltuions. J. Am. Chem. Soc. 19, 930–934.

Ostwald, W., 1900. Über die vermeintliche Isomerie des roten und gelben Quesck-silberoxyds und die Oberflachenspannung fester Körper. Z. Phys. Chem. 34, 495–503.

Palla, B.J., Shah, D.O., 2002. Stabilization of High Ionic Strength Slurries Using Surfactant Mixtures: Molecular Factors That Determine Optimal Stability. J. Colloid Interface Sci. 256, 143–152.

Rane, S.S., Choi, P., 2005. Polydispersity index: How accurately does it measure the breadth of the molecular weight distribution? Chem. Mater. 17, 926.

Shang, J., Gao, X., 2014. Nanoparticle counting: towards accurate determination of the molar concentration. Chem. Soc. Rev. 43, 7267–7278.

Shegokar, R., Müller, R.H., 2010. Nanocrystals: Industrially feasible multifunctional formulation technology for poorly soluble actives. Int. J. Pharm. 399, 129–139.

Speight, M.V., 1968. Growth kinetics of grain-boundary precipitates. Acta. Metall. 16, 133–135.

Van Eerdenbrugh, B., Vermant, J., Martens, J.A., Froyen, L., Van Humbeeck, J., Augustijns, P., Van Den Mooter, G., 2009. A screening study of surface stabilization during the production of drug nanocrystals. J. Pharm. Sci. 98, 2091-2103.

Voorhees, P.W., 1985. The Theory of Ostwald ripening. J. Sat. Phys. 38, 231–252.

Wagner, C.Z., 1961. Theory of precipitate change by redissolution. Elektrochem. 65, 581–591.

Wang, H., Pan, Q., Rempel, G.L., 2011. Micellar nucleation differential microemulsion polymerization. Eur. Polym. J. 47, 973–980.

Wieser, J., Pichler, A., Hotter, A., Griesser, U., Langes, C., 2013. Patent Number US 8,563,555 B2.

Wieser, J., Pichler, A., Hotter, A., Griesser, U., Langes, C., 2012. Patent Number US 2012/0101277 A1.

Yin, S., Huang, F., Zhang, J., Zheng, J., Lin, Z., 2011. The Effects of Particle Concentration and Surface Charge on the Oriented Attachment Growth Kinetics of CdTe Nanocrystals in H2O. J. Phys. Chem. C. 115, 10357–10364.

3.1. INTRODUCTION

In order to fully utilise the potential of NPs as drug carriers, NP characterisation must be accurate and reliable to ensure delivery of high quality products to the marketplace. The accuracy of particle size distribution (PSD) measurements is dependent upon the technique employed for analysis. The inconsistency between measurements performed via different techniques increases with sample complexity and polydispersity. For this reason, it is recommended that size characterisation is performed using at least two methods that employ different sizing techniques (Bell et al., 2012; Anderson et al., 2013).

There are a number of well established particle sizing techniques currently adopted within industry, each having their own advantages and limitations. Methods should be quick to perform, low in cost whilst providing a detailed analysis of the sample in question. Traditional sizing methods include SEM and DLS, as well as size exclusion chromatography and analytical ultracentrifugation (Bootz et al., 2004; Brown and Schuck, 2006). SEM provides three-dimensional images of the particle and can therefore reveal alternative information such as particle morphology. However, when employed as a sizing technique, in order to obtain statistically significant PSDs it would be necessary to measure hundreds or thousands of individual particles, unless automated analysis software were available (Bootz et al., 2004). SEM requires drying and coating of particles with a conductive layer such as gold. Therefore, particle characteristics can be inherent of the preparation procedure which can have an impact upon original particle properties (McKinlay et al., 2004).

DLS sizes particles dispersed in a liquid medium based on their translational diffusion coefficient and Brownian motion. Intensity fluctuations of laser light scattered by the particles is quantified via an autocorrelation function comparing the initial scattering intensity to the intensity after specified time periods. A slow decay in the autocorrelation function is caused by the presence of large particles moving slowly; whereas fast decay indicates the presence of fast moving small particles. The diffusion coefficient can be obtained from the measured decay rate, which is directly proportional to the inverse radius of the particles via the Stokes–Einstein equation (Einstein, 1908). Hydrodynamic diameter is then calculated based upon the Stoke – Einstein equation (Eq. 3.1):

$$d_H = \frac{k\,T}{3\,D\,\pi\,n} \qquad \text{(Eq. 3.1)}$$

where d_H = hydrodynamic diameter, k = the Boltzmann constant, T = temperature, D = diffusion coefficient and η = viscosity of the medium (Svedberg, 1906). DLS offers advantages in terms of speed and the need for little sample preparation. However, this technique can be problematic when analysing multimodal complex dispersions with intensity based distributions being biased towards larger particles (Calzolai et al., 2011; Anderson et al., 2013). DLS has the capability of measuring the hydrodynamic diameter of particles within the range 1 nm to 10 µm.

Nanoparticle tracking analysis (NTA) has emerged in recent years as an alternative tool for NP size characterisation. Particles are sized based on their light scattering capabilities and Brownian motion when dispersed in a liquid medium. Particles in the sample scatter light projected from a laser, which is then tracked using a camera. The software tracks individual particles and determines their size using the Stokes – Einstein equation (Eq. 3.1), therefore not only can NTA provide particle size measurements but also valuable information regarding particle concentration (Bell et al., 2012). Since individual particles are tracked, high peak to peak resolution of PSDs can be achieved (Filipe et al., 2010). NTA has the capability of accurately sizing particles between 30 nm to 1000 nm. NTA has the added bonus of instantaneous visualisation of light scattering centres (particles) which can provide key information with regards to sample homogeneity (Joubert et al., 2011). In order for particles to be tracked via NTA they must scatter light of an intensity above a certain threshold. The amount of light scattered is dictated by the particle scattering cross-section and intensity of incident light (Gallego-Urrea et al., 2011). The Mie theory and Rayleigh approximation are two approaches utilised when studying light scattering. Rayleigh scattering solely applies to small, dielectric spherical particles, whilst Mie theory entails a general scattering solution with no limit on particle size. Rayleigh scattering predominates for particles smaller than the wavelength of incident light. For particles that are larger than a wavelength, Mie scattering prevails (Hahn, 2009). Light scattering properties of materials are a result of both particle size and composition. It is therefore possible to distinguish between particles of a similar size based on their refractive indices (RI) (Gallego-Urrea et al., 2011). Filipe et al. (2010) utilised NTA for the purpose of live monitoring of heat induced protein aggregation, revealing valuable information regarding aggregation kinetics and aggregate size. Different sized populations were distinguishable based on their scattering intensities (Filipe et al., 2010). Yang et al. (2014) employed NTA for protein characterisation concluding that scattering intensity information can be used to determine protein aggregate structure (Yang et al., 2014).

The intent of this study was to perform a critical comparison of the particle sizing techniques DLS and NTA for azole anti-fungal nano-dispersions. Techniques employed and sample characteristics will be considered in detail with regards to interpretation of data. NPs were formed using three different APIs: ITR, KETO and POS. PEG, MPEG and DMPEG with a molecular weight 2000 Da were investigated as potential stabilizers at various concentrations. Work in Chapter 2, investigating the colloidal stability of these azole anti-fungal nano-dispersions utilised DLS alone. Results showed that DMPEG was the most effective stabilizer for all API nano-dispersions whilst ITR NPs had the greatest overall stability of all three APIs concerned. Kinetic modelling confirmed nanoparticle growth was driven by OR. DMPEG encouraged OR for POS NPs whilst driving the crystallisation process as confirmed by solid state characterisation and morphological examination (Chapter 2). A sharp increase in the variability associated with DLS data at specific time points was noted. This fact, along with information obtained from SEM analysis suggested possible crystallisation of APIs was taking place during the DLS analysis, most notably for POS. Considering the anisotropic nature of crystals in contrast to amorphous materials, the application of NTA may provide a deeper insight into the crystallisation pathways by which these APIs proceed, as well as further information regarding particle concentration values. Given the additional capabilities offered by NTA technology, tracking these processes may facilitate the discovery of novel findings regarding the physical processes at play. We present the innovative application of NTA for the purpose of live monitoring of NP crystallisation pathways *in situ* for the first time during the course of this study.

3.2. Materials and Methods

3.2.1 Materials

Itraconazole (ITR) was a gift from Welding in GmbH (Hamburg, Germany). Ketoconazole (KETO) was purchased from Glentham Life Sciences Ltd. (Wiltshire, UK). Posaconazole (POS) was purchased from Glentham Life Sciences Ltd. (Wiltshire, UK). Poly(ethlyene glycol) (PEG), poly(ethylene glycol) methyl ether (MPEG) and its dimethoxylated derivative (DMPEG) with average molecular weights of 2000 Da (Dalton) were purchased from Aldrich Chemical Co., Ltd. (Dorset, UK). Acetone Chromasolv® HPLC grade was obtained from Sigma Aldrich (Dorset, UK).

3.2.2 METHODS

3.2.2.1 Anti-Solvent Precipitation of ITR, POS and KETO Nanoparticles (NPs)

NPs were formed as previously described in Chapter 2. Polymeric stabilizers (PEG, MPEG and DMPEG) were included at the same concentrations as those employed in Chapter 2: 0.5, (0.05 % w/v), 1 (0.1 % w/v) and 1.5 mg/ml (0.15 % w/v).

3.2.2.2 Nanoparticle Tracking Analysis

Size characterisation determination was performed by NTA using a NanoSight NS300 device (Malvern Instruments), equipped with a red laser 638 nm and SCMOS camera. Data collection and analysis was performed using NTA 3.0 software. Anti-solvent (deionised water/stabilizer solution) and solvent (API/acetone) phases were kept at 25 °C, solutions were filtered using 0.45 µm polytetrafluoroethylene (PTFE) filters (VWR, Ireland) prior to NP formation and injected using sterile syringes into the sample chamber. Samples were diluted with the appropriate anti-solvent phase (water or stabilizer/water) using a 1:17 dilution (v/v) (0.25 ml of nano-dispersion added to 4 ml of anti-solvent phase) prior to analysis in order to achieve the desired particle concentration, between 10^7 and 10^9 total particles/ml. Temperature was controlled at 25 °C for the duration of the study. Particle size was recorded every minute for 30 minutes, therefore a standard operating procedure (SOP) was created using standard measurement: 30 captures of 55 second duration, to account for ~ 5 second delay between each capture. The sample was advanced every minute changing the particles in view to ensure a truly representative sample of particles were measured. All measurements were performed in triplicate. Samples were measured with manual shutter and gains adjustment. Particle size was corrected for viscosity of the continuous phase. The sample chamber was manually cleaned using MilliQ water and 10% ethanol in water solution (v/v). Upon completion, no particles were visibly present in the sample chamber through the viewing window.

3.2.2.3 Dynamic Light Scattering (DLS)

The mean particle size of NPs were measured using the Zetasizer Nano ZS series (Malvern Instruments, UK). The software used for analysing and capturing measurements was Malvern Zetasizer software version 7.12. Mean particle size measurements were measured *in situ* using a 12 o.d. mm 1ml PCS8501 glass cuvette. All measurements were carried out at 25 °C. The analysis was performed in triplicate for each sample with mean particle diameter recorded every minute for 30 minutes. Particle size was corrected for viscosity of the continuous phase.

Viscosity of the continuous phase was measured in triplicate at 25 °C using a Vibro Viscometer SV-10 (A&D, Japan).

3.3. Results and Discussion

Previous work on particle size analysis of the azole drugs (ITR, KETO and POS) carried out using DLS presented a number of key outcomes (Chapter 2). ITR NPs had the best stability of all API nano-dispersions, in both the presence and absence of stabilizers. DMPEG was the most effective stabilizer overall for all API nano-dispersions. For ITR NPs, DMPEG was the most effective when employed at 0.5 mg/ml concentration. In contrast, for KETO NPs DMPEG was most effective at the highest concentration 1.5 mg/ml. Increased variability around 15 minutes was observed in DLS data for KETO NPs stabilized with PEG and MPEG. This could suggest possible crystallisation and indeed KETO NPs were confirmed as PXRD crystalline at 30 minutes (Chapter 2). PXRD analysis also confirmed that POS NPs initially formed an unstable amorphous phase, which was isolated within a few minutes of formation and then replaced by a more stable ordered crystalline phases of form I POS within 30 minutes. POS NPs had the poorest stability, with the presence of stabilizers appearing to promote crystallisation and destabilize nano-dispersions. POS NPs stabilized with MPEG were the least stable, with increased variability in data observed at the earliest time of 15 minutes, suggesting possible crystallisation. The use of NTA may facilitate efforts to continuously monitor this process. Therefore, all API nano-dispersions were analysed using NTA in a manner similar to Chapter 2, using DLS to allow for comparisons to be drawn between the two sets of data generated via these different techniques.

3.3.1 Itraconazole

ITR PSDs shown in Fig. 3.1 highlight clear differences existing between data obtained using DLS and NTA.

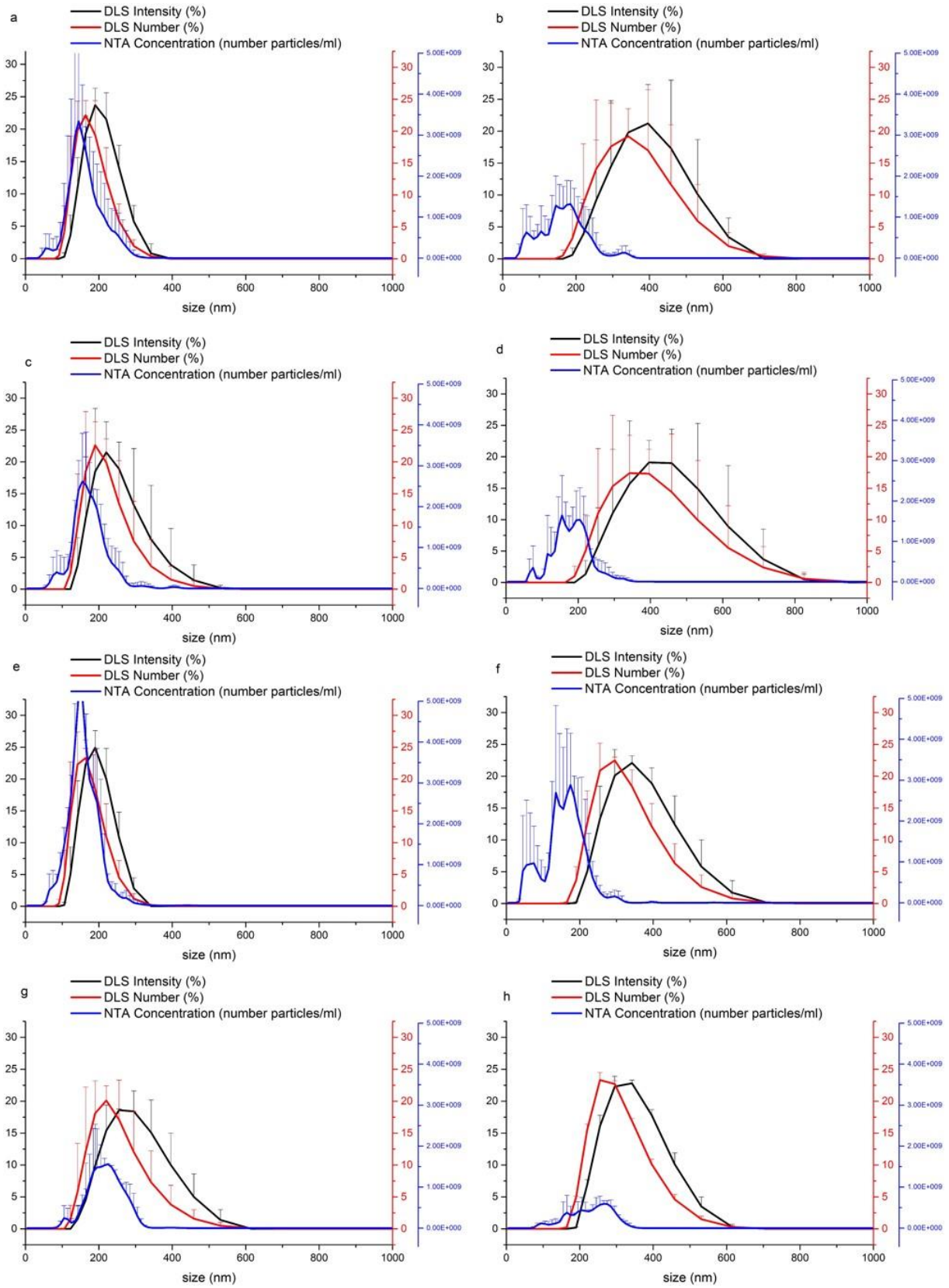

Fig. 3.1 ITR particle size distributions for NTA (number based) and DLS (number and intensity based) for (a) stabilizer free ITR NPs at 1 minute (b) stabilizer free ITR NPs at 30 minutes (c) ITR PEG 0.5 mg/ml NPs at 1 minute (d) ITR PEG 0.5 mg/ml NPs at 30 minutes (e) ITR MPEG 0.5

mg/ml NPs at 1 minute (f) ITR MPEG 0.5 mg/ml NPs at 30 minutes (g) ITR DMPEG 0.5 mg/ml NPs at 1 minute (h) ITR DMPEG 0.5 mg/ml NPs at 30 minutes. (n = 3)

Previous work in Chapter 2 measured increase in particle size (%) over 30 minutes using DLS for each ITR nano-dispersion, with values ranging between 100-250%. In addition to DLS intensity based distributions, DLS number based distributions have been included for completeness (Fig. 3.1 and 3.2). However, it should be noted that these number based values have been derived from an intensity distribution. In a number based distribution, all particles within the distribution are given equal weighting irrespective of their size. In contrast, with an intensity based distribution, larger particles have the ability to skew the distribution towards larger particle sizes (Demeester et al., 2005). Therefore as expected, in all distributions number based values are lower than their intensity based equivalents obtained using DLS. For ITR PSDs at 1 minute, the three distributions are in close agreement (Fig. 3.1a, c, e, and g), NTA and DLS values correspond well. However at 30 minutes, the same does not remain true, with a greater difference existing between the DLS and NTA distributions (Fig. 3.1b, d, f, and h). Interestingly, it is worth noting that the most stable ITR DMPEG 0.5 mg/ml NPs have the lowest variability for both NTA and DLS as demonstrated by the small error bars in Fig. 3.1g and h, indicating high measurement precision for this sample. This was also the only sample to show a decrease in variability, with both techniques, between minute 1 and 30 (Fig. 3.1g and h). Table 3.1 shows particle size data at 1 minute for ITR, NTA versus DLS.

Table 3.1. Mean particle size and size distribution measurements obtained for ITR nano-dispersions using DLS and NTA at 1 minute. (n = 3)

	DLS (intensity based)		NTA (number based)	
	Z-ave ± SD (nm)	PDI ± SD	Mean ± SD (nm)	Concentration (number particles/ml) ± RSD
Stabilizer free ITR NPs	184 ± 10	0.04 ± 0.03	161 ± 30	$2.9 \cdot 10^{10}$ ± 20.3
ITR PEG 0.5 mg/ml	232 ± 19	0.07 ± 0.06	171 ± 18	$2.5 \cdot 10^{10}$ ± 16.0
ITR PEG 1 mg/ml	235 ± 54	0.10 ± 0.07	174 ± 28	$2.0 \cdot 10^{10}$ ± 31.0
ITR PEG 1.5 mg/ml	179 ± 21	0.11 ± 0.09	206 ± 6	$2.1 \cdot 10^{10}$ ± 11.4
ITR MPEG 0.5 mg/ml	152 ± 13	0.05 ± 0.04	153 ± 7	$4.0 \cdot 10^{10}$ ± 5.3
ITR MPEG 1 mg/ml	180 ± 7	0.02 ± 0.02	183 ± 20	$2.3 \cdot 10^{10}$ ± 19.1
ITR MPEG 1.5 mg/ml	244 ± 13	0.04 ± 0.03	205 ± 33	$1.6 \cdot 10^{10}$ ± 32.5
ITR DMPEG 0.5 mg/ml	242 ± 56	0.08 ± 0.06	202 ± 24	$1.8 \cdot 10^{10}$ ± 10.6
ITR DMPEG 1 mg/ml	246 ± 77	0.13 ± 0.03	207 ± 23	$1.9 \cdot 10^{10}$ ± 25.8
ITR DMPEG 1.5 mg/ml	179 ± 13	0.03 ± 0.03	181 ± 16	$2.3 \cdot 10^{10}$ ± 14.3

*PDI = polydispersity index, SD = standard deviation, RSD = relative standard deviation

Both techniques confirm DMPEG is the most effective stabilizer for ITR NPs at the lowest concentration of 0.5 mg/ml (Fig. 3.1g and h, Fig. A.2.1). Fig. 3.1 shows a marked decrease in NTA particle concentration between 1 minute and 30 minutes for all ITR nano-dispersions (Fig. 3.1 and Fig. A.2.2). ITR NTA distributions at 30 minutes appear to be multimodal and polydisperse in comparison to mono-modal distributions observed for all samples using both techniques at 1 minute (Fig. 3.1). However, the complexity of ITR PSDs at 30 minutes that was visible with NTA, was not evident with DLS. This reiterates the ability of NTA to achieve greater peak resolution, distinguishing particle population's close in size, simply not possible with DLS (Filipe et al., 2010).

3.3.2 KETOCONAZOLE

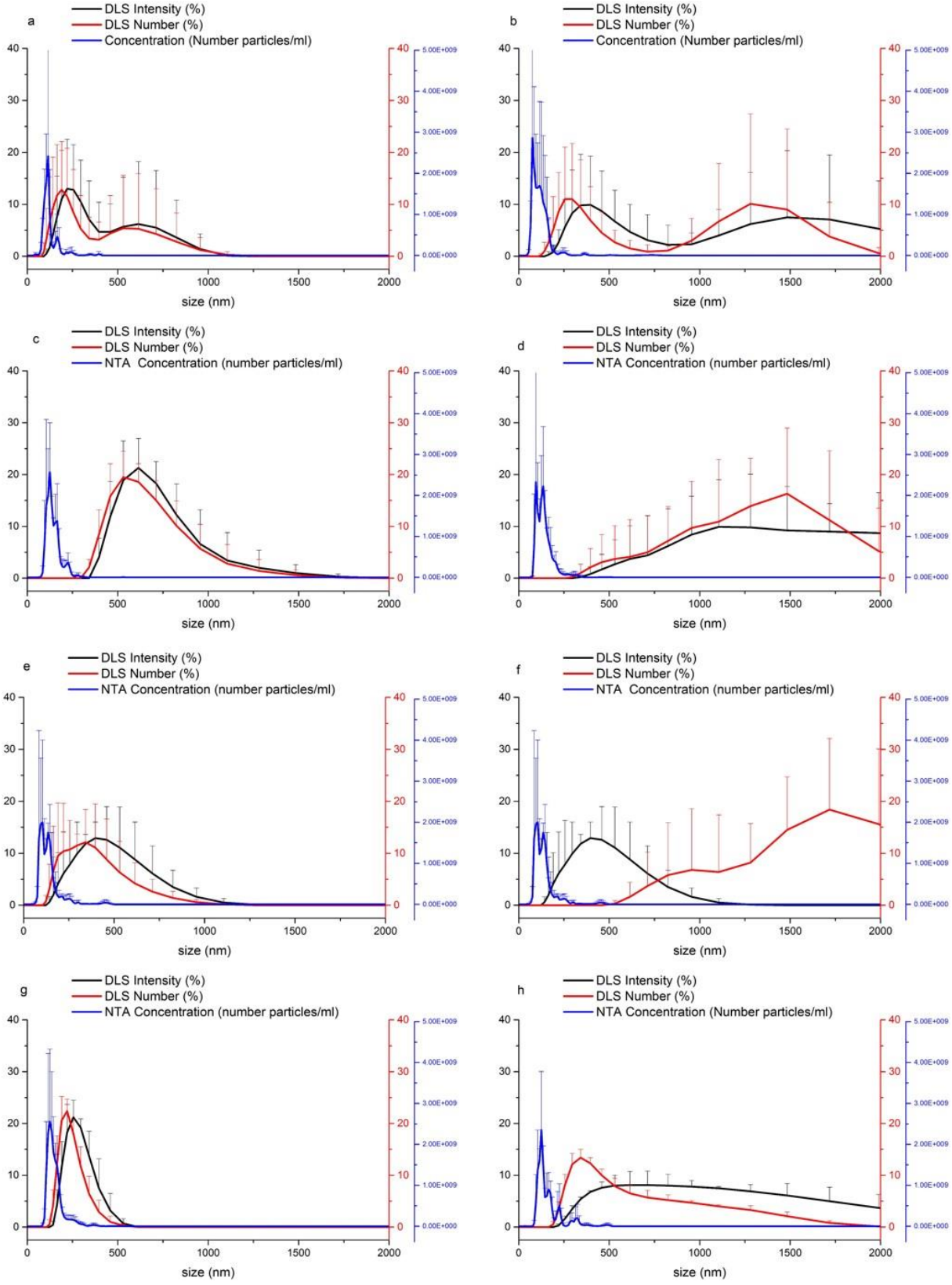

Fig. 3.2 KETO particle size distributions for NTA (number based) and DLS (number and intensity based) for (a) stabilizer free KETO NPs at 1 minute (b) stabilizer free KETO NPs at 30 minutes (c) KETO PEG 0.5 mg/ml NPs at 1 minute (d) KETO PEG 0.5 mg/ml NPs at 30 minutes (e) KETO

MPEG 0.5 mg/ml NPs at 1 minute (f) KETO MPEG 0.5 mg/ml NPs at 30 minutes (g) KETO DMPEG 0.5 mg/ml NPs at 1 minute (h) KETO DMPEG 0.5 mg/ml NPs at 30 minutes.

KETO PSDs show a great variation between DLS and NTA, with NTA sizing these samples much smaller than DLS throughout (Fig. 3.2). This feature has been noted elsewhere in the literature (Filipe et al., 2010). Great differences are evident at 30 minutes between the two techniques, with DLS having much broader PSDs. Large error bars are associated with both techniques for KETO distributions, indicating low measurement precision for these nano-dispersions. However, again the most stable KETO NPs containing DMPEG, have the smallest DLS error bars and variability associated with those measurements at both 1 and 30 minutes (Fig. 3.2g and h). There is little difference between the NTA distributions between 1 and 30 minutes for all KETO nano-dispersions, in comparison with the DLS peaks, where a significant shift to a larger and broader distribution at 30 minutes was observed (Fig. 3.2). All other KETO nano-dispersions behaved in the same manner, with the exception being KETO DMPEG 1.5 mg/ml (Fig. A.2.3). Interestingly, this was the most the effective stabilizer for KETO nano-dispersions as confirmed by DLS. This sample was associated with the lowest variability and showed closest agreement between the two techniques (Fig. A.2.3). Table 3.2 contains particle size data obtained via NTA and DLS at 1 minute for KETO nano-dispersions.

Table 3.2. Mean particle size and size distribution measurements obtained for KETO nano-dispersions using DLS and NTA at 1 minute. (n = 3)

	DLS (intensity based)		NTA (number based)	
	Z-ave ± SD (nm)	PDI ± SD	Mean ± SD (nm)	Concentration (number particles/ml) ± RSD
Stabilizer free KETO NPs	204 ± 10	0.09 ± 0.07	117 ± 10	$9.7 \cdot 10^9$ ± 66.0
KETO PEG 0.5 mg/ml	639 ± 83	0.05 ± 0.04	140 ± 7	$1.6 \cdot 10^{10}$ ± 41.3
KETO PEG 1 mg/ml	658 ± 152	0.10 ± 0.07	133 ± 18	$1.9 \cdot 10^{10}$ ± 8.4
KETO PEG 1.5 mg/ml	520 ± 102	0.15 ± 0.09	153 ± 21	$1.3 \cdot 10^{10}$ ± 33.8
KETO MPEG 0.5 mg/ml	406 ± 129	0.15 ± 0.05	146 ± 10	$1.5 \cdot 10^{10}$ ± 20.7
KETO MPEG 1 mg/ml	642 ± 84	0.10 ± 0.10	133 ± 5	$1.9 \cdot 10^{10}$ ± 21.1
KETO MPEG 1.5 mg/ml	345 ± 56	0.15 ± 0.05	133 ± 7	$1.1 \cdot 10^{10}$ ± 38.2
KETO DMPEG 0.5 mg/ml	258 ± 22	0.08 ± 0.06	149 ± 13	$1.7 \cdot 10^{10}$ ± 43.5
KETO DMPEG 1 mg/ml	269 ± 24	0.14 ± 0.04	169 ± 15	$1.3 \cdot 10^{10}$ ± 46.9
KETO DMPEG 1.5 mg/ml	248 ± 14	0.10 ± 0.05	166 ± 13	$2.7 \cdot 10^{10}$ ± 15.6

*PDI = polydispersity index, SD = standard deviation, RSD = relative standard deviation

KETO particle sizes upon initial formation are much larger when measured via DLS compared with NTA equivalents (Table 3.2). Whilst ITR nano-dispersions show good agreement between the two techniques with particle sizes ranging between 150-250 nm (Table 3.1). PDI measurements would suggest that KETO nano-dispersions are the most polydisperse of all API nano-dispersions i.e. are multimodal. This fact is also supported by the larger error bars associated with DLS data for KETO nano-dispersions compared with that of NTA (Table 3.2). Decreased variability associated with NTA KETO samples suggests good reproducibility for these datasets compared with DLS equivalents (Table 3.2). In Chapter 2, stabilizer free KETO NPs were highlighted as being particularly unstable via DLS. This corresponds to the highest variability of all KETO nano-dispersions in particle concentration measured via NTA which can be found in Table 3.2. Further information regarding NTA particle concentration measurements is presented in Fig. A.2.4.

3.3.3 POSACONAZOLE

Analysis of POS nano-dispersions proved to be challenging. The tendency of these samples to visibly crystallise and precipitate crystals larger than 1 micron in size within the time scale of the study, meant it was not possible to obtain size data via NTA for every time point. POS crystals visibly precipitate within 30 minutes as shown by photographs (Fig. A.2.5) and SEM images (Fig. 2.8). Large crystals could be seen in the viewing field of the software causing pixel blooming and therefore obscuring smaller particles present in the sample (Fig. A.2.6a and b). In this instance, the NTA software views the large crystals as noise and will not measure their size or will attempt to size them as many small particles, an issue noted elsewhere in the literature (Gallego-Urrea et al., 2011). POS NTA particle concentration measurements shown in Table A.2.1 also displayed high variability when compared with ITR and KETO equivalents. This provides further evidence for exclusion of POS nano-dispersions from size comparisons. Therefore, particle size comparison between DLS and NTA was limited to the assessment of ITR and KETO nano-dispersions alone.

3.3.4 MONITORING OF CRYSTALLISATION PATHWAYS USING NTA

Rayleigh approximation has been previously used by Luo et al. (2016) to explain the light scattering behaviour of gold NPs (Joubert et al., 2011; Luo et al., 2016). Due to the larger size of the ITR, KETO and POS NPs studied in this case, the same approach could not be adopted (Joubert et al., 2011; Luo et al., 2016). Therefore, it seemed logical to apply Mie theory (Gallego-Urrea et al., 2011) to determine if NTA could be used to explain changes in NPs, occurring primarily due to solid state transformations and not a change in particle size. Mie scattering requires refractive index (RI) values for accurate size measurement. It is known that cubic crystals and isotropic materials can have only one RI, whilst triclinic crystals have three indices commonly denoted as α, ß and *y* (Carlton, 2011). The APIs in question are biaxial triclinic crystal systems, therefore having three RI values (Peeters et al., 1979, 1996, and 2004). Unfortunately, exact values for the APIs studied are not know, however a number of organic pharmaceutical materials exhibit RI values between 1.4 to above 1.7 (Watanabe and Ohnuma, 2000). For instance, sulphanilamide polymorphic forms have RI values ranging from 1.548 to 1.8 (Lin et al., 1974). Therefore, it appears that crystallisation of a particle from an isotropic phase (an amorphous form) to a triclinic crystal has the potential to be recorded by NTA technology due to changes in RI value.

This hypothesis was tested further using the Mie theory in Scatlab 1.2 software with the option “direct intensity graph” (Scatlab Project: http://www.scatlab.org) and scattering power as a

function of size was calculated for ITR, KETO and POS based on an average RI value of 1.65 (Wong et al., 2006; Palmberger et al., 2015; Touzet et al., 2018). Calculations were based on 638 nm light, the same wavelength as that used by NTA. The dispersant RI was taken as 1.33, with water being the liquid medium. The real part of the RI of the NP material was set to 1.65 and the complex part was set to 0.001, both parameters being typical of organic materials. Scattered light intensities were calculated for angles ranging 70-110°. All other parameters were left at zero (Gallego-Urrea et al., 2011). Also, scattering intensity in a range of RI values at 90° angle was calculated to reflect the triclinic nature of these APIs.

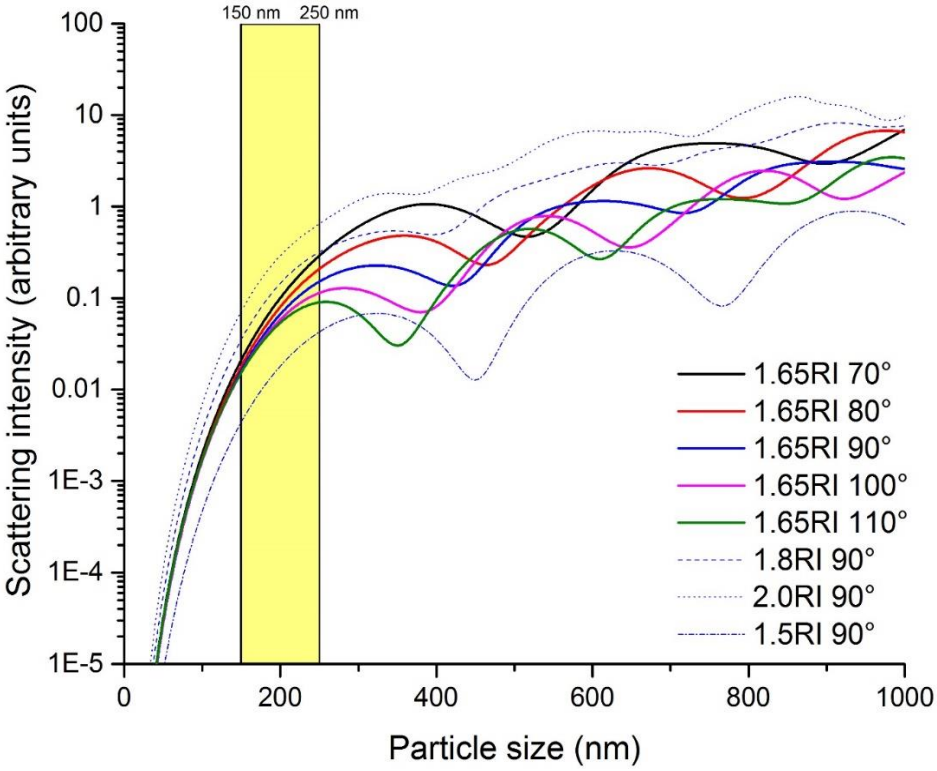

Fig. 3.3 Mie plot showing intensity of scattered light, calculated for the studied APIs using Mie theory in Scatlab 1.2 at a range of angles 70-110°. (yellow box highlights lowest particle size of NPs upon initial formation). RI= refractive index

This Mie plot shown in Fig. 3.3 demonstrates that the scattering intensity increases rapidly for smaller sized particles in contrast with larger sized particles, where a plateau in intensity is reached from 200 nm and above. All APIs form NPs above 150 nm (Table 3.1, 3.2 and A.2.1). A range of RI values (1.5 - 2.0) were investigated, with Fig. 3.3 demonstrating the key impact of this parameter upon particle scattering power. Therefore, we can conclude that changes in scattering intensity are predominantly dictated by material composition and not particle size.

Scattergrams presented below show particle size (nm) versus the intensity (a.u.) of light scattered by NPs under analysis. It is possible to distinguish between particles of similar size based on their differing refractive indices using these graphical representations of light scattering. Particular attention should be paid to the scale of the Y-axis in the scattergrams shown.

3.3.4.1 Itraconazole

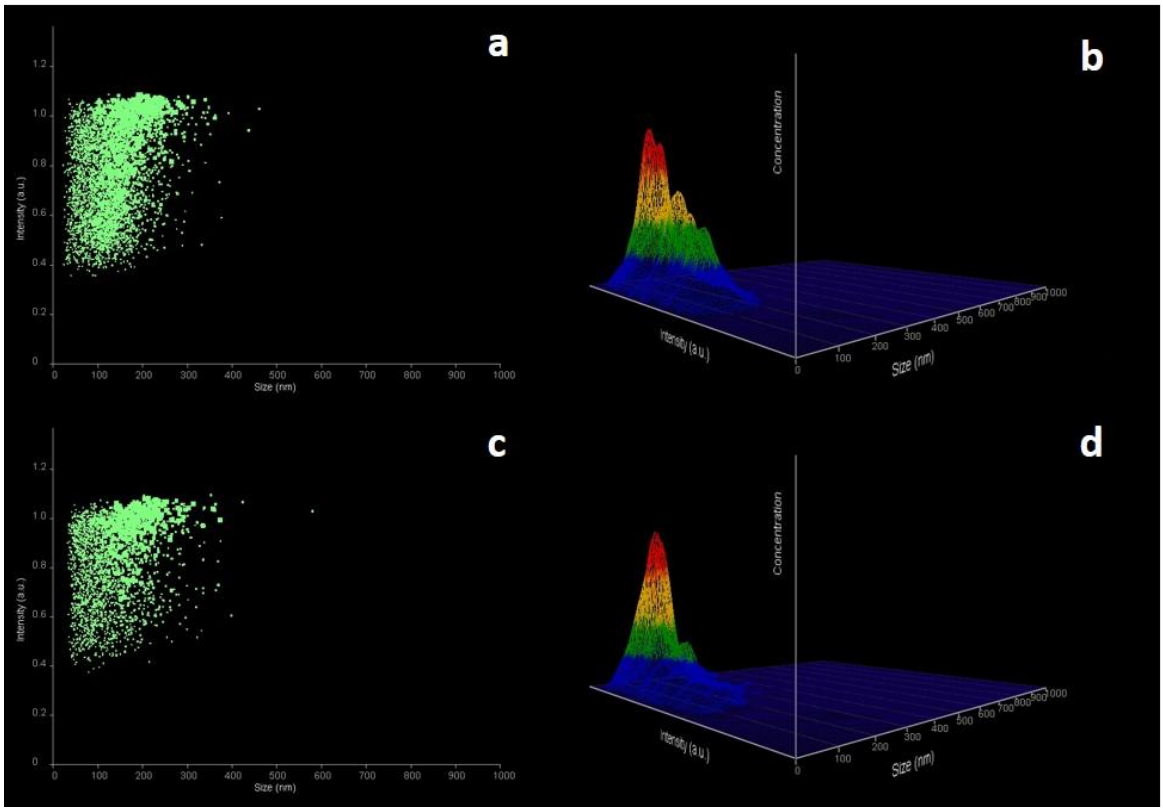

Fig. 3.4 NTA scattergram intensity (a.u.) vs. light with corresponding 3-D graph (size vs. intensity vs. concentration) for stabilizer free ITR NPs at (a and b) 1 minute and (c and d) 30 minutes.

ITR nano-dispersions showed little difference between 1 and 30 minutes in their scattering abilities (Fig. 3.4). ITR NPs scattered at the lowest level of intensity below 1.2 a.u.. ITR NPs appear X-ray disordered upon initial formation. However, these NPs are in fact likely to be LC in nature, given the similarities existing between the NP formation procedures employed by Mugheirbi and those adopted in these studies (Tarnacka et al., 2013; Mugheirbi et al., 2014; Mugheirbi and Tajber, 2015). An ability to flow like a liquid with some degree of long range order could reduce their ability to refract light. The greater stability of ITR nano-dispersions as confirmed by particle size measurements obtained via both techniques is supported by the stable range of light scattered throughout the 30 minutes (Fig. 3.4).

3.3.4.2 Ketoconazole

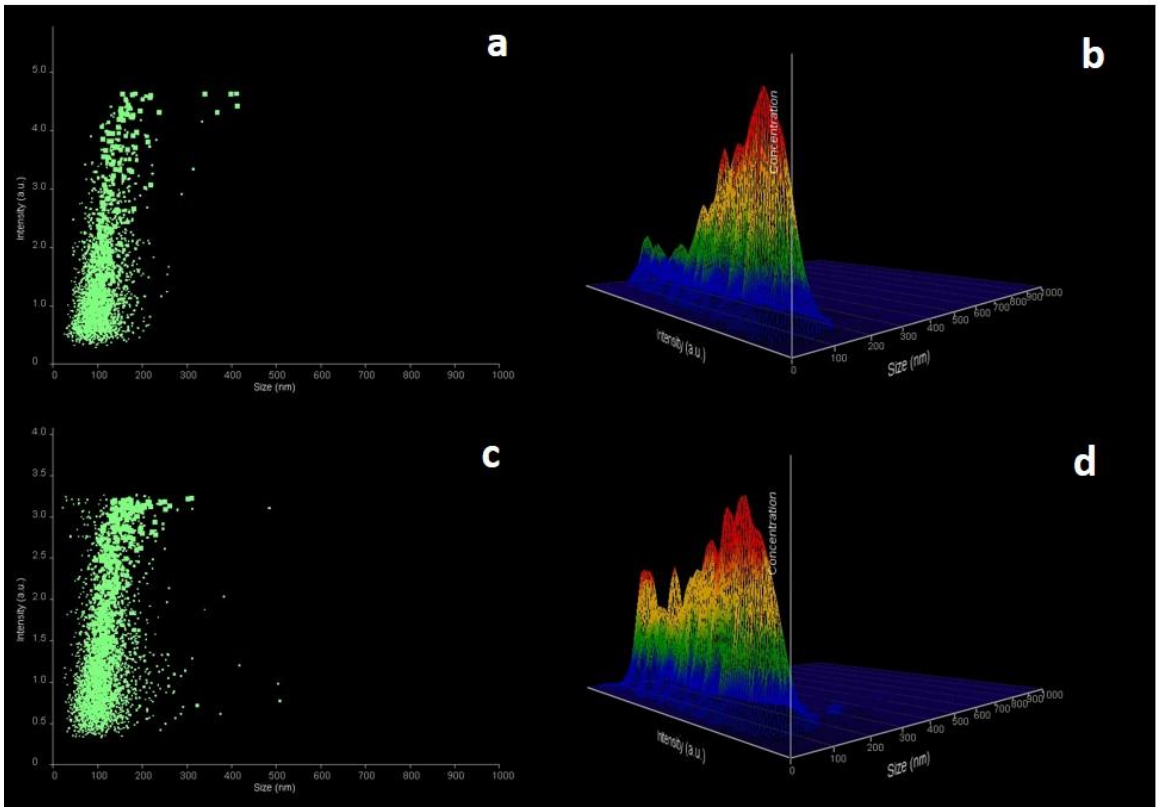

Fig. 3.5 NTA scattergram intensity (a.u.) vs. light with corresponding 3-D graph (size vs. intensity vs. concentration) for stabilizer free KETO NPs at (a and b) 1 minute and (c and d) 30 minutes.

Equivalent scattergrams for KETO showed a decrease in the range of intensity of light scattered by particles over the 30 minutes (Fig. 3.5). KETO NPs scattered light up to an intensity 5 a.u. at 1 minute, with a large sized cluster of particles scattering below 1.5 a.u. (Fig. 3.5a). This may suggest the presence of both amorphous and crystalline KETO NPs in this sample, with the majority being amorphous. PXRD analysis (Fig. 2.7) confirms the crystalline nature of the KETO NPs at 30 minutes. An increase in the size of the particle cluster scattering at higher intensity can be seen at 30 minutes (Fig. 3.5c), however a significant number of particles scattering below 1.5 a.u. remain. This may suggest the simultaneous presence of both amorphous and crystalline KETO NPs at 30 minutes, with an increase in the number of crystalline particles.

It is possible that the decrease in the intensity of scattered light associated with KETO NPs can be explained by the dissolution of these particles. Wittbold and Tatarkiewicz, (2017) previously tracked the process of crystallisation and dissolution by observing varying intensity of scattered light of proteins using MANTA technology. Crystallisation was characterized by an

increased intensity, whilst dissolution was represented by a decrease in the intensity of scattered light (Wittbold and Tatarkiewicz, 2017).

3.3.4.3 Posaconazole

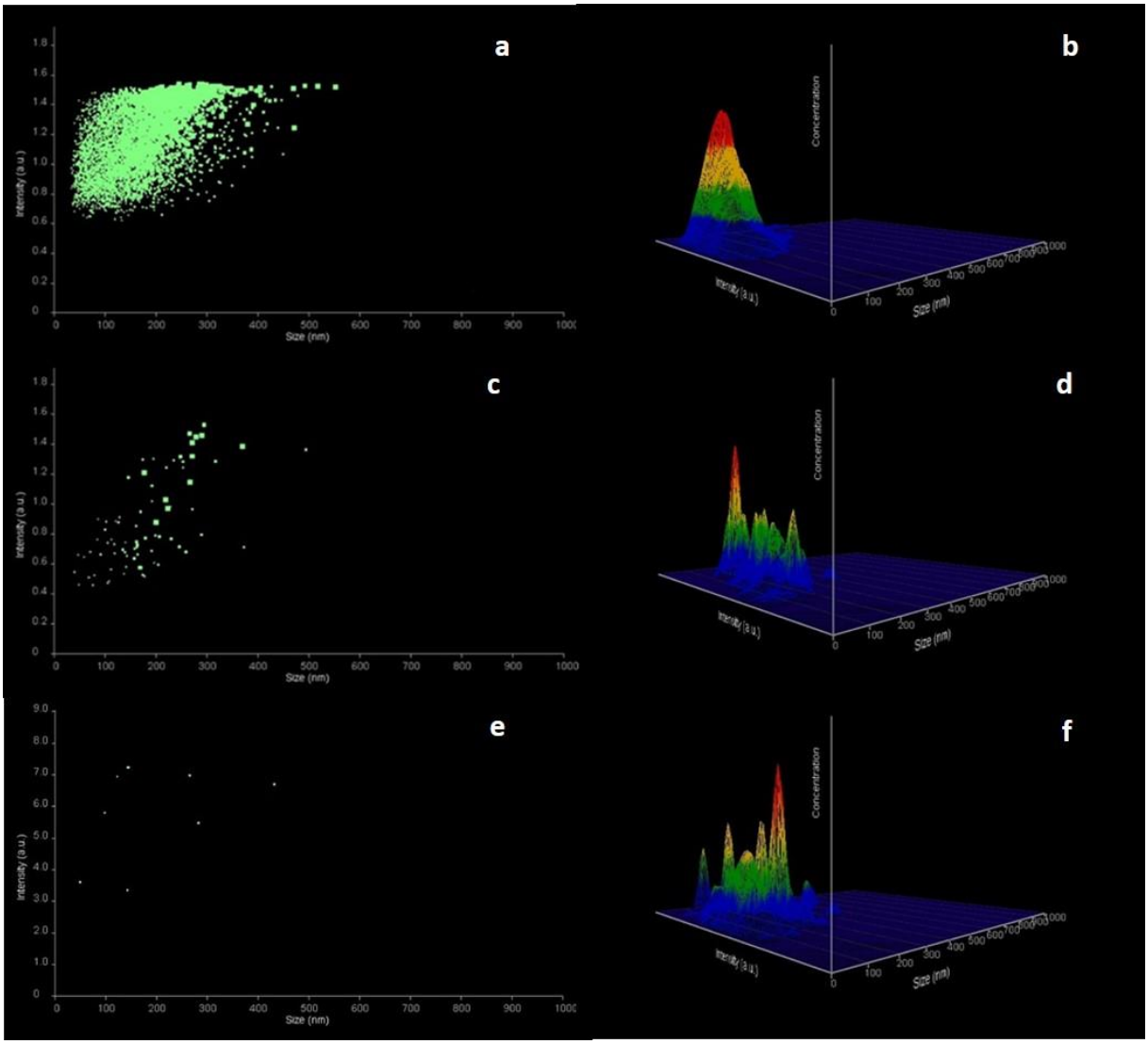

Fig. 3.6 NTA scattergram intensity (a.u.) vs. light with corresponding 3-D graph (size vs. intensity vs. concentration) for stabilizer free POS NPs at (a and b) 1 minute (c and d) 7 minutes and (e and f) 8 minutes.

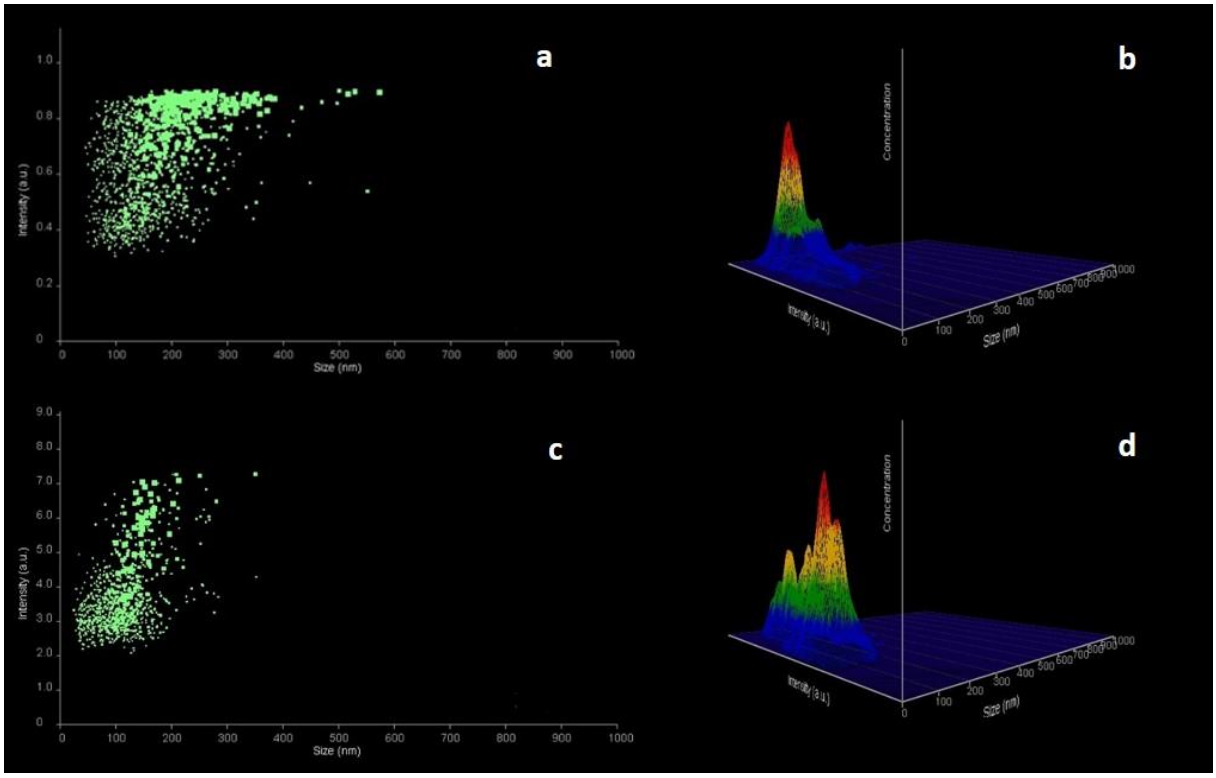

Fig. 3.7 NTA scattergram intensity (a.u.) vs. light with corresponding 3-D graph (size vs. intensity vs. concentration) for POS MPEG 1.5 mg/ml NPs at (a and b) 3 minutes and (c and d) 4 minutes.

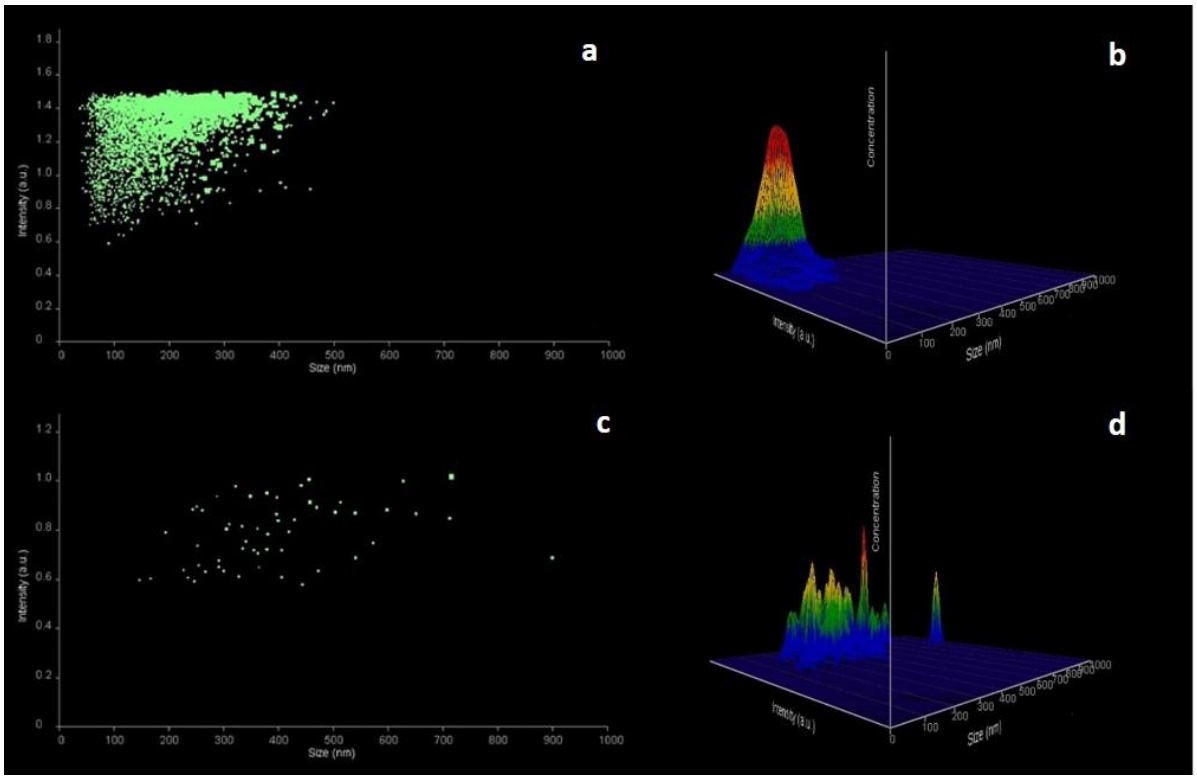

Fig. 3.8 NTA scattergram intensity (a.u.) vs. light with corresponding 3-D graph (size vs. intensity vs. concentration) for POS DMPEG 1 mg/ml NPs at (a and b) 1 minute and (c and d) 30 minutes.

Presented are examples of stabilizer free POS nano-dispersions (Fig. 3.6), as well as POS MPEG 1.5 mg/ml which crystallised the fastest (Fig. 3.7), and POS DMPEG 1 mg/ml which showed no signs of crystallisation over the 30 minutes demonstrated by the lack of change in scattering intensity of those particles (Fig. 3.8). This is in contrast with the DLS data presented in Chapter 2 and SEM analysis of POS DMPEG 0.5 mg/ml nano-dispersions, suggesting crystallisation within 30 minutes. Examples of scattergrams and 3-D graphs for other polymer-stabilized nano-dispersions can be found in Fig. A.2.7-24. Notably, previous work performed using DLS on these systems presented similar findings. POS MPEG 1.5 mg/ml showed signs of possible crystallisation represented by remarkable increases in particle size and variability as the experiment proceeded. In addition, POS DMPEG 1 mg/ml showed no evidence of possible crystallisation, with a consistent increase in particle size observed (Chapter 2). A significant increase in the intensity of the light scattered by the POS NPs (refer to Y-axis) was observed over the 30 minutes of the study (Fig. 3.6 and 3.7). For all POS nano-dispersions (except POS DMPEG 1 mg/ml) prior to crystallisation, particle light scattering ranges fall between 0.1 – 1.5 a.u. (Fig. 3.6a to 3.8a) compared to the scattering range 1 - 7 a.u. post crystallisation (Fig. 3.6e and 3.7c). The 3D graphs included provide a graphical representation of size versus intensity

versus concentration, in this way providing information regarding the concentration of particles scattering light at particular intensities (Fig. 3.6 to 3.8). We can conclude that prior to crystallisation, unstable disordered amorphous particles tend to scatter light at a decreased intensity. In contrast, post crystallisation ordered stable crystalline particles scatter light at an increased intensity. This is in agreement with the typical characteristics of amorphous materials, they are isotropic having one RI of light, whereas the crystalline form of POS is anisotropic, having three RIs (Singh and Dunmur, 2002; Hahn et al., 2009). POS NPs undergo initial association in an unstructured way making them amorphous in nature, with a tendency to crystallise quickly within the 30 minute time period as shown previously by SEM and PXRD analysis (Fig. 2.7 and 8). Amorphous-to-crystalline pathways have a thermodynamic origin. In this instance, unstable amorphous particles undergo phase transformation to a thermodynamically stable ordered crystalline phase over 30 minutes. Whereby, thermodynamically unstable phases are replaced by more stable phases (Han and Aizenberg, 2007; Pouget et al., 2009). As previously mentioned, considering Mie theory, we can conclude that the change in the light scattering power of POS NPs is caused by a change in material composition and not increased particle size. For the first time, NTA has been successfully utilised for the innovative application of monitoring crystallisation *in situ* (Fig. 3.9).

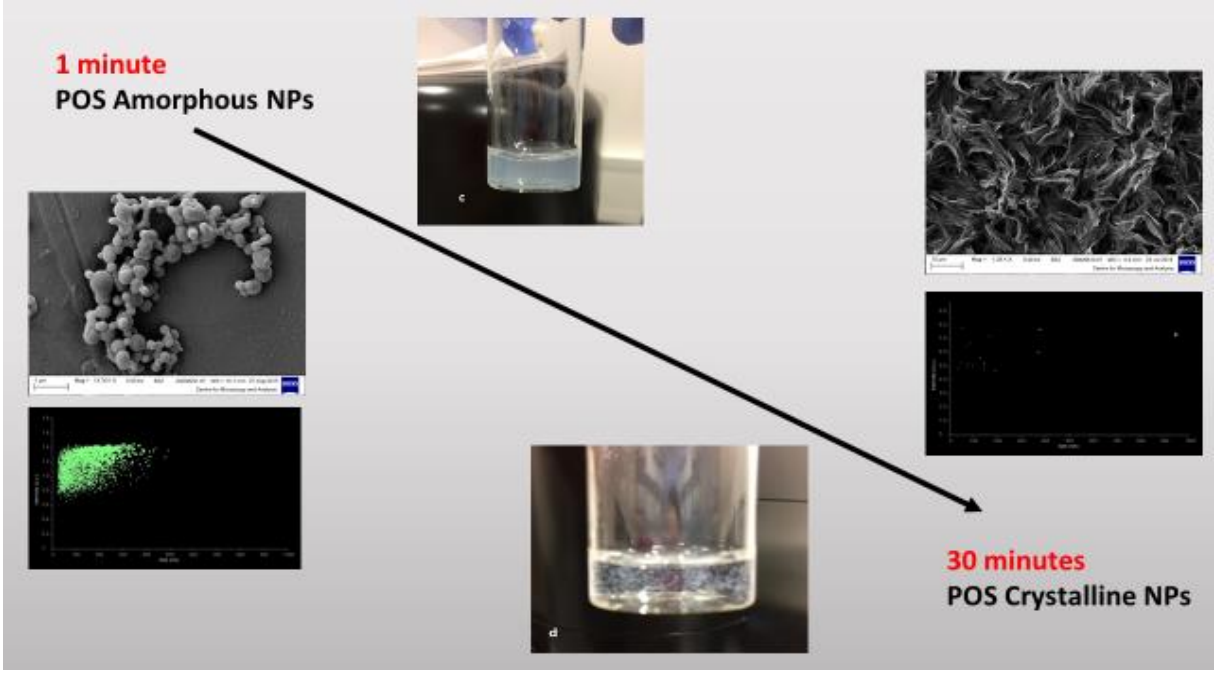

Fig. 3.9 Schematic representation of "non-classical crystallisation" pathway followed by POS NPs over 30 minutes of study.

Table 3.3 contains information regarding the time-point at which crystallisation occurs for each POS nano-dispersion. This information is also displayed in a schematic representation in Fig. 3.10.

Table 3.3. Time-point (minutes) for crystallisation of POS nano-dispersions using NTA during 30 minutes monitoring. (n = 3)

Formulation	**Time-point for crystallisation (minutes) ± SD (n=3)**
Stabilizer free POS NPs	7.5 ± 0.5
POS MPEG 0.5 mg/ml	13.5 ± 0.5
POS MPEG 1 mg/ml	9.5 ± 1.0
POS MPEG 1.5 mg/ml	3.5 ± 1.0
POS PEG 0.5 mg/ml	15.5 ± 1.0
POS PEG 1 mg/ml	12.5 ± 0.5
POS PEG 1.5 mg/ml	4.5 ± 1.0
POS DMPEG 0.5 mg/ml	6.5 ± 0.5
POS DMPEG 1 mg/ml	>30
POS DMPEG 1.5 mg/ml	27.5 ± 0.5

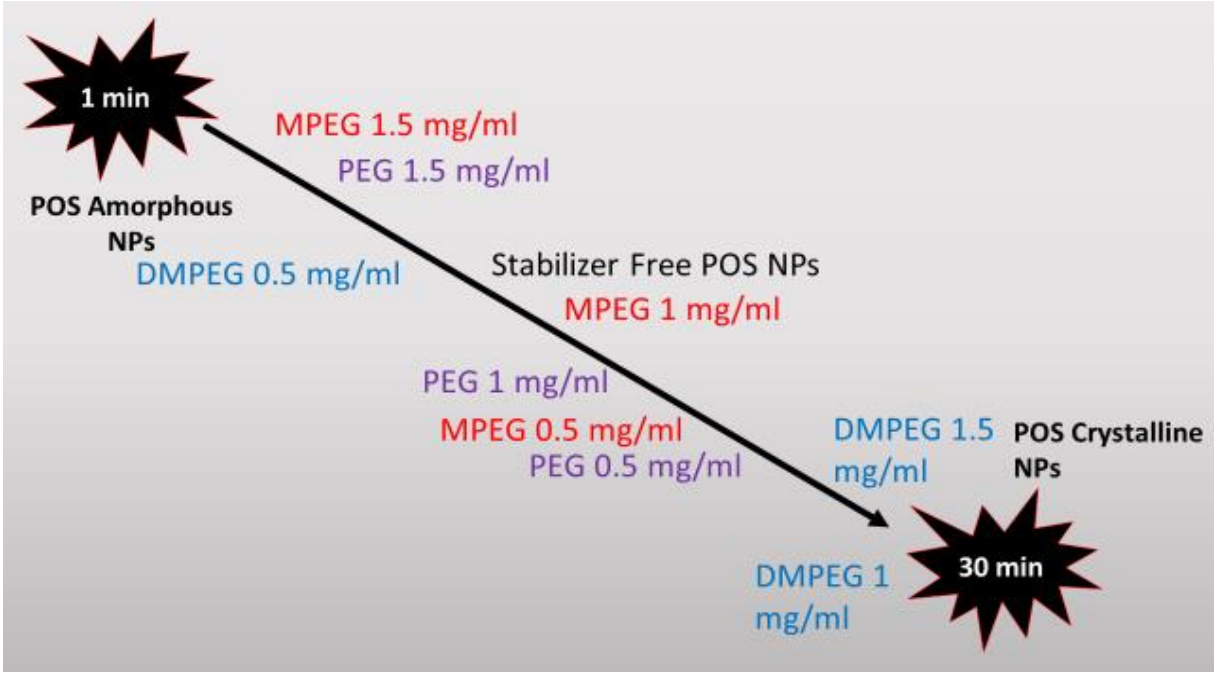

Fig. 3.10 Schematic representation of 30 minute timeline showing point of crystallisation for POS NPs with different stabilizers.

For POS NPs stabilized by MPEG and PEG, when the stabilizer concentration is increased crystallisation occurs faster (Table 3.3). In other words, increasing stabilizer concentration (MPEG and PEG) appears to encourage crystallisation and the formation of ordered crystalline

phases. On the other hand, when POS NPs are stabilized by DMPEG; increasing DMPEG concentration appears to delay crystallisation. This finding is in agreement with DLS studies whereby DMPEG was the most effective stabilizer for POS nano-dispersions (Fig. A.2.25). However, NTA suggests that DMPEG is most effective at a concentration of 1 mg/ml, in contrast to 1.5 mg/ml as suggested by DLS (Fig. 2.5). It may be the case that increasing DMPEG concentration up to a threshold of 1 mg/ml inhibits crystallisation, therefore achieving greater NP stability. Beyond this point any further increase in concentration is of no benefit, with a possible saturation limit being reached.

3.3.5 Critical Evaluation of Nanoparticle Tracking Analysis (NTA) versus Dynamic Light Scattering (DLS)

Ultimately, both NTA and DLS confirmed ITR NPs have the greatest stability. DLS confirmed DMPEG was the most effective stabilizer for ITR and KETO. This is reflected by small error bars and therefore relatively low variability associated with the NTA PSDs of these samples (Fig. 3.1h, 3.2h and Fig. A.2.3L). In general, upon initial formation ITR nano-dispersions showed the best agreement in particle size data obtained via the two techniques (Table 3.1). Greater differences in particle size values were observed for KETO and POS nano-dispersions at the same time point (Table 3.2 and A.2.1). It seems likely that the presence of larger sized particles or aggregates within samples at 30 minutes are skewing DLS distributions towards larger particle sizes (Demeester et al., 2005). This has been noted elsewhere in the literature, with the presence of a small number of large particles within the sample obstructing the accurate size determination of the smaller dominant population (Berne and Pecora, 2000). Further evidence of this is provided within Fig. A.2.6, whereby large particles obscure the viewing field. It is also possible that some degree of particle sedimentation is occurring at 30 minutes for samples undergoing analysis, most notably for POS whereby micron sized crystals were present (Fig. 2.8). For accurate size determination via both DLS and NTA, it is critical that the process of diffusion (Brownian motion) is much faster than the process of sedimentation. It is possible that larger particles present at 30 minutes may be subject to different rates of sedimentation as a consequence of their environment, which differs for DLS and NTA. This could be responsible for inconsistencies in corresponding measurements between the two techniques. It should be noted that intensity based DLS data is being compared with number based equivalents derived using NTA. Therefore, it seems that a number of large sized particles within the nano-dispersions are having profound impact on the mean particle size measured using DLS.

Fig. 3.1 highlighted the increase in sample complexity shown by NTA between 1 minute and 30 minutes. This confirms the ability of NTA to achieve greater peak resolution for multimodal size distributions (Dragovic et al., 2011). NTA can resolve particle populations with a 1.5 fold difference in size compared with DLS, which requires particle populations to have a two or three fold difference in particle size (Filipe et al., 2010). Perhaps, NTA is more suitable for the analysis of polydisperse samples, giving a truer picture of the sample. Samples having a PDI below 0.07 are considered to be monodisperse (International Organization for Standardization, 2017).

In some cases, NTA mean size values were larger than their DLS counterparts by a small margin. This may be explained by the lower size detection limit of DLS compared with NTA. Therefore, DLS has the ability to size smaller sized particles (<30 nm) in the distribution with greater accuracy, resulting in smaller mean size values. In the case of KETO and POS, Table 3.2 and A.2.1 shows DLS particle sizes are greater than their NTA counterparts, a feature noted elsewhere in the literature (Filipe et al., 2010). There a few possible explanations for this. Firstly, PDI measurements would suggest that KETO nano-dispersions are the most polydisperse of all studied API nano-dispersions i.e. are multimodal and therefore may yield less reliable size data via DLS. This fact is also supported by the larger error bars associated with DLS data for KETO nano-dispersions compared with that of NTA (Fig. 3.2). Small error bars associated with NTA KETO samples suggest good reproducibility for these datasets (Table 3.2). The polydispersity of the KETO nano-dispersions (Table 3.2 and Fig. 3.2) may explain the difference in particle size values obtained for the two techniques. DLS, being an intensity based technique may not size polydisperse samples such as KETO accurately. Perhaps NTA measurements give a more realistic representation of PSDs for KETO, making NTA the more suitable technique for analysis of KETO nano-dispersions.

Both ITR and KETO DLS derived mean count rates follow a similar trend, with count rates decreasing over the 30 minute period (Fig. 3.11a). It has been shown previously that count rates can act as a surrogate for NP concentration, however they are dependent upon both particle size and concentration (Hassan et al., 2015). Fig. 3.11b provides evidence of decreasing ITR particle concentration over 30 minutes according to NTA. Therefore, DLS and NTA are in agreement in this respect. Fig. 3.11b shows KETO NTA total particle concentration is lower than ITR, however beyond 10 minutes no difference exists. It appears that DLS derived count rates can indeed be used as a surrogate for particle concentration. On the other hand other

studies have concluded that NTA concentration measurements are possibly inaccurate, and perhaps this data should be considered relative rather than absolute (Gallego-Urrea et al., 2011; Krueger et al., 2016). Ultimately, the ability of NTA to provide particle concentration values remains an advantage over DLS.

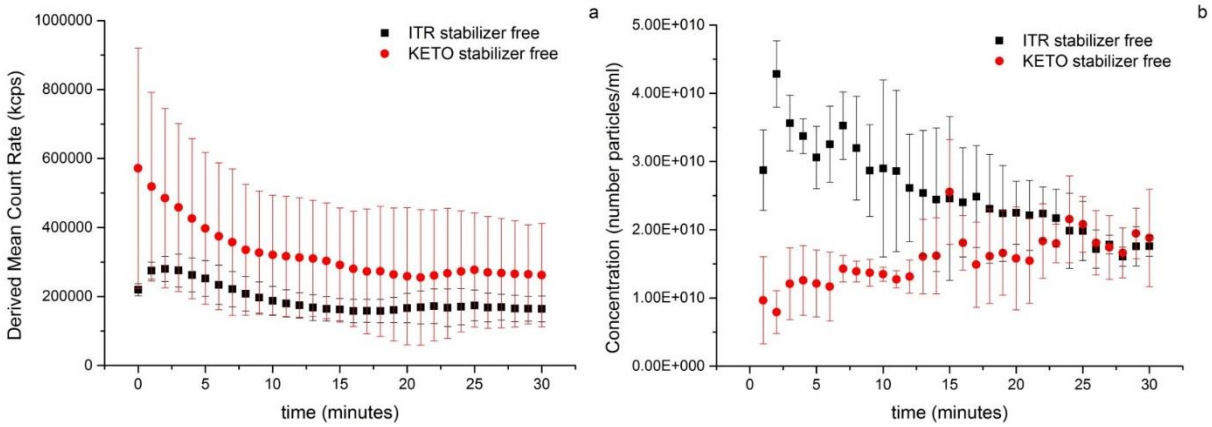

Fig. 3.11 (a) DLS derived mean count rate (kcps) versus time (minutes) and (b) NTA concentration (number particles/ml) versus time (minutes) for ITR and KETO stabilizer free NPs.

There may be a number of factors impacting measurements obtained via NTA and DLS. Measurements carried out using NTA involved a preparation procedure, whereby NPs were formed outside of the sample chamber and quickly injected into the sample chamber upon formation. In this instance, NPs are exposed to two different environments, initial formation in sterile glass vials followed by injection via a syringe into the sample chamber. In contrast, measurements performed using DLS were truly obtained *in situ* i.e. NPs were formed inside the glass cuvette and size analysis was initiated almost instantaneously, hence measurements begin at 0 minutes for the DLS datasets in contrast to 1 minute with NTA. In the case of DLS, NPs are exposed to a single homogeneous environment for the duration of the 30 minutes. NPs are also exposed to some shearing forces with NTA when undergoing injection into the sample chamber and advancing the sample, not imposed by DLS. These forces may cause breakage of particle aggregates and therefore smaller average particle size values for NTA throughout the analysis for KETO samples (Fig. 3.2). Sample dilution was employed for NTA analysis alone, in this way the increased volume of water or stabilizer/water solution present may have had an impact on API solubility; supersaturation levels and hence the dissolution or crystallisation processes at play. It is also worth noting the markedly different physical appearance of the KETO NPs as shown in photographs (Fig. A.2.5c and d). It is evident that the KETO nano-dispersions were visibly different to the other API nano-dispersions. They

appeared as clear solutions both upon NP formation and by the end of the 30 minute study. POS and ITR nano-dispersions exhibited a blue “hue”, typical of NPs when suspended in liquid medium (Fig. A.2.5a, b, e and f).

NTA measurements require the operator to select suitable analysis settings prior to sample measurement, a form of visual validation which is subject to operator bias (Filipe et al., 2010). The settings required for KETO NP analysis were profoundly different to that of ITR and POS (screenshot of setting can be found within Fig. A.2.26 and 27). Much higher settings were required in order to obtain a clear and suitable view of the KETO NPs for size measurements. For example, for KETO NPs stabilized with MPEG 1 mg/ml, a camera level of 12 was utilised, while a camera level of 5 and 4 was used for ITR and POS equivalents. For this reason, NTA sizes KETO NPs with greater difficulty.

Both techniques confirmed POS NPs were the least stable. They also confirmed DMPEG to be the best stabilizer as demonstrated by its ability to delay crystallisation for the longest period of time (Fig. 3.10 and Table. A.2.1). DLS studies concluded that DMPEG 1.5 mg/ml was the most effective concentration whilst NTA favours a 1 mg/ml concentration (Fig. 2.5 and 3.10). It may be the case that increasing DMPEG concentration up to a threshold of 1 mg/ml inhibits crystallisation therefore achieving greater NP stability. Beyond this point any further increase in concentration is of no benefit, perhaps a saturation limit is reached. The slight difference in effective concentration suggested by the two techniques can be explained by the analysis environment and the comparison of a number versus intensity based technique.

There are a number of other factors to be considered when interpreting data and assessing the suitably of these sizing techniques. DLS requires little skill on the part of the operator, whilst NTA requires the operator to select suitable detection and analysis settings, which are dependent upon operator judgement and experience. In addition, NTA requires sample particle concentration to be in the range of 10^7 to 10^9 particles per ml. Therefore, determining the correct dilution factor can be time consuming for the user, with dilution possibly impacting upon original particle properties and accurate analysis. On the other hand, DLS has the ability to adjust the attenuator employed based on sample concentration automatically removing operator bias. NTA also has the disadvantage of longer measurement time over DLS, as multiple measurements are necessary in order to obtain statistically meaningful results. Although NTA has greater peak resolution, this comes with reduced sensitivity to particles

smaller than 30 nm. Samples with average particle sizes below 30 nm may be more suitable for DLS. The particle sizing technique selected should consider all prior information known about the sample, as well as the critical sample characteristics to be determined, as these will have a great impact upon end product performance.

An obvious advantage of NTA over DLS lies in its ability to visualise sample changes *in situ*. The novel application of NTA for the purposes of monitoring the dynamic, complex journey of crystallisation *in situ* has the potential to provide researchers with lucrative information regarding the physical processes taking place during sample analysis.

3.4. CONCLUSIONS

Critical to the success of the NP formulation process is the utilisation of more than one particle sizing technique. This research, revealed the detailed and diverse amount of information that can be provided via particle size characterisation using both NTA and DLS for nano-dispersions. Both techniques concluded ITR NPs were the most stable and POS NPs the least stable. Both techniques confirmed DMPEG was the most effective stabilizer for POS nano-dispersions. It seems that a number of large sized particles within the nano-dispersions have a profound impact upon the mean particle size measured using DLS. Hence, DLS and NTA sizing techniques should be used in a complimentary manner, making it possible to characterize nano-dispersions in a quick and detailed way. Combining information derived via both techniques provides the user with the opportunity to gain a complete holistic picture of the sample under analysis. The suitability of the particle sizing technique utilised is dependent upon the sample in question undergoing analysis, as well as critical sample characteristics to be determined. For the first time, NTA was successfully utilised for the innovative purpose of *in situ* monitoring of crystal growth. Mie theory was successfully employed to explain the relationship between material composition and particle light scattering power. This finding can provide an alternative means to conventional methods for assessing the progress of the dynamic crystallisation process on the nano-scale in real time. Such information can serve to deepen our understanding of these complex physical processes.

References

Anderson, W., Kozak, D., Coleman, V.A., Jämting, Å.K., Trau, M., 2013. A comparative study of submicron particle sizing platforms: Accuracy, precision and resolution analysis of polydisperse particle size distributions. J. Colloid Interface Sci. 405, 322–330.

Bell, N.C., Minelli, C., Tompkins, J., Stevens, M.M., Shard, A.G., 2012. Emerging techniques for submicrometer particle sizing applied to stober silica. Langmuir 28, 10860–10872.

Berne, B., Pecora, R., 2000. Dynamic light scattering with applications to chemistry, biology and physics. Mineola, Dover.

Bootz, A., Vogel, V., Schubert, D., Kreuter, J., 2004. Comparison of scanning electron microscopy, dynamic light scattering and analytical ultracentrifugation for the sizing of poly(butyl cyanoacrylate) nanoparticles. Eur. J. Pharm. Biopharm. 57, 369–375.

Brown, P.H., Schuck, P., 2006. Macromolecular size-and-shape distributions by sedimentation velocity analytical ultracentrifugation. Biophys. J. 90, 4651–4661.

Calzolai, L., Gilliland, D., Garcìa, C.P., Rossi, F., 2011. Separation and characterization of gold nanoparticle mixtures by flow-field-flow fractionation. J. Chromatogr. A 1218, 4234–4239.

Carlton, R.A., 2011. Pharmaceutical Microscopy.

Demeester, J., Smedt, S., Sanders, N., Haustraete, J., 2005. Light Scattering, in: Jiskoot, W., Crommelin, D.J. (Ed.), Methods for Structural Analysis of Protein Pharmaceuticals. Arlington: AAPS.

Dragovic, R.A., Gardiner, C., Brooks, A.S., Tannetta, D.S., Ferguson, D.J.P., Hole, P., Carr, B., Redman, C.W.G., Harris, A.L., Dobson, P.J., Harrison, P., Sargent, I.L., 2011. Sizing and phenotyping of cellular vesicles using Nanoparticle Tracking Analysis. Nanomedicine Nanotechnology, Biol. Med. 7, 780–788.

Einstein, A., 1908. Elementare theorie der brownschen bewegung. Zeitschrift fur Elektrochemie und Angew. Phys. Chemie 14, 235–239.

Filipe, V., Hawe, A., Jiskoot, W., 2010. Critical evaluation of nanoparticle tracking analysis (NTA) by NanoSight for the measurement of nanoparticles and protein aggregates. Pharm. Res. 27, 796–810.

Gallego-Urrea, J.A., Tuoriniemi, J., Hassellöv, M., 2011. Applications of particle-tracking analysis to the determination of size distributions and concentrations of nanoparticles in environmental, biological and food samples. TrAC - Trends Anal. Chem. 30, 473–483.

Hahn, D.W., 2009. Light Scattering Theory. Aerosp. Eng. 27, 1–13.

Han, T.Y.J., Aizenberg, J., 2007. Calcium Carbonate Storage in Amorphous Form and Its

Template-Induced Crystallization. Chem. Mater. 20, 1064–1068.

Hassan, P., Rana, S., Verma, G., 2015. Making sense of brownian motion: colloid characterization by dynamic light scattering. Langmuir 31, 3–12.

International Organization for Standardization, 2017. Particle Size Analysis – Dynamic Light Scattering (DLS); ISO 22412:2017.

Joubert, M.K., Luo, Q., Nashed-Samuel, Y., Wypych, J., Narhi, L.O., 2011. Classification and characterization of therapeutic antibody aggregates. J. Biol. Chem. 286, 25118–25133.

Krueger, A.B., Carnell, P., Carpenter, J.F., 2016. Characterization of Factors Affecting Nanoparticle Tracking Analysis Results With Synthetic and Protein Nanoparticles. J. Pharm. Sci. 105, 1434–1443.

Lin, H.O., Baenziger, N.C., Guillory, J.K., 1974. Physical properties of four polymorphic forms of sulfanilamide I: Densities, refractive indexes, and X-ray diffraction measurements. J. Pharm. Sci. 63, 145–146.

Luo, P., Roca, A., Tiede, K., Privett, K., Jiang, J., Pinkstone, J., Ma, G., Veinot, J., Boxall, A., 2016. Application of nanoparticle tracking analysis for characterising the fate of engineered nanoparticles in sediment-water systems. J. Environ. Sci. (China) 64, 62–71.

McKinlay, K.J., Allison, F.J., Scotchford, C.A., Grant, D.M., Oliver, J.M., King, J.R., Wood, J.V., Brown, P.D., 2004. Comparison of environmental scanning electron microscopy with high vacuum scanning elctron microscopy as applied to the assessment of cell morphology. J. Biomed. Mater. Res. Part A. 69, 359–366.

Mugheirbi, N.A., Paluch, K.J., Tajber, L., 2014. Heat induced evaporative antisolvent nanoprecipitation (HIEAN) of itraconazole. Int. J. Pharm. 471, 400-411.Mugheirbi, N.A., Tajber, L., 2015. Mesophase and size manipulation of itraconazole liquid crystalline nanoparticles produced via quasi nanoemulsion precipitation. Eur. J. Pharm. Biopharm. 96, 226–236.

Niederberger, M., Cölfen, H., 2006. Oriented attachment and mesocrystals: non-classical crystallization mechanisms based on nanoparticle assembly. Phys. Chem. Chem. Phys. 8, 3271–3287.

Palmberger, S., Mohr, C., Stubauer, G., 2015. Patent Application Publication Pub. No.: US 2017/0139001 A1.

Peeters, O.M., Blaton, N.M., De Ranter, C.J., 1996. {\it cis}-2-{\it sec}-Butyl-4-{4-[4-(4-{[2-(2,4-dichlorophenyl)-2-(1{\it H}-1,2,4-triazol-1-ylmethyl)-1,3-dioxolan-4-yl]methoxy}phenyl)-1-piperazinyl]phenyl}-2,4-dihydro-3{\it H}-1,2,4-triazol-3-one (Itraconazole). Acta Crystallogr. Sect. C 52, 2225–2229.

Peeters, O.M., Blaton, N.M., De Ranter, C.J., 1979. {\it cis}-1-Acetyl-4-(4-{[2-(2,4-dichlorophenyl)-2-(1{\itH}-1-imidazolylmethyl)-1,3-dioxolan-4-yl]methoxy}phenyl)piperazine: ketoconazole. A crystal structure with disorder. Acta Crystallogr. Sect. B. 35, 2461–2464.

Peeters, O.M., Blaton, N.M., Gerber, J.G., Gal, J., 2004. (+)-{\it cis}-1-Acetyl-4-(4-{[(2{\it R},4{\it S})-2-(2,4-di{\-}chloro{\-}phenyl)-2-(1{\itH}-imidazol-1-ylmeth{\-}yl)-1,3-dioxolan-4-yl]{\-}methoxy}phenyl){\-}piperazine [(2{\it R},4{\it S})-(+)-ketoconazole]. Acta Crystallogr. Sect. E 60, o367-o369.

Pouget, E.M., Bomans, P.H.H., Goos, J.A.C.M., Frederik ,P.M., de With, G., Sommerdijk, N.A.J.M., 2009. CaCO3 Formation Revealed by Cryo-TEM. Science 323, 1455–1458.

Singh, S., Dunmur, D.A., 2002. Liquid Crystal: Fundamentals, in: Liquid Crystals: Fundamentals. p. 62.

Svedberg, T., 1906. Uber die eigenbewegung der teilchen in kolloidalen losungen. Zeitschrift fur Elektrochemie und Angew. Phys. Chemie. 12, 853–860.

Tarnacka, M., Adrjanowicz, K., Kaminska, E., Kaminski, K., Grzybowska, K., Kolodziejczyk, K., Wlodarczyk, P., Hawelek, L., Garbacz, G., Kocot, A., Paluch, M., 2013. Molecular dynamics of itraconazole at ambient and high pressure. Phys. Chem. Chem. Phys. 15, 20742–20752.

Touzet, A., Pfefferlé, F., der Wel, P. van, Lamprecht, A., Pellequer, Y., 2018. Active freeze drying for production of nanocrystal-based powder: A pilot study. Int. J. Pharm. 536, 222–230.

Watanabe, A., Ohnuma, N., 2000. Crystallographic characteristics of crystal habits and their peculiarity to the substance (study of crystalline drugs by means of a polarizing microscope). J. Pharm. Soc. Jpn. 120, 290-297.

Wong, J., Papadopoulos, P., Werling, J., Rebbeck, C., Doty, M., Kipp, J., Konkel, J., Neuberger, D., 2006. Itraconazole suspension for intravenous injection: determination of the real component of complete refractive index for particle sizng by static light scattering. PDA. J. Pharm. Sci. Technol. 60, 302–313.

Yang, D.T., Lu, X., Fan, Y., Murphy, R.M., 2014. Evaluation of Nanoparticle Tracking for Characterization of Fibrillar Protein Aggregates. AIChE J. 60, 1236–1244.

4.1 INTRODUCTION

To date, literature has focused on qualitative techniques for obtaining detailed information regarding the physical processes involved in NP formation and stabilization. There is a need for quantitative descriptors, capable of describing these sequence of events. A combination of experimental work, theoretical calculations and detailed characterisation of NP surfaces, has the potential to further our understanding of these complex processes. Manipulation of particle characteristics achieved via greater process control may enable us to explore the full potential of nanoscience.

Exploration of NP stabilization mechanisms remains a challenging aspect of nano-formulation development. Difficulties arise due to the nano-scale dimension of the work as well as the heterogeneous nature of the NPs themselves (Boles et al., 2016a). In particular, NP coating layer exact composition and conformation can be difficult to determine. With the absence of one single technique capable of providing all of this information, it is necessary to employ a number of complementary techniques in order to build a complete picture of this small but vital aspect of NP structure. Drug stabilizer interactions can provide some indication as to the propensity for effective NP stabilization.

For this reason, attempts have been made to quantify the level of interaction between stabilizer and drug beyond the nano-scale. It should be noted that the impact of the NP environment itself should not be overlooked when determining the dominant factors involved in NP stabilization. NPs within a dispersion medium always show Brownian motion and hence undergo frequent collisions with each other. Colloidal stability is determined by the interaction between the neighbouring NPs during these collisions. When attraction dominates, NPs will aggregate, and finally, coalescence may occur. On the other hand, when repulsion dominates, a stable system will result. This idea was originally proposed by Derjaguin, Landau, Verwey, and Overbeek and is referred to as the DLVO theory (Ishikawa et al., 2005; Berg, 2010). The DLVO theory assumes that the behaviour of colloidal NPs can be simplified by the interaction potential between two neighbouring NPs (Ishikawa et al., 2005; Berg, 2010).

A polymer in solution approach has been previously used to estimate the level of drug-stabilizer interaction. Marsac et al. (2009) first proposed basing the solubility of drug in polymers on the solubility of drug in a liquid analogue and/or monomer in the liquid state (Marsac et al., 2009). Knopp et al. (2016) used this method to estimate drug-polymer solubility at room temperature of a number of model compounds and compared their findings with that of melting point depression determinations (Knopp et al., 2016). It has been proposed that

drug-polymer interactions in the solid state can be predicted from solubility of drug in the polymer solution (Knopp et al., 2016). However, in this instance our interest lies more so with interactions in the liquid state which resembles the conditions of NP formation during the anti-solvent precipitation process, and may have an impact of API solubility and supersaturation. Quantifying the level of API-stabilizer interaction in this way may provide an indication as to the likelihood of effective NP stabilization.

A number of approaches, both theoretical and experimental, have been used in this work. They include: Hansen Solubility Parameters (HSPs), the Flory-Huggins (F-H) lattice model for isotropic (for liquid/amorphous systems) and the Maier-Saupe-McMillan (M-S-M) theory (for anisotropic, liquid crystalline systems).

HSPs can be used to predict miscibility of different components of a system. If two materials have similar solubility parameters in theory they should be miscible when mixed (Hansen, 2000). In this instance, the relation between miscibility and effective NP stabilization have been investigated. These account for three different aspects of a substance: dispersion (van der Waals), polarity and hydrogen bonding. Previously, HSPs have been utilised for the purpose of predicting molecular affinity between API and polymers (David and Sincock, 1992; Hansen, 2007). These predictions are exclusively based on the chemical structures of the various compounds concerned, experimental data is not required. In this study, the HSPs concept has been applied to estimate the level of drug-polymer interaction.

Thermal analysis of different drug/polymer weight ratios using the melting point depression method was performed, resulting in the construction of phase diagrams based on the F-H lattice model as described by the equation below (Eq. 4.1):

$$\left(\frac{1}{T_m^O} - \frac{1}{T_m}\right) = \frac{R}{\Delta H_{fus}} \left[\ln \emptyset + \left(1 - \frac{1}{m}\right)(1 - \emptyset) + x(1 - \emptyset)^2\right] \qquad \text{(Eq. 4.1)}$$

Where T_m and T_m^O are the melting points of the drug in the binary mixture and pure drug respectively, $\emptyset$ is the volume fraction, ΔH_{fus} is the heat of fusion of the pure drug, m is the volume of the polymer to that of the lattice site (defined by the volume of drug accounting for molecular weight and density) and x is the Flory-Huggins interaction parameter (Marsac et al., 2009). The F-H approach is based on lattice theory whereby molecular weights of different components are accounted for when predicting the entropy of mixing. This approach typically describes the miscibility behaviour of two stable amorphous components (Qian et al., 2010). The concept of melting point depression for drugs with polymers is well established within scientific literature (Mohan et al., 2002; Xie et al., 2002; Knopp et al., 2015). The theory is

based on melting of a crystal occurring at the temperature when the chemical potential of the crystal is equal to the chemical potential of the melt. Addition of an amorphous polymer to the crystal (if miscible) reduces the chemical potential of the crystalline material, producing melting point depression. In the case of ITR, a more complex situation exists whereby, ITR has the propensity to form LC phases. Such properties must be accounted for and considered in the construction of ITR phase diagrams. Hence, the F-H theory was combined with the M-S-M theory to account for the anisotropy of the ITR LC phases. In this way, the total Gibbs free energy of the system can be explained by a combination of two components, the free energy ($f^{(a)}$) caused by the anisotropic ordering of the molecules, and the free energy ($f^{(i)}$) of mixing of isotropic liquids (Crawford and Žumer, 1996).

M-S-M theory describes the free energy ($f^{(a)}$) caused by anisotropic ordering of molecules for the nematic (LC_{N-I}) and/or smectic (LC_{SmA-N}) LC arrangements as described in Eq. 4.2 (Soulé et al., 2009):

$$\frac{\Delta f^{(a)}}{RT} = \emptyset \left[\frac{1}{2} v (S^2 + \xi \sigma^2)\emptyset - \ln Z\right] \quad \text{(Eq. 4.2)}$$

Where *v* can be defined as the temperature dependent parameter ($v=4.54T_{I\_N}/T$, where T_{I_N} refers to the isotropic-nematic transition temperature) describing the interactions between the molecules in the nematic phase. S is the nematic order parameter, where S = 0.5 ($3\langle\cos^2\theta\rangle-1$), with θ being the angle between the reference axis and the director of the LC molecule. ξ refers to the smectic interaction parameter. Z is the partition function in the smectic order.

While, the F-H free energy ($f^{(i)}$) of mixing of isotropic liquids can be described by Eq. 4.3 (Srivastava et al., 2012):

$$\frac{\Delta f^{(i)}}{R\,T} = \emptyset \ln \emptyset + \frac{1-\emptyset}{m} \ln(1-\emptyset) + x\,\emptyset\,(1-\emptyset) \quad \text{(Eq. 4.3)}$$

Where T is the temperature (in K), R is the gas constant (in $J.mol^{-1}.K^{-1}$), Ø is the volume fraction of ITR, *m* is the volume ratio of the polymer to drug volume, and x is the Flory Huggins interaction parameter. Melting point depression is kinetically favourable for these systems due to the low melting point of the polymer ~ 60 °C. Hence at the melting temperature of the API, the polymer is in a molten state and the drug can easily interact and equilibrate with the polymer in the liquid state. This technique requires both drug and polymer to be chemically stable over the temperature range of interest. Additionally, a sufficient level of physical interaction between components is required for melting point depression to be apparent. If

we extend the F-H equation to fit crystalline drug-polymer systems, we can relate solubility of a drug in a polymer to the melting point depression of the drug (Marsac et al., 2009). Enthalpic interactions are reflected in the interaction parameter (x), since this term describes the relative strength of the cohesive and adhesive interactions. This interaction parameter magnitude and sign, reflects the energetic interactions between species within the system, and therefore miscibility between the components. A negative value would indicate many strong adhesive interactions favouring miscibility. In contrast, a positive value would be typical of a system characterising stronger cohesive interactions, and therefore immiscibility (Rubinstein and Colby, 2006). Much debate exists in the literature regarding the role of miscibility in physical stabilization of amorphous solid dispersions (Taylor and Zografi, 1997; Law et al., 2001). However, such information is lacking in relation to the stability of nano-dispersions.

The polymer, PEG is commonly utilised as a stabilizer for NPs, as it has the advantage of having a well-defined chemical composition ensuring the reproducibility of its performance. In this instance, PEG was chosen because it is a biocompatible material that can improve colloidal stability, with a resistance to non-specific protein binding (Liu et al., 2007). PEG can act as an inert protective coat, repelling proteins due to its strong interaction with water, leading to the formation of a tight hydration shell surrounding NPs. Previous work by Boles et al. (2016), has highlighted the importance of PEG grafting density and chain length upon protein adsorption and cellular uptake, with long dense capping layers proving favourable (Boles et al., 2016b). In contrast, it has been reported elsewhere that larger NP coating layers (increasing overall particle size) can limit NP access to confined regions within the body, as well as impeding renal clearance (Choi et al., 2007). Therefore, detailed surface characterisation of NPs can prove valuable in predicting *in vivo* performance. However, current literature tends to overlook the impact that the structure and composition of those NPs has upon their performance. Standardised techniques for such purposes have not yet been established. One approach for the indirect assessment of surface PEG monitors the change in particle size induced by the addition of PEG. The measured size will depend on core NP size, as well the amount of polymer bound to API particle surfaces (Rabanel et al., 2014). In this instance, adsorbed layer characterisation is performed via DLS.

PEG, MPEG and DMPEG were employed as stabilizers in the formation of azole anti-fungal NPs investigated in Chapters 2 and 3. In this Chapter, numerous techniques have been coupled in an attempt to gain greater understanding surrounding the nature of the relationship between drug-polymer and its impact upon NP stabilization. The impact of material composition and

solid state properties have been used to predict localisation of the polymer within the NP structure.

4.2 Materials and Methods

4.2.1 Materials

Itraconazole (ITR) was a gift from Welding GmbH (Hamburg, Germany). Ketoconazole (KETO) and posaconazole (POS) were purchased from Glentham Life Sciences Ltd. (Wiltshire, UK). Potassium dihydrogen phosphate reagent, poly(ethlyene glycol) (PEG), poly(ethylene glycol) methyl ether (MPEG) and its dimethoxylated derivative (DMPEG) with average molecular weights of 2,000 Da were purchased from Aldrich Chemical Co., Ltd. (Dorset, UK). Methanol HPLC grade was purchased from Fisher Scientific (Loughborough, UK). Acetone and acetonitrile Chromasolv® HPLC grade was obtained from Sigma Aldrich (Dorset, UK). MilliQ water was used in all instances. Potassium hydroxide pellets were purchased from Merck KGaA (Darmstadt, Germany).

4.2.2 Methods

4.2.2.1 Hansen Solubility Parameter Calculation via Hoftyzer–Van Krevelen group contribution method

HSPs were calculated from the chemical structures using the Van Krevelen method (Van Krevelen and Te Nijenhuis, 2009). Weight average molecular weights were used to determine the solubility parameters for the drugs and polymers (Scott, 1992). Total HSP contribution was divided into three partial solubility parameters: dispersion (δ_d), polar (δ_p) and hydrogen bonding (δ_h). Hence, total solubility parameter was calculated as follows (Eq. 4.4 to 4.7):

$$\delta_{t} = (\delta_d^2 + \delta_p^2 + \delta_h^2)^{0.5} \quad \text{(Eq. 4.4)}$$

$$\delta_d = \frac{\sum_{i=1}^{n} F_{dt}}{\sum_{i=1}^{n} v_i} \quad \text{(Eq. 4.5)}$$

$$\delta_p = \frac{\left(\sum_{i=1}^{n} F_{pi}^2\right)^{0.5}}{\sum_{i=1}^{n} V_i} \quad \text{(Eq. 4.6)}$$

$$\delta_h = \left(\frac{\sum_{i=1}^{n} F_{hi}}{\sum_{i=1}^{n} V_i}\right)^{0.5} \quad \text{(Eq. 4.7)}$$

Where I is the structural group within the molecule, F_{di} is the group contribution of the dispersion forces, F_{pi} is the group contribution of the polar forces, F_{hi} is the group contribution of the hydrogen bonding forces, and V_i is the group contribution of the molar volume. A small difference in the parameter suggests good miscibility.

4.2.2.2 Thermal Analysis

4.2.2.2.1 Melting Point Depression

Physical mixtures of KETO and polymer were prepared via weighing of samples in the range 90:10 to 20:80 (w/w) KETO/polymer mixtures, followed by manual grinding of powders in a mortar and pestle. DSC measurements of KETO/polymer systems were performed using a Mettler Toledo DSC 821e (Greifensee, Switzerland) under nitrogen purge. All samples were accurately weighed (3-10 mg) and placed in pin-holed aluminium pans. The samples were subjected to heating in a 25 – 200 °C temperature range at 10 °C/min heating rate. All DSC measurements were performed in duplicate.

Physical mixtures of ITR and polymer were prepared via weighing of samples in the range 95:5 to 30:70 (w/w) ITR/polymer mixtures, followed by manual grinding of powders in a mortar and pestle. DSC measurements of ITR/polymer systems were performed using a Perkin Elmer Diamond DSC (Waltham, MA, USA). The unit was refrigerated with a ULSP B.V. 130 cooling system (Ede, Netherlands), with a nitrogen flow of 40 ml/min. Gas flow was controlled using a PerkinElmer Thermal Analysis Gas Station (TAGS). All samples were accurately weighed (3-5 mg) in aluminium pans. Samples were subjected to a 25 – 180 °C temperature range at 10 °C/min heating rate, followed by cooling to 25 °C at 300 °C/min rate, and a second heating cycle of 25 – 200 °C at 10 °C/min. Endothermic peaks of DSC curves were used to determine delta H. For the purpose of this study onset values were used in all calculations (Knopp et al., 2016). All DSC measurements were performed in duplicate.

4.2.2.2.2 Thermogravimetric Analysis (TGA)

TGA for all polymers studied was performed using a Mettler TG50 module linked to a Mettler MT5 balance (Mettler, Toledo, Switzerland). Sample weights ~ 10 mg were utilised and placed in open aluminium pans. Measurements were carried out in the temperature range of 25 °C to 200 °C at 10 °C/min heating rate. All analysis was performed in the furnace under nitrogen purge. Measurements obtained were analysed using Mettler Toledo STARe software (version 6.10). TGA analysis was employed to ensure melting point determination would not be affected by possible polymer decomposition. Results confirmed all compounds were stable within the desired temperature range of 25 to 180 °C.

4.2.2.3 Powder X-ray Diffraction (PXRD)

PXRD measurements at room temperature were performed on samples placed on a standard glass sample holder using a Rigaku Miniflex II desktop X-ray diffractometer (Rigaku, Japan) with a Haskris cooling unit (Grove Village, IL, USA). Analysis was recorded from 2 to 40 on the 2θ

scale at a step of 0.05 °/s. The X-ray tube was operated under a voltage of 30 kV and current of 15 mA.

4.2.2.4 Solubility of KETO and ITR in Polymer Solutions

Solubility of KETO and ITR in polymer solutions was determined at 25 °C using the shake-flask method. An excess of API was added to the stabilizer solution in a glass vial which was tightly sealed and allowed to equilibrate for 2 hours with continuous stirring at 1000 rpm. Polymer solutions consisted of 0.5, 1 and 1.5 mg/ml in deionised water. Each combination of API and stabilizer concentration was measured in triplicate. For KETO, 1 ml of this solution was centrifuged for 1 hour in a Thermo Scientific Heraeus Fresco 17 centrifuge at 13,000 rpm and 25 °C. KETO concentration was quantified using HPLC.

For ITR, 0.4 ml of the supernatant was kept in a block heater overnight at 55 °C. This residue was reconstituted with 0.2 ml of mobile phase and transferred to a 0.2 ml HPLC micro insert. ITR concentration was quantified using HPLC.

The concentrations of ITR and KETO were measured using a Waters Symmetry® C_{18} 5 µm (4.6 mm x 150 mm) column attached to a Waters HPLC system equipped with a Waters 2695 separations module and a 2996 photodiode array detector (ITR λ = 260 nm, POS λ = 260 nm, KETO = 240 nm).

For ITR, the mobile phase used consisted of acetonitrile: buffer pH 6.8 (60:40) (v/v). A 0.1M phosphate buffer solution was prepared by dissolving 6.8 mg of potassium dihydrogen phosphate in 1L of deionised water. 1M potassium hydroxide solution was prepared by dissolving 5.6 g of potassium hydroxide in 0.1L of deionised water, this solution was used to adjust the phosphate buffer pH to 6.8. For KETO, the mobile phase used consisted of methanol: water (75:25) (v/v). A flow rate of 1 ml/min and run time of 14 minutes was used in all cases.

For ITR, a 100 µl injection volume was employed due to low solubility values. For solubility studies of KETO, a 50 µl injection volume was used. For solubility determination calibration curves used were in the concentration range of 0.0002 to 0.5 mg/ml. Column temperature was maintained at 25 °C for the duration using a column heater.

4.2.2.5 Adsorbed Polymer Layer Characterisation

Relative stability of NPs in the absence of a stabilizer was required for the study. For this reason, only ITR NPs were selected for this study. ITR NPs were formed as previously in Chapter 2. In addition, subsequent to NP formation the residual acetone was removed in a rotary evaporator apparatus, with the water bath at 30 °C. The sample was placed under vacuum at

60 mbar for 30 minutes rotating at 160 rpm. The dispersion was stored at 4 °C overnight. Sample temperature was controlled at 25 °C, prior to analysis. All stabilizer solutions were kept at 25 °C before addition to the NP solution. Particle size was measured at 25 °C in a 1 ml glass cuvette (part number PCS8501) using a Zetasizer Nano ZS series (Malvern Instruments, UK) before addition of polymer solution. Following this, the ITR NP dispersion and the polymer solution (at varying concentrations) were added to a glass vial in a 1:1 ratio (v/v) and stirred at 200 rpm for 5 minutes inside a jacketed water vessel at 25 °C. The polymer adsorption process is known to occur in around 1 minute (Couture and van de Ven, 1991). For this reason, study length was maintained at 5 minutes. Particle size measurements were then repeated as previously stated. The viscosity of continuous phase was corrected by inputting the measured viscosity value for each polymer solutions to the software.

4.2.2.6 Mathematical Modelling and Statistical Analysis

Modelling of phase diagrams and statistical analysis was performed in Origin 2018. Non-linear least squares curve fits to experimentally determined data were obtained by applying the Levenberg-Marquardt iteration algorithm until the Chi-square tolerance value of 1×10^{-9} was reached and the fit converged. No weighting for parameters was applied.

4.3 Results and Discussion

As previously mentioned, it is important to consider the key outcomes of the previous chapters in this thesis. ITR NPs had the best stability all API nano-dispersions, in both the presence and absence of stabilizers. DMPEG was the most effective stabilizer for ITR and KETO nano-dispersions. In the case of POS, nano-dispersions had greater stability in the absence of a stabilizer. In the case of ITR NPs, DMPEG was most effective stabilizer at the lowest concentration of 0.5 mg/ml. For KETO NPs, DMPEG was the most effective stabilizer at the higher concentration of 1.5 mg/ml. POS NPs has the poorest stability of all APIs. MPEG appeared to have a negative impact on the stability of POS NPs, i.e. were the least effective stabilizer for those NPs (Chapters 2 and 3). The solubility parameter concept can be useful in predicting the degree of interaction between formulation components and therefore product stability. Voelkel et al. (2008) employed HSPs for nano-materials in an effort to understand the miscibility of the different components of the system in an effort to predict product stability (Voelkel et al., 2008). In order to determine the degree of miscibility between drug and polymer in a quick and simple manner, HSPs were calculated for compounds. Structures for these compounds can be found with Fig. 2.1.

4.3.1 HANSEN SOLUBILITY PARAMETERS (HSPs) VIA HOFTYZER–VAN KREVELEN GROUP CONTRIBUTION METHOD

Table 4.1. Calculated HSPs for drugs and polymers using the Hoftyzer–Van Krevelen group contribution method.

Component	Calculated δt (MPa$^{\wedge 1/2}$)
PEG	20.36
MPEG	20.22
DMPEG	20.68
ITR	26.78
KETO	24.01
POS	25.02

HSPs presented in Table 4.1 confirm MPEG has the lowest parameter, while ITR has the highest overall. Calculated parameters suggest some degree of miscibility between all APIs and stabilizers. The smallest difference in parameters exists between DMPEG and all APIs. However, the largest difference in values for drug and polymer exists between ITR and MPEG. For all APIs, they are most miscible with DMPEG and least with MPEG.

Following on from this, determining the degree of drug-polymer interaction was attempted through the application of more complex techniques. Alternative techniques, such as melting point depression and phase diagram construction via the application of F-H theory require additional information. This methodology accounts for a range of compound characteristics, with the calculated interaction parameter requiring experimental determination. Limitations of F-H theory are well known, with more advanced models emerging however, it is still regarded as a good starting point in beginning to understand drug-polymer interactions (Flory, 1953). POS polymer systems were not included in thermal analysis studies for a number of reasons. As highlighted in Chapter 2, POS exhibits rich solid state polymorphism. Up to seven different polymorphs of POS have been reported in the literature (Andrews et al., 2004; Wieser et al., 2012 and 2013). For this reason, it was not possible to construct the phase diagram for POS, as a metastable form of POS may produce unreliable results with thermal analysis. In addition, the tendency for POS to crystallise quickly was evident in DLS (Chapter 2) and NTA studies (Chapter 3). The same trends were not evident for KETO and ITR nano-dispersions.

4.3.2 THERMAL ANALYSIS

4.3.2.1 Ketoconazole/polymer Mixtures - Thermograms

Prior to construction of the phase diagram, DSC measurements were carried out for pure components (Fig. 4.1 and A.3.1) and binary mixtures consisting of KETO and polymer.

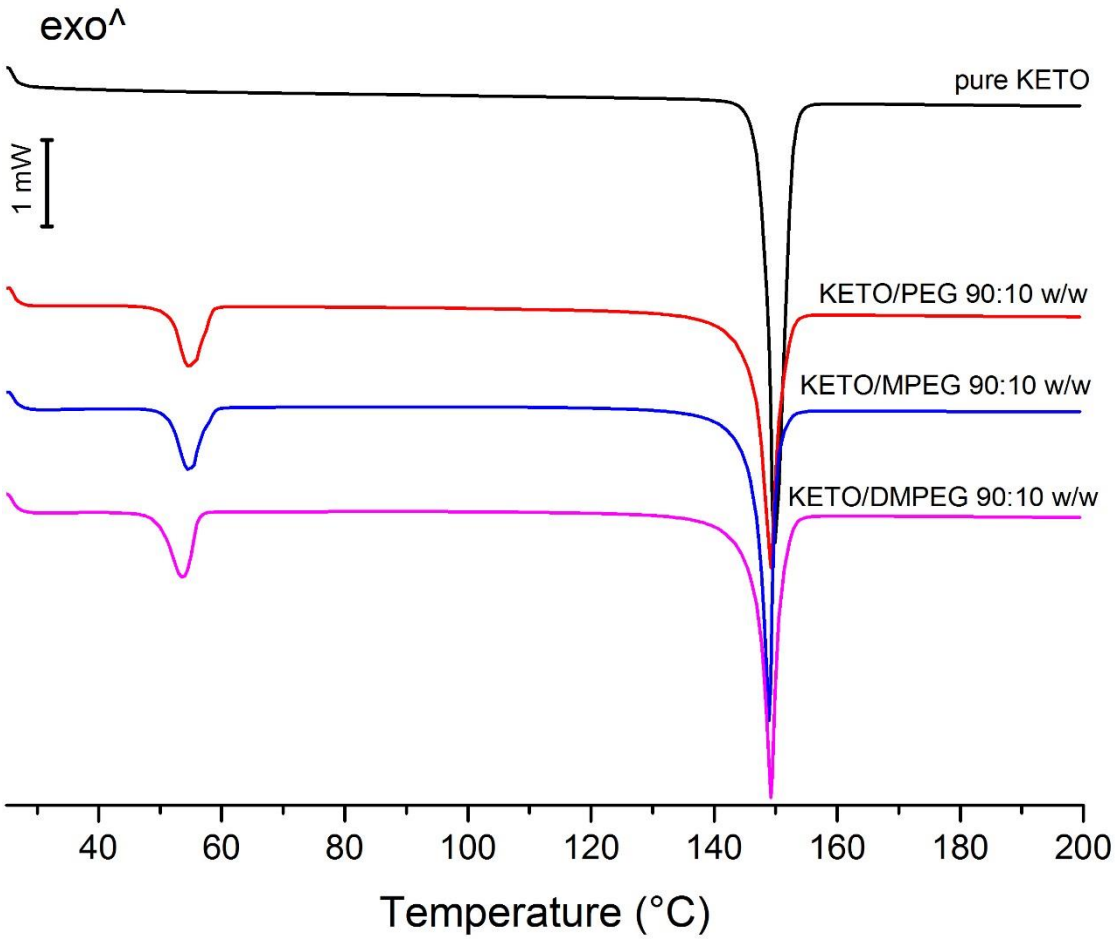

Fig. 4.1. DSC curves for pure KETO and physical mixtures of KETO/PEG, KETO/MPEG and KETO/DMPEG containing 10% (w/w) polymer.

DSC measurements for pure polymers showed only one melting event at 50.3 °C for PEG, 53.4 °C for MPEG and 49.6 °C for DMPEG (Fig. A.3.1). DSC measurements for pure KETO display a single endothermic event at 148 °C (Fig 4.1). In the case of KETO/polymer systems, two melting events are observed (Fig. A.3.2). The first peak appearing at a lower temperature can be attributed to the melting of the polymer, whilst the second melting event at a higher temperature corresponds with the melt of crystalline KETO (148 °C) (Fig. 4.1).

4.3.2.2 Solubility of Polymer in KETO

Theeuwes et al. (1974) first described the use of DSC for determining the solubility of solid drugs in polymers (Theeuwes et al., 1974). This simple theory is based on the assumption that

the amount of drug solubilised in the mixture does not contribute to the melting endotherm of the dispersed drug fraction. Hence, plotting the ΔH_f values versus drug concentration at a range of compositions followed by extrapolation to zero ΔH_f, allows for the solubility of the drug in the polymer to be estimated (Gramaglia et al., 2005). This DSC method has been used to determine the solubility of numerous drugs (Bodmeier and Paeratakal, 1989; Gramaglia et al., 2005). Based on this approach it is also possible to estimate polymer solubility in drug by plotting polymer ΔH_f values versus polymer concentration at a range of compositions followed by extrapolation to zero ΔH_f. In this instance, polymer solubility in KETO has been determined by plotting polymer ΔH_f values versus polymer concentration. Relationships for polymer enthalpy of fusion versus polymer weight fraction for KETO polymer binary systems are presented in Fig. 4.2:

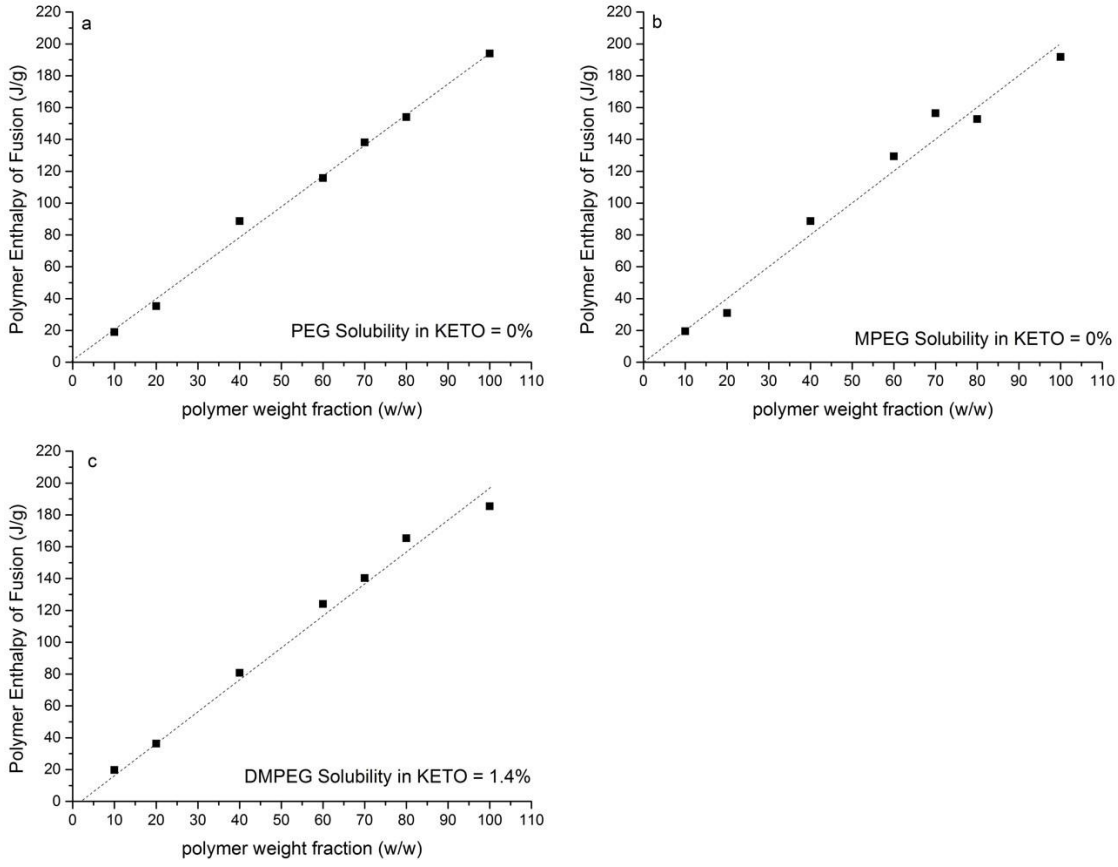

Fig. 4.2. Polymer enthalpy of fusion (J/g) versus polymer weight fraction for (a) PEG (b) MPEG and (c) DMPEG. The data points are based on a single heating cycle. The broken line represents linear fits to the data.

Table 4.2. Polymer solubility in KETO as (% w/w) and KETO weight fraction.

	Polymer Solubility (polymer (% w/w))	Polymer Solubility (KETO weight fraction)
KETO/PEG	0	1.00
KETO /MPEG	0	1.00
KETO /DMPEG	1.4	0.96

According to Fig 4.2 and Table 4.2, both PEG and MPEG are insoluble in KETO. Both polymers are crystalline throughout these composition ranges. However, DMPEG is very slightly soluble in KETO. When DMPEG exists in a disordered state, up to 1.4% (w/w) will be soluble in KETO, above this concentration DMPEG will exist in a crystalline state.

4.3.2.3 Phase Diagrams for KETO/polymer Systems

The F-H approach was successfully utilised to create phase diagrams for all KETO/polymer systems (Fig. 4.3). A greater decrease in the onset temperature for KETO melting (148 °C) would suggest greater miscibility between the components of the binary system. DSC curves presented in Fig. A.3.2 confirm that increasing polymer content caused a reduction in the onset melting temperature of pure KETO (148 °C). The largest reduction in onset temperature was observed for KETO/PEG, 106 °C, while the smallest reduction in onset temperature was observed for KETO/MPEG, 120 °C (Fig. A.3.2).

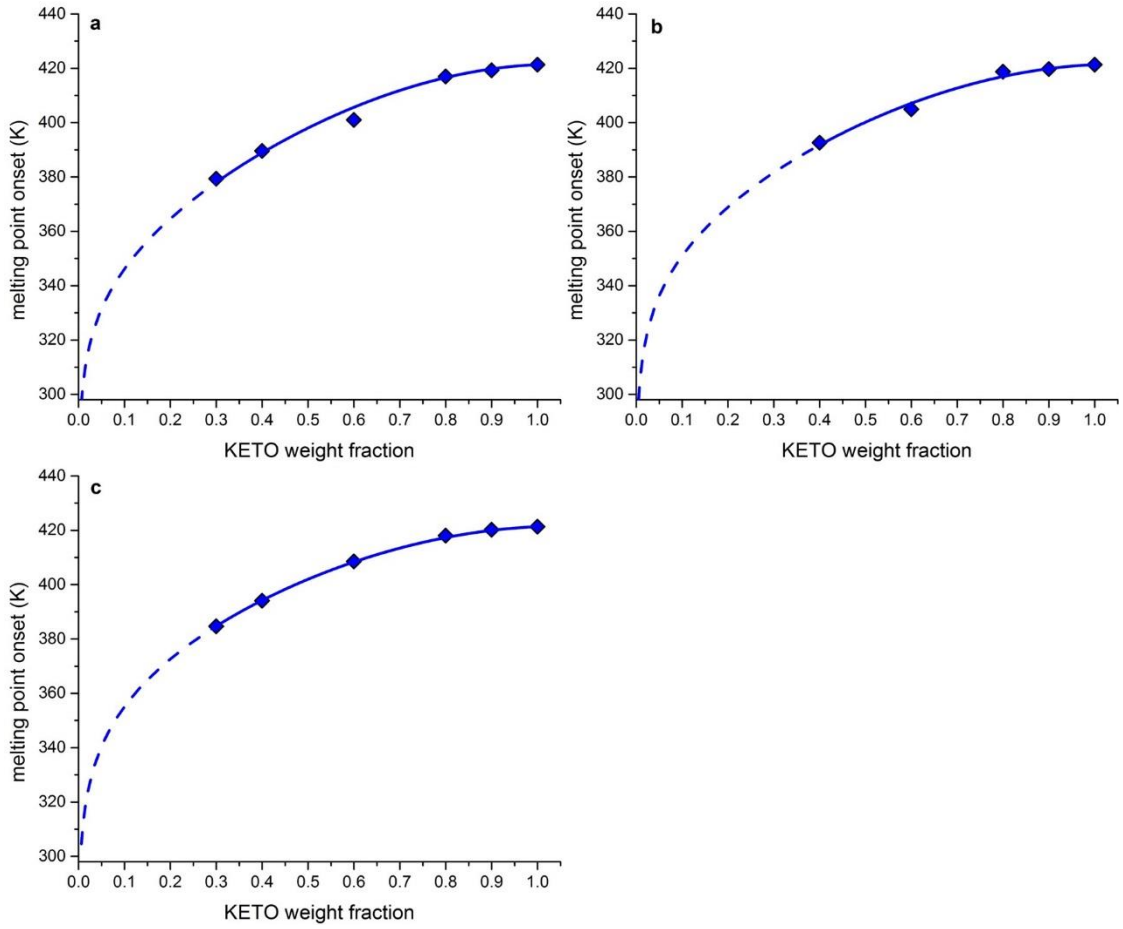

Fig. 4.3. Experimental data fit to melting point depression equation (solid line) for KETO/polymer systems. Fitted using F-H lattice model (Eq.4.1) for KETO/polymer systems: (a) KETO/PEG (b) KETO/MPEG and (c) KETO/DMPEG based on onset values. Broken lines indicate prediction beyond the experimental range.

Table 4.3. Chi interaction parameter (X) for KETO obtained using onset values.

	Polyethylene glycol (PEG) ± SD	Polyethylene glycol methyl ether (MPEG) ± SD	Polyethylene glycol dimethyl ether (DMPEG) ± SD
Onset	-1.875 ± 0.138	-1.574 ± 0.137	-1.32 ± 0.02

As per Table 4.3, KETO miscibility can be ranked accordingly: PEG > MPEG > DMPEG. The sign of X is indicative of the degree of miscibility existing between two components. When $X < 0$, miscibility exists between the components, in contrast, if $X > 0$ an immiscible system is likely (Kozyra et al., 2018). Table 4.3 suggests miscibility between KETO and all polymers. The

interaction parameter X = -1.32 for DMPEG is the closest to zero suggesting, the KETO/DMPEG system has the lowest miscibility (Table 4.3). In contrast, the interaction parameter X = -1.875 for PEG is the most negative, suggesting the highest miscibility in the KETO/PEG system (Table 4.3).

We can assume that when the polymers exist in crystalline form they will not be soluble or miscible in KETO (Fig 4.2). However, based on the F-H theory when both components exist in the amorphous (liquid) forms they should be fully miscible (Fig 4.3), with miscibility ranked as follows: PEG > MPEG > DMPEG. Furthermore, if the polymer exists in the crystalline form alongside amorphous KETO the situation arises whereby phase separation occurs between crystalline polymer and amorphous KETO. An exception to this exists in the case of DMPEG, whereby solubility determinations presented in Fig 4.2 confirm crystalline DMPEG is very slightly soluble (1.4% (w/w)) in amorphous KETO. Hence, it seems likely that limited solubility is an ideal prerequisite for effective NP stabilization.

A graphical summary of the thermal analysis of KETO/polymer systems is presented in Fig. 4.4.

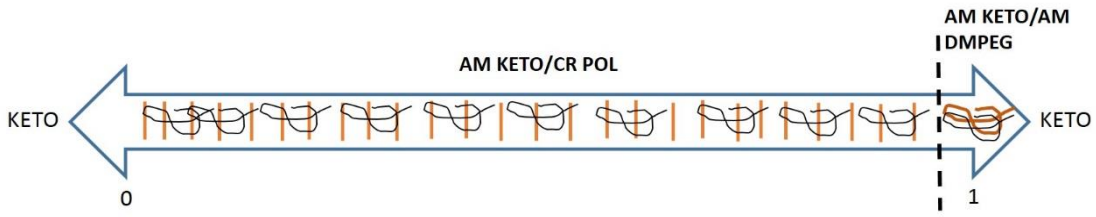

Fig. 4.4 Graphical representation of KETO phase identification in KETO/polymer mixtures (w/w). *AM = amorphous, CR = crystalline and POL = polymer

As Fig 4.4 demonstrates KETO can exist in a variety of phases when supercooled in a binary mixture with polymer. Throughout the range of KETO/polymer compositions studied KETO will exist in an amorphous state. Furthermore, polymer will exist in crystalline form. However, in the case of KETO/DMPEG systems, DMPEG will be crystalline when mixed with up to 0.984 KETO weight fraction. Above this concentration of KETO, DMPEG will exist in amorphous form (Fig 4.4).

4.3.2.4 ITR/polymer Mixtures - Thermograms

Prior to construction of the phase diagram, DSC measurements were carried out for pure components (Fig. 4.5 and A.3.1) and binary mixtures consisting of ITR and polymer.

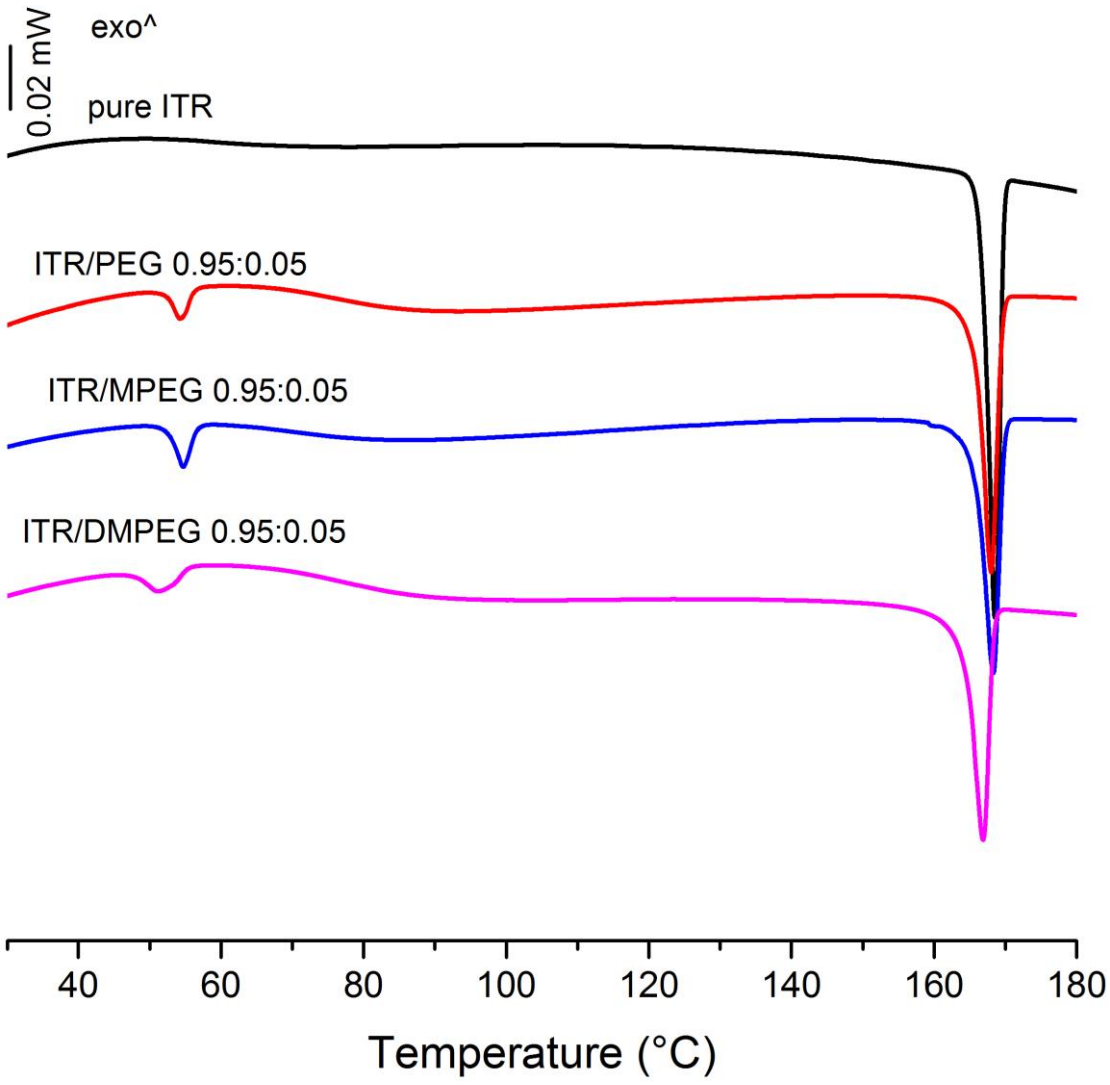

Fig. 4.5 DSC curves for pure ITR, and physical mixtures of ITR/PEG, ITR/MPEG and ITR/DMPEG on first heating. Number denotes weight fraction of ITR.

DSC measurements for pure polymers showed only one melting event as previously mentioned (Fig. A.3.1). DSC measurements for pure ITR showed a melting event at 167 °C (Fig 4.5). Typical DSC curves, representing the first heating for ITR polymer systems, can be seen in Fig. 4.5 where two melting events are observed. The first peak, appearing at a lower temperature can be attributed to the melting of the polymer, whilst the second melting event at a higher temperature corresponds with the melt of crystalline ITR (167 °C).

4.3.2.5 Solubility of Polymers in ITR

Given the likelihood of the disordered nature of ITR when formulated as a NP, this analysis focused on second heating data only. Relationships for polymer enthalpy of fusion versus polymer weight fraction are presented in Fig. 4.6:

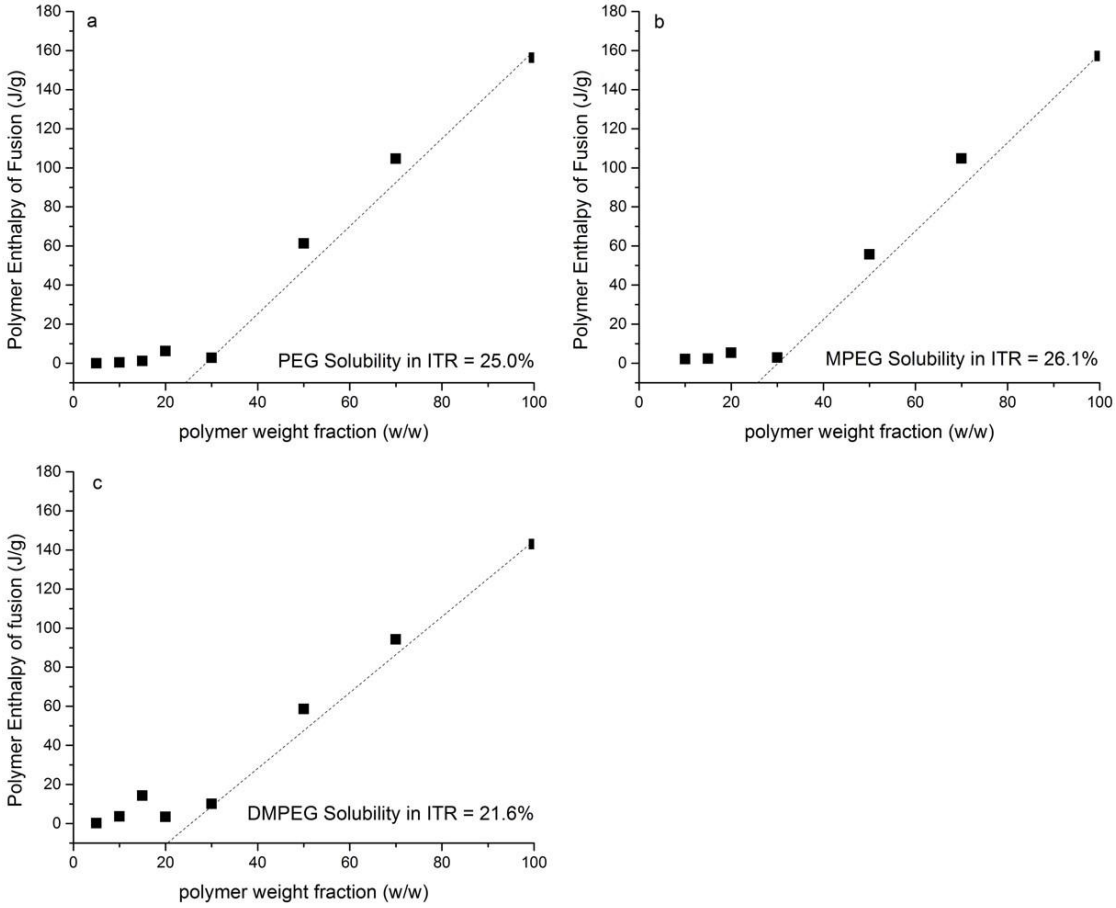

Fig. 4.6 Polymer enthalpy of fusion (J/g) versus polymer weight fraction for (a) PEG (b) MPEG and (c) DMPEG. The data points represent second heating measurements. The broken line represents linear fits to the data.

Table 4.4. Polymer solubility in ITR as (% w/w) and ITR weight fraction.

	Polymer Solubility (polymer (% w/w))	Polymer Solubility (ITR weight fraction)
ITR/PEG	25.0	0.75
ITR/MPEG	26.1	0.739
ITR/DMPEG	21.6	0.784

According to Fig. 4.6 and Table 4.4, the polymers have considerable solubility in ITR, in contrast to being very slightly or practically insoluble in KETO (Table 4.2). Table 4.4 suggests that the lowest solubility exists for the ITR and DMPEG system.

4.3.2.6 Liquid Crystal Properties of ITR

ITR has the unique capability of forming liquid crystalline (LC) phases. It is likely ITR exists as a LC following NP formation in this thesis. This is based on the findings of Mugheirbi et al. (2014), whereby similar conditions were employed during ITR NP formation. Few reports exist in the literature documenting this phenomenon. Six et al. (2001) reported two reversible endothermic transitions at 74 and 90 °C. The author concluded, the transition of an isotropic liquid into a chiral nematic mesophase was responsible for the event at 90 °C, while the event observed at 74 °C was most likely due to rotational restriction of the molecules (Six et al., 2001). Tarnacka et al. (2013) and Mapesa et al. (2014) used dielectric spectroscopy to further investigate the thermodynamic properties of ITR. They attributed the endothermal event observed at 74 °C to the formation of a smectic A phase (LC_{SmA-N}), while the event at 90 °C was related to that of a nematic phase (LC_{N-I}) (Tarnacka et al.,2013; Mapesa et al., 2014). Most recently, Mugheirbi et al. (2016) identified a process induced nematic phase following nano-sization and spray drying of ITR, in addition to a smectic phase following a 1:1 water/ITR complex formation (Mugheirbi et al., 2016). In light of the unusual behaviour of ITR, thermal analysis studies were designed as such: ITR was subjected to heating to 180 °C (ITR melting point = 167 °C), flash cooling to 25 °C at 300 °C/min, followed by re-heating to 180 °C at 10 °C/min. Evidence of the LC thermal transitions of pure ITR can be seen in Fig. 4.7.

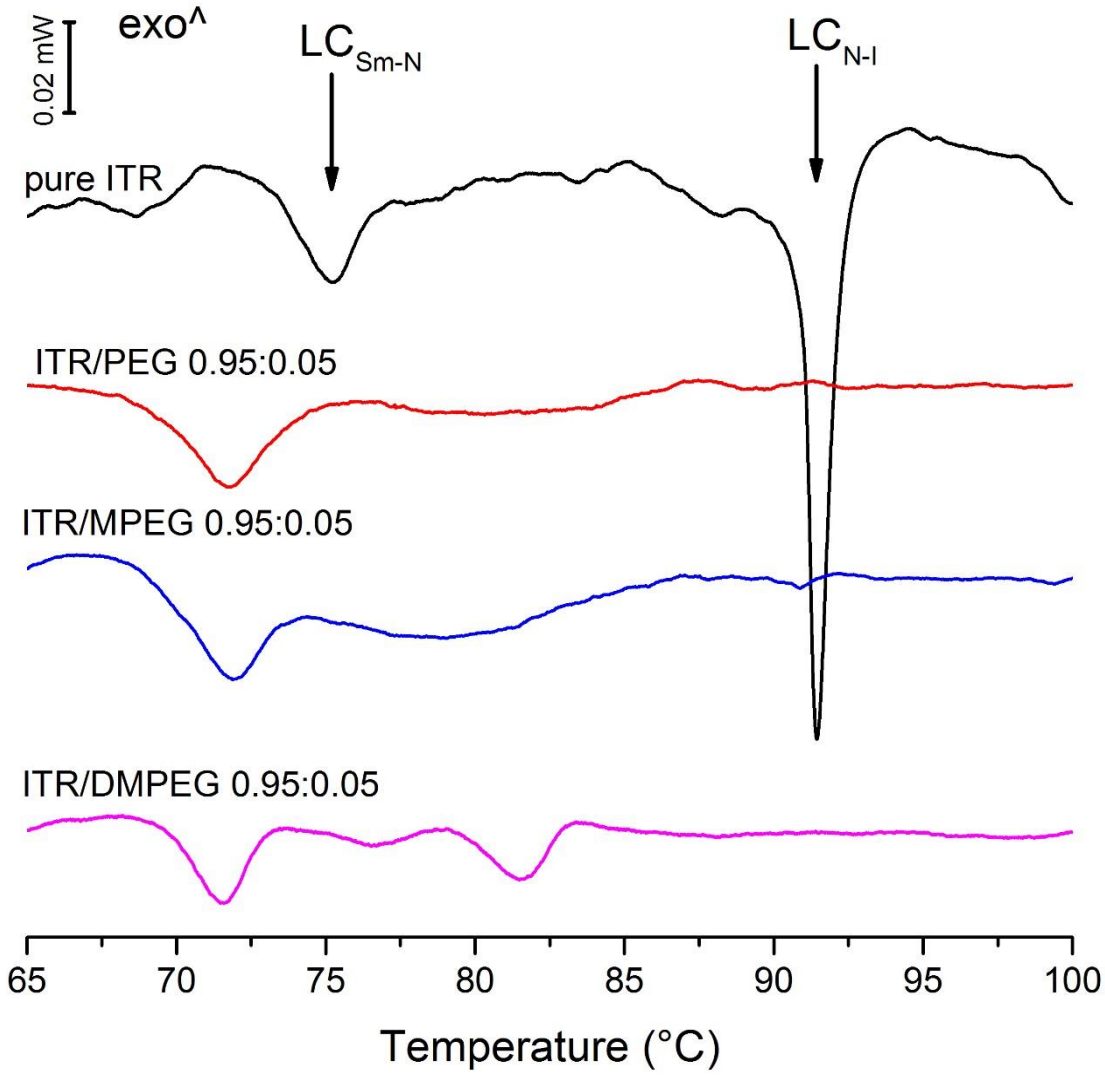

Fig. 4.7 DSC curves for pure ITR, physical mixtures of ITR/PEG, ITR/MPEG and ITR/DMPEG on second heating. Number denotes weight fraction of ITR.

Fig. 4.7 confirms the presence of an endothermal event at 74 °C caused by the formation of a smectic A phase (LC_{SmA-N}), while the endothermal event at 90 °C can be attributed to the formation of a nematic phase (LC_{N-I}) for pure ITR. In the case of ITR polymer systems, the event observed at ~ 74 °C can be attributed to the smectic (LC_{SmA-N}) phase of ITR. In the case of ITR/DMPEG, the additional endothermal transition at ~ 80 °C might represent the nematic phase (LC_{N-I}) transition (Fig. 4.7). There may be a number of reasons for PEG and MPEG systems limiting LC phase formation to the smectic phase (LC_{SmA-N}) only. It is possible that interference from the polymer or strong polymer-polymer interactions, with the latter being more likely, are responsible for this phenomena. The presence of the nematic phase (LC_{N-I}) transition in the ITR/DMPEG systems reaffirms the different behaviour of this polymer (Fig. 4.7). It is evident from Fig. 4.5 that increasing polymer content resulted in a decrease in the onset

temperature of the melting of pure ITR (166 °C) during the first heating. ITR/DMPEG systems resulted in the largest decrease in onset temperature, 141.2 °C. While, ITR/PEG systems had the smallest decrease in onset melting temperature, 157.3 °C. The same trend was apparent for the ITR LC_{SmA-N} event, with increasing polymer content resulting in a decrease in the onset temperature (Fig. 4.7). ITR/MPEG systems exhibited the largest decrease in the onset temperature, 66.9 °C, while, ITR/PEG systems decreased the temperature to 69.7 °C and DMPEG decreased the temperature to 69.2 °C. A greater reduction in onset temperature would suggest greater miscibility of drug and polymer.

4.3.2.7 Phase Diagrams of ITR Polymer Systems

Melting point depression method was employed in the production of phase diagrams for the ITR/polymer systems considering the isotropic and anisotropic phases ITR is capable of forming. The F-H theory can be useful in determining the degree of miscibility between components within a system (Caron et al., 2011). The reader is referred to section 4.1 and Eq. 4.3 regarding more detailed information on F-H theory. However, in this instance ITR has the capability of forming liquid crystalline phases. Therefore, the F-H theory was coupled with the M-S-M approach for anisotropic ordering, to aid in the construction of phase diagrams. The reader is referred to Eq. 4.2 for more detailed information regarding M-S-M theory. Phase diagram construction for the smectic-isotropic (liquid) line of ITR was based on measurement of LC transitions in samples that were heated beyond the melting point of pure ITR (167 °C), followed by cooling to 25 °C at 300 °C/min and a second heating to 180 °C at 10 °C/min. In the case of fitting the ITR solid-liquid (isotropic) transition for ITR/polymer systems, the χ parameter was determined using the melting point depression method based on the F-H theory using Eq. 4.1.

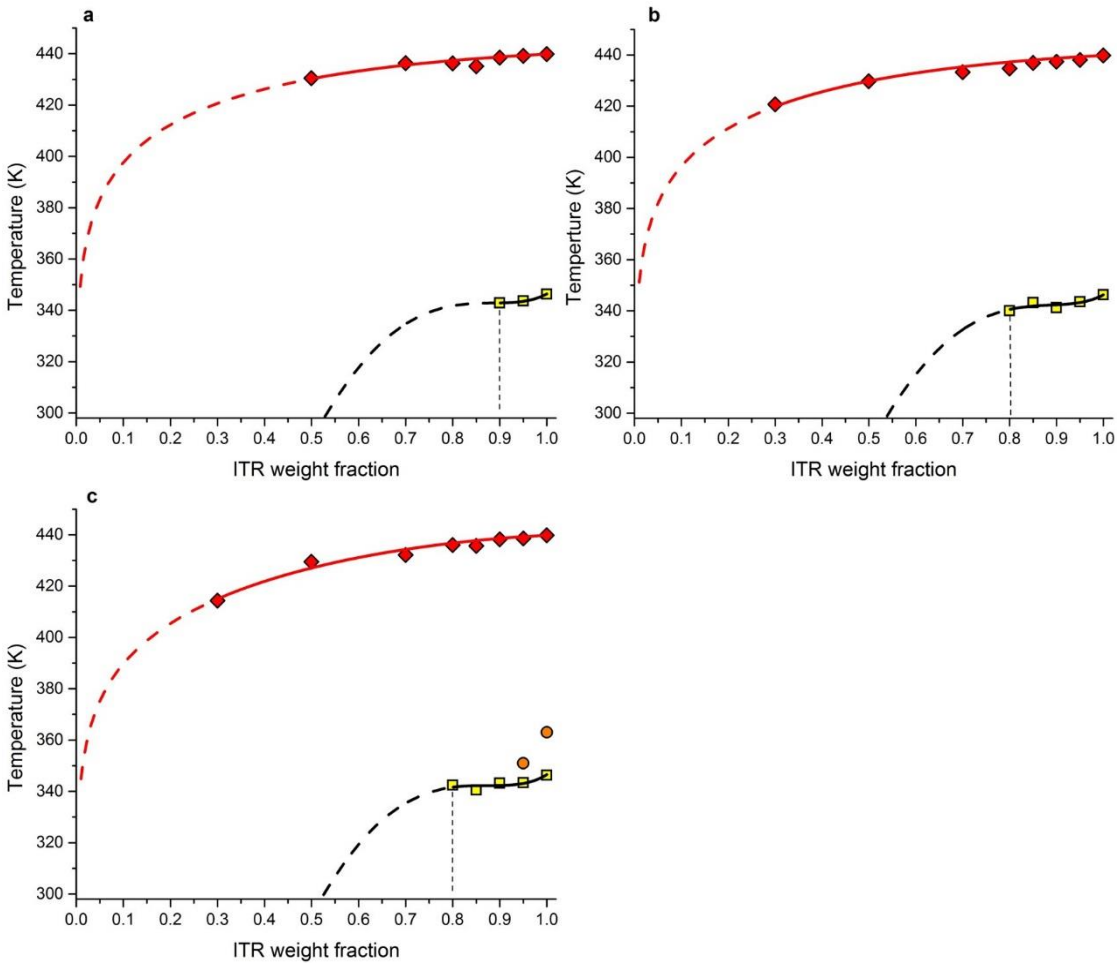

Fig. 4.8. Phase diagrams for ITR/polymer systems: (a) ITR/PEG (b) ITR/MPEG (c) ITR/DMPEG. Red lines are solid-isotropic (liquid) lines determined by fitting experimental points using the F-H theory. Black lines are fitted LC lines (smectic-nematic) using the F-H and M-S-M theories. Broken lines indicate prediction beyond the experimental range.

Table 4.5. Chi interaction parameter (X) for various ITR/polymer systems estimated using the F-H theory (solid-isotropic (liquid) lines) and a combination of F-H and M-S-M theories. Obtained using onset values.

	Based on crystalline ITR (solid-isotropic (liquid) line) ± SD	Based on LC ITR (smectic-isotropic (liquid) line) ± SD
PEG	0.142 ± 0.161	0.688 ± 0.013
MPEG	0.083 ± 0.097	0.667 ± 0.118
DMPEG	-0.282 ± 0.100	0.731 ± 0.125

The experimental enthalpy of the $LC_{SmA\text{-}N}$ transition was taken to determine the boundary of the phase persistence as highlighted by black lines parallel to the y-axis in Fig. 4.8. $LC_{SmA\text{-}N}$ phase persistence of 90% exists for ITR/PEG systems (Fig. 4.8a), while 80% persistence is

evident for MPEG and DMPEG systems (Fig. 4.8b and c). According to the calculated interaction parameters in Table 4.5, accounting for the LC nature of ITR, immiscibility exists between all components, as indicated by the positive X parameters. Constructed phase diagrams suggest that, the LC_{SmA-N} phase is present only at high ITR content, up to 90% (w/w) for PEG, and 80% (w/w) for MPEG and DMPEG. Furthermore, component immiscibility is evident from the positive F-H interaction parameters obtained for ITR/PEG and ITR/MPEG considering the solid-liquid line (constructed using crystalline ITR) with the χ value for the ITR/DMPEG being close to zero (Table 4.5).

A graphical summary of the thermal analysis of ITR/polymer systems is presented in Fig. 4.9.

Fig. 4.9 Graphical representation of ITR phase identification in "supercooled" ITR/polymer mixtures (w/w). *AM = amorphous, CR = crystalline and POL = polymer.

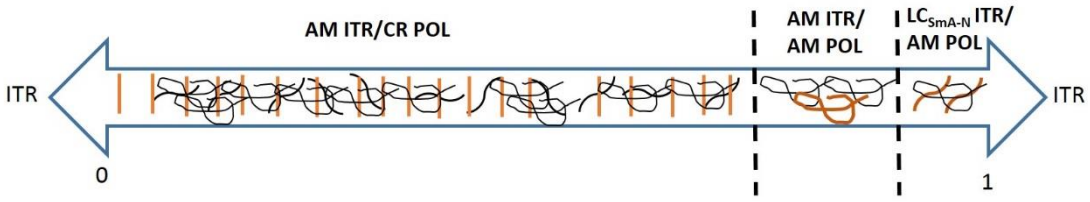

As Fig 4.9 demonstrates ITR can exist in a variety of phases when supercooled in a binary mixture with polymer. ITR will exist in an amorphous state, and polymer in a crystalline state when ITR is present below 0.75 (weight fraction). Increasing ITR weight fraction above 0.75, results in disorder of the polymer. Above 0.9 ITR weight fraction, ITR will form a smectic A (LC_{SmA-N}) phase existing alongside amorphous polymer within the system. The phase inducing behaviour of PEG has been noted elsewhere in the literature. Ge et al. (2009) studied the PEG-induced lamellar to isotropic phase transition of a LC system. Lamellar to isotropic phase transition was observed with increasing PEG content (Ge et al., 2009), with PEG 2000 observed to have a prominent effect on the lamellar LC structure, in agreement with our findings.

4.3.3 Drug Solubility in Polymer Solutions

Previously mentioned techniques have focused on binary systems. Investigation of drug solubility in polymer solutions provides a platform for assessing the interactions present within a ternary system. In this instance, the system consists of drug, polymer and water. In this way, similar conditions to those present during NP formation can be replicated. Table 4.6 represents drug solubility in polymer solutions for all APIs. Measurements were performed at 25 °C to replicate the conditions of NP formation.

Table 4.6a. Drug solubility (µg/ml) in polymer solutions for ITR in aqueous stabilizer solutions at 25 °C stirred for 2 hours at 1000 rpm. (n = 3)

Stabilizer Concentration (mg/ml)	ITR Solubility in PEG (µg/ml) ± SD	ITR Solubility in MPEG (µg/ml) ± SD	ITR Solubility in DMPEG (µg/ml) ± SD
0.5	0.61 ± 0.18	0.17 ± 0.02	0.11 ± 0.02
1	0.59 ± 0.33	1.72 ± 0.11	0.11 ± 0.02
1.5	6.96 ± 0.69	1.46 ± 0.13	0.15 ± 0.03

Table 4.6b. Drug solubility (µg/ml) in polymer solutions for KETO in aqueous stabilizer solutions at 25 °C stirred for 2 hours at 1000 rpm. (n = 3)

Stabilizer Concentration (mg/ml)	KETO Solubility in PEG (µg/ml) ± SD	KETO Solubility in MPEG (µg/ml) ± SD	KETO Solubility in DMPEG (µg/ml) ± SD
0.5	9.73 ± 0.41	10.32 ± 0.73	30.07 ± 0.58
1	10.27 ± 0.55	12.19 ± 0.18	66.39 ± 2.53
1.5	10.00 ± 0.77	11.25 ± 1.78	92.76 ± 0.22

KETO had the greatest solubility in all polymer solutions compared with ITR, markedly so for DMPEG (Table 4.6b). ITR had the lowest solubility in DMPEG, with 0.15 µg/ml solubility being achieved in 1.5 mg/ml DMPEG (Table 4.6a).

4.3.4 MISCIBILITY PREDICTIONS

Miscibility is generally confined to the mixing of liquids or an amorphous compound in a polymer, being determined by the balance between entropy and enthalpy of mixing (Marsac et al., 2009). F-H theory is based on the two components of enthalpy and entropy. Entropy always favours mixing whereas enthalpy, will either facilitate or prevent mixing depending on the degree of interaction between the components of the system. Solubility is a more general term used in reference to the ability of a solid solute to dissolve in a liquid solvent, more specifically the solubility of a crystalline compound in a polymer (Qian et al., 2010). The above findings confirm the disordered nature of KETO and ITR, thereby satisfying the assumptions of the F-H and M-S-M models. The methods utilised in this work allow for approximations regarding interaction parameters to be made based on experimental data. In this way the

thermodynamics of mixing of various systems can be compared. Calculated HSPs presented in Table 4.1 suggest some degree of miscibility between all drugs and polymers. DMPEG had the closest value of all polymers to the drugs however the greatest difference exists between MPEG and ITR (Table 4.1). This would suggest the lowest degree of miscibility between MPEG and ITR, of all combinations.

The F-H lattice theory can be useful in predicting drug-polymer interactions as it accounts for the large size discrepancy between the drug and polymer (Marsac et al., 2006). Results of thermal analysis confirmed miscibility between KETO and all polymers, with the lowest degree of miscibility between KETO and DMPEG (Table 4.3). Many strong cohesive intermolecular interactions between components favour miscibility. In light of the findings presented in Chapter 2, DMPEG was the most effective stabilizer for KETO NPs. Propensity for effective NP stabilization is predicted by lower miscibility between KETO and polymer in this case (Chapters 2 and 3).

Phase diagram construction for ITR/polymer systems gave due consideration to the possibility of ITR existing in LC or fully crystalline state. Both scenarios resulted in calculated interaction parameters suggesting immiscibility in all systems. Given the capability of ITR to form liquid crystalline phases, data obtained upon second heating of binary mixtures requires more careful consideration. During melting point depression, thermal energy applied to system provides the driving force for disruption to the order of ITR molecules. It is likely that generation of supersaturation during the NP formation process provides the necessary energy to the system, introducing disorder. Therefore, based on the assumption that ITR exists in a disordered (glassy) state, it can be concluded that immiscibility exists between all components. Furthermore, the highest degree of immiscibility exists between ITR and DMPEG (Table 4.5). Miscibility predictions based on the above are associated with a degree of uncertainty due to measurement precision and the validity of assumptions which the F-H theory is based on (Knopp et al., 2015). However, DMPEG was the most effective stabilizer for ITR nano-dispersions at the lowest effective concentration of 0.5 mg/ml according to the findings of Chapter 2. Therefore, we can conclude that immiscibility of drug and polymer can act as a good predictor for the effective stabilization of ITR NPs.

The investigation of solubility of polymer in ITR confirms the lowest solubility (21.6%) of all systems for DMPEG in ITR (Fig. 4.6 and Table 4.4). Miscibility and solubility trends ITR/DMPEG systems are in agreement, as they have poor miscibility (Table 4.5) and solubility (Fig. 4.6). So whether ITR exists in a glassy or crystalline state, minimal interaction between ITR and DMPEG

will exist. It appears, that a combination of low solubility and miscibility between ITR and DMPEG is a good predictor for effective stabilization of ITR NPs by DMPEG (Chapter 2).

Solubility in polymer solutions data can be indicative of the thermodynamics of mixing at room temperature. ITR had the lowest solubility in DMPEG solutions (Table. 4.6a). KETO had the highest solubility in DMPEG solution (Table. 4.6b). We can conclude that for KETO, an increased API solubility in polymer solution correlates with effective NP stabilization. However, the opposite is true for ITR. Decreased ITR solubility in polymer solutions is a better predictor for effective NP stabilization. It is worth noting that solubility can also be influenced by several experimental factors, such as stirring time, sedimentation time, temperature, amount of solid excess, and the technique of phase-separation (Baka et al., 2008).

It is likely that some miscibility between the drug and polymer may be necessary for stabilization. Stabilizers may act solely, or in a combination via two mechanisms, adhering to API particle surfaces and/or integrating within API particle matrices. During NP formation a number of physical processes occur simultaneously. Solvent exchange results in the transformation of droplets into solid particles. Indeed, this fact was depicted through the presence of pin-prick “blowholes” evident on the surface of particles seen in SEM micrographs presented in Chapter 2. There is no doubt these processes are determined by the miscibility of the various components. On the other hand, in the light of the findings of this work it seems likely that drug-polymer immiscibility provides favourable conditions for effective stabilization of ITR NPs. In the case of KETO NPs, it seems that low miscibility between components is a good predictor for effective NP stabilization. However, limited miscibility between the API and stabilizer may lead to confinement of polymer exclusively to NP surfaces, with limited integration throughout the particle core. Therefore, some degree of miscibility may be necessary for sufficient physio-adsorption and anchorage of polymer chains onto particle surfaces.

Fig 4.10 displays a graphical representation of material solid state properties and the likely impact of this upon polymer localization within the NPs.

Fig. 4.10 Graphical representation of the impact of NP solid state upon polymer localization within the NP. *LC = liquid crystal, NP = nanoparticles.

When considering thermal analysis and HSPs for the purpose of predicting drug–polymer miscibility, it should be noted that these techniques have been used on binary systems (API and polymer). However, in reality during the process of NP formation and consequent stabilization, solvents are present. The influence of these components upon the NP environment should not be overlooked and may account for some discrepancy in results/predictions. The drug solubility in polymer solution approach is based on a ternary system which may be considered an advantage in this case.

4.3.5 ITR-POLYMER ADSORPTION LAYER CHARACTERISATION

In light of the above findings, immiscibility and minimal interaction between ITR and polymer suggests confinement of polymer onto ITR particle surfaces, with little or no polymer integration throughout the particle matrix. The polymer adsorption process is said to consist of three stages: diffusion of polymer molecules to particle surfaces, followed by formation of a dense layer until full coverage is achieved, and finally attainment of equilibrium layer thickness. Polymer adsorption layer characterisation may provide insightful findings with regards to polymer behaviour during NP stabilization. Investigations into the size of the adsorbed polymer coating layer were confined to ITR nano-dispersions. These nano-dispersions proved the most stable over an extended period of time, ensuring any increase in particle size could be attributed to polymer coating layer itself and not particle growth. Table 4.9 contains data relating to the formation of polymer adsorbed layers measured using DLS. Polymer monomer size measurements are contained within Table 4.7. Fig. 4.11 contains a graphical representation of adsorbed polymer layer formation.

Table 4.7. Free polymer particle size for each polymer (only) obtained using DLS at 25 °C following manual shaking for 5 minutes. (n = 3)

Polymer Type	Polymer particle size (nm) ± SD
PEG	2.6 ± 0.6
MPEG	2.8 ± 0.7
DMPEG	2.8 ± 0.7

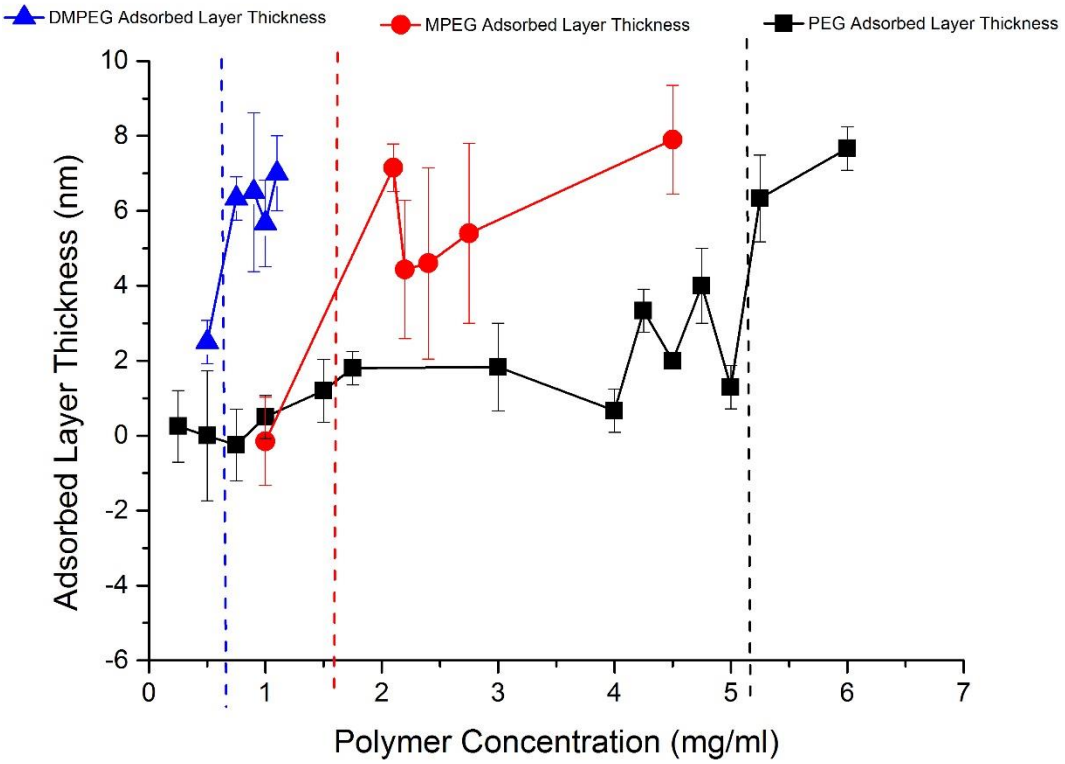

Fig. 4.11. Adsorbed layer thickness versus polymer concentration for DMPEG, MPEG and PEG ITR NPs obtained using DLS. Broken lines indicate polymer concentration whereby layer formation occurs. (n = 3)

An increase in particle size can be attributed to the formation of an adsorbed polymer coating layer onto ITR particle surfaces. A negative value for coating layer was obtained at lower polymer content for all polymers (negative data points have been omitted from Fig. 4.11 for the purpose of optimal visual representation of data). A statistically significant difference in these values is unlikely, indicating likely absence of the polymer coating layer at lower polymer concentration. This highlights a significant limitation of this technique when characterising a polymer layer in the nano-metre size range.

DLS studies showed an increase in overall particle size subsequent to polymer addition, equating to layer thickness larger than the size of free polymer molecules in solution, which were measured as ~ 3 nm as shown by Fig. A.3.4. and Table 4.7. Polymer layer thickness was measured in the range of 6 - 7 nm, regardless of the polymer type utilised in layer formation. However, the polymer type was critical in determining layer formation. It has previously been shown that particle surface interactions are highly dependent upon polymer concentration and type (Xing et al., 2015). We can confirm that the polymer type and concentration are directly affecting adsorbed layer formation in this instance. The process of polymer layer formation occurs at a different polymer concentration for each polymer (Fig. 4.11). Beyond this concentration, a plateau in layer thickness is reached where it seems likely that all possible ITR adsorption sites are occupied. When polymer content reaches this critical threshold, polymer molecules are capable of imposing steric hindrance between neighbouring particles, therefore inhibiting the OR process and particle growth. ITR adsorption sites became saturated at the lowest polymer concentration of 0.75 mg/ml, when the adsorbed coating layer consists of DMPEG. In contrast, the adsorbed layer formed by PEG takes place at a much higher polymer concentration of around 5 mg/ml (Fig. 4.11). Further polymer addition to the coating layer at this point is limited by the availability of sites on ITR particle surfaces, and steric hindrance imposed by polymers already adsorbed (Couture and van de Ven, 1991).

Interestingly, it seems possible that depletion stabilization, followed by depletion flocculation, may occur when DMPEG is used at higher concentrations. This may explain the marked variability in coating layer thickness above 4 mg/ml for DMPEG measurements (Fig. 4.11). In addition, visible precipitates could be seen in the dispersion following DMPEG addition to ITR NPs. At low polymer concentration, surface coverage is below saturation point. With increasing polymer concentration particle surfaces become covered by adsorbed polymer, with steric stabilization resulting. Any further increase in polymer concentration beyond this saturation point, leads to non-adsorbed polymers producing depletion interaction, which then gives rise to depletion flocculation (Kim et al., 2015).

Determining the nature of adsorbed polymer layers presents a particularly difficult challenge. Of course, limitations of DLS capability in quantifying polymer layer formation and thickness should be highlighted. DLS may not have sufficient sensitivity to detect the small changes in particle size involved with adsorption of polymer layers onto NP surfaces accurately. DLS measurements are based on spherical approximation of the particle under analysis. No information can be drawn regarding layer conformation from size data obtained. The technique assumes perfect uniformity in polymer layers surrounding particle surfaces. DLS is

not the particle sizing technique of choice when high peak resolution is desirable. DLS software lacks the capability of distinguishing between free polymer and polymer adsorbed onto NPs in solution. Complimentary techniques such as small angle X-ray scattering may be more informative regarding size and shape, as opposed to shape alone with DLS. NP formation is followed by addition of the polymer. During studies performed on ITR NPs stabilized with these polymers in Chapters 2 and 3, polymer was present in the anti-solvent phase prior to NP formation. This may have implications for the role of the polymer during the NP formation process. Polymer may be confined to NP surfaces during DLS adsorbed layer investigations. However, when present in the anti-solvent phase polymers have increased opportunity to embed within the particle core, as well as migrate towards particle surfaces.

So the question remains, what is the relationship between drug-polymer miscibility or solubility and the process of adsorbed polymer layer formation? It is apparent that layer thickness is not dependent upon polymer type. Therefore, miscibility and solubility relationships have no impact upon this aspect of NP stabilization. However, our findings indicate that drug-polymer immiscibility and low polymer solubility in the drug enables adsorbed layer formation at lower polymer concentration for ITR NPs. When the strength of polymer-polymer interactions outweighs drug-polymer interactions, adsorbed layer formation occurs more readily. This gives rise to more effective NP stabilization. Immiscibility and low solubility between the ITR and DMPEG is a good predictor for rapid adsorbed layer formation, and hence effective NP stabilization.

4.3.6 Eutectic Phase Formation

The presence of a suspected eutectic mixture for ITR/polymer systems following a single heating and cooling was detected with DSC (Fig. A.3.3), at a weight ratio of ITR/polymer 0.3:0.7. Eutectic formation has been established as a valuable tool for dissolution rate improvement. PEG has been noted as an ideal component in the formation of simple binary eutectic mixtures due to its low melting point and miscibility with drugs at higher temperatures (Law et al., 2002). The ability of PEG to form eutectic mixtures with numerous APIs has been noted in the literature (Vippagunta et al., 2007; Baird and Taylor, 2011). The process of mixing between two components is considered the ideal solution model, with transition temperature being lower than that of the pure components concerned, as demonstrated by the DSC curve presented in Fig. A.3.3. The presence of an ideal eutectic mixture assumes complete insolubility between the two components across all concentrations (Meltzer and Pincu, 2012). For this reason, it seems eutectic formation in this instance (KETO and ITR) would be unlikely. However, to complete the investigation of KETO and ITR solid state

properties, the Schroder-van Laar equation was used to calculate the eutectic transition temperature of a mixture of drug and polymer (Meltzer and Pincu, 2012) (Eq. 4.8):

$$\ln x_i = -\frac{\Delta_{fus}H_i^O}{R}\left(\frac{1}{T} - \frac{1}{T_{fusi}}\right) \quad \text{(Eq. 4.8)}$$

Where x_i is the mole fraction of the components at that temperature T, $\Delta_{fus}H_i^O$ is the molar enthalpy of fusion of the component *i, R* is the gas constant and T_{fusi} is the melting temperature of the pure component.

4.3.6.1 KETO/Polymer Eutectic Phase Formation

A comparison between experimentally determined eutectic points for the KETO/polymer systems with predictions derived using the Schroder-van Laar equation was attempted (Fig. 4.12).

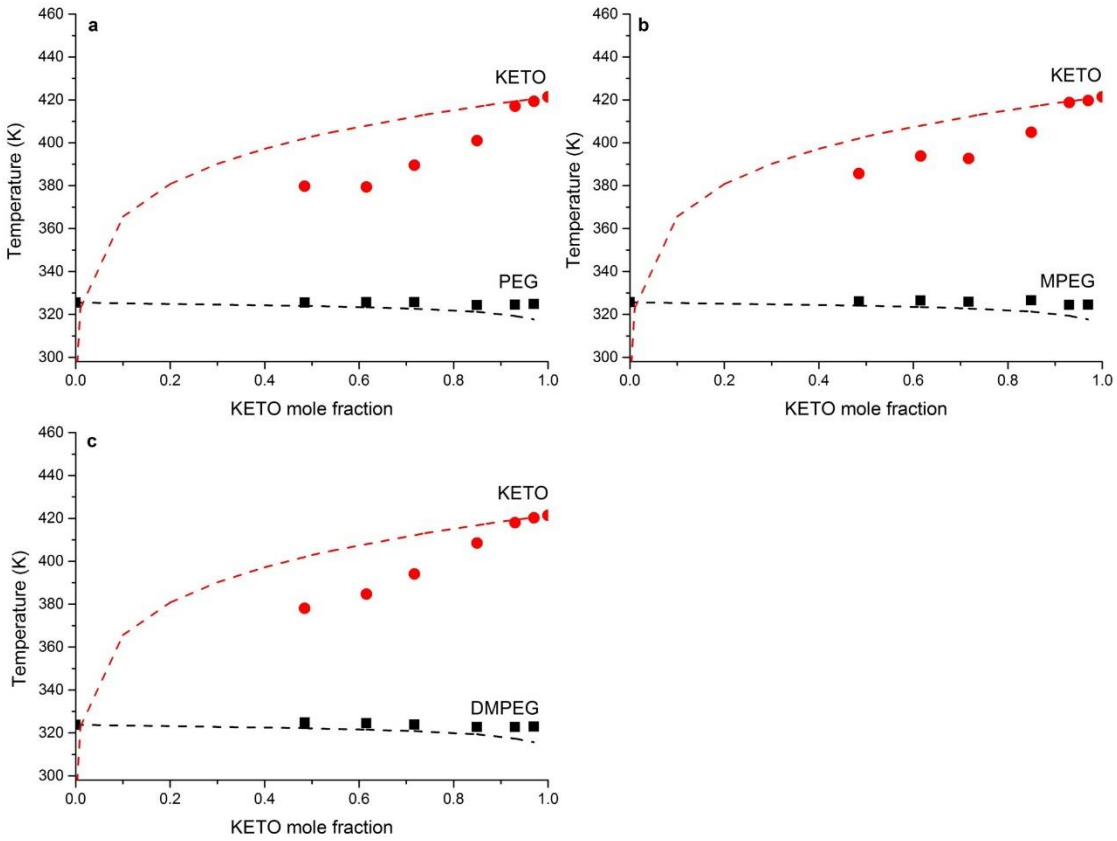

Fig. 4.12. Solid – liquid phase diagram for binary mixture of KETO and (a) PEG (b) MPEG (c) DMPEG. Solid symbols represent experimentally determined data points obtained using DSC analysis. Broken lines represent ideal curves predicted by the Schroder Van-Laar equation. Red circles represent KETO and black squares represent polymers. KETO/polymer samples were subjected to a single heating cycle.

Table 4.8. Predicted eutectic compositions and temperatures for KETO/polymer systems during first heating.

	Eutectic Composition (KETO mole fraction)	Eutectic Composition (KETO weight fraction)	Eutectic Temperature (K)
KETO/PEG	0.0153	0.0041	325.42
KETO/MPEG	0.0157	0.0042	325.60
KETO/DMPEG	0.0118	0.0032	323.74

The solid-liquid diagrams presented in Fig. 4.12 show that the experimental points deviate greatly from those predicted using the Schroder Van-Laar equation. According to the predictions, PEG would form a eutectic with KETO at 0.0041 KETO weight fraction, MPEG at

0.0042 and DMPEG at the lower KETO weight fraction of 0.0032. KETO has ability to form simple eutectic systems, this has been observed elsewhere in the literature with Karolewicz et al. (2014) reporting the formation of a simple eutectic system containing 0.044 (w/w) or 4.4% (w/w) KETO and 95.6% (w/w) Pluronic F127 at 52.0 °C (Karolewicz et al., 2014).

4.3.6.2 ITR/Polymer Eutectic Phase Formation

The presence of a suspected eutectic mixture following a single heating and cooling was detected with PXRD (Fig. A.3.3), for ITR – PEG binary system at a weight ratio of ITR/polymer 0.3:0.7. For completeness, the likelihood of eutectic formation was investigated for all ITR polymer binary systems. The ideal phase diagram was compared with the real phase diagram obtained from DSC curves for the first heating of binary systems and can be found in Fig. 4.13.

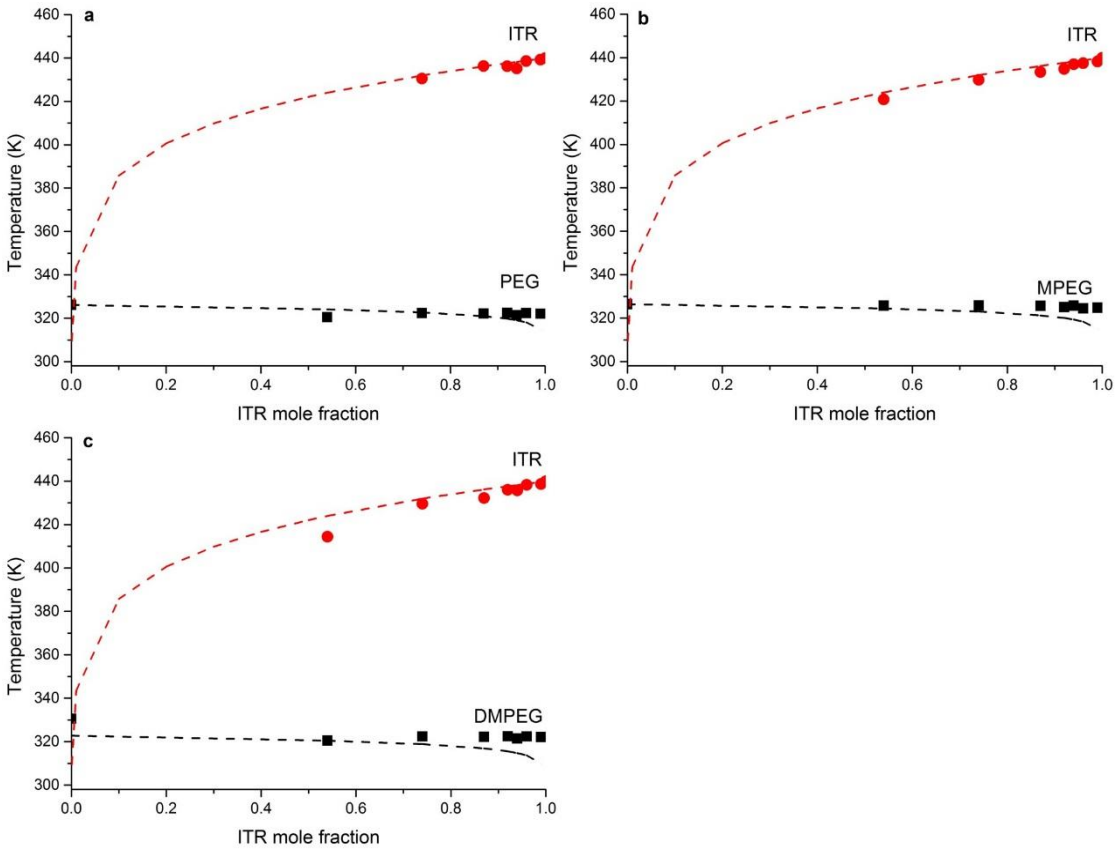

Fig. 4.13 Solid – liquid phase diagram for binary mixture of ITR and (a) PEG (b) MPEG (c) DMPEG. Solid symbols represent experimentally determined data points obtained using DSC analysis. Broken lines represent ideal curves predicted by the Schroder Van-Laar equation. Red circles represent ITR and black squares represent polymers during first heating.

Table 4.9. Predicted eutectic compositions and temperatures for ITR/polymer systems during first heating.

	Eutectic Composition (ITR mole fraction)	Eutectic Composition (ITR weight fraction)	Eutectic Temperature (K)
ITR/PEG	0.0033	0.0012	326.1
ITR/MPEG	0.0034	0.0012	326.5
ITR/DMPEG	0.0026	0.00092	322.7

The experimental and solidus-liquidus curves correlate well with each other, confirming ideality in all cases (Fig. 4.7). This is in contrast to the behaviour of KETO/polymer systems, whereby experimental points deviate greatly from the ideal behaviour (Fig. 4.3). Predicted eutectic compositions and temperatures can be found within Table 4.9. According to these

predictions, PEG would form a eutectic containing 0.0033 ITR mole fraction, MPEG at 0.0034 and DMPEG at 0.0026 (Table 4.9). However, the suspected experimental eutectic point was detected at 0.13 ITR mole fraction (0.3 ITR weight fraction) (Fig. A.3.3). Furthermore, with predicted eutectic compositions having such little polymer content it seems that crystalline eutectic formation between crystalline ITR and crystalline polymer is unlikely.

Baird and Taylor (2011) have previously attributed deviations from ideal behaviour to drug-polymer interactions. Drug solubility in molten polymer is dependent upon crystal lattice energy of the compound and strength of specific interactions between drug and polymer relative to the strength of interactions in the pure liquid phases. Compounds with weak crystal lattice energies and strong interactions with the polymer would have high eutectic composition and vice versa (Baird and Taylor, 2011). The authors attributed discrepancies between predicted and experimental eutectic points to strong drug-polymer interactions, providing an additional thermodynamic driving force for the mixing process.

4.4 CONCLUSIONS

Calculated HSPs suggest some degree of miscibility between all drugs and polymers. Phase diagrams were constructed for KETO/polymer and ITR/polymer systems. Eutectic compositions and temperatures were calculated for KETO and ITR/polymer systems. Based on those findings presented in Table 4.8 and 4.9, eutectic formation is unlikely for all KETO and ITR binary systems investigated. KETO systems deviated greatly from ideality, with ITR equivalents displaying good agreement between experimental and solid-liquidus curves. High ITR loading was necessary for the formation of LC ITR phases. The findings of this work have revealed key findings in relation to NP stabilization and drug-polymer interactions. DMPEG was proven to be the most effective stabilizer in terms of achieving colloidal stability for all API NPs, as shown in Chapter 2. Effective stabilization of KETO NPs may require some degree of miscibility for sufficient physio-sorption of polymer chains onto API surfaces. In the case of ITR, quantification of drug-polymer miscibility confirms immiscibility and low solubility between components. These are good predictors for effective NP stabilization, and readiness of adsorbed polymer layer formation. Accurate prediction of drug-polymer interaction may facilitate more efficient stabilizer selection for nano-dispersions.

References

Andrews, D.R., Leong, W., Sudhakar, A., 2004. United States Patent US006958337B2.

Baird, J.A., Taylor, L.S., 2011. Evaluation and modeling of the eutectic composition of various drug-polyethylene glycol solid dispersions. Pharm. Dev. Technol. 16, 201–211.

Baka, E., Comer, J.E.A., Takács-Novák, K., 2008. Study of equilibrium solubility measurement by saturation shake-flask method using hydrochlorothiazide as model compound. J. Pharm. Biomed. Anal. 46, 335–341.

Berg, J.C., 2010. An Introduction to Interfaces and Colloids: The Bridge to Nanoscience, Hackensack. ed. World Scientific.

Bodmeier, R., Paeratakal, O., 1989. Evaluation of drug-containing polymer films prepared from aqueous latexes. Pharm. Res. 723–730.

Boles, M.A., Ling, D., Hyeon, T., Talapin, D.V., 2016a. The surface science of nanocrystals. 15, 141–154.

Boles, M.A., Ling, D., Hyeon, T., Talapin, D.V., 2016b. Erratum: The surface science of nanocrystals. Nat. Publ. Gr. 15, 364.

Caron, V., Tajber, L., Corrigan, O.I., Healy, A.M., 2011. A comparison of spray drying and milling in the production of amorphous dispersions of sulfathiazole/polyvinylpyrrolidone and sulfadimidine/ polyvinylpyrrolidone. Mol. Pharm. 8, 532–542.

Choi, H.S., Liu, W., Misra, P., Tanaka, E., Zimmer, J.P., Itty Ipe, B., Bawendi, M.G., Frangioni, J. V, 2007. Renal clearance of quantum dots. Nat Biotech 25, 1165–1170.

Couture, L., van de Ven, T.G.M., 1991. Hydrodynamic layer thickness of poly(ethylene oxide) adsorbed on polystyrene latex. Colloids and Surfaces 54, 245–260.

Crawford, G. P., Žumer, S., 1996. Liquid Crystals in Complex Geometries; London ; Bristol, PA: Taylor & Francis.

David, D.J., Sincock, T.F., 1992. Estimation of miscibility of polymer blends using the solubility parameter concept. Polymer (Guildf). 33, 4505–4514.

Flory, P.J., 1953. Principles of Polymer Chemistry. Cornell University Press, Ithaca.

Ge, L., Guo, R., Zhang, X., 2009. PEG-induced lamellar-to-isotropic phase transition in the system of TX-100/n-C8H17OH/H2O. J. Phys. Chem. B. 113, 1993–2000.

Gramaglia, D., Conway, B.R., Kett, V.L., Malcolm, R.K., Batchelor, H.K., 2005. High speed DSC (hyper-DSC) as a tool to measure the solubility of a drug within a solid or semi-solid matrix. Int. J. Pharm. 301, 1–5.

Hansen, C., 2007. Hansen Solubility Parameters: A Users Handbook. CRC Press.

Hansen, C., 2000. Hansen Solubility Parameter: A User's Handbook. CRC Press.

Ishikawa, Y., Katoh, Y., Ohshima, H., 2005. Colloidal stability of aqueous polymeric dispersions: Effect of pH and salt concentration. Colloids Surf. B. Biointerfaces. 42, 53–58.

Karolewicz, B., Górniak, A., Owczarek, A., Żurawska-Płaksej, E., Piwowar, A., Pluta, J., 2014. Thermal, spectroscopic, and dissolution studies of ketoconazole–Pluronic F127 system. J. Therm. Anal. Calorim. 115, 2487–2493.

Kim, S., Hyun, K., Moon, J.Y., Clasen, C., Ahn, K.H., 2015. Depletion Stabilization in Nanoparticle–Polymer Suspensions: Multi-Length-Scale Analysis of Microstructure. Langmuir 31, 1892–1900.

Knopp, M.M., Gannon, N., Porsch, I., Rask, M.B., Olesen, N.E., Langguth, P., Holm, R., Rades, T., 2016. A Promising New Method to Estimate Drug-Polymer Solubility at Room Temperature. J. Pharm. Sci. 105, 2621–2624.

Knopp, M.M., Tajber, L., Tian, Y., Olesen, N.E., Jones, D.S., Kozyra, A., Löbmann, K., Paluch, K., Brennan, C.M., Holm, R., Healy, A.M., Andrews, G.P., Rades, T., 2015. Comparative Study of Different Methods for the Prediction of Drug-Polymer Solubility. Mol. Pharm. 12, 3408–3419.

Kozyra, A., Mugheirbi, N.A., Paluch, K.J., Garbacz, G., Tajber, L., 2018. Phase diagrams of polymer dispersedliquid crystal systems of itraconazole/component immiscibility induced by molecular anisotropy. Mol Pharm. 15, 5192-5206.

Law, D., Krill, S.L., Schmitt, E.A., Fort, J.J., Qiu, Y., Wang, W., Porter, W.R., 2001. Physicochemical considerations in the preparation of amorphous ritonavir and poly(ethylene glycol) 8000 solid dispersions. J. Pharm. Sci. 90, 1015–1025.

Law, D., Wang, W., Schmitt, E.A., Qiu, Y., Krill, S.L., Fort, J.J., 2002. Properties of rapidly dissolving eutectic mixtures of poly(ethylene glycol) and fenofibrate: The eutectic microstructure. J. Pharm. Sci. 92, 505–515.

Liu, Y., Shipton, M.K., Ryan, J., Kaufman, E.D., Franzen, S., Feldheim, D.L., 2007. Synthesis ,

Stability , and Cellular Internalization of Gold Nanoparticles Containing Mixed Peptide - Poly (ethylene glycol) Monolayers. 79, 2221–2229.

Mapesa, E. U., Tarnacka, M., Kamińska, E., Adrjanowicz, K., Dulski, M., Kossack, W., Tress, M., Kipnusu, W. K., Kamiński, K., Kremer, F., 2014. Molecular Dynamics of Itraconazole Confined in Thin Supported Layers. RSC. Adv. 4, 28432–28438.

Marsac, P.J., Li, T., Taylor, L.S., 2009. Estimation of Drug–Polymer Miscibility and Solubility in Amorphous Solid Dispersions Using Experimentally Determined Interaction Parameters. Pharm. Res. 26, 139-151.

Marsac, P.J., Shamblin, S.L., Taylor, L.S., 2006. Theoretical and practical approaches for prediction of drug-polymer miscibility and solubility. Pharm. Res. 23, 2417–2426.

Meltzer, V., Pincu, E., 2012. Thermodynamic study of binary mixture of citric acid and tartaric acid. Cent. Eur. J. Chem. 10, 1584–1589.

Mohan, R., Lorenz, H., Myerson, A.S., 2002. Solubility measurement using differential scanning calorimetry. Ind. Eng. Chem. Res. 41, 4854–4862.

Mugheirbi, N.A., Paluch, K.J., Tajber, L., 2014. Heat induced evaporative antisolvent nanoprecipitation (HIEAN) of itraconazole. Int. J. Pharm. 471, 400-411.Mugheirbi, N.A., Fleischer, K., Tajber, L., 2016. A Rare Case of Mesomorphic Behavior-Molecular Reorientation of Itraconazole Liquid Crystal Induced by a Hygrothermal Treatment. Cryst. Growth Des. 16, 1329–1336.

Qian, F., Huang, J., Hussain, M.A., 2010. Drug–Polymer Solubility and Miscibility: Stability Consideration and Practical Challenges in Amorphous Solid Dispersion Development. J. Pharm. Sci. 99, 2941–2947.

Rabanel, J.M., Hildgen, P., Banquy, X., 2014. Assessment of PEG on polymeric particles surface, a key step in drug carrier translation. J. Control. Release. 185, 71–87.

Rubinstein, M., Colby, R.M., 2006. Polymer Physics. Oxford University Press.

Scott, G., 1992. Properties of polymers. Their correlation with chemical structure; their numerical estimation and prediction from additive group contributions., in: Endeavour 16. pp. 97–98.

Six, K., Verreck, G., Peeters, J., Binnemans, K., Berghmans, H., Augustijns, P., Kinget, R., Van den Mooter, G., 2001. Investigation of Thermal Properties of Glassy Itraconazole:

Identification of a Monotropic Mesophase. Thermochim. Acta. 376, 175–181.

Soulé, E. R., Abukhdeir, N. M., Rey, A.D., 2009. Thermodynamics, Transition Dynamics, and Texturing in Polymer-Dispersed Liquid Crystals with Mesogens Exhibiting a Direct Isotropic/Smectic-A Transition. Macromolecules 42, 9486–9497.

Srivastava, J.K., Singh, R.K., Dhar, R., Singh, S., 2012. Phase Diagrams and Morphology of Polymer dispersed liquid crystals: An Analysis. Liq. Cryst. 39, 1402-1413.

Tarnacka, M., Adrjanowicz, K., Kaminska, E., Kaminski, K., Grzybowska, K., Kolodziejczyk, K., Wlodarczyk, P., Hawelek, L., Garbacz, G., Kocot, A., 2013. Molecular Dynamics of Itraconazole at Ambient and High Pressure. Phys. Chem. Chem. Phys. 15, 20742–20752.

Taylor, L.S., Zografi, G., 1997. Spectroscopic Characterization of Interactions Between PVP and Indomethacin in Amorphous Molecular Dispersions. Pharm. Res. 14, 1691–1698.

Theeuwes, F., Hussain, A., Higuchi, T., 1974. Quantitative analytical method for determination of drugs dispersed in polymers using differential scanning calorimetry. J. Pharm. Sci. 63, 427–429.

Van Krevelen, D.W., Te Nijenhuis, K., 2009. Chapter 7 – Cohesive Properties and Solubility, Properties of Polymers., in: Elsevier, Amsterdam, Fourth Edition. pp. 189–227.

Vippagunta, S.R., Wang, Z., Hornung, S., Krill, S.L., 2007. Factors Affecting the Formation of Eutectic Solid Dispersions and Their Dissolution Behavior. J. Pharm. Sci. 96, 294–304.

Voelkel, A., Batko, K., Adamska, K., Pozna, B.S., 2008. Determination of Hansen Solubility Parameters by Means of Gas – Solid Inverse Gas Chromatography. Adsorpt. Sci. Technol. 26, 93–102.

Wieser, J., Pichler, A., Hotter, A., Griesser, U., Langes, C., 2013. Patent Number US 8,563,555 B2.

Wieser, J., Pichler, A., Hotter, A., Griesser, U., Langes, C., 2012. Patent Number US 2012/0101277 A1.

Xie, X.L., Li, R.K.Y., Tjong, S.C., Tang, C.Y., 2002. Flory-huggins interaction parameters of LCP/thermoplastic blends measured by DSC analysis. J. Therm. Anal. Calorim. 70, 541–548.

Xing, X., Hua, L., Ngai, T., 2015. Depletion versus stabilization induced by polymers and nanoparticles: The state of the art. Curr. Opin. Colloid Interface Sci. 20, 54–59.

CHAPTER V: ISOLATION AND CHARACTERISATION OF ITRACONAZOLE NANOSTRUCTURED MICROPARTICLES (NMPS) VIA SPRAY DRYING WITH RATIONAL SELECTION OF OPTIMUM SUGAR BASE FOR TABLETTING

5.1. INTRODUCTION

New drug candidates generally have poor water solubility and/or dissolution rates. NPs benefit from high surface area to volume ratio and often increased solubility, resulting in enhanced bioavailability (Kalepu and Nekkanti, 2015). Aqueous nano-dispersions are however associated with problems such as aggregation and long term instability. To overcome these issues they can be isolated in the dry state (Chacón et al., 1999). A variety of drying techniques exist for the isolation of NPs from liquid to powder form including freeze drying, spray drying and spray-freeze drying (Malamatari et al., 2016).

Spray drying is a process whereby a liquid feed is atomised into a fine spray and dried using a hot gas resulting in evaporation of solvent (Masters, 1976). Spray drying is considered industrially preferable due to its favourable speed and cost. Product characteristics can be fine-tuned via careful manipulation of process parameters. Isolation of NPs by spray drying is usually based on co-processing with carrier/matrix materials and thus converting NPs into easily redispersible nanostructured microparticles (NMPs) (Tsapis et al., 2002). During secondary processing of these materials, additional stresses can destabilize the NPs (Chaubal and Popescu, 2008). Spray drying can induce crystal form change of the matrix material and/or NPs via input of energy (Teeranachaideekul et al., 2008). An understanding of the impact of critical process parameters upon product characteristics such as NP redispersibility is an essential part of the formulation process. In this work, careful consideration will be given to matrix former type and concentration used in the downstream processing of ITR NMPs. Whilst the crystalline state is considered the most stable and therefore less problematic in terms of downstream processing and storage stability, crystalline materials can also exist in different polymorphic forms, each having its own physical properties. This, in itself, can present issues during downstream processing of these materials. The amorphous state offers gains in terms of dissolution and enhanced bioavailability, conferred by lack of long range order and absence of crystal lattice (Healy et al., 2017). However, the metastable nature of amorphous solids can result in crystallisation during processing and storage, associated with changes in the physicochemical properties of the resulting material.

Whilst the literature is rich in information regarding spray drying of nano-dispersions, fewer reports exist regarding their processing into solid oral dosage forms. In this instance, nano-dispersions are first spray dried, followed by compaction of spray dried powders into tablets. Agglomeration of NPs is likely during the drying process in the absence of matrix formers (Hecq et al., 2006). The addition of these compounds can ensure adequate NP redispersion in water.

During consolidation of a powder bed, porosity of the material decreases. Compact volume is reduced, particles move closer to one another, interactions are created, particles stick together and a compact is formed (Adolfsson and Nyström, 1996). Wetting and disintegration of products should be good to maintain NP dissolution enhancement. Matrix formers are added to dispersions prior to the drying step. Water soluble sugars are typically utilised for this purpose (Kesisoglou et al., 2007). Commonly used sugars include mannitol, lactose, trehalose and raffinose (Amaro et al., 2015). Microparticles (MPs) formed during spray drying should rapidly redisperse when hydrated to release NPs with their original particle size. Thus, particle dissolution should occur in a short time frame to facilitate drug absorption *in vivo* (Chaubal and Popescu, 2008). Production of a dosage form with sufficient tensile strength, capable of rapid release of NPs presents a challenging task (Tan et al., 2017).

In this research, ITR nano-dispersions are first produced via a bottom up anti-solvent precipitation method as described in Chapters 2 and 3. Subsequently, sugars are added to these aqueous nano-dispersions prior to spray drying. NMPs are then compacted into solid oral dosage forms. A number of sugars were investigated and assessed in terms of their ability to adequately redisperse ITR NMPs. ITR was selected as a model drug. Being a BCS Class II compound, it exhibits poor aqueous solubility as well as a strong food effect (Van Eerdenbrugh et al., 2008b). Five different water soluble sugars and one sugar alcohol (collectively referred to later as sugars) exhibiting a variety of physical properties were explored for inclusion as potential matrix formers, aiding the redispersibility of solidified nano-dispersions. ITR NMPs were characterized in terms of their solid state and physical properties, particle morphology and redispersibility. A subset of these formulations were selected for further tabletting studies. Resulting tablets were examined using a number of standard or modified pharmacopeia tests. The impact of the presence of ITR NMPs upon the processability and tabletability of SD sugars was assessed. This work thus encompasses the complete pharmaceutical manufacturing process, starting with the making of NPs through to final solid dosage form design. During the initial stages of formulation development, often only limited amounts of material are available. Tests performed in this work are done so on a small scale making them beneficial in terms of cost and time during product development from an industrial perspective.

5.2. MATERIALS AND METHODS

5.2.1 MATERIALS

Itraconazole (ITR) was a gift from Welding GmbH (Hamburg, Germany). Trehalose dihydrate, D-mannitol, sucrose, raffinose pentahydrate, maltose monohydrate, lactose monohydrate were all obtained from Sigma Aldrich (Arklow, Ireland). Acetone Chromasolv® HPLC grade was obtained from Sigma Aldrich. MilliQ water was used in all instances.

5.2.2 METHODS

5.2.2.1 Nano-dispersion Preparation

In Chapters 2 and 3 details were provided regarding preparation of ITR nano-dispersions. Solutions of ITR dissolved in acetone (solvent phase) and water (anti-solvent phase) were maintained at 25 °C. Solvent phase was filtered using a 0.45 µm syringe polytetrafluoroethylene (PTFE) filter (VWR, Ireland) and anti-solvent phase was filtered using a hydrophilic PTFE 0.2 µm syringe filter (VWR, Ireland) prior to NP formation. ITR NPs were formed in a round bottom flask using a solvent phase (2 mg/ml ITR in acetone = 80% saturated solution), solvent phase was rapidly injected via a Sterican 12 mm needle into an anti-solvent phase, using a 1:10 solvent to anti-solvent (v/v) ratio (2 ml solvent phase added to 20 ml anti-solvent phase). The dispersion was subsequently transferred to a rotary evaporator and subjected to 60 mbar pressure, 160 rpm at 30 °C for 30 minutes in order to evaporate acetone. These conditions were found to be optimal for solvent evaporation and NP stability based on research carried out by R.Cruz (not yet published). R.Cruz utilised identical conditions for ITR NP formation.

5.2.2.2 Spray drying

ITR nano-dispersions were prepared as described in Section 5.2.2.1. Solid sugar was added to the liquid medium (20 ml) to achieve the desired sugar (taking an anhydrous equivalent) concentration: 1, 3 or 5% (w/v) and this was used as the liquid feed for NMP production using a Buchi B-290 mini spray dryer (Flawil, Switzerland) with a 1.5 mm cap and 0.7 mm tip. The pump speed was 30% (9-10 ml/min). The aspirator was set to 100%. A mixture of nitrogen (with a pressure of 6 bar) and air was used as a drying gas. Inlet temperature was set to 160 °C. The ITR:sugar ratios in the dry products were as follows: 1:50 (w/w) for 1% (w/v) sugar feed, 1:150 (w/w) for 3% (w/v) sugar feed and 1:250 (w/w) for 5% (w/v) sugar feed. Sugar solutions (5% w/v) without NPs, made in deionised water, were also spray dried for comparison purposes.

5.2.2.3 Microparticle Characterisation

5.2.2.3.1 Powder X-ray Diffraction (PXRD)

PXRD was carried out at room temperature using a Rigaku Miniflex II, desktop X-ray diffractometer (Tokyo, Japan) equipped with a Cu Kαradiation X-ray source and a Haskris cooler (Illinois, USA). The samples were mounted on a low background silicon sample holder and scanned over a 2θ range 2-40° with a step width of 0.05, scan rate 0.05° per second and signal collection time of 1 s per step. The output voltage and current of the tube (Cu, 1 kW normal focus) were 30 kV and 15 mA, respectively. PXRD diffraction patterns for alpha, beta and delta mannitol were obtained using Cambridge Crystallographic Data Centre (CCDC) reference codes; DMANTL 08, DMANTL 09 and DMANTL 10 (Yang et al., 2011).

5.2.2.3.2 Differential Scanning Calorimetry (DSC)

DSC was performed using a Mettler Toledo DSC (Schwerzenbach, Switzerland). The purge gas was nitrogen. Approximately 5-10 mg samples were analysed in sealed 40 µl aluminium pans with pierced lids. Samples were heated from 25 to 250 °C at a rate of 10 °C/min. Thermograms were analysed using Mettler Toledo STARe software (version 6.10).

5.2.2.3.3 Thermal Gravimetric Analysis (TGA)

TGA was carried using a Mettler TG50 measuring module coupled to a Mettler Toledo MT5 balance (Schwerzenbach, Switzerland). Approximately 2-5 mg samples were analysed in an open aluminium pans, using nitrogen as the purge gas. Samples were heated from 25 to 100 °C at a rate of 10 °C/min. Mettler Toledo STARe software (version 6.10) was used to analyse thermograms obtained.

5.2.2.3.4 Dynamic Vapour Sorption (DVS)

Powdered samples were analysed with a Dynamic Vapour Sorption (DVS) Advantage-1 automated gravimetric vapour sorption analyser (Surface Measurement Systems Ltd., London, UK). The temperature was maintained constant at 25.0 ± 0.1 °C. In all measurements, 30 mg of powder was loaded into a sample net basket and placed in the system. All samples were equilibrated at 0% of RH until constant mass (dm/dt ≤ 0.002 mg/min). The reference mass was recorded as a mass equilibrated at 0% RH. Sorption-desorption analysis was then carried between 0% and 90% RH, in steps of 10% RH. At each stage, the sample mass was equilibrated (dm/dt ≤ 0.002 mg/min for at least 10 minutes) before moving to the next RH level. Two sequential cycles of sorption and desorption were performed. An isotherm was calculated from the complete sorption and desorption profile. PXRD was performed on all samples following DVS analysis to detect possible crystallisation.

5.2.2.3.5 Dynamic Light Scattering (DLS)

Particle size measurements were performed at two stages for nano-dispersions: following removal from the rotary evaporator, and also after redispersion of ITR NMPs in deionised water followed by gentle shaking. Measurements were obtained using a Zetasizer Nano ZS (Malvern Instruments, UK). Measurement position and attenuator factor were automatically optimised by the software. All measurements were carried out at 25 °C in a folded zeta cell (DTS1061). The analysis was performed in triplicate for each sample. Viscosity of the continuous phase was measured using a Vibro Viscometer SV-10 (A&D, Japan) at 25 °C and particle size values corrected for the actual viscosity of the dispersion medium. Redispersibility index was used as an assessment tool to evaluate the redispersibility of NMPs and calculated as follows:

$$Redispersibility\ Index\ = \frac{particle\ size\ (nm)\ before\ redispersion}{particle\ size\ (nm)\ after\ redispersion} \times 100$$

5.2.2.3.6 Nanoparticle Tracking Analysis (NTA)

Particle size characterisation of ITR NMPs was performed with a NanoSight NS300 and analysed using NTA 3.2 software as per Chapter 3. A defined mass of NMPs was redispersed in 1 ml of deionised water producing a dispersion containing the original concentration of sugar (as in the spray drying feed) or 1% (w/v) sugar. Samples were injected into the sample chamber using sterile syringes. All measurements were performed at 25 °C. Software was programmed to capture five 30 second videos, with the sample being advanced in between each video. Samples were measured using manual shutter and gains adjustments.

5.2.2.3.7 Scanning electron microscopy (SEM)

SEM was performed using a Zeiss Ultra Scanning electron microscope (Germany) equipped with a secondary electron detector. Samples were sputter coated with 40 nm gold palladium for 90 seconds under vacuum prior to analysis and analysed using a 6 kV accelerating voltage. Analysis of dry NMPs was performed in addition to redispersed ITR NPs. NPs were redispersed by addition of a defined mass of NMP powder to deionised water, followed by gentle, manual shaking. Sample aliquots were mounted directly onto aluminium stubs. Sample surface was washed using deionised water and left to dry under nitrogen purge overnight. Dry NMP powders were glued onto carbon tabs and mounted onto aluminium stubs prior to coating.

5.2.2.4 Tabletting

Flat faced tablets (200 mg) were compressed using a Natoli NP-RD10 (Saint Charles, MO, USA) laboratory scale single punch tablet press supplied with an Enerpac (Menomonee Falls, WI, USA) P-392 manual pump with a RC-104 hydraulic cylinder and standard 8 mm diameter punch

and die tooling (I Holland, Limited, UK). Every 200 mg tablet contained 1% (w/w) or 2 mg of ITR NPs. Compaction properties of tablets were assessed using a number of different compaction pressures in the range 49 to 249 MPa. Pressure was released 60 seconds after the desired compaction pressure was achieved.

5.2.2.4.1 Tablet characterisation

5.2.2.4.1.1 Tablet hardness, tensile strength, solid fraction, density

Weight (Wt in g) of freshly produced tablets was recorded immediately after compaction. Tablet thickness (t in cm) and diameter (D in cm) were measured by an electronic calliper. Crushing strength (F) is a measure of the load at which a tablet breaks, whereas tensile strength (σ) is a measurement of the resistance to fracture. Hardness (N) of the tablets were measured using a portable tablet hardness tester (Electrolab India PVT. LTD.). Each hardness value reported is an average of five measurements. Tensile strength (σ) of the 8 mm round flat faced tablet was calculated based on breaking force values using Eq. 5.1:

$$\sigma = \frac{2F}{\pi\, d\, h} \qquad \text{(Eq. 5.1)}$$

Where *d* is tablet diameter, and *h* is tablet thickness. Compaction pressure was then calculated based on applied force and cross-sectional area of the punch. Solid fraction (SF) and porosity (ε) were calculated based on true density (ρ_{true}) of SD powders which were measured using a gas pycnometer AccuPyc II 1340 (Micrometrics, Georgia, USA). SF was calculated according to true density (ρ_{true}), tablet volume (v) and weight (Wt) as per Eq. 5.2:

$$SF = \frac{Wt}{P_{true}.v} \qquad \text{(Eq. 5.2)}$$

Porosity (ε) was calculated based on SF as per Eq. 5.3:

$$\varepsilon = 1 - SF \qquad \text{(Eq. 5.3)}$$

5.2.2.4.1.2 Tablet Disintegration

Disintegration of tablets was studied using the disintegration tester, Dist 300 (PharmaTest, Hainburg, Germany) as per the United States Pharmacopeia (USP) compendial test (701) Disintegration (USP 39 NF 34, 2016). 900 ml of deionised water at 37 °C was used as the media and disintegration time was recorded. All samples were measured in triplicate.

5.2.2.4.1.3 Solubility of ITR NMPs compacted tablets in 0.1M hydrochloric acid

In addition, disintegration of tablets made of ITR NMP was performed in 500 ml 0.1M hydrochloric acid (HCl), with the intent of replicating gastric conditions in the body, using the disintegration tester, Dist 300 apparatus, at 37 °C. Sample aliquots (2 ml) were taken at specific

time points over a 30 minute time period. Each sample was filtered through a 0.1 µm PTFE membrane filter (Sartorius Stedim, Germany). The concentration of ITR in each sample was then measured using a Shimadzu Pharmspec UV-1700 UV-vis spectrophotometer (Japan) at 262 nm without dilution using low volume 10 mm quartz cuvettes. Analysis was performed in triplicate and an average concentration plotted against time.

5.2.2.4.1.4 SEM, PXRD, NTA of Compacted SD powder

Subsequent to hardness testing, broken cross sections of tablets were monitored for changes using SEM as described in Section 5.2.2.3.7, with samples being glued onto carbon tabs and mounted onto aluminium stubs prior to coating. Following compaction under pressure material was analysed using PXRD, as described in Section 5.2.2.3.1. A defined mass of material consisting of ITR NMPs was redispersed in deionised water following compaction into tablets. This liquid medium which contained redispersed ITR NPs was analysed using NTA as per Section 5.2.2.3.6.

5.2.2.5 Statistical Analysis

Statistical analysis was performed using Minitab 16 software. Data was analysed using two-sample student *t* tests or a one-way analysis of variance (ANOVA) with Tukey's multiple comparison test. A p value of ≤ 0.05 was considered significant.

5.3. Results and Discussion

5.3.1 Spray drying of NMPs

In the liquid state, NPs have physical and chemical stability issues (Wang et al., 2013). Transformation of nano-dispersions into solids can overcome these issues. Spray drying offers a viable approach for the production of intermediate powders which can undergo further processing steps, resulting in the production of optimal dosage forms for patient use. The addition of matrix formers prior to drying prevents particle aggregation, whilst enhancing redispersibility of NPs upon hydration (Van Eerdenbrugh et al., 2008a)**.** Tables A.4.1 and A.4.2 contain information regarding the physical properties of sugars studied in this work.

As all ITR NMPs spray dried with sugars were subjected to identical processing conditions within the spray dryer, any differences observed on the micro and nano-scale can be attributed to the presence of the sugar itself. Fig. 5.1 confirms the presence of a mannitol polymorphic mixture obtained upon spray drying, consisting of beta and alpha polymorphs.

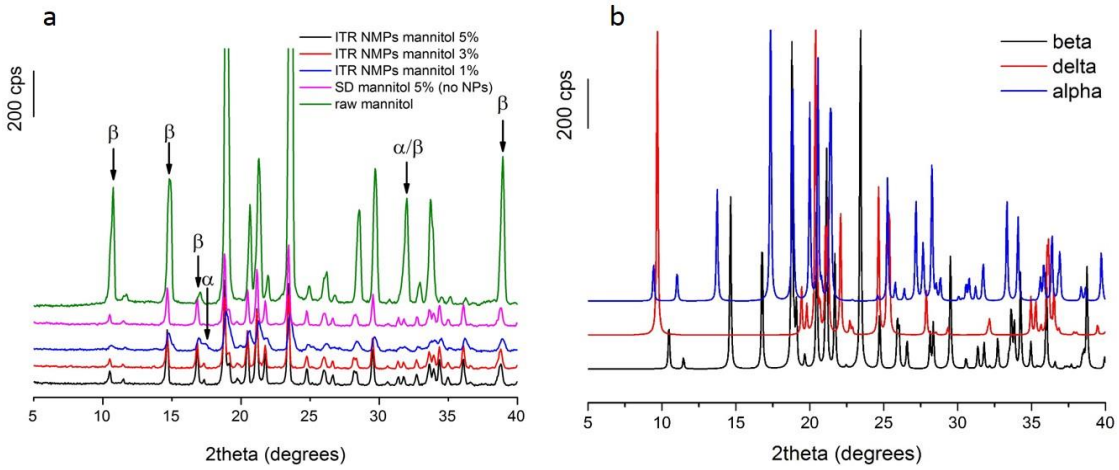

Fig. 5.1. PXRD diffraction patterns of (a) mannitol starting material powder (raw mannitol), mannitol spray dried on its own from 5% (w/v) feed and ITR NMPs with mannitol (spray dried from 1, 3 or 5% (w/v) feed), (b) mannitol polymorphs – alpha, beta and delta.

The simultaneous presence of different mannitol polymorphs produced upon spray drying is well documented (Hulse et al., 2009). Considering the Ostwald step rule, the least stable polymorph initially forms during crystallisation followed by a transition to the most stable form. However, if equilibrium is not reached, loss of mobility can occur faster than transition to the more stable form, with the outcome resulting in an end product consisting of a mixture of non-equilibrium states (Vehring, 2008). All other sugars investigated were amorphous upon spray drying, as verified by PXRD and DSC analysis (Fig. A.4.1 to A.4.4). Glass transition (T_g) temperatures for all amorphous SD powders were consistent with literature values provided in Table 5.1, being below 115 °C. This was followed by an exothermic event indicative of crystallisation, and finally a melting endotherm. The amorphous form is not at thermodynamic equilibrium, meaning these materials have a strong tendency to revert back to their stable crystalline state (Liu et al., 2007). TGA analysis of all SD sugars processed from 5% (w/v) solutions confirmed the weight loss (corresponding to moisture loss) to be between 4.7 and 7.1%, despite the use of a high inlet temperature (160 °C) in this case.

Fig. 5.2 presents findings from the morphological examination of SD samples.

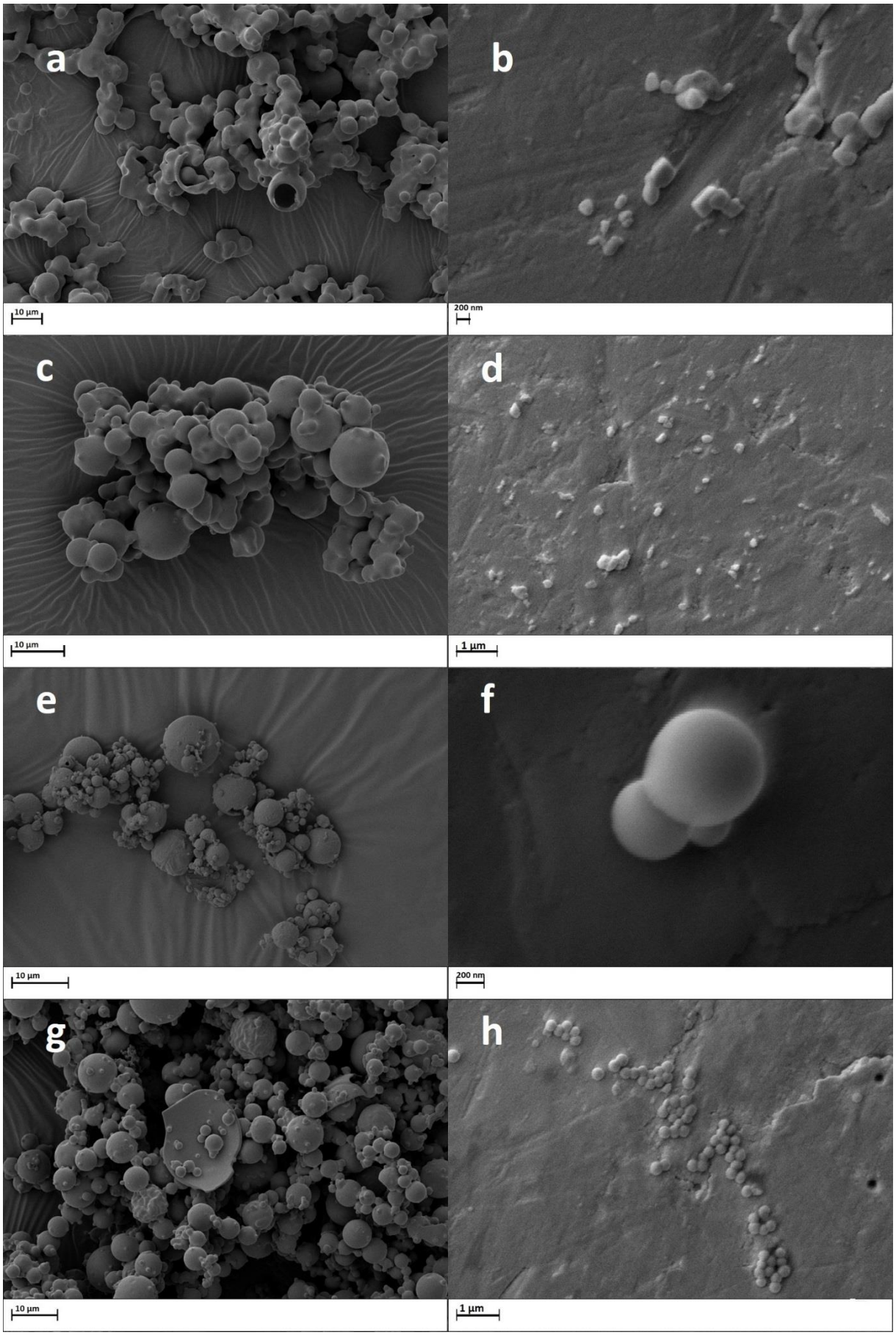
a
10 µm
b
200 nm
c
10 µm
d
1 µm
e
10 µm
f
200 nm
g
10 µm
h
1 µm

Fig. 5.2. SEM images of ITR NMPs spray dried with lactose from 5% (w/v) feed (a) dry powder (b) redispersed in deionised water; ITR NMPs spray dried with trehalose from 5% (w/v) feed (c) dry powder (d) redispersed in deionised water; ITR NMPs spray dried with mannitol from 5% (w/v) feed (e) dry powder (f) redispersed in deionised water; ITR NMPs spray dried with raffinose from 5% (w/v) feed (g) dry powder (h) redispersed in deionised water.

Morphological examination of SD powders revealed spherical morphology generally, with lactose and trehalose NMPs having a more fused appearance, (Fig. 5.2a and c) compared with mannitol and raffinose equivalents, which are more discrete in nature (Fig. 5.2e and g, Fig. A.4.6). Notably, this morphology does not appear to affect NP redispersibility (Fig. 5.3 and Table 5.3).

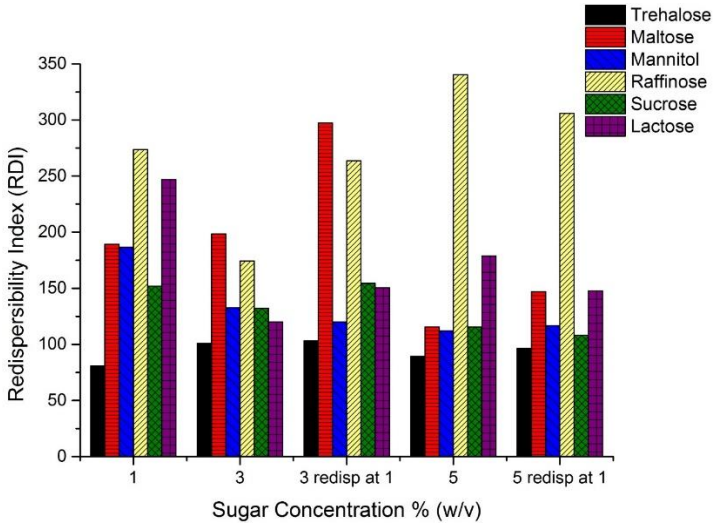

Fig. 5.3. Redispersibility index (RDI) of ITR NMPs redispersed at original sugar concentration (1, 3 or 5% w/v)) and at 1%. Redisp = redispersed

Table 5.3. NTA redispersibility measurements for ITR NMPs processed from 5% (w/v) sugar feed redispersed at 1%.

Sugar	Average particle size upon redispersion after spray drying ± SD (nm)	D10 (nm)	D50 (nm)	D90 (nm)
Lactose	145 ± 53	79	124	196
Trehalose	135 ± 41	66	126	174
Sucrose	127 ± 59	51	111	195
Mannitol	139 ± 77	33	116	242
Raffinose	236 ± 74	148	215	320
Maltose	181 ± 56	112	166	230

*SD = standard deviation

Surface pores and hollow particles were evident particularly for lactose (Fig. 5.2a), mannitol (Fig. 5.2e) and raffinose (Fig. A.4.6) NMPs. The inlet temperature 160 °C employed in this work would be considered in the high range of temperatures normally utilised for the spray drying of nano-dispersions, with literature reporting 80 to 150 °C as being typical (Chaubal and Popescu, 2008; Nekkanti et al., 2009; Pilcer et al., 2009; Mou et al., 2011). Hollow particles therefore seem likely to be present in all samples, as these are determined by evaporation rate, which is a function of inlet temperature in the spray dryer. Fig. 5.2g and Fig. A.4.6 confirm that ITR NPs are embedded within hollow sugar MPs. SEM images of redispersed NPs confirm their nano-size range (Fig. 5.2). Lactose and trehalose redispersed NPs (Fig. 5.2b and d) show an irregular appearance with a smooth surface texture compared with mannitol and trehalose which are uniform (Fig. 5.f and h). This uniformity appears to coincide with favourable redispersibility (Fig. 5.3 and Table 5.3).

With respect to redispersibility, assessed via DLS and NTA (Fig. 5.3 and Table 5.3), trehalose, sucrose and mannitol displayed the best redispersibility according to RDI values calculated via DLS in Fig. 5.3. These correspond with the smallest NTA particle size values, ranging from 127 – 139 nm, again making them potential options warranting further exploration. In terms of ranking redispersibility by DLS and NTA, good agreement was demonstrated between the techniques with raffinose displaying the largest particle size upon redispersion with both techniques (Fig. 5.3 and Table 5.3). DLS is an intensity based technique, where larger particles have the potential to skew the particle size distribution towards larger sizes. NTA is a number based technique, where all particles are given equal weighting within the distribution regardless of their size. Also, DLS sizes accurately in the range of 1 nm to 10 micron, whereas NTA sizes between 30 nm and 1 micron (Calzolai et al., 2011). With this in mind, large undispersed aggregates present in samples would generate larger average particle sizes for DLS compared with NTA. These micron sized aggregates may not be seen with NTA. It seems likely that the poor redispersibility of ITR NPs, imparted by the presence of raffinose as a matrix former (Fig. 5.3 and Table 5.3) may be ascribed to its lower aqueous solubility, in comparison to other investigated sugars, as denoted in Table 5.2. This may result in a slower dissolution rate, and therefore release of ITR NPs into the surrounding aqueous medium.

Upon spray drying into ITR NMPs, sucrose immediately presented processability issues, namely extremely poor flowability, and a “stickiness” making it impossible to work with. For this reason, it was discarded from all further investigations. Trehalose ITR NMP samples were placed inside a dessicator and stored at 4 °C for four days. Subsequently, this sample was assessed using PXRD, for evidence of crystallisation. Fig. A.4.5 confirms no crystallisation

occurred during that time. Despite mannitol exhibiting polymorphism as shown in Fig. 5.1a and b, its confirmed crystallinity upon spray drying set it aside as a suitable candidate for further exploration. Moving forward, all efforts were focused on mannitol and trehalose as potential matrix formers for enhancing the redispersibility of ITR NPs upon rehydration.

As trehalose and mannitol showed the most promise for use as ITR NP matrix formers, physical stability of the sugars, processed with and without NPs, were investigated by DVS. Fig. 5.4 presents isotherms for DVS analysis. PXRD analysis of all samples post DVS testing is shown in Fig. A.4.7.

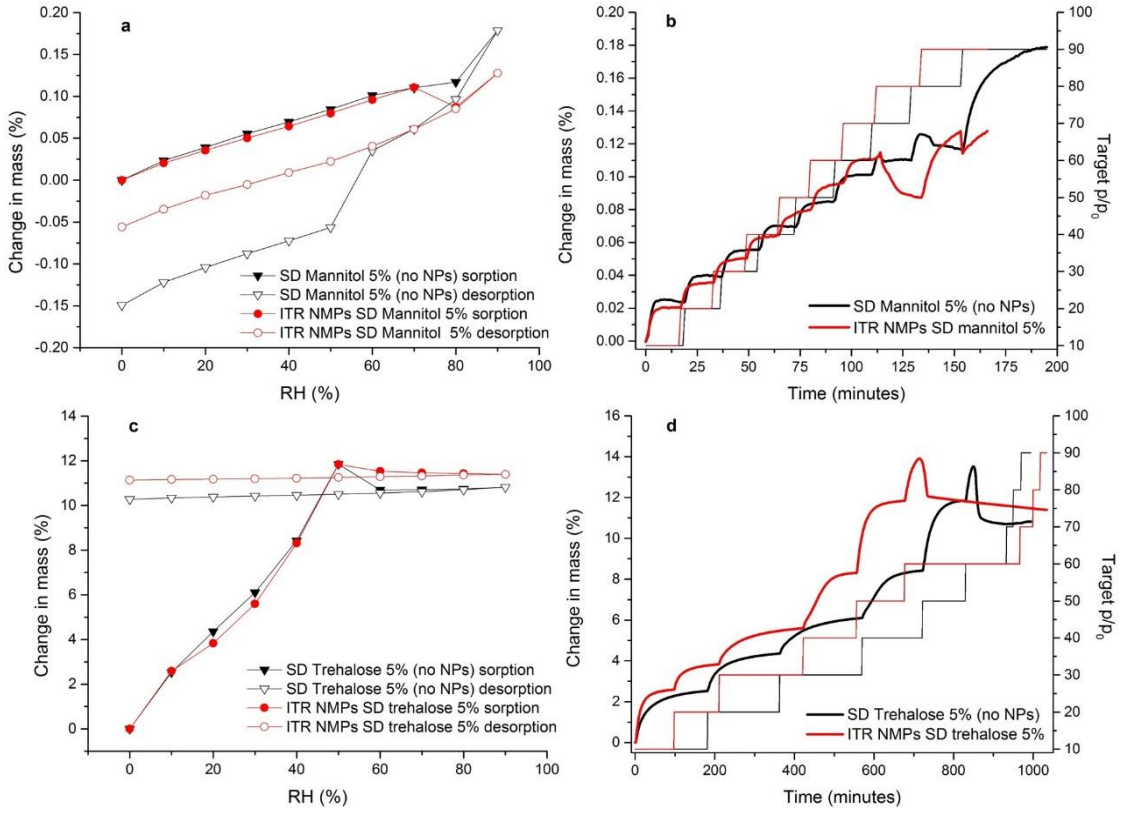

Fig. 5.4. Cycle 1 DVS (a) sorption-desorption isotherm and (b) kinetic profile for SD mannitol samples (10-90% RH only); and (c) sorption-desorption isotherm and (d) kinetic profile for SD trehalose samples (10-90% RH only).

Cycle 1 of sorption/desorption showed a moisture uptake of 0.18% for SD mannitol only and 0.13% for ITR NMPs with mannitol up to 90% RH (Fig. 5.4a). It seems likely that the hydrophobic nature of ITR may have been the limiting factor determining this. Between 70 to 90% RH, a decrease in mass followed by an increase was observed in both mannitol samples. The kinetic profile presented in Fig. 5.4b, confirms this event at 80% RH, markedly so for ITR nanostructured MPs. It is likely that these events are caused by the moisture-induced reorganisation of small crystallites present within the sample. Furthermore, simultaneous crystallisation of a small number of amorphous regions present within these samples, introduced as a result of the spray drying process is likely. As gravimetric sorption techniques are capable of quantifying amorphous content below 1% (Saleki-Gerhardt et al., 1994), PXRD is not capable of detecting these low levels of disorder (Fig. A.4.7a to f). The decrease in mass occurs earlier for the NMP powder in comparison to the SD powder with no NPs, suggesting that moisture can penetrate the sample more easily, maybe due to extra voids created by the presence of NPs. DVS did not appear to induce any polymorphic changes in mannitol samples (Fig. A.4.7c to f).

Cycle 1 of sorption/desorption shows a remarkable moisture uptake of amorphous SD trehalose powders up to 50% RH (Fig. 5.4c). Trehalose SD alone showed a mass increase of 11.85% at 50% RH, with ITR NMPs exhibiting a similar trend with a comparable mass of 11.84% at 50% RH (Fig. 5.4c). Subsequently, this is followed by a decrease in mass resulting from expulsion of water caused by crystallisation of amorphous regions in the samples (Buckton and Darcy, 1995). This RH threshold is unaffected by the presence of ITR NPs (Fig. 5.4c). The crystalline state of all trehalose samples was confirmed by PXRD analysis after DVS testing (Fig. A.4.7g to l). Cycle 2 of sorption/desorption for trehalose SD powders shows little moisture uptake suggesting all of the amorphous content of the samples crystallised during cycle 1 (Fig. A.4.9b). Excess water retained within the crystal lattice of both trehalose samples is responsible for the desorption isotherm not returning to its original value (Fig. A.4.9b). This sugar has the propensity to crystallise to its dihydrate form, supported by a 10-11% weight gain seen in Fig. 5.4c. Similar to the mannitol SD samples, solid state changes in trehalose-based ITR NMPs occurred quicker than in SD trehalose processed without NPs, although trehalose NMPs took much longer to achieve a stable mass at 60% RH compared with SD trehalose.

5.3.2 TABLETTING STUDIES

Upon consideration of the different sugar concentrations employed in initial studies, 5% (w/v) was selected for tabletting studies. A favourable yield was the basis for this decision. Achieving an optimum yield should not be overlooked as a desirable process output from an industrial perspective (Cue and Zhang, 2009). In light of the above findings, tabletting studies were confined to ITR NMPs based on mannitol and trehalose. Due to a limited availability of material, a range of compaction pressures were screened using the SD powders without NPs and the optimum selected for ongoing tabletting studies including ITR NMPs.

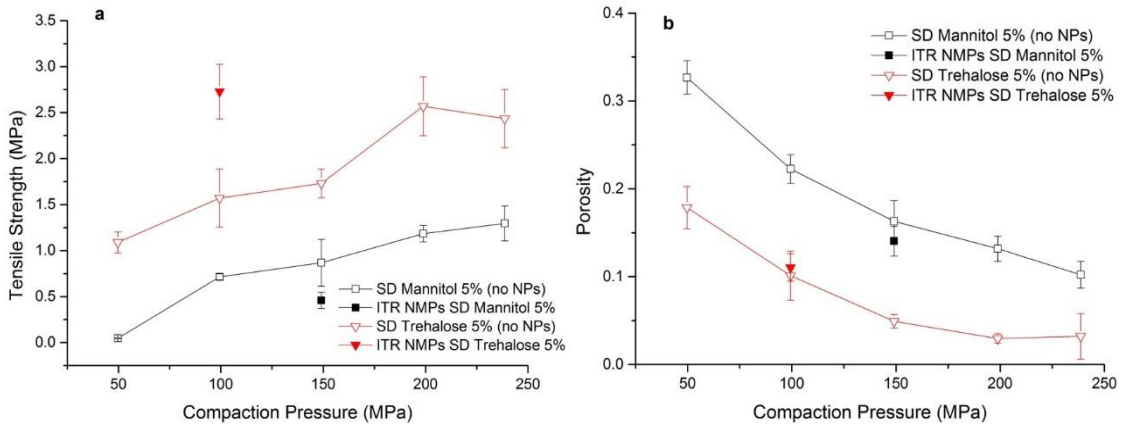

Fig. 5.5. (a) Tabletability profile for mannitol tablets and trehalose tablets, and (b) compressibility profile for mannitol tablets and trehalose tablets compacted between 50 and 250 MPa. Analysis was performed in triplicate.

A continuous increase in tensile strength is achieved up to a specific limit for both mannitol and trehalose tablets (studies on SD powders with no NPs, Fig. 5.5a), beyond which any increase in compaction pressure did not result in any further improvement in tensile strength (Adolfsson and Nyström, 1996). Therefore, we can conclude that the relationship between tablet hardness and compression force is non-linear over a broad range. For trehalose tablets this compaction pressure threshold (200 MPa) resulted in close to zero porosity and was accompanied by a plateau in tensile strength (2.5 MPa) (Fig. 5.5a and b). This threshold was reached at 239 MPa for mannitol tablets (Fig. 5.5b). It is apparent that, compaction profiles require careful inspection to avoid selecting a compaction pressure which imparts no further improvement upon tablet tensile strength but only a declining dissolution rate (Garr and Rubinstein, 1991).

Good compactibility describes a material capable of achieving desired tablet hardness at low compaction pressure (Pitt et al., 1989). With this in mind, careful selection of optimum compaction pressures to be employed for ITR NMP tabletting studies was imperative. When trehalose SD on its own, was compacted at 99 MPa, a tensile strength of 1.5 MPa was achieved (Fig. 5.5a). Furthermore, it was necessary to compact SD mannitol at 149 MPa to achieve a tablet with a tensile strength of 0.9 MPa (Fig. 5.5a). Statistical analysis using a one way ANOVA, confirmed the significantly greater tensile strength of trehalose over mannitol tablets ($p = 0.0005$). This increased tensile strength of trehalose tablets was accompanied by low porosity, ranging from 0.025 to 0.175, compared with mannitol 0.1 to 0.32 when compacted at the same pressure (Fig. 5.5b). Increase in compaction pressure for trehalose tablets above 200 MPa produced no further volume reduction, attributed to limited space available for fragmentation

and plastic deformation (Adolfsson and Nyström, 1996). True density values used to calculate porosity can be found within Table. A.4.3. It is also important to bear in mind, that any unnecessary increase in compaction pressure can induce physical changes upon the compacted materials. For amorphous trehalose, application of surplus energy during compaction could cause crystallisation, resulting in altered physicochemical material properties. Likewise for mannitol, the polymorphic mixture present within the sample may be susceptible to transformation to the most stable polymorphic form with a different set of physical properties.

The density of SD uncompressed powders can be found within Table. A.4.1. The presence of ITR NPs significantly increased the tensile strength of trehalose tablets when compacted at 99 MPa, according to a two-sample t-test ($p = 0.001$) (Fig. 5.5a). In contrast, the presence of ITR NPs significantly decreased the tensile strength of mannitol tablets when compacted at 149 MPa, according to a two-sample t-test ($p = 0.014$) (Fig. 5.5a). It seems likely, that the presence of ITR NPs in the MPs contributed to an increase in inter-particle voids, as also conjectured from DVS study, therefore reducing density. Notably, despite identical density and porosity values for ITR NMPs with both mannitol and trehalose, trehalose tablets exhibited much greater tensile strength (Fig. 5.5). Therefore, we can conclude that this increase in tensile strength is likely due to the difference in the solid state form of the SD powders, and not density. Compaction did not induce any changes in the physical form of mannitol (Fig. 5.7a). Trehalose showed itself to be resistant to physical change upon compaction (Fig. 5.7b).

The shape of the compressibility profiles can be valuable. The mannitol tablets made of SD powder containing no NPs, showed a linear decline in porosity suggesting a plateau had not yet been reached within this pressure range. A further decrease in porosity could have been achieved with greater compaction pressure above 239 MPa (Fig. 5.5). The trehalose profile (for compacts produced using SD powder containing no NPs) displays a different shape whereby, a plateau in porosity is reached at 200 MPa, this would suggest no further decrease in porosity would have been achieved beyond this compaction pressure range (Fig. 5.5b). The presence of ITR NPs within mannitol and trehalose SD samples (NMPs versus SD powders with no NPs) had no impact upon the porosity of the materials. There was no statistically significant difference in the porosity of the two NMP samples ($p = 0.052$).

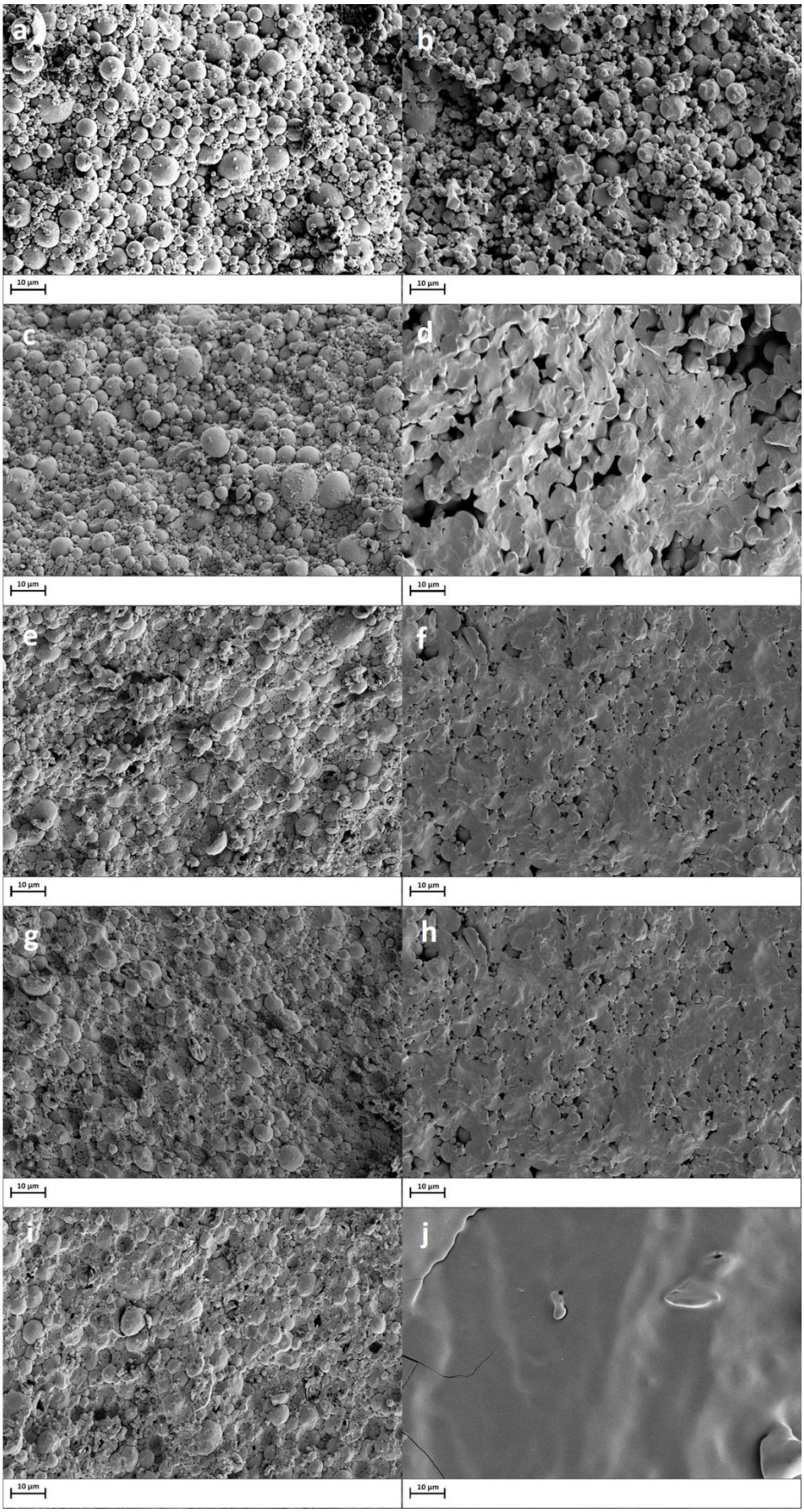
a
10 µm
b
10 µm
c
10 µm
d
10 µm
e
10 µm
f
10 µm
g
10 µm
h
10 µm
i
10 µm
j
10 µm

Fig. 5.6. Scanning electron micrograph images of sugars spray dried on their own (from a 5% (w/v) feed) and compacted (a) mannitol compacted at 50 MPa (b) trehalose compacted at 50 MPa (c) mannitol compacted at 99 MPa (d) trehalose compacted at 99 MPa (e) mannitol compacted at 149 MPa (f) trehalose compacted at 149 MPa (g) mannitol compacted at 199 MPa (h) trehalose compacted at 199 MPa (i) mannitol compacted at 239 MPa (j) trehalose compacted at 239 MPa. Images represent broken cross sections of tablets.

SEM images shown in Fig. 5.6, combined with tabletability and compressibility profiles in Fig. 5.5, indicate adequate porosity without compromising tensile strength for compacts formed at the above mentioned pressures (Fig. 5.6d and e). Hence, ITR NMPs with mannitol were compacted at 149 MPa, and ITR NMPs with trehalose at 99 MPa, into single oral dosage forms (as shown in Fig. 5.5a). In addition, it is thought that particle morphology can explain differences in the compactibility of materials. Fig. 5.6 contains SEM images depicting the surface cross sections of broken tablets comprised of SD sugars alone after hardness testing. The left panels relate to mannitol 5% (w/v) SD powders and the right panels relate to trehalose 5% (w/v) SD powders, both compacted within the pressure range 49-239 MPa. Fig. 5.6 confirms mannitol particles are more regular and spherical compared with the irregular appearance of trehalose. These properties allow for greater particle rearrangement, favouring interparticulate bond formation, resulting in compacts of greater tensile strength (Fig. 5.5a). These compacts have superior mechanical strength enabling them to withstand packaging and transportation conditions, whilst safeguarding the delivery of the ITR at an enhanced dissolution rate.

Fig. 5.5b confirms trehalose tablets (made of ITR NMPs) possess lower porosity, corresponding with greater tensile strength, when compared with mannitol equivalents.

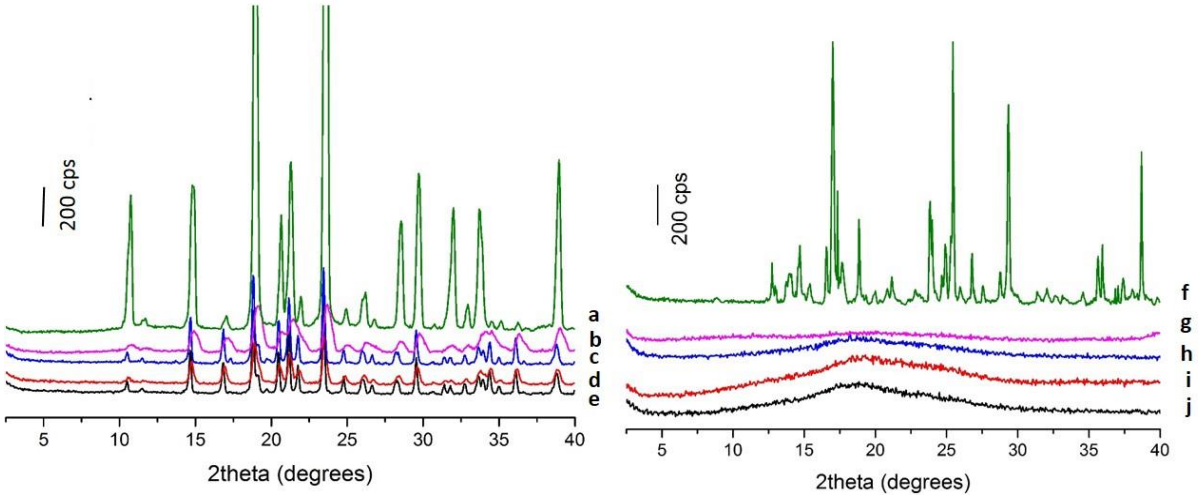

Fig. 5.7. PXRD diffraction patterns for (a) raw mannitol (b) ITR NMPs with mannitol 5% (w/v) compacted at 149 MPa (w/v) (c) ITR NMPs with mannitol 5% (d) SD mannitol 5% (w/v) compacted at 149 MPa (e) SD mannitol 5% (f) raw trehalose (g) SD trehalose 5% (w/v) (h) SD trehalose 5% (w/v) compacted at 99 MPa (i) ITR NMPs SD with trehalose 5% (w/v) (j) ITR NMPs SD with trehalose 5% (w/v) compacted at 99 MPa.

The mechanical properties and processability of materials can be affected by their solid state form, including tensile strength and compactibility (Hulse et al., 2009). Fig. 5.7 and Fig. A.4.10 confirm the crystalline nature of mannitol when compacted, as well as the amorphous nature of trehalose. Crystalline material possesses greater long range order in their structure making them less brittle and elastic. Stronger inter-particle and intermolecular forces must be overcome in order to achieve adequate compaction, and hence increased tensile strength of tablets. Crystallinity will reduce the ability of molecular chains to move when compressed under force. Greater movement of amorphous molecular chains will produce tablets of greater tensile strength. The superior compactibility of amorphous forms has been well documented (Maggi et al., 1998; Paluch et al., 2013). The findings of this work support existing evidence within the literature, with amorphous trehalose compacts exhibiting superior mechanical properties when compared with crystalline mannitol equivalents (Fig. 5.5) (Paluch et al., 2013).

The impact of compaction upon the redispersibility of SD ITR NMPs with mannitol and trehalose was assessed via NTA (Table 5.4).

Table 5.4. NTA measurements comparing redispersibilty of ITR NMPs, as uncompressed powders and after compression into tablets.

NMP system	Particle size after redispersion of compacted tablets (nm) ± SD	D10 (nm)	D50 (nm)	D90 (nm)
Mannitol SD, uncompressed	139 ± 77	33	116	242
Mannitol SD, compressed at 149 MPa	201 ± 70	113	192	276
Trehalose SD, uncompressed	135 ± 41	66	126	174
Trehalose SD, compressed at 99 MPa	112 ± 45	40	99	158

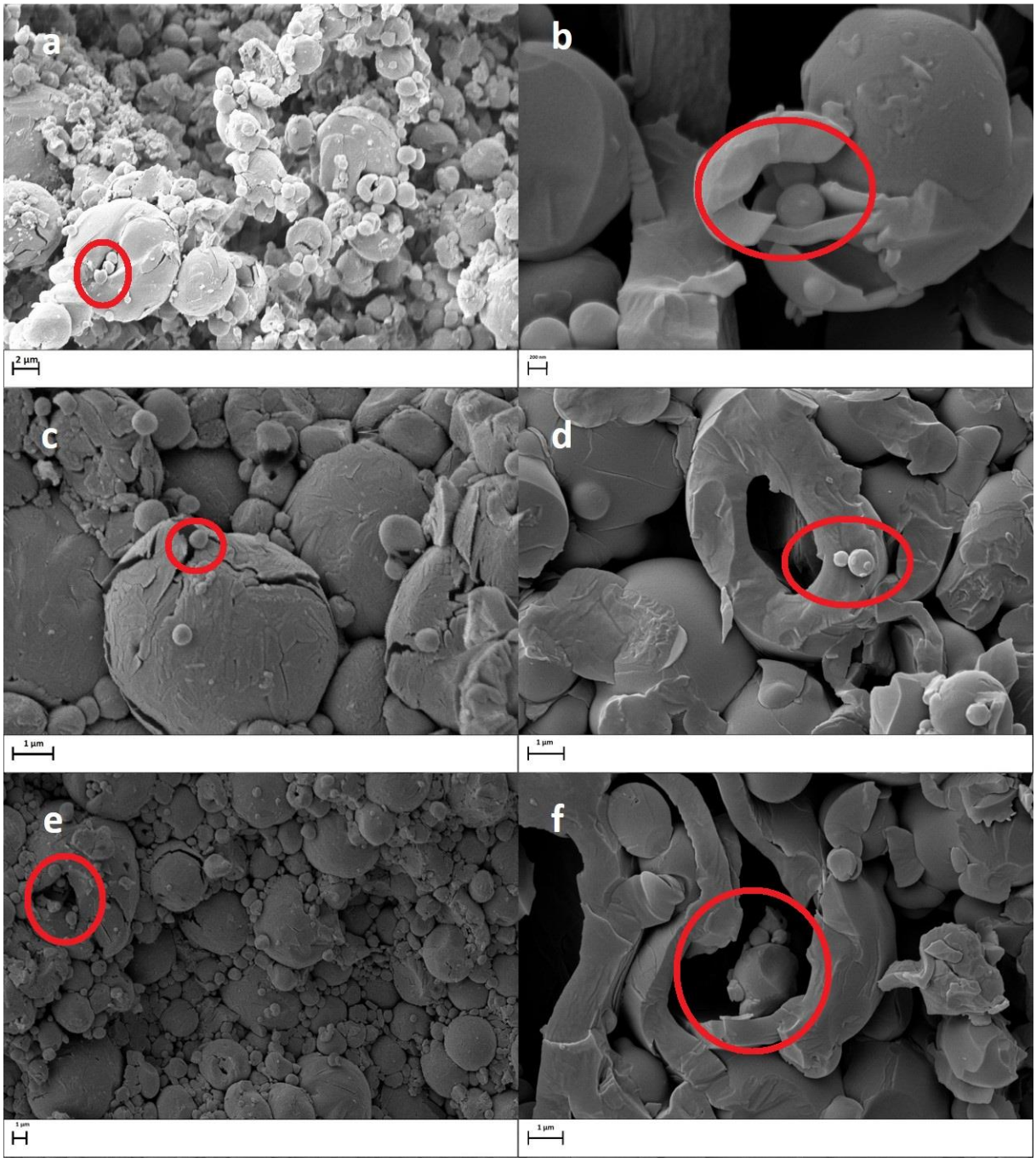

Fig. 5.8. SEM images of ITR NMPs SD with mannitol shown in (a), (c) and (e), and ITR NMPs SD with trehalose shown in (b), (d) and (f). Red circles highlight the presence of ITR NPs.

SEM images in Fig. 5.8 confirm the presence of ITR NPs within the MP core and on the MP surface itself. The presence of ITR NPs within mannitol SD MPs reduced the tensile strength of tablets (Fig. 5.5a). Trehalose equivalents exhibited a marked increase in tensile strength (Fig. 5.5a). Upon redispersion of ITR nanostructured MPs SD with trehalose, NTA measurements confirmed similar average NP sizes of 112 nm, compared with 135 nm for the uncompressed sample (Table 5.4). ITR NMPs compressed with mannitol redispersing to particle sizes of

around 200 nm, compared with 139 nm for uncompressed powder (Table 5.4). Notably, trehalose samples were associated with lower measurement variability than mannitol. Disintegration times for SD mannitol compacted at 149 MPa and SD trehalose compacted at 99 MPa can be found in Fig. 5.9a. Solubility profiles for ITR nanostructured MPs compacted with mannitol and trehalose are presented in Fig. 5.9b.

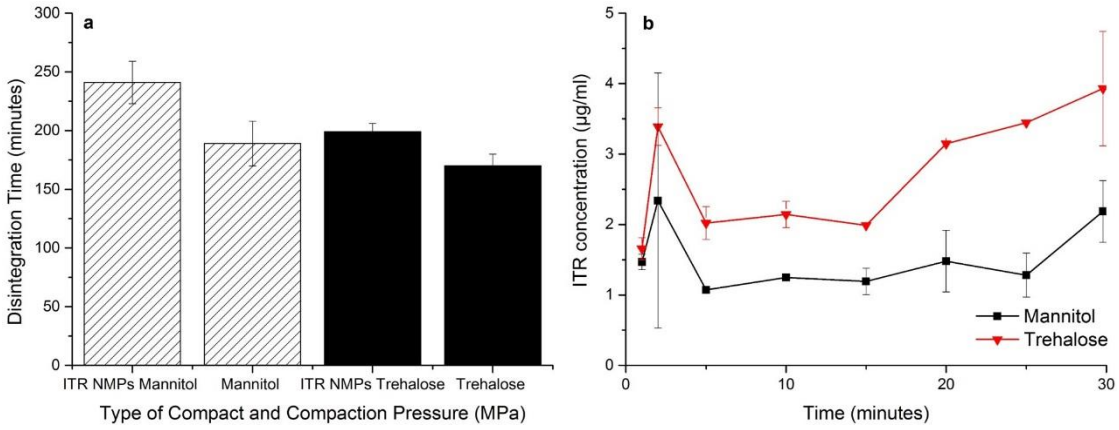

Fig. 5.9. (a) Disintegration testing for SD mannitol 5% (w/v) compacted at 149 MPa and trehalose 5% (w/v) compacted at 99 MPa. Analysis performed on three individual tablets in 900 ml of deionised water at 37 °C. (b) Solubility profiles for ITR NMPs mannitol tablets compacted at 149 MPa and ITR NPs trehalose tablets compacted at 99 MPa in 0.1M HCl at 37 °C. The average of three measurements is shown ± standard deviation.

Dosage forms with fast disintegration time accompanied by adequate tensile strength are considered optimal. The increased mechanical strength of NMP trehalose tablets had no impact upon tablet disintegration time in water, with no change in time observed (Fig. 5.9a). However, a longer disintegration time was observed for ITR NMP mannitol tablets, despite the reduced mechanical strength of those tablets and the higher aqueous solubility of mannitol compared with trehalose (Table 5.2). Considering that porosity of the compacts made of NMPs were comparable to those made of SD materials containing no NPs, it appears that the solid state character of these materials may be the dominant factor in determining their disintegration in water, with amorphous trehalose exhibiting superior properties. Disintegration times for SD mannitol and trehalose (with no NPs) compacted at a range of pressures can be found within Table. A.4.4.

Given the concentration of ITR used when formulating the NMPs (section 5.2.2.4), a theoretical maximum concentration of 4 µg/ml ITR could be solubilised in the 500 ml of acidic media used (Fig. 5.9b). Both types of tablets exhibited erratic solubility profiles in 0.1M HCl as seen in Fig. 5.9b. An initial burst in ITR concentration was observed after 2 minutes for both

types of tablets as shown in Fig. 5.9b, followed by a decrease in ITR concentration. Fig. 5.9b also confirms that initial drug loading for both sugars was similar but evidently the presence of trehalose within compacted tablets resulted in greater solubilisation of ITR. Trehalose tablets solubilised up to 4 µg/ml ITR after 30 minutes, whilst mannitol tablets solubilised around 2 µg/ml, almost half that of trehalose. Trehalose has been noted for its ability to act as a "water-structure marker". The interaction between trehalose and water is stronger than that of water and water, thus trehalose has a "destructuring" effect on the tetrahedral hydrogen bonded network of water (Jain and Roy, 2009). This is supported by the high hydrogen bond donor and acceptor counts noted in Table 5.2 for trehalose. The glucose ring structure of trehalose may be more effective at disrupting the hydrogen bonded water network during solubilisation compared with the short chain structure of mannitol. This fact, accompanied by its amorphous character may explain the reason for greater ITR solubilisation in the presence of trehalose compared with mannitol at 30 minutes (Fig. 5.9) ($p = 0.001$). Matrix former type has a significant impact upon end product performance. This fact reiterates the importance of careful consideration of excipients within the final formulation and their impact upon end product performance.

5.4. CONCLUSIONS

Trehalose proved to be a better matrix former for ITR NPs boasting superior performance in numerous aspects when compared with mannitol. Namely, compressed ITR NMPs made with trehalose redispersed to smaller average particle sizes upon hydration compared with uncompressed equivalents, confirmed by both NTA and DLS. In addition, trehalose NMPs compressed into tablets exhibited increased tensile strength, compared with mannitol compressed NMPs, with adequate disintegration time maintained. Furthermore, trehalose was capable of solubilising a greater amount of ITR at 30 minutes in gastric conditions (0.1M HCl) when compared with mannitol. Solid state effects dominate in determining tablet properties, with amorphous trehalose exhibiting favourable mechanical and disintegrant properties. The matrix former type has a profound impact upon end product performance. We can conclude that, matrix former selection for NP isolation by spray drying warrants careful consideration. This research embodies the complete pharmaceutical development process, demonstrating a logical structured approach to the drug product development process.

References

Adolfsson, Å., Nyström, C., 1996. Tablet strength, porosity, elasticity and solid state structure of tablets compressed at high loads. Int. J. Pharm. 132, 95–106.

Amaro, M.I., Tewes, F., Gobbo, O., Tajber, L., Corrigan, O.I., Ehrhardt, C., Healy, A.M., 2015. Formulation, stability and pharmacokinetics of sugar-based salmon calcitonin-loaded nanoporous/nanoparticulate microparticles (NPMPs) for inhalation. Int. J. Pharm. 483, 6–18.

Badawy, S.I.F., Shah, K.R., Surapaneni, M.S., Szemraj, M.M., Hussain, M., 2010. Effect of spray-dried mannitol on the performance of microcrystalline cellulose-based wet granulated tablet formulation. Pharm. Dev. Technol. 15, 339–345.

Buckton, G., Darcy, P., 1995. Research paper: The use of gravimetric studies to assess the degree of crystallinity of predominantly crystalline powders. Int. J. Pharm. 123, 265–271.

Calzolai, L., Gilliland, D., Garcìa, C.P., Rossi, F., 2011. Separation and characterization of gold nanoparticle mixtures by flow-field-flow fractionation. J. Chromatogr. A. 1218, 4234–4239.

Chacón, M., Molpeceres, J., Berges, L., Guzmán, M., Aberturas, M.R., 1999. Stability and freeze-drying of cyclosporine loaded poly(d,l lactide–glycolide) carriers. Eur. J. Pharm. Sci. 8, 99–107.

Chaubal, M. V., Popescu, C., 2008. Conversion of nanosuspensions into dry powders by spray drying: A case study. Pharm. Res. 25, 2302–2308.

Cue, B.W., Zhang, J., 2009. Green process chemistry in the pharmaceutical industry. Green Chem. Lett. Rev. 2, 193–211.

Duret, C., Wauthoz, N., Sebti, T., Vanderbist, F., Amighi, K., 2012. New inhalation-optimized itraconazole nanoparticle-based dry powders for the treatment of invasive pulmonary aspergillosis. Int. J. Nanomedicine 7, 5475–5489.

Foster, K.D., Bronlund, J.E., Paterson, A.H.J., 2006. Glass transition related cohesion of amorphous sugar powders. J. Food Eng. 77, 997–1006.

Garr, J.S.M., Rubinstein, M.H., 1991. The effect of rate of force application on the properties of microcrystalline cellulose and dibasic calcium phosphate mixtures. Int. J. Pharm. 73, 75–80.

Healy, A.M., Worku, Z.A., Kumar, D., Madi, A.M., 2017. Pharmaceutical solvates, hydrates and amorphous forms: A special emphasis on cocrystals. Adv. Drug Deliv. Rev. 117, 25–46.

Hecq, J., Deleers, M., Fanara, D., Vranckx, H., Boulanger, P., Le Lamer, S., Amighi, K., 2006. Preparation and *in vitro/in vivo* evaluation of nano-sized crystals for dissolution rate enhancement of ucb-35440-3, a highly dosed poorly water-soluble weak base. Eur. J. Pharm. Biopharm. 64, 360–368.

Hulse, W.L., Forbes, R.T., Bonner, M.C., Getrost, M., 2009. The characterization and comparison of spray-dried mannitol samples characterization of spray-dried mannitol. Drug Dev. Ind. Pharm. 35, 712–718.

Jain, N.K., Roy, I., 2009. Effect of trehalose on protein structure. Protein Sci. 18, 24–36.

Kalepu, S., Nekkanti, V., 2015. Insoluble drug delivery strategies: review of recent advances and business prospects. Acta Pharm. Sin. B 5, 442–453.

Kesisoglou, F., Panmai, S., Wu, Y., 2007. Nanosizing - Oral formulation development and biopharmaceutical evaluation. Adv. Drug Deliv. Rev. 59, 631–644.

Liu, Y., Bhandari, B., Zhou, W., 2007. Study of glass transition and enthalpy relaxation of mixtures of amorphous sucrose and amorphous tapioca starch syrup solid by differential scanning calorimetry (DSC). J. Food Eng. 81, 599–610.

Maggi, L., Conte, U., Bettinetti, G.P., 1998. Technological properties of crystalline and amorphous α-cyclodextrin hydrates. Int. J. Pharm. 172, 211–217.

Malamatari, M., Somavarapu, S., Taylor, K.M.G., Buckton, G., 2016. Solidification of nanosuspensions for the production of solid oral dosage forms and inhalable dry powders. Expert Opin. Drug Deliv. 13, 435-450.

Masters, K., 1976. Spray Drying. Wiley, London.

Matteucci, M.E., Paguio, J.C., Miller, M.A., Williams, R.O., Johnston, K.P., 2009. Highly supersaturated solutions from dissolution of amorphous Itraconazole microparticles at pH 6.8. Mol. Pharm. 6, 375–385.

Mou, D., Chen, H., Wan, J., Xu, H., Yang, X., 2011. Potent dried drug nanosuspensions for oral bioavailability enhancement of poorly soluble drugs with pH-dependent solubility. Int. J. Pharm. 413, 237–244.

Nekkanti, V., Pillai, R., Venkateshwarlu, V., Harisudhan, T., 2009. Development and

characterization of solid oral dosage form incorporating candesartan nanoparticles. Pharm. Dev. Technol. 14, 290–298.

Paluch, K.J., Tajber, L., Corrigan, O.I., Healy, A.M., 2013. Impact of alternative solid state forms and specific surface area of high-dose, hydrophilic active pharmaceutical ingredients on tabletability. Mol. Pharm. 10, 3628–3639.

Pilcer, G., Vanderbist, F., Amighi, K., 2009. Preparation and characterization of spray-dried tobramycin powders containing nanoparticles for pulmonary delivery. Int. J. Pharm. 365, 162–169.

Pitt, K.G., Newton, J.M., Richardson, R., Stanley, P., 1989. The Material Tensile Strength of Convex-faced Aspirin Tablets. J. Pharm. Pharmacol. 41, 289–292.

Ramos, M., Pinto, J.J., Diogo, S.S., Hermínio, P., 2005. Molecular Mobility in Raffinose in the Crystalline Pentahydrate Form and in the Amorphous Anhydrous Form. Pharm. Res. 22, 1142–1148.

Roos, Y., Karel, M., 1991. Plasticizing Effect of Water on Thermal Behavior and Crystallization of Amorphous Food Models. J. Food Sci. 56, 38–43.

Saleki-Gerhardt, A., Ahlneck, C., Zografi, G., 1994. Assessment of disorder in crystalline solids. Int. J. Pharm. 101, 237–247.

Simperler, A., Kornherr, A., Chopra, R., Bonnet, P.A., Jones, W., Motherwell, W.D.S., Zifferer, G., 2006. Glass transition temperature of glucose, sucrose, and trehalose: An experimental and in silico study. J. Phys. Chem. B 110, 19678–19684.

Storey, B.T., Noiles, E.E., Thompson, K.A., 1998. Comparison of Glycerol, Other Polyols, Trehalose, and Raffinose to Provide a Defined Cryoprotectant Medium for Mouse Sperm Cryopreservation. Cryobiology. 37, 46–58.

Tan, E.H., Parmentier, J., Low, A., Möschwitzer, J.P., 2017. Downstream drug product processing of itraconazole nanosuspension: Factors influencing tablet material properties and dissolution of compacted nanosuspension-layered sugar beads. Int. J. Pharm. 532, 131–138.

Teeranachaideekul, V., Junyaprasert, V.B., Souto, E.B., Muller, R.H., 2008. Development of ascorbyl palmitate nanocrystals applying the nanosuspension technology. Int. J. Pharm. 354, 227–234.

Tsapis, N., Bennett, D., Jackson, B., Weitz, D.A., Edwards, D.A., 2002. Trojan particles: Large porous carriers of nanoparticles for drug delivery. Proc. Natl. Acad. Sci. USA. 99, 12001-12005.

USP 39 NF 34, 2016. General Chapter 701, Disintegration in USP 39 NF 34 through Second Supplement. (Accessed 2 July 2018). http://www.uspnf.com/uspnf/pub/index?usp=39&nf=34&s=2&officialOn=December 1, 2016.

Van Eerdenbrugh, B., Froyen, L., Van Humbeeck, J., Martens, J.A., Augustijns, P., Van den Mooter, G., 2008a. Drying of crystalline drug nanosuspensions-The importance of surface hydrophobicity on dissolution behavior upon redispersion. Eur. J. Pharm. Sci. 35, 127–135.

Van Eerdenbrugh, B., Van den Mooter, G., Augustijns, P., 2008b. Top-down production of drug nanocrystals: Nanosuspension stabilization, miniaturization and transformation into solid products. Int. J. Pharm. 364, 64–75.

Vehring, R., 2008. Pharmaceutical particle engineering via spray drying. Pharm. Res. 25, 999–1022.

Wang, Y., Zheng, Y., Zhang, L., Wang, Q., Zhang, D., 2013. Stability of nanosuspensions in drug delivery. J. Control. Release 172, 1126–1141.

Yalkowsky, S.H., Dannenfelser, R.M., 1992. The Aquasol database of Aqueous Solubility. Fifth Ed, Tucson, AZ: Univ Az, College of Pharmacy.

Yu, L., Mishra, D.S., Rigsbee, D.R., 1998. Determination of the Glass Properties of Mannitol Using Sorbitol as an Impurity. J. Pharm. Sci. 87, 774–777.

6.1. General Discussion and Conclusions

As the title of this thesis suggests the main aim of this project was to formulate azole anti-fungal compounds as NPs. Stability of those NPs was assessed and attempts to understand the mechanisms dictating their effective stabilization were made. The process of Ostwald ripening (OR) was studied in detail alongside NP aggregation and growth. The particle sizing techniques of DLS and NTA were compared in a critical manner. The crystallisation pathways for each API were investigated using a cohort of techniques. Attempts were made to understand why specific stabilizers were more effective than others and to deduce the exact location of the stabilizers. Isolation of those NPs and their compaction into solid dosage forms completed this research project. All three APIs: ITR, KETO and POS were explored throughout the project, with a particular focus on ITR in terms of secondary processing. This was necessary due to the particular stability of ITR NPs, as well as time and resource constraints. Moreover, the work in thesis can serve as a proof of concept for streamlining the drug development process. This work encompasses the complete development process beginning with NP fabrication optimisation, finishing with NP isolation via spray drying with optimal dosage form design. The end product of this process was a solid oral dosage form possessing adequate tensile strength and quick dissolution properties thereby ensuring delivering of enhanced bioavailability and clinical effect to the patient in the form of a convenient and acceptable tablet. The logical approach and clear research strategy undertaken in this work can now be adopted by other researchers. They can optimise their processes whilst achieving their goals in a more efficient and timely manner. Ultimately, reduced pharmaceutical drug development times should result. In addition, this research strategy can be adopted as a suitable approach for the nano-sization of other APIs.

The work in Chapter 2 began with the aim of designing a stabilizer selection screening tool which could act as a valuable aid for the formulation scientist in the drug development process. To date, stabilizer selection is generally achieved through a trial and error approach. The small scale of this study (1 ml) and lack of control with regards to variable parameters such as stirring may be seen as a limitation. However, I believe the simplicity of this technique should be seen as an advantage for the application of this technique within the lab setting. The simplicity of the NP fabrication procedure adopted made this study possible. *In situ* NP formation made instant data collection feasible. Numerous stabilizers were explored at varying concentrations in an attempt to identify the most effective. DLS produced interesting results. Evidence pointed towards OR, making the application of kinetic modelling an attractive approach. It is

recognised that growth of these NPs over the time scale of the study may point to potential difficulties posed in the translation of such products into viable nano-medicines. However, NP growth over this short time scale made the research question under investigation worthwhile.

Evidence also existed for crystallisation of the APIs during the studies, in particular for POS. Ideally, more evidence would confirm the exact solid state of the nano-dispersions, with PXRD employed as the main technique for solid state characterisation. Indeed, experimental analysis highlighted the challenges faced in the isolation of the unstable, high energy amorphous phase of a NP. Much time and effort was put into achieving this elusive task. Regardless of this, the likelihood of ITR forming liquid crystalline phases following similar NP fabrication procedures had been noted by Mugheirbi and Tajber (2015). Despite much time and effort, it was simply not possible to isolate KETO NPs upon initial formation for solid state characterisation. However, the crystalline nature of KETO NPs had been observed elsewhere in the literature (Liu et al., 2011). In the case of POS, a sufficient amount of evidence was collected supporting the solid state transformation of an initial amorphous POS to a stable crystalline phase (Fig. 2.5a to d, 2.7, 2.8d). Large variability observed in DLS results around the 15 minute time point also supported this hypothesis. Crystallisation of amorphous POS had also been noted elsewhere in the literature (Mugheirbi et al., 2017). Crystallisation during sample preparation for SEM may have been a possibility, however as previously mentioned hypotheses regarding crystallisation pathways were not based on SEM analysis alone. Furthermore, SEM analysis of nano-dispersions poses a difficult task, making the inclusion of sample preparation steps such as centrifugation necessary. With regards to the initial research question of designing a stabilizer selection tool one may argue this was not achieved through the work completed in Chapter 2. To some extent, this is correct, however the findings of Chapter 2 did highlight the impact of small differences in API and stabilizer structure, and how these can greatly impact NP behaviour, with crystallisation mechanisms being API, stabilizer type and concentration dependent. It was clear that more detailed analysis was required in order to deduce clear and concise outcomes with regards to API crystallisation pathways.

The work in Chapter 3 utilised NTA and DLS in the characterisation of NPs introduced in Chapter 2. Evidence for crystallisation existed as mentioned above, with a need for more detailed analysis to provide solid support for these hypotheses. Thorough characterisation of NPs is a prerequisite for the robust and reproducible manufacture of successful nano-formulations. Therefore, the concepts explored in Chapter 3 are extremely relevant and

attractive from an industrial perspective. The use of NTA seemed logical in understanding the complex processes at play in depth. The use of numerous particle sizing techniques proved capable of providing comprehensive information regarding particle size.

Detailed evaluation of DLS and NTA revealed good correlation in some instances, in particular for ITR, however discrepancies existed for KETO and POS. The relative stability of ITR NPs confirmed by DLS made them ideal candidates for assessment using NTA. Good correlation was found between the two techniques for these NPs. Discrepancies existed between the techniques for KETO and POS, these were attributed to the physical processes of dissolution and crystallisation. The decrease in light scattering intensity observed for KETO NPs was explained by the dissolution of those particles. Wittbold and Tatarkiewicz (2017) had previously tracked the processes of crystallisation and dissolution via observation of variation in the intensity of light scattered by proteins using MANTA technology. The authors were able to correlate the process of crystallisation with an increase in light intensity whilst dissolution was represented by a decrease in intensity (Wittbold and Tatarkiewicz, 2017). Findings confirmed each API behaved differently with regards to their crystallisation pathways. The numerous NTA scattergrams included in Chapter 3 were exported directly from the NTA software itself. Ideally, these plots would all share a uniform y-axis so the differences in these could be more clearly demonstrated to the reader. The latest version of the NTA software allows for adjustments to the x-axis, but not the y-axis of interest in this case. Attempts were made to plot the raw data used in producing these graphs, however this was not possible due to the nature of the data. In the light of the vast amount of data collected, a detailed critical comparison was provided for these two particle sizing techniques, which may now be a valuable source of information for other researchers in this field.

Interestingly, in Chapter 3 a novel concept was explored regarding the live monitoring of crystallisation on the nano-scale. The nature of crystallisation processes is of major interest across a variety of disciplines. Light scattering properties of the different materials were utilised in the monitoring of solid state transformations for POS NPs. The effect of the stabilizer itself upon the light scattering properties of the NPs should not be overlooked. It is recognised that these findings are limited but justified by the novelty of this concept. Exploration of the application of this concept, with regards the crystallisation of other APIs would be extremely interesting. The innovative application of NTA for the purpose of monitoring these complex physical processes can serve to benefit other researchers in the field. This technique has the

potential to unlock real time valuable information with regards the physical process of crystallisation. Application of these studies for other nano-formulations in biological fluids may be of much interest to other researchers.

In Chapter 4, a cohort of techniques were employed in an attempt to determine the nature of drug-polymer interactions and their impact upon NP stabilization. HSPs were calculated for all APIs and polymers, confirming some degree of miscibility between all components. API solubility in polymer aqueous solutions was investigated, concluding low solubility of ITR in DMPEG solutions. Whilst, KETO had high solubility in DMPEG solutions (Fig. 4.11b). Thermal analysis was employed in the construction of phase diagrams for KETO and ITR. POS was omitted from these particular studies due to its rich polymorphic character, which would have brought into question the validity of such work. The Flory-Huggins (F-H) lattice model for isotropic (for liquid/amorphous) systems was utilised in the case of KETO. The most positive chi parameter was obtained for KETO and DMPEG, suggesting the lowest miscibility between these two components. In the complex case of ITR, the capability of ITR to form liquid crystalline phases was accounted for in the design of thermal analysis studies and construction of phase diagrams. F-H theory was coupled with the M-S-M theory to account for the anisotropy of the ITR molecules. Binary ITR/polymer systems were subjected to consecutive heating cycles using a Perkin Elmer DSC, to allow for the sensitive detection of the LC phase. Given the propensity for ITR to form LC phases, data obtained during the second heating was given careful consideration.

Phase diagram construction for ITR/polymer systems was performed considering the possibility of ITR existing in LC or fully crystalline state. Both scenarios resulted in calculated interaction parameters suggesting immiscibility in all systems. Given the capability of ITR to form liquid crystalline phases, data obtained from second heating was given due consideration. During thermal treatment of samples, the supply of thermal energy to the system provided the driving force for disruption to the order of ITR molecules. This can be compared with the generation of supersaturation during the NP formation process, which provides the necessary energy to the system, introducing disorder. Therefore, given the likelihood for ITR to exist in a disordered (glassy) state, it was concluded that immiscibility existed between all components. Furthermore, the highest degree of immiscibility existed between ITR and DMPEG (Table 4.7). It is recognised that these miscibility predictions are associated with a degree of uncertainty due to measurement precision and the validity of

assumptions which the F-H theory is based on (Knopp et al., 2015). The most positive chi parameter was derived for ITR and DMPEG systems, confirming highest degree of immiscibility between these two components. It was concluded, immiscibility between ITR and polymer was a good predictor for effective stabilization of ITR NPs. In the case of KETO, effective NP stabilization was predicted by low miscibility between KETO and polymer (DMPEG).

Given the relative stability of ITR NPs in the absence of a stabilizer (Chapter 2), the likelihood of ITR existing as a LC and the limited miscibility between components, confirmed by the positive chi parameters calculated in Chapter 4, would suggest likely confinement of polymer onto ITR particles surfaces with limited integration throughout the particle core. Therefore, it seemed logical to explore the nature of adsorbed polymer coating layers onto API particle surfaces, using ITR NPs and DLS analysis. Due to the limited sensitivity and detection of DLS, as well as the nano-scale size of this layer, it is difficult to draw concise conclusions based on exact sizing of the polymer coating layer. However, it is possible to see clear trends in the manner in which these layers are formed. DMPEG adsorbed layers formed at a lower polymer concentration compared with PEG and MPEG (Fig 4.12). PEG adsorbed layers required the greatest amount of polymer for layer formation to occur. Layer formation at lower polymer concentrations correlated well with more effective NP stabilization. Limitations in the application in this study are highlighted in the fact that polymer addition follows NP formation. When NPs are formed in Chapters 2 and 3, stabilizer is already present within the anti-solvent phase prior to moment of formation. The results of Chapter 4 highlighted the simplicity and ease with which HSPs can be calculated. However, the need for more detailed experimental analysis was evident. The complex nature of ITR and its physical properties became apparent as thermal analysis for ITR became increasingly complex. The need for detailed analysis, brings with it increasing complexity, in terms of analysis and understanding.

In Chapter 5, ITR NMPs were successfully produced via spray drying with a variety of matrix formers. Challenges faced in this work highlighted the need for close control and monitoring of the variable parameters involved in the NP fabrication procedure. Successful scale-up of nano-formulation manufacture requires detailed understanding of the physical and chemical properties of the NPs themselves. This knowledge can provide the means for reducing batch to batch variability, whilst ensuring a robust manufacturing process which is transferable on an industrial scale. The skills of a multi-disciplinary team would be necessary to ensure successful scale-up of nano-formulation manufacture. The relevance of this particular NP

fabrication procedure to industrial manufacture is underlined in its simplicity. Ambient conditions are employed reducing cost. NPs are formed in a single step as described in Chapter 2, 3 and 5, this is followed by solvent evaporation. In this way, toxicity concerns are removed, in line with regulatory requirements. The few steps involved in this process also reduce the opportunity for possible batch variability. The transferability of this process from lab scale to pilot scale may provide further research areas of interest.

Crystalline mannitol and amorphous trehalose exhibited the most promising results as potential matrix formers. These conclusions were based on numerous properties, namely solid state and redispersibility. From the outset, DLS was relied on as the most suitable technique for measuring particle size and assessing redispersibility. However, following exploration of the suitability of NTA for this purpose, it appeared that this technique may in fact provide more insightful information with regards redispersibility. Ideally, ITR NP size would have been assessed by both NTA and DLS following initial formation. Unfortunately, initial particle size was only measured via DLS. Dosage form design explored a range of compaction pressures for the production of both mannitol and trehalose tablets. Compaction pressures were selected for ITR NMP studies based on tensile strength and porosity. ITR NMPs compressed with trehalose exhibited greater tensile strength when compacted at lower compaction pressure than mannitol equivalents. This increase in tensile strength did not compromise the disintegration time of these compacts. In an attempt to mimic gastric conditions, the amount of ITR solubilised from mannitol and trehalose ITR NMP tablets was assessed using a modified disintegration method outlined in Section 5.2.2.4.1.2. Trehalose tablets were capable of solubilising a greater amount of ITR compared with mannitol equivalents. It is likely that the amorphous character of these compacts was the contributing factor in determining this. Trehalose proved to exhibit superior performance as a matrix former in this instance. Given the limited resources available in performing these studies, larger scale studies would be of great interest. These may provide further support for our findings. The research strategy adopted in Chapter 5, highlighted the potential time and resource constraints encountered during the drug development process. Studies should focus on a subset of variables for investigation. Rational selection of excipients for the optimisation of end product performance offers an attractive approach from an industrial perspective.

6.2 KEY FINDINGS OF THIS WORK

- Azole anti-fungal nano-dispersions were formed using a bottom up anti-solvent precipitation method at 25 °C *in situ*. Stabilizer type and concentration were investigated for their impact upon colloidal stability. PEG, MPEG and DMPEG with a molecular weight 2000 Da were selected as stabilizers.
- Colloidal stability was monitored using DLS. ITR NPs had the best stability of all API nano-dispersions, in both the presence and absence of stabilizers.
- DMPEG was the most effective stabilizer overall for all API nano-dispersions, however POS nano-dispersions had greater stability in the absence of a stabilizer.
- In the case of ITR, DMPEG was most effective at the lowest concentration of 0.5 mg/ml. For KETO, DMPEG was the most effective at the higher concentration of 1.5 mg/ml. POS NPs had greatest stability in the absence of a stabilizer.
- The application of kinetic modelling revealed NP growth was driven by OR. The presence of DMPEG caused OR growth to become an interface controlled process following a parabola trend. DMPEG encouraged OR for POS NPs, whilst driving the crystallisation process.
- The rate of OR appeared to be inherent of the crystallisation pathway by which these APIs proceed. Crystallisation mechanisms were found to be API, stabilizer type and concentration dependent.
- DLS and NTA concluded ITR NPs were the most stable, and POS NPs the least stable. Both techniques confirmed DMPEG was the most effective stabilizer for POS nano-dispersions.
- Mie light scattering theory was used to explain the relationship between material composition and particle scattering power. A change in material refractive index, associated with an amorphous to crystalline solid state transformation, was predominantly responsible for the observed change in the light scattering power of POS nano-dispersions. The presence of polymer may have an impact upon the light scattering power of the NPs.
- For the first time, NTA was successfully utilised for the innovative purpose of in situ monitoring of crystal growth.
- Thermal analysis and phase diagram construction for KETO/polymer systems was performed using F-H theory. Negative interaction parameters suggested all polymers were miscible with KETO, with DMPEG having the lowest miscibility.

- Thermal analysis and phase diagram construction was performed in light of ITR propensity to form LC phases. F-H theory was coupled with M-S-M theory for this reason. Calculated interaction parameters confirmed positive parameters in all instances. Immiscibility existed between ITR and all polymers.
- DSC was used to determine the solubility of solid ITR and KETO in polymers. Polymers were insoluble in KETO, with the exception of DMPEG, where up to 1.4% (w/w) is soluble in KETO. In contrast, polymers had considerable solubility in ITR, with DMPEG having the lowest solubility in ITR.
- Drug solubility in polymer solutions confirmed the low solubility of ITR in DMPEG solutions, as well as the high solubility of KETO in DMPEG solutions.
- Drug-polymer immiscibility provided favourable conditions for effective stabilization of ITR NPs. In the case of KETO NPs, low miscibility between components was a good predictor for effective NP stabilization.
- DLS was used for the characterisation of polymer adsorbed layer onto ITR NPs. Results confirmed polymer type was critical in determining layer formation. Polymer type and concentration directly affected adsorbed layer formation. DMPEG coating layer formation occurred at the lowest concentration of 0.75 mg/ml. ITR-polymer immiscibility and low polymer solubility in ITR, enabled adsorbed layer formation at lower polymer concentration for ITR NPs.
- Isolation of ITR NMPs was achieved via spray drying with a variety of matrix formers. Dry powders were characterised, establishing ITR NMPs spray dried with mannitol and trehalose had the most favourable redispersibility confirmed by DLS and NTA.
- Trehalose ITR NMPs tablets exhibited increased tensile strength when compressed compared with compressed mannitol ITR NMPs, with no impact upon disintegration rate observed. Trehalose ITR NMPs tablets were capable of solubilising a greater amount of ITR in gastric conditions. Overall, trehalose proved to be a better matrix former for ITR NPs boasting superior performance in numerous aspects when compared with mannitol.
- Solid state effects dominate in determining tablet properties containing the studied NPs.

6.3 RECOMMENDATIONS FOR FUTURE RESEARCH

- Investigation into the performance of other polymers such as polyvinyl alcohol (PVA), as stabilizers could provide more insightful findings regarding NP stabilization mechanisms. The impact of alternative solvents in place of acetone such as ethanol, may also provide additional information.
- Chapter 3 presented the novel application of NTA for the purposes of crystallisation monitoring. POS was unique in its capability to form NPs, with a tendency to quickly convert to micron sized crystals within a short time frame. It would be interesting to use this technique to study the crystallisation of other APIs.
- Manipulation of alternative parameters for NTA studies would provide an interesting research topic. With the NTA instrument it is possible to control temperature within the range of 15 to 35 °C. The impact of temperature on crystallisation and dissolution processes would be of interest.
- In Chapter 4, a cohort of techniques were employed for the quantification of drug polymer interactions. In the case of POS, the applications of these techniques was limited due to its rich polymorphism and the complications this would present during analysis. A thorough exploration of alternative techniques that could be used for this purpose, in the case of POS would be useful.
- Chapter 5 presented the isolation and dosage form design of ITR NMPs. A thorough investigation into the stability and shelf life of these dosage forms should be performed.
- Ideally, the availability of more time and resources would be useful in performing more extensive studies on spray drying and dosage form design of NMPs. Larger study sizes would improve the statistical reliability of the results. Access to suitable facilities for conducting larger scale studies would be of interest. Input from other researchers with multidisciplinary backgrounds could prove useful in the up-scale of this work.
- The transferability of the enhanced dissolution and bioavailability for these nano-formulations to *in vivo* conditions warrants further exploration. *In vitro-in vivo* correlation studies could provide an interesting means for further study.

References

Knopp, M.M., Tajber, L., Tian, Y., Olesen, N.E., Jones, D.S., Kozyra, A., Löbmann, K., Paluch, K., Brennan, C.M., Holm, R., Healy, A.M., Andrews, G.P., Rades, T., 2015. Comparative Study of Different Methods for the Prediction of Drug-Polymer Solubility. Mol. Pharm. 12, 3408–3419.

Liu, P., Rong, X., Laru, J., Van Veen, B., Kiesvaara, J., Hirvonen, J., Laaksonen, T., Peltonen, L., 2011. Nanosuspensions of poorly soluble drugs: Preparation and development by wet milling. Int. J. Pharm. 411, 215–222.

Mugheirbi, N.A., Tajber, L., 2015. Mesophase and size manipulation of itraconazole liquid crystalline nanoparticles produced via quasi nanoemulsion precipitation. Eur. J. Pharm. Biopharm. 96, 226–236.

Mugheirbi, N.A., O'Connell, P., Serrano, D.R., Healy, A.M., Taylor, L.S., Tajber, L., 2017. A Comparative Study on the Performance of Inert and Functionalized Spheres Coated with Solid Dispersions Made of Two Structurally Related Antifungal Drugs. Mol. Pharm. 14, 3718–3728.

Wittbold, W., Tatarkiewicz, K., 2017. Biological characterization using protein crystal measurements. BioProcess Int. 15, 48–51.

APPENDIX 1

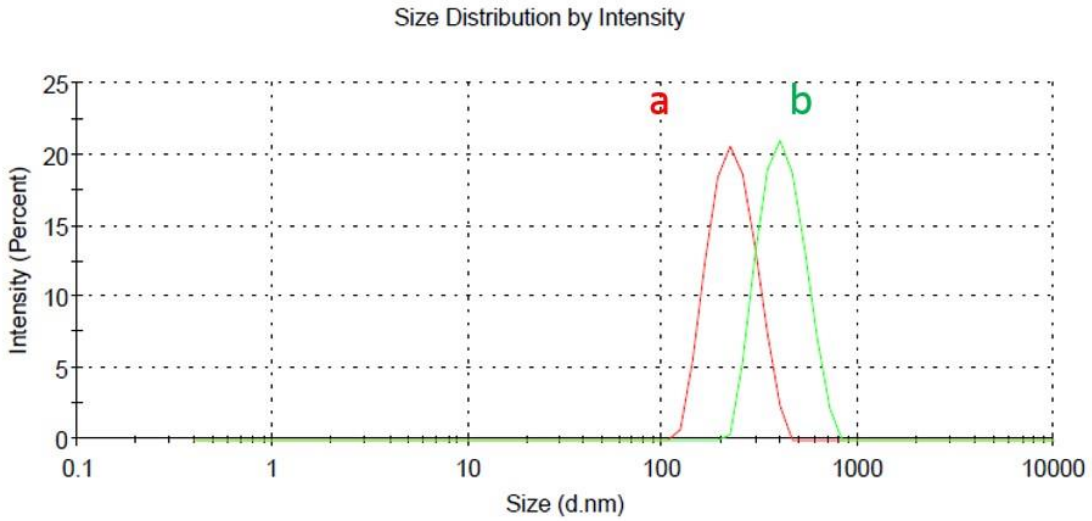

Fig. A.1.1 DLS intensity based particle size distribution at (a) 0 (b) 30 minutes for ITR NPs stabilized with DMPEG 0.5 mg/ml.

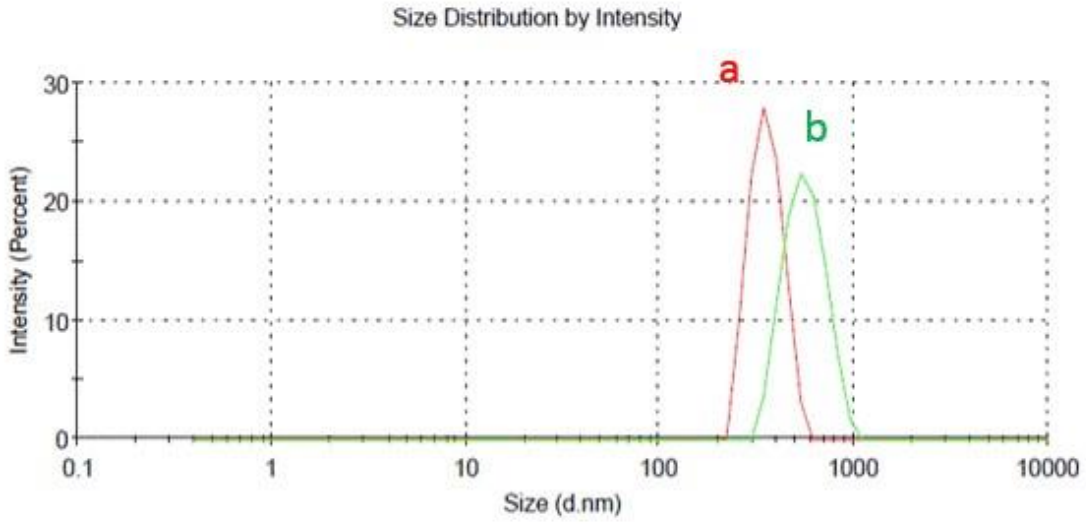

Fig. A.1.2 DLS intensity based particle size distribution at (a) 0 (b) 30 minutes for ITR NPs stabilized with DMPEG 1 mg/ml.

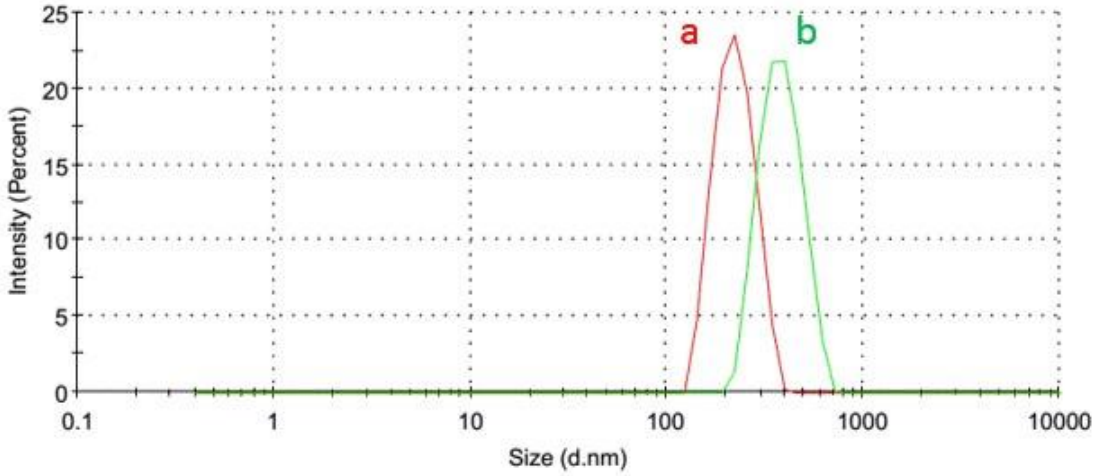

Fig. A.1.3 DLS intensity based particle size distribution at (a) 0 (b) 30 minutes for ITR NPs stabilized with MPEG 1 mg/ml.

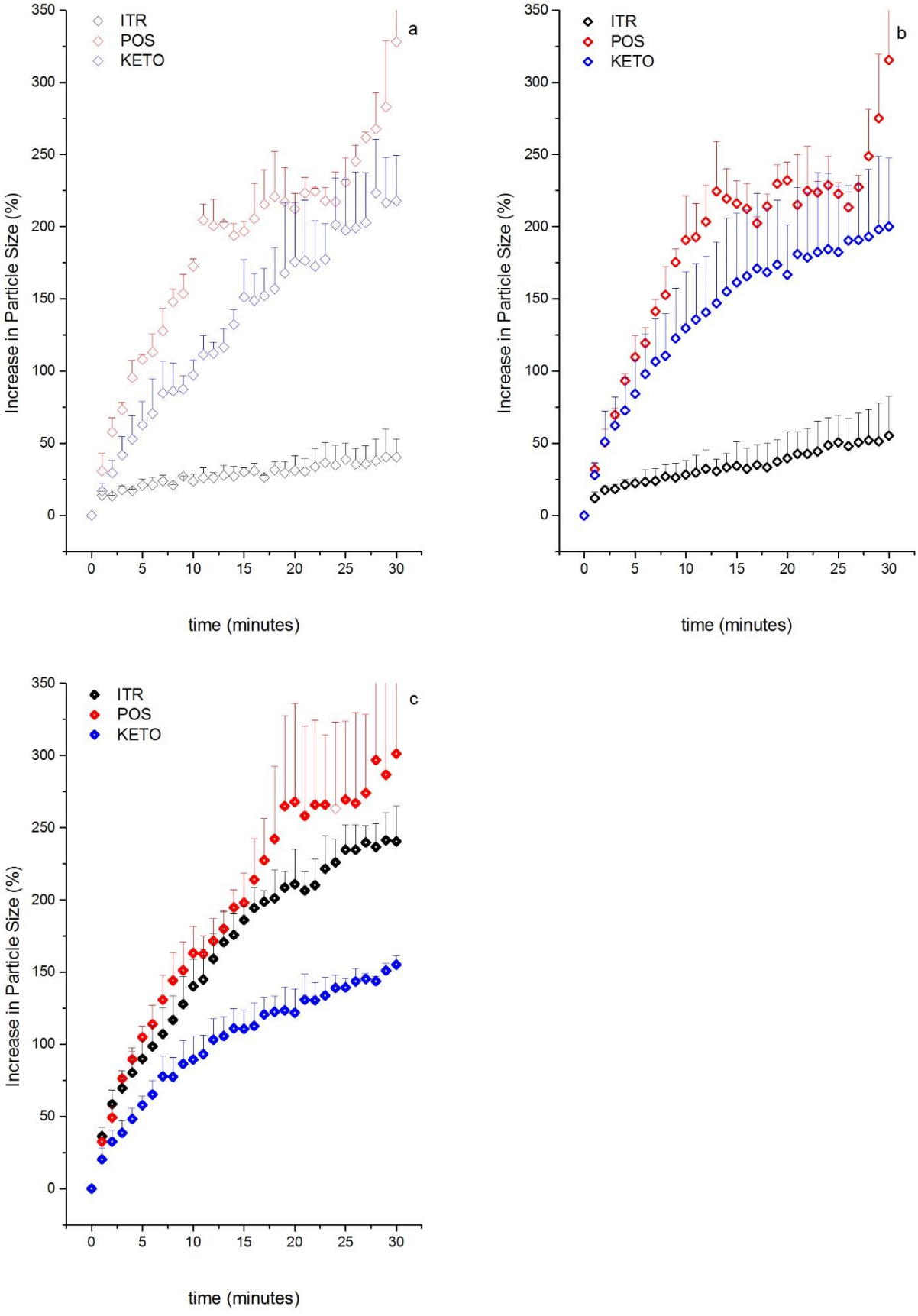

Fig. A.1.4 Plot of increase in particle size (%) versus time for NPs (a) with DMPEG 0.5 mg/ml (b) DMPEG 1 mg/ml and (c) DMPEG 1.5 mg/ml.

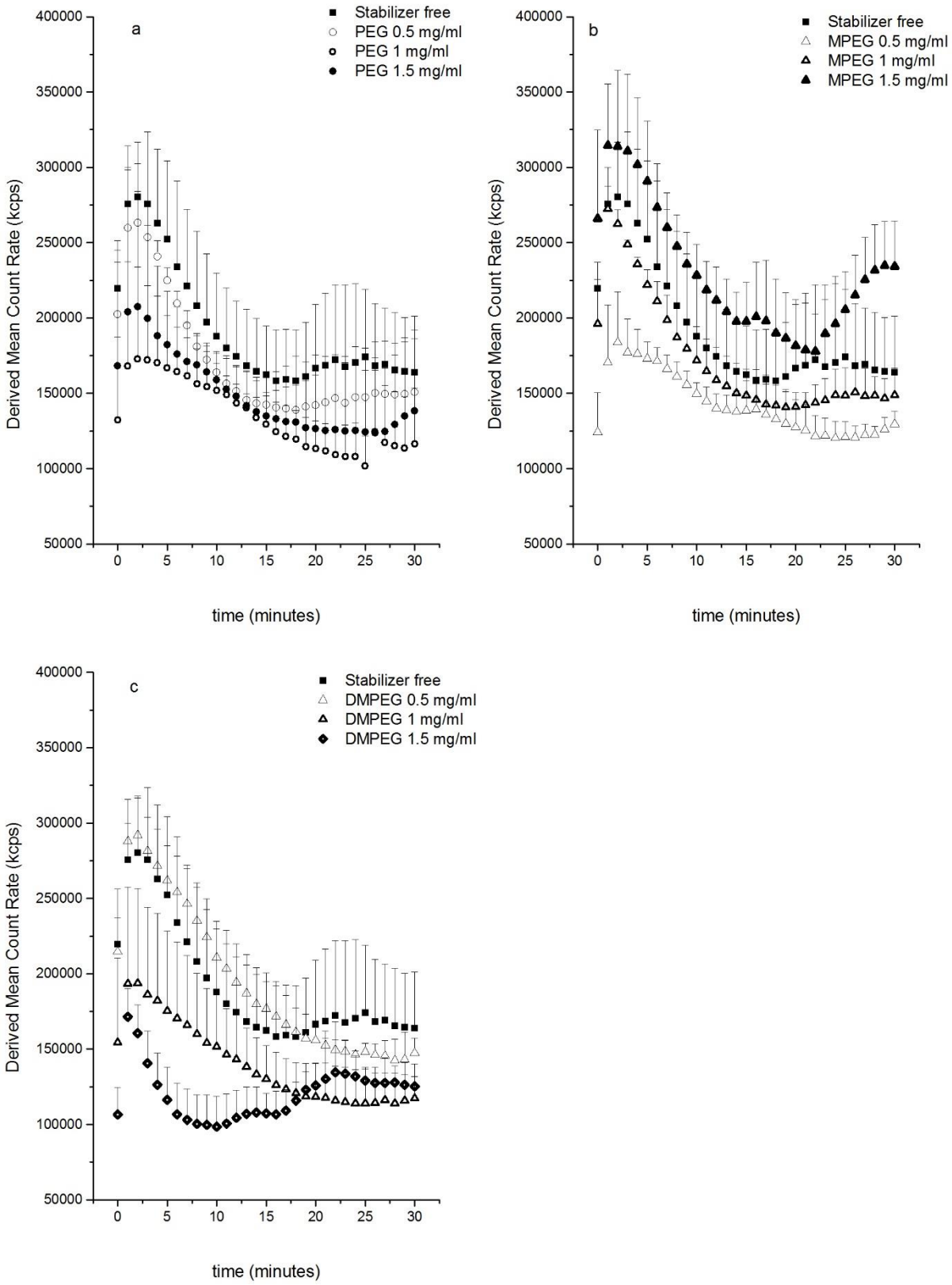

Fig. A.1.5 Derived Mean Count Rate (kcps) versus time (min) for ITR NPs with (a) PEG (b) MPEG and (c) DMPEG.

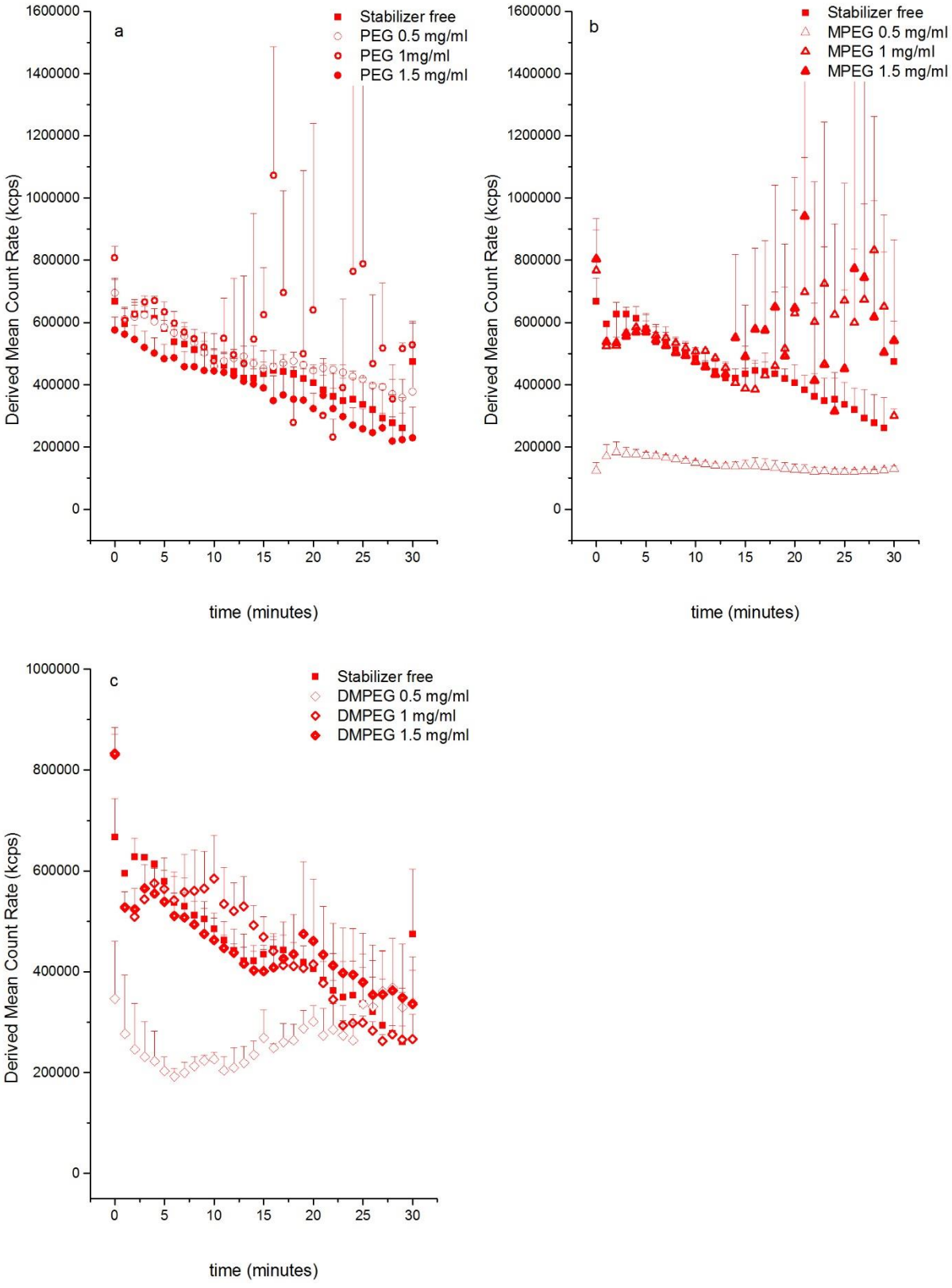

Fig. A.1.6 Derived Mean Count Rate (kcps) versus time (min) for POS NPs with (a) PEG (b) MPEG and (c) DMPEG.

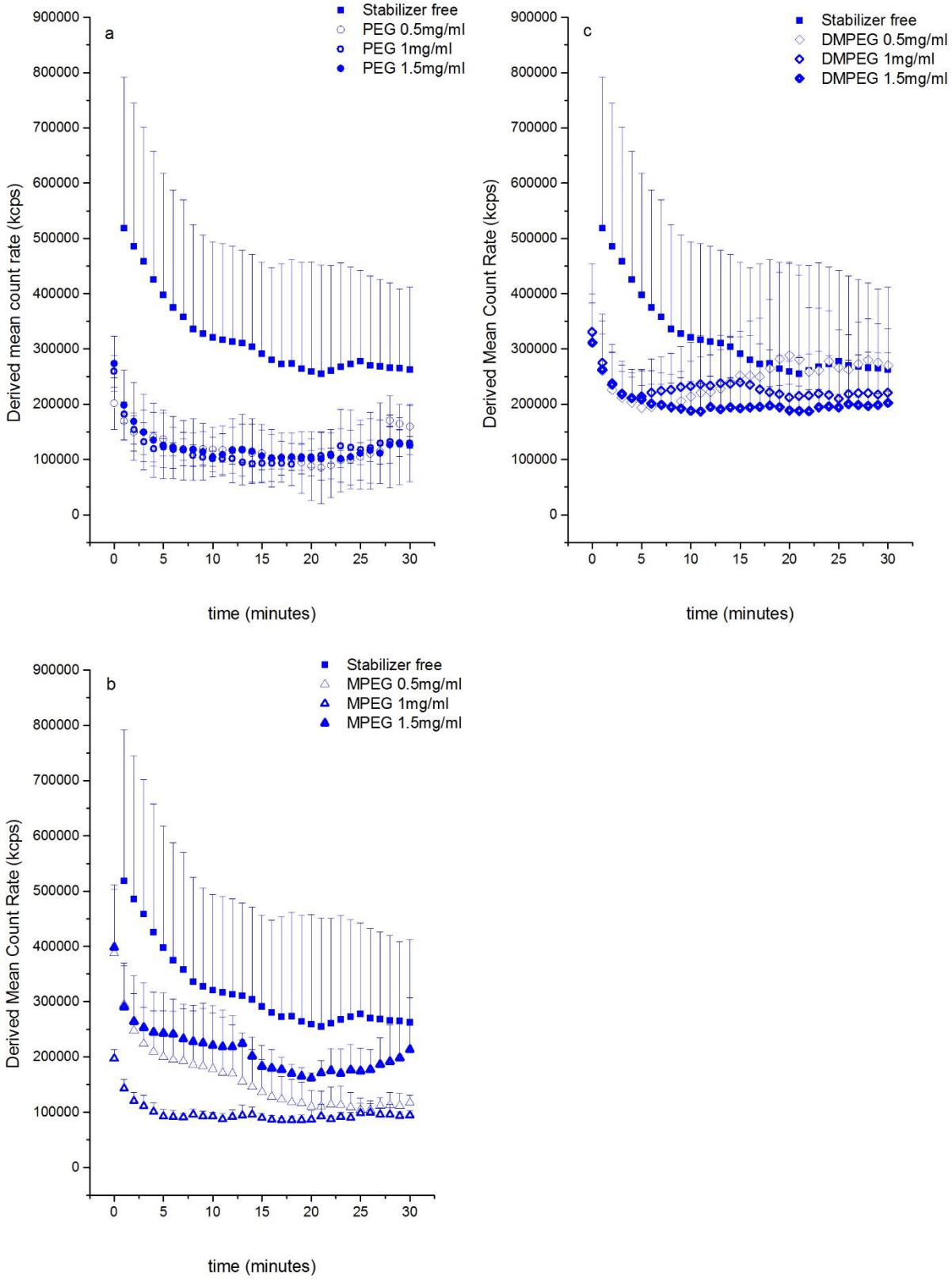

Fig. A.1.7 Derived Mean Count Rate (kcps) versus time (min) for KETO NPs with (a) PEG (b) MPEG and (c) DMPEG.

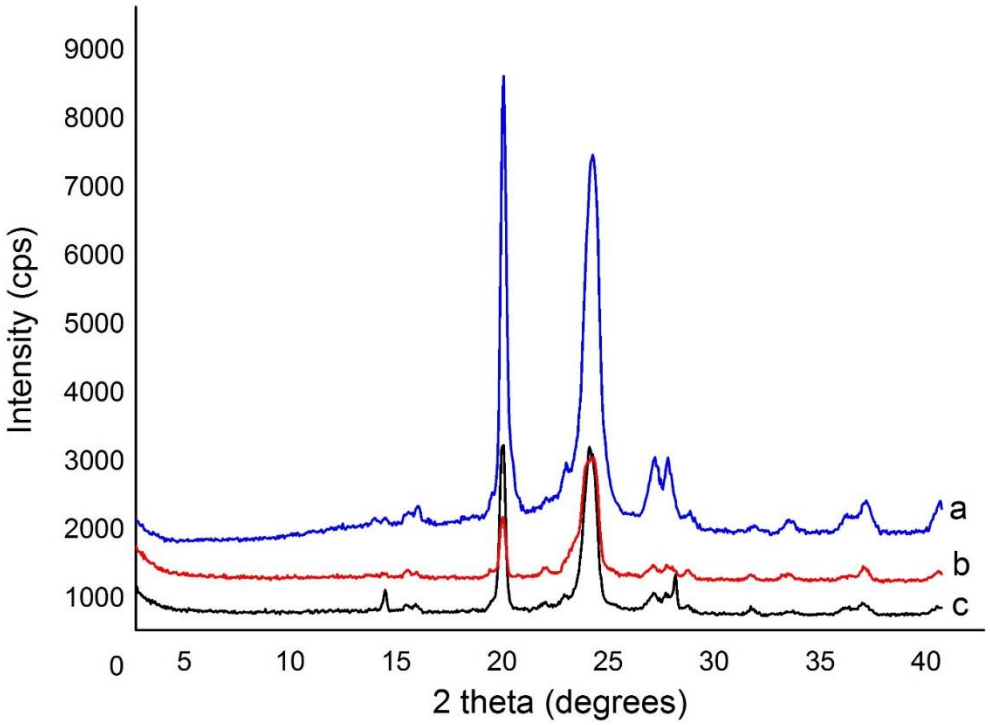

Fig. A.1.8 PXRD diffraction patterns of (a) dimethyl ether polyethylene glycol (DMPEG) (b) methyl ether polyethylene glycol (MPEG) (c) polyethylene glycol (PEG).

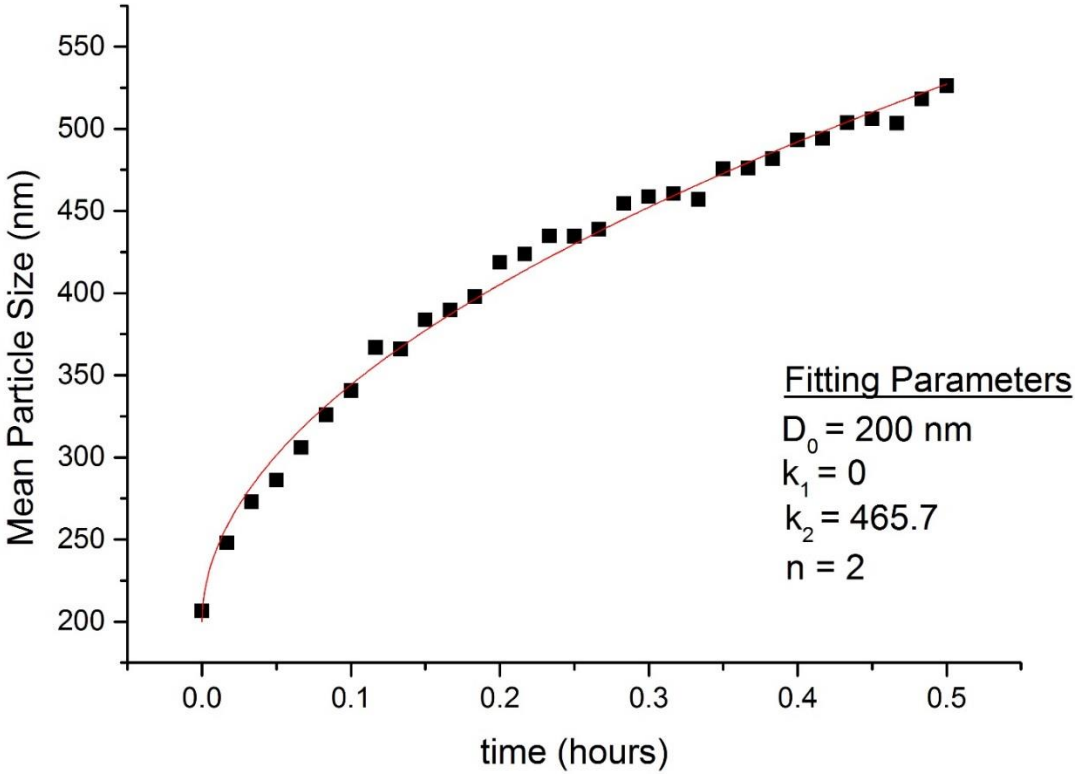

Fig. A.1.9 Experimental data and fitting results for mean particle size versus time for KETO DMPEG 1.5 mg.ml NPs.

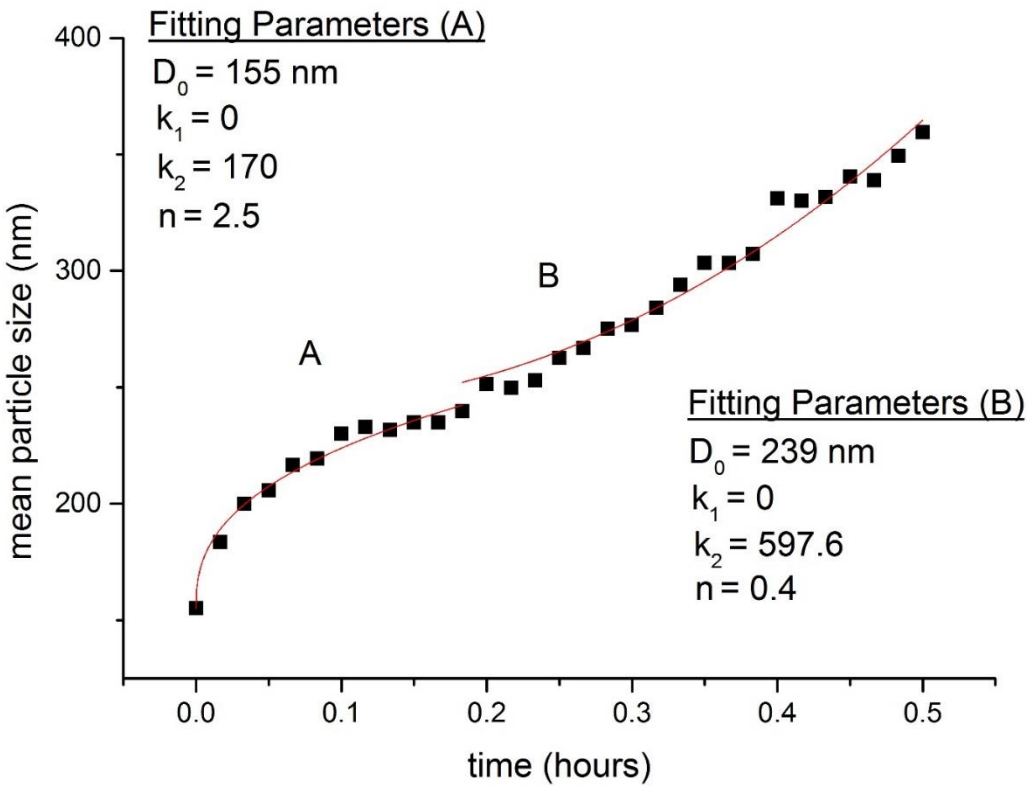

Fig. A.1.10 Experimental data and fitting results for mean particle size versus time for ITR stabilizer free NPs.

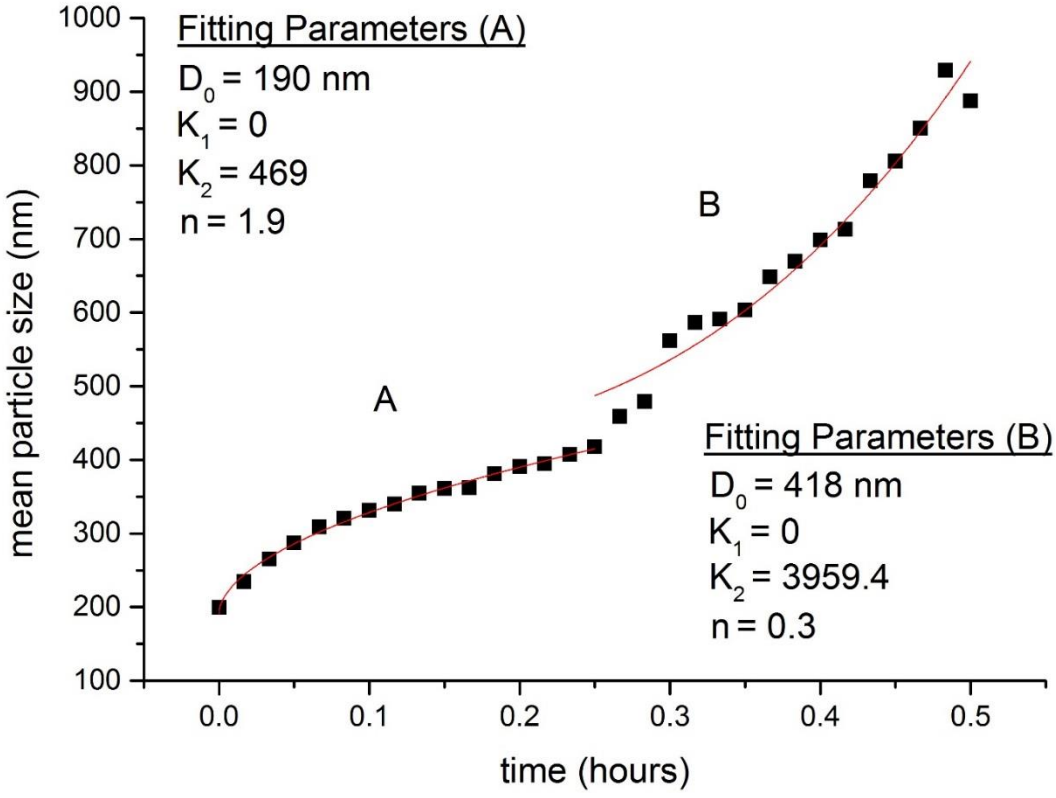

Fig. A.1.11 Experimental data and fitting results for mean particle size versus time for stabilizer free KETO NPs.

APPENDIX 2

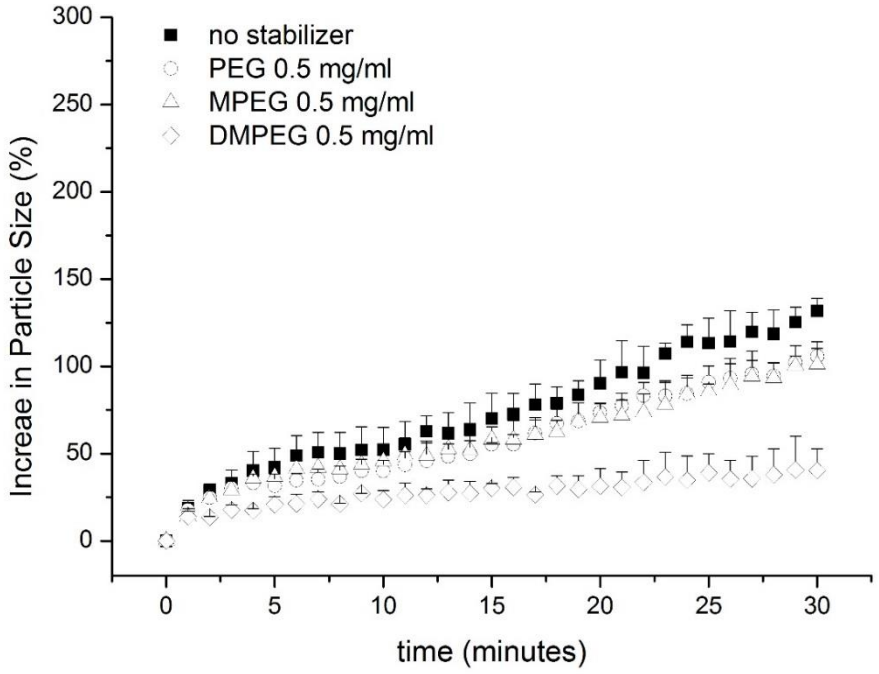

Fig. A.2.1 Increase in particle (%) versus time (minutes) for ITR nano-dispersions over 30 minutes obtained via DLS.

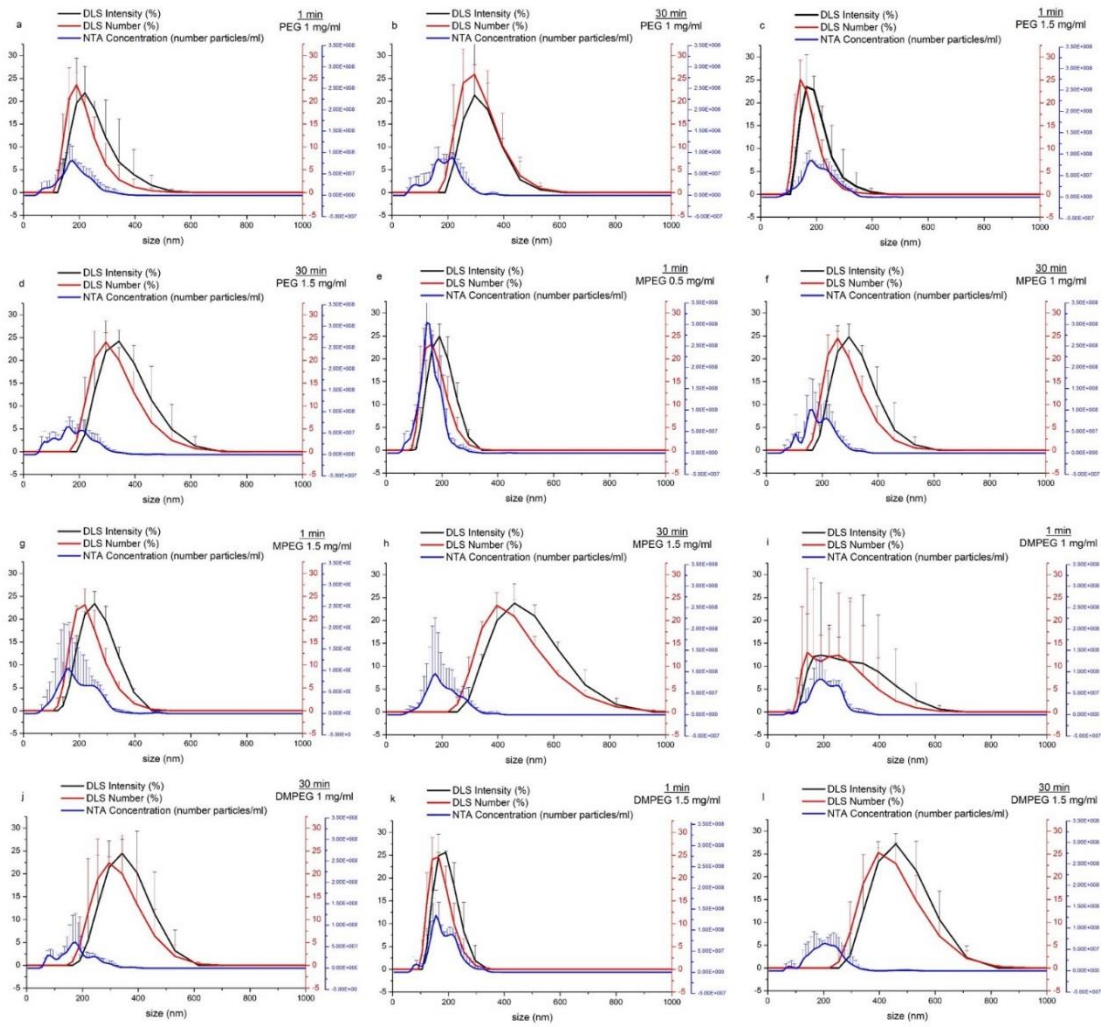

Fig. A.2.2 ITR particle size distributions for NTA (number based) and DLS (number and intensity based).

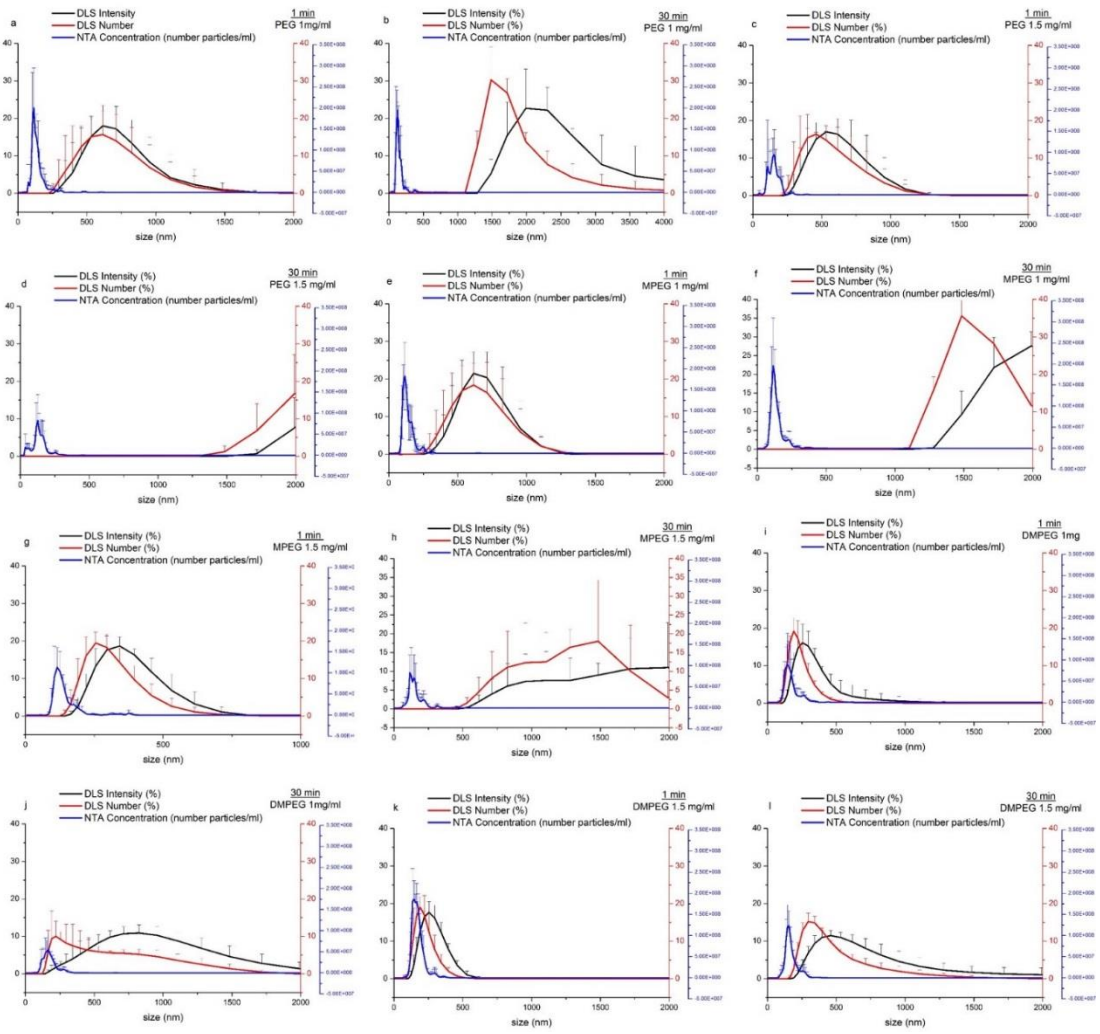

Fig. A.2.3 KETO particle size distributions for NTA (number based) and DLS (number and intensity based.

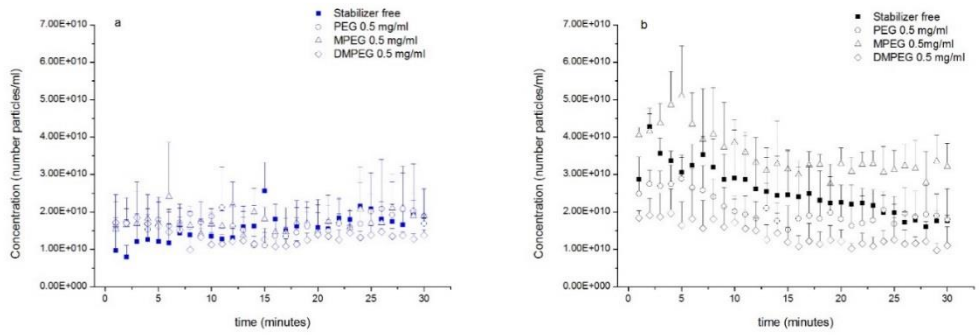

Fig. A.2.4 NTA concentration (number particles/ml) versus time (minutes) for (a) KETO NPs and (b) ITR NPs.

Table A.2.1. Mean particle size and size distribution measurements obtained for POS nano-dispersions using DLS and NTA at 1 minute. (n = 3)

	DLS (intensity based)		NTA (number based)	
	Z-ave ± SD (nm)	PDI ± SD	Mean ± SD (nm)	*Concentration (number particles/ml) ± RSD
Stabilizer free POS NPs	316 ± 29	0.0425 ± 0.03	195 ± 0	$5.3 \cdot 10^{10}$ ± 10.4
POS PEG 0.5 mg/ml	334 ± 19	0.058 ± 0.04	192 ± 27	$3.5 \cdot 10^{10}$ ± 28.3
POS PEG 1 mg/ml	315 ± 23	0.07 ± 0.05	197 ± 23	$4.1 \cdot 10^{10}$ ± 26.8
POS PEG 1.5 mg/ml	479 ± 123	0.06 ± 0.03	195 ± 42	$4.1 \cdot 10^{10}$ ± 53.7
POS MPEG 0.5 mg/ml	418 ± 109	0.04 ± 0.02	245 ± 124	$2.2 \cdot 10^{10}$ ± 63.6
POS MPEG 1 mg/ml	270 ± 27	0.05 ± 0.04	188 ± 35	$1.4 \cdot 10^{11}$ ± 142.9
POS MPEG 1.5 mg/ml	280 ± 17	0.07 ± 0.03	215 ± 40	$1.9 \cdot 10^{11}$ ± 163.2
POS DMPEG 0.5 mg/ml	318 ± 39	0.09 ± 0.14	190 ± 28	$4.2 \cdot 10^{10}$ ± 26.2
POS DMPEG 1 mg/ml	319 ± 18	0.07 ± 0.03	226 ± 18	$2.5 \cdot 10^{10}$ ± 48.0
POS DMPEG 1.5 mg/ml	315 ± 11	0.10 ± 0.05	217 ± 17	$2.0 \cdot 10^{10}$ ± 32.0

*PDI = polydispersity index, SD = standard deviation, RSD = relative standard deviation

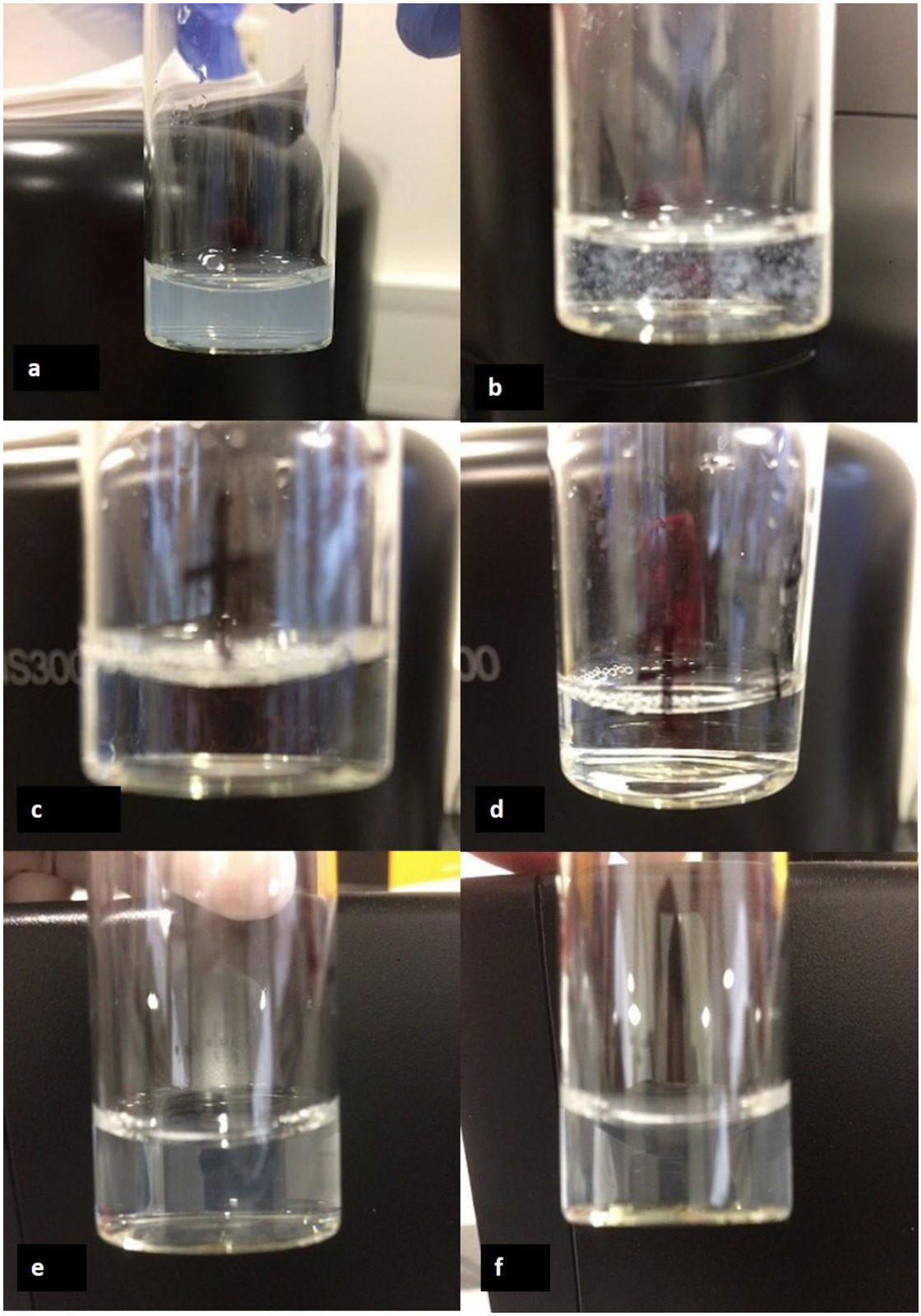

Fig. A.2.5 Photographs of POS MPEG 0.5 mg/ml NPs at (a) 0 minutes and (b) after 30 minutes; KETO DMPEG 1mg/ml NPS at (c) 0 minutes (d) after 30 minutes; ITR stabilizer free NPs at (e) 0 minutes and (f) 30 minutes.

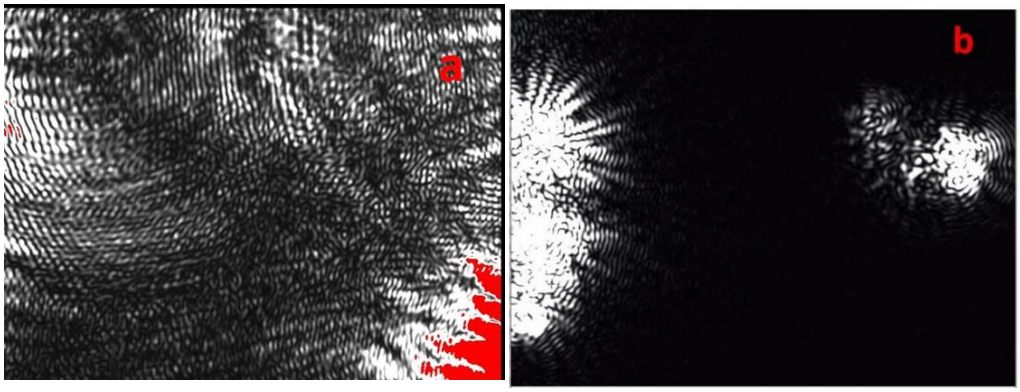

Fig. A.2.6 Screenshot of viewing field in NTA software for (a) POS DMPEG 0.5 mg/ml at 30 minutes and (b) POS PEG 0.5 mg/ml at 30 minutes.

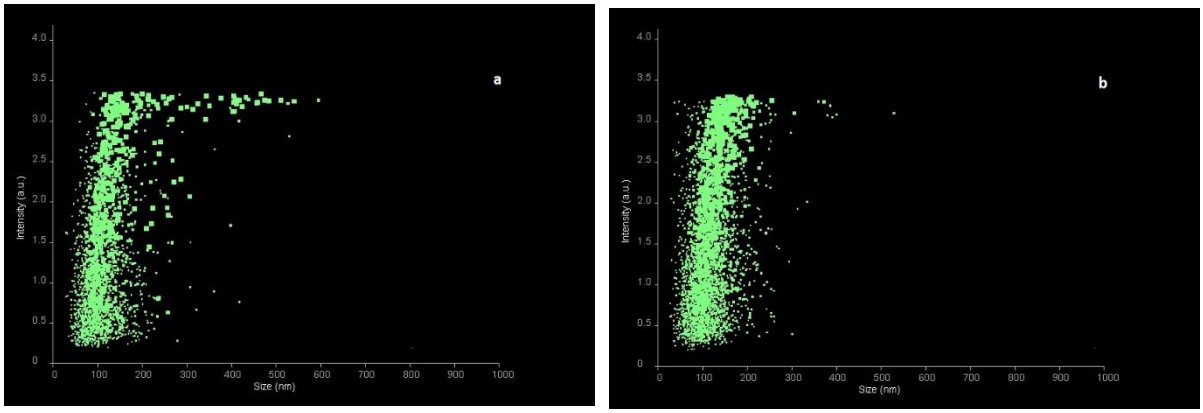

Fig. A.2.7 NTA scattergram intensity (a.u.) vs. light for KETO MPEG 0.5 mg/ml NPs at (a) 1 minutes and (b) 30 minutes.

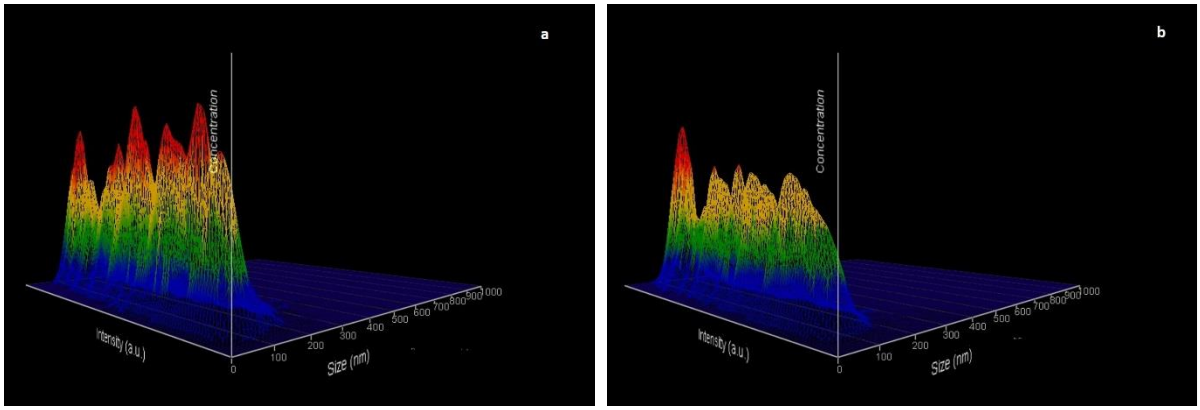

Fig. A.2.8 3-D graph (size vs. intensity vs. concentration) for KETO MPEG 0.5 mg/ml NPs at (a) 1 minutes and (b) 30 minutes.

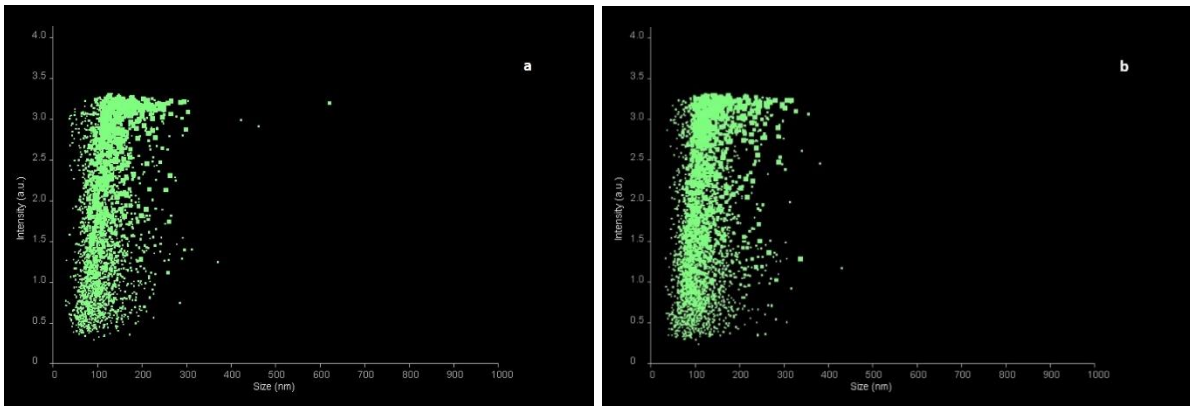

Fig. A.2.9 NTA scattergram intensity (a.u.) vs. light for KETO MPEG 1 mg/ml NPs at (a) 1 minutes and (b) 30 minutes.

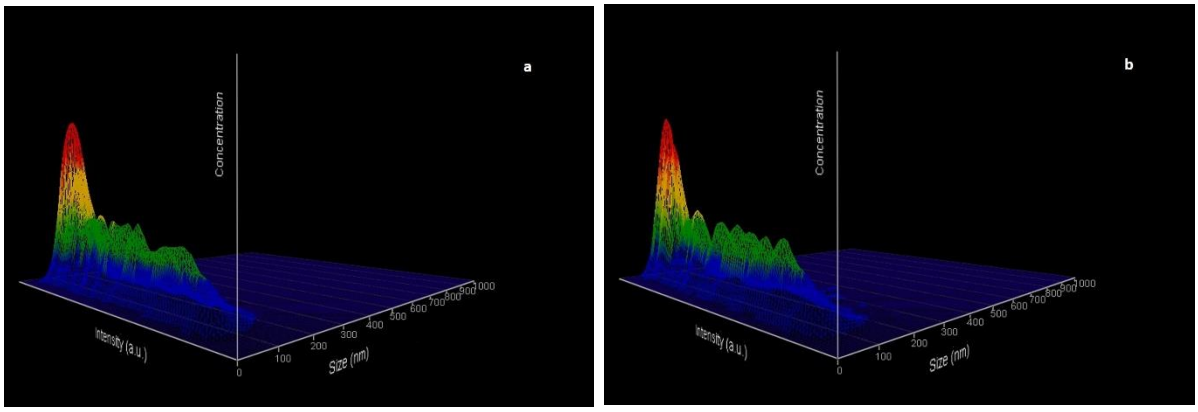

Fig. A.2.10 3-D graph (size vs. intensity vs. concentration) for KETO MPEG 1 mg/ml NPs at (a) 1 minutes and (b) 30 minutes.

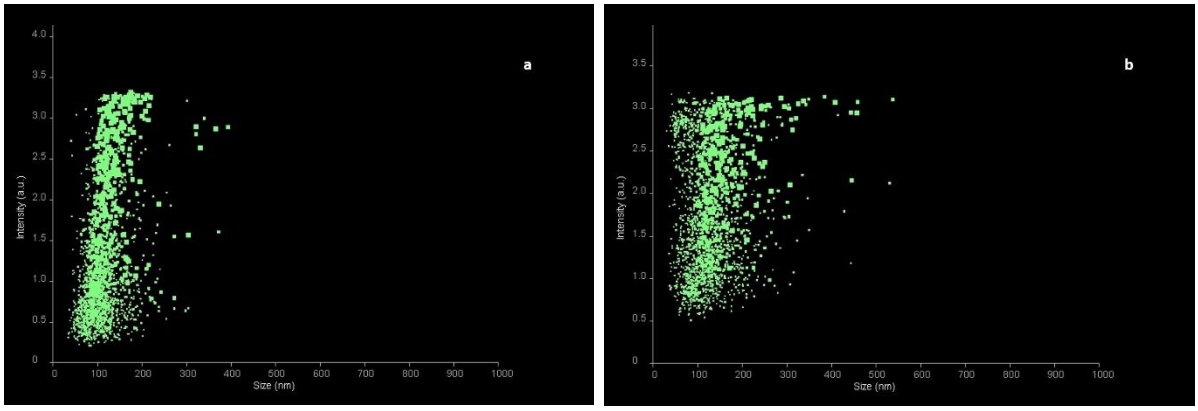

Fig. A.2.11 NTA scattergram intensity (a.u.) vs. light for KETO MPEG 1.5 mg/ml NPs at (a) 1 minutes and (b) 30 minutes.

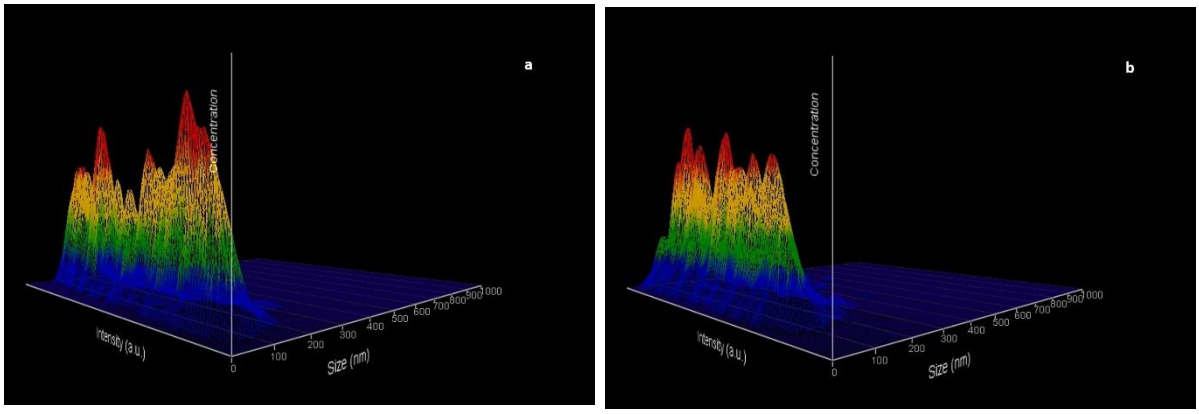

Fig. A.2.12 3-D graph (size vs. intensity vs. concentration) for KETO MPEG 1.5 mg/ml NPs at (a) 1 minutes and (b) 30 minutes.

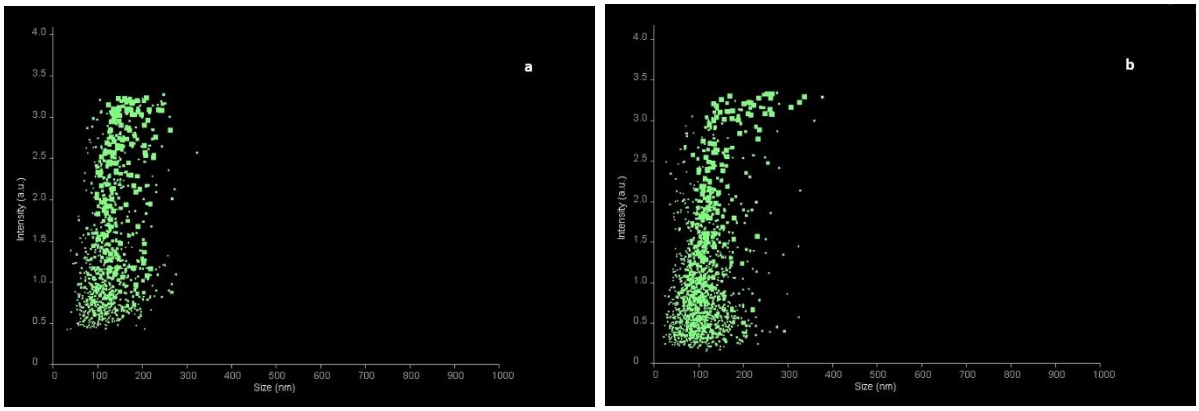

Fig. A.2.13 NTA scattergram intensity (a.u.) vs. light for KETO PEG 0.5 mg/ml NPs at (a) 1 minutes and (b) 30 minutes.

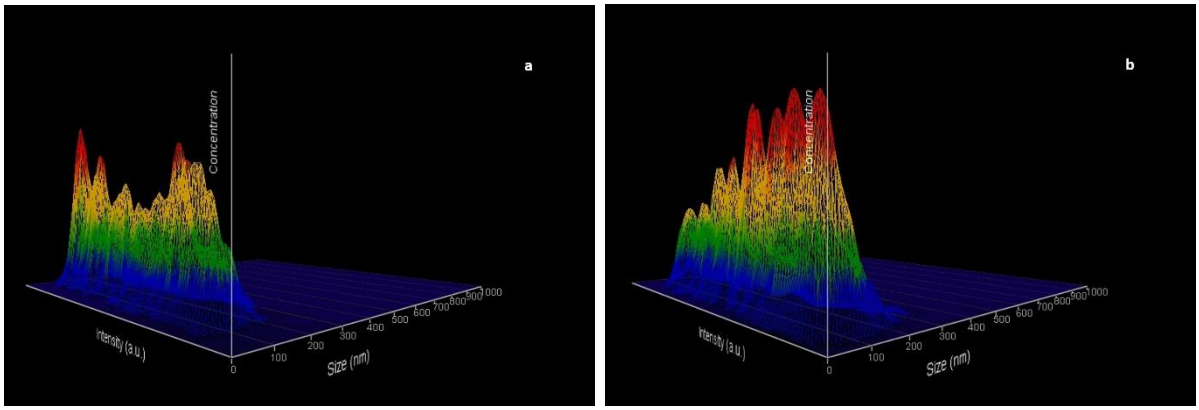

Fig. A.2.14 3-D graph (size vs. intensity vs. concentration) for KETO PEG 0.5 mg/ml NPs at (a) 1 minutes and (b) 30 minutes.

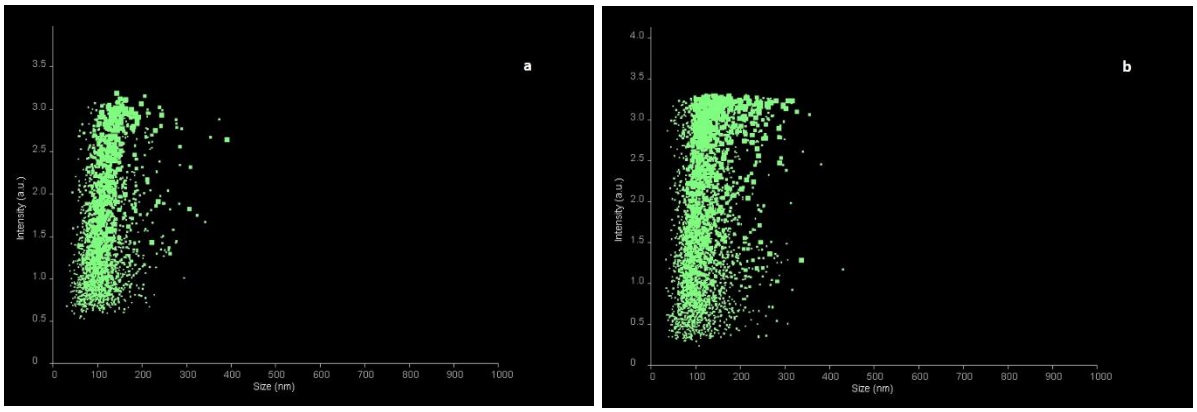

Fig. A.2.15 NTA scattergram intensity (a.u.) vs. light for KETO PEG 1 mg/ml NPs at (a) 1 minutes and (b) 30 minutes.

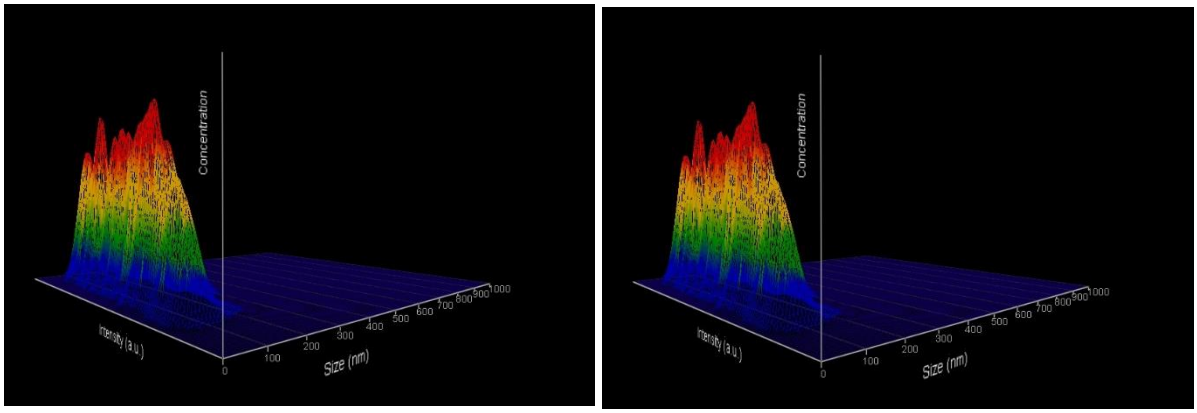

Fig. A.2.16 3-D graph (size vs. intensity vs. concentration) for KETO PEG 1 mg/ml NPs at (a) 1 minutes and (b) 30 minutes.

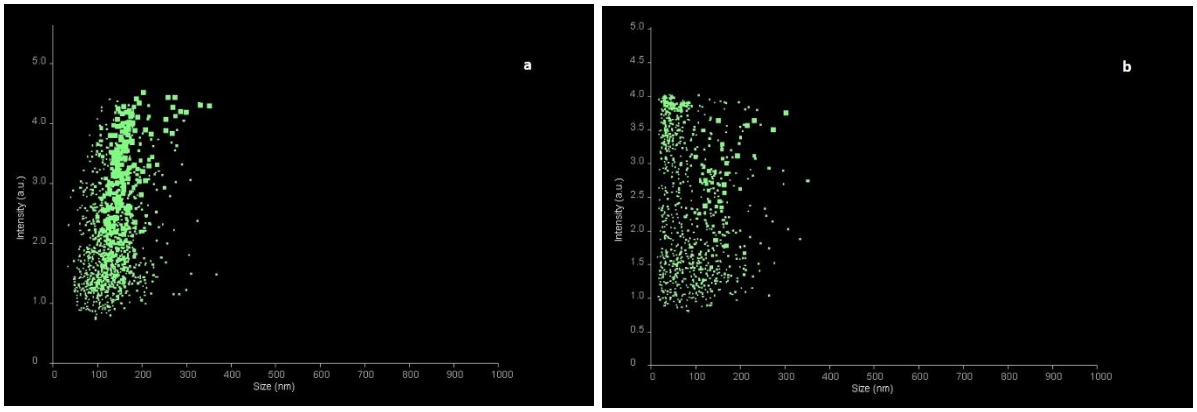

Fig. A.2.17 NTA scattergram intensity (a.u.) vs. light for KETO PEG 1.5 mg/ml NPs at (a) 1 minutes and (b) 30 minutes.

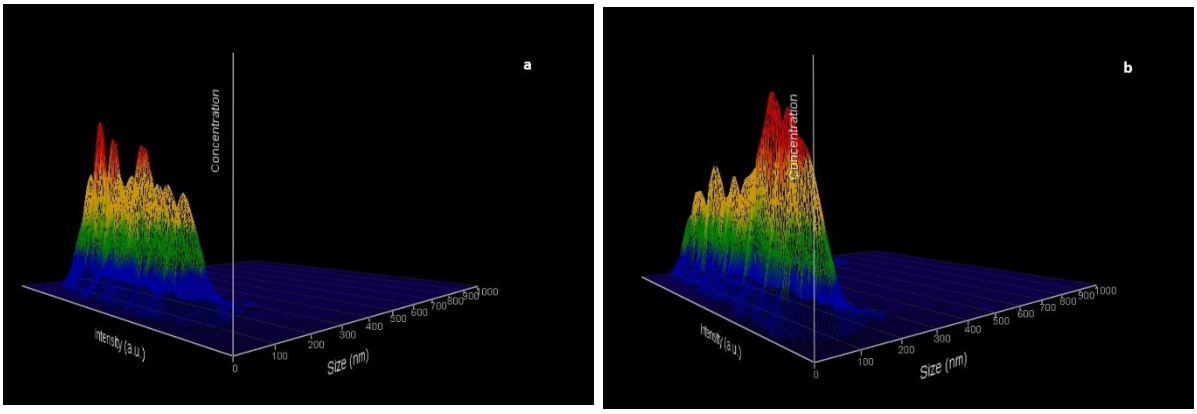

Fig. A.2.18 3-D graph (size vs. intensity vs. concentration) for KETO PEG 1.5 mg/ml NPs at (a) 1 minutes and (b) 30 minutes.

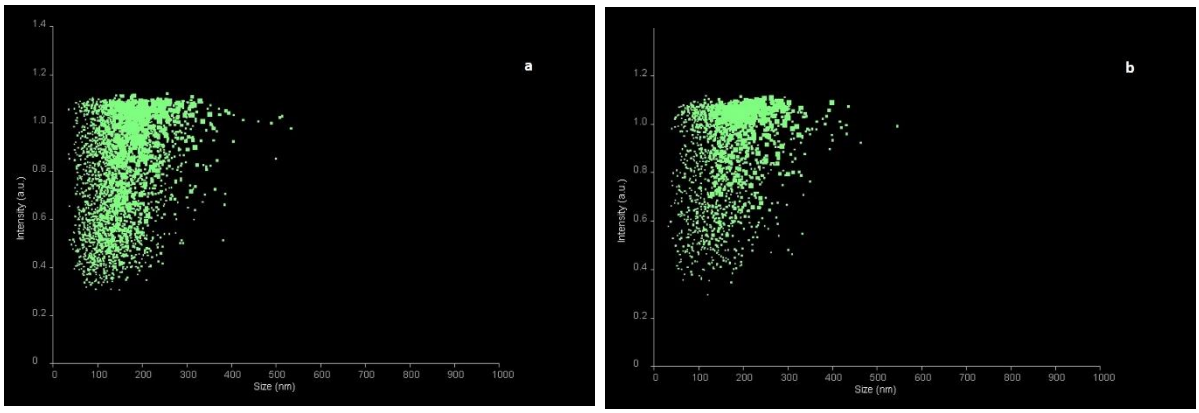

Fig. A.2.19 NTA scattergram intensity (a.u.) vs. light for ITR PEG 0.5 mg/ml NPs at (a) 1 minutes and (b) 30 minutes.

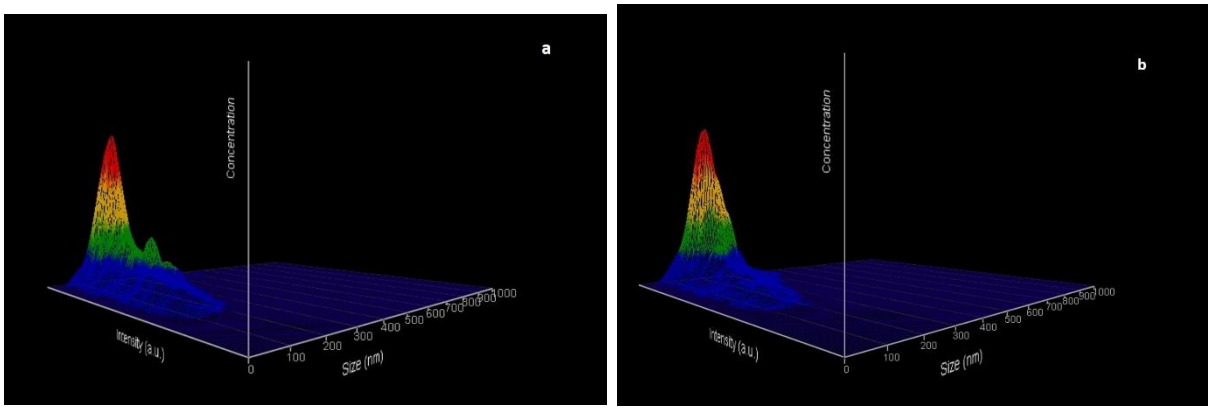

Fig. A.2.20 3-D graph (size vs. intensity vs. concentration) for ITR PEG 0.5 mg/ml NPs at (a) 1 minutes and (b) 30 minutes.

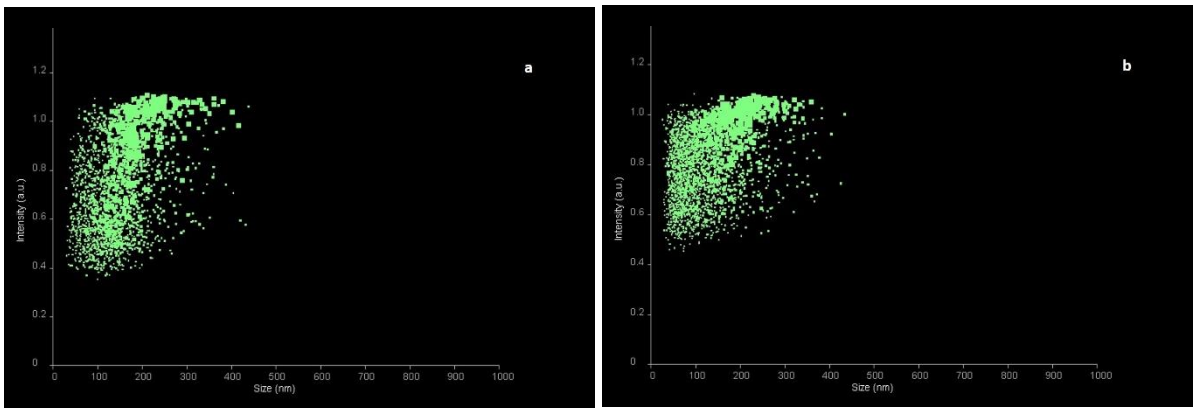

Fig. A.2.21 NTA scattergram intensity (a.u.) vs. light for ITR PEG 1 mg/ml NPs at (a) 1 minutes and (b) 30 minutes.

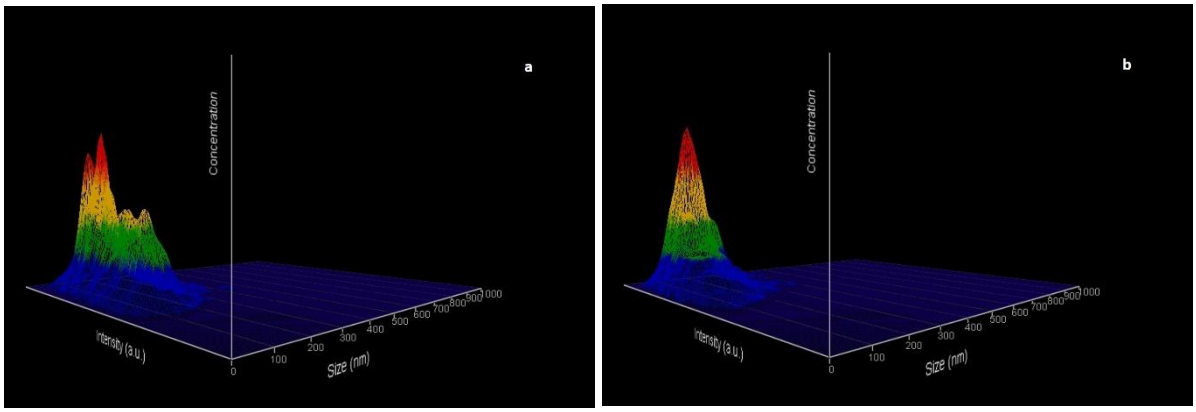

Fig. A.2.22 3-D graph (size vs. intensity vs. concentration) for ITR PEG 1 mg/ml NPs at (a) 1 minutes and (b) 30 minutes.

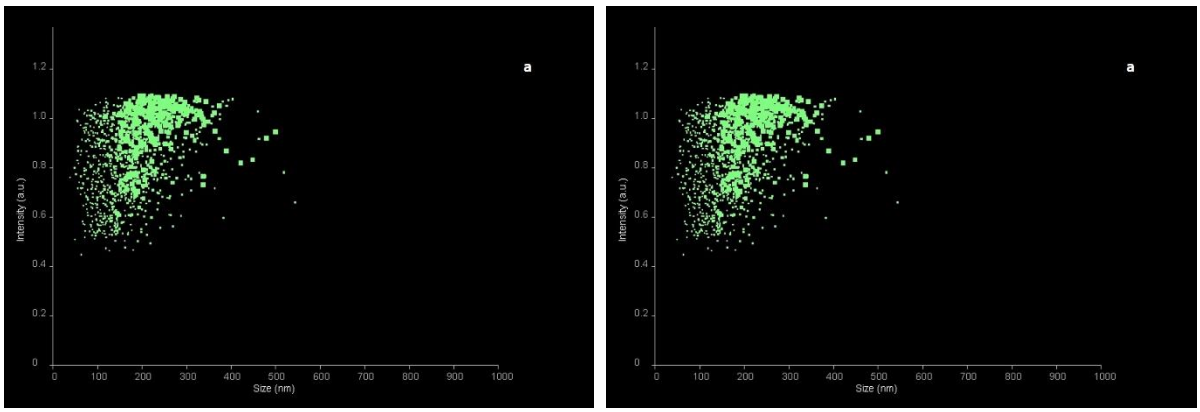

Fig. A.2.23 NTA scattergram intensity (a.u.) vs. light for ITR PEG 1.5 mg/ml NPs at (a) 1 minutes and (b) 30 minutes.

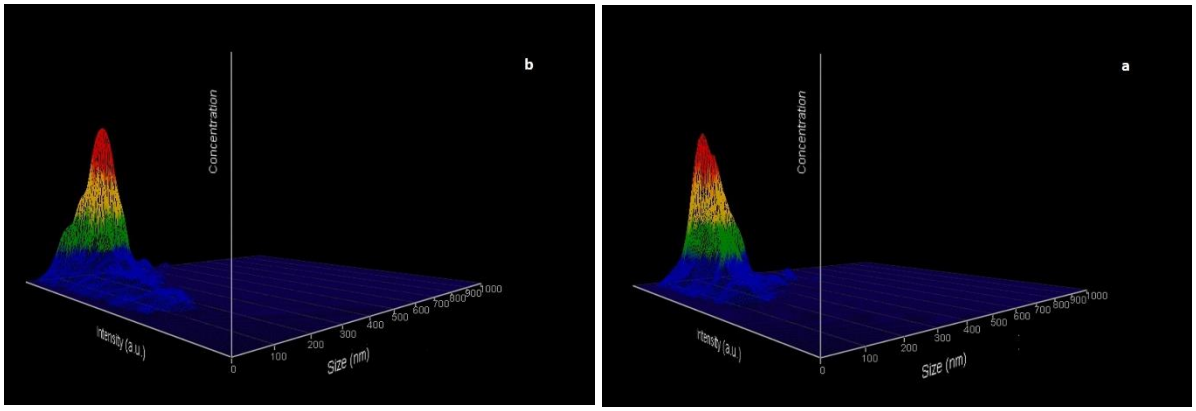

Fig. A.2.24 3-D graph (size vs. intensity vs. concentration) for ITR PEG 1.5 mg/ml NPs at (a) 1 minutes and (b) 30 minutes.

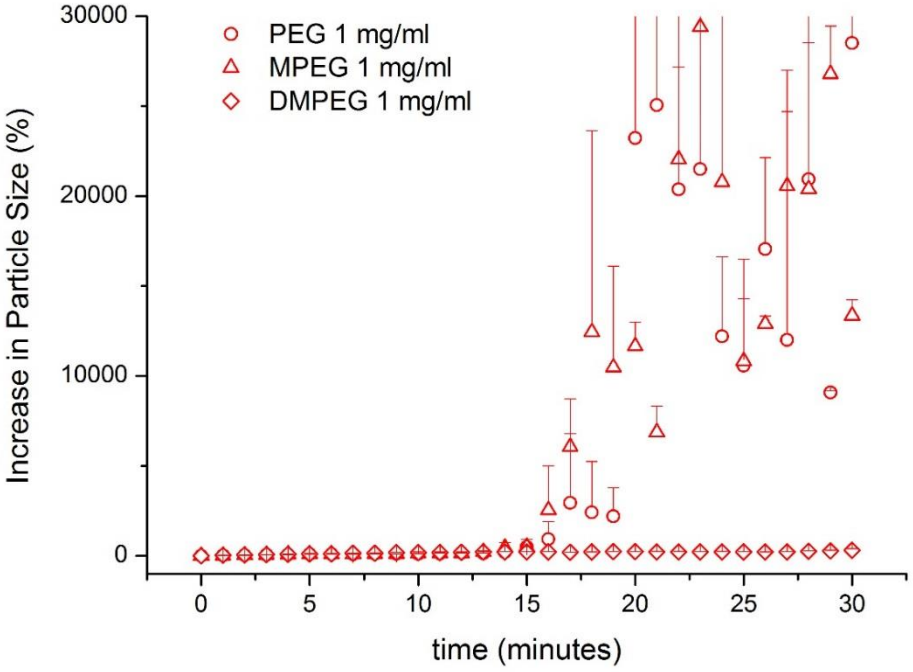

Fig. A.2.25 Increase in particle (%) versus time (minutes) for POS nano-suspensions over 30 minutes obtained via DLS.

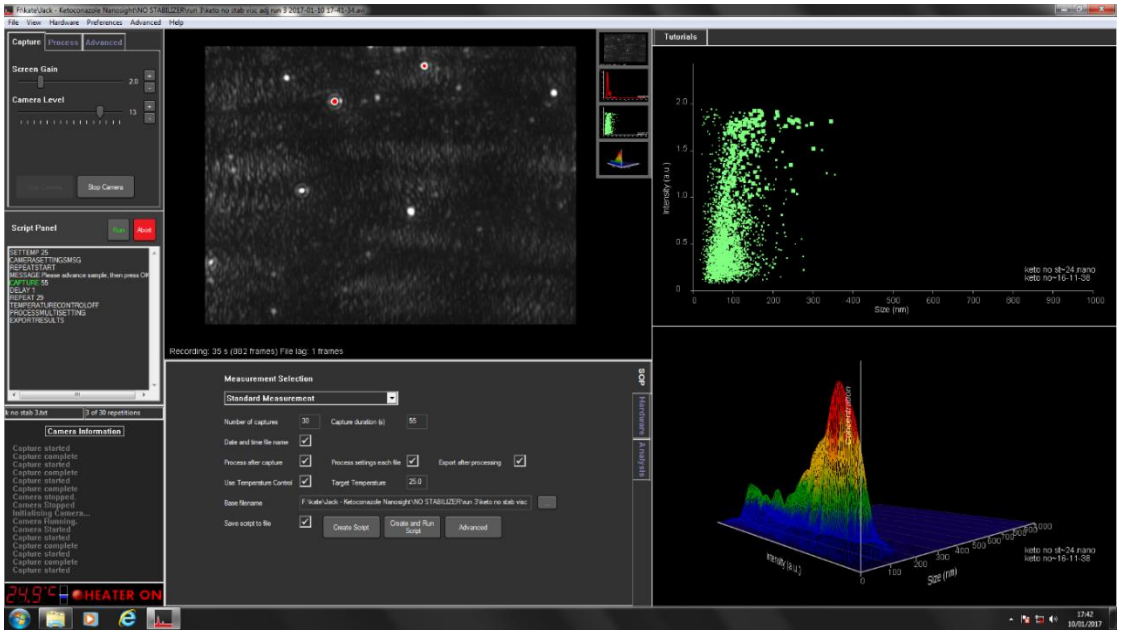

Fig. A.2.26 Screen shot of detection settings used for KETO NPs analysis via NTA.

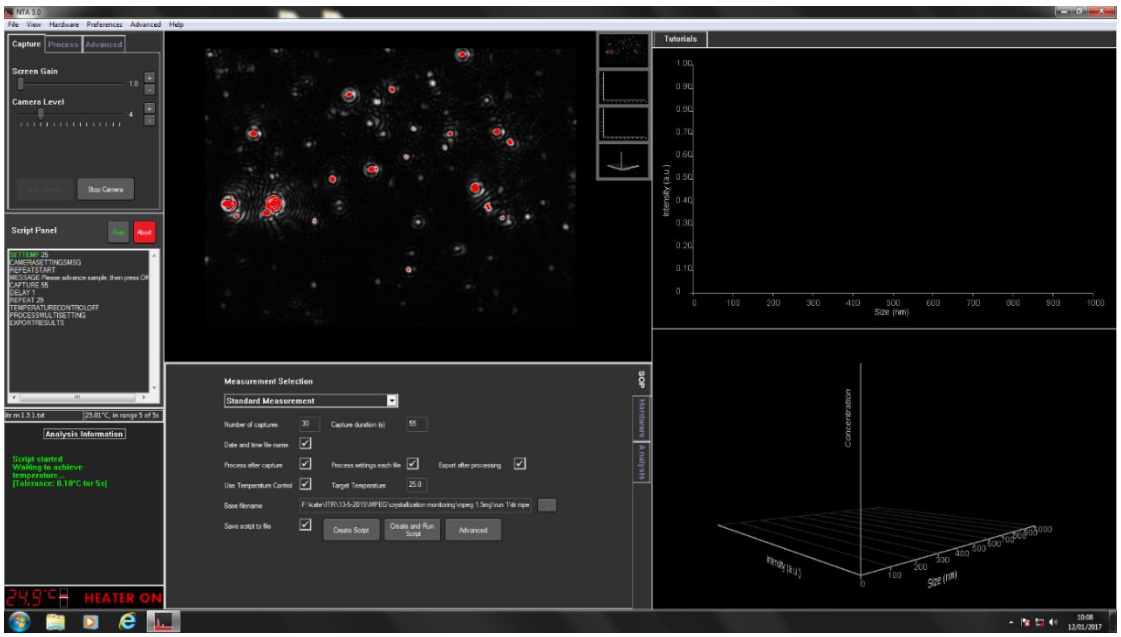

Fig. A.2.27 Screen shot of detection settings used for ITR NPs analysis via NTA.

APPENDIX 3

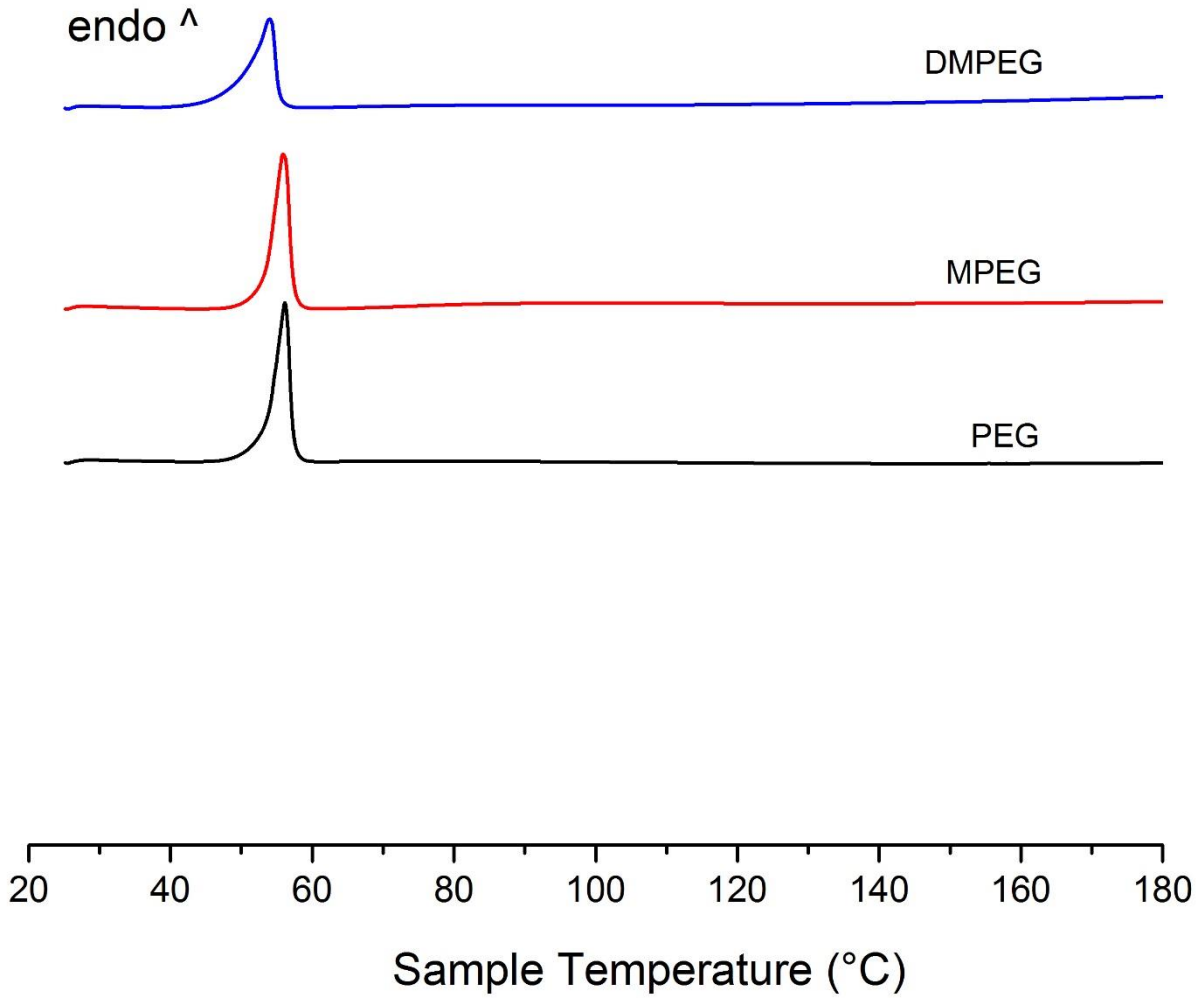

Fig. A.3.1. DSC curves for pure DMPEG, MPEG and PEG.

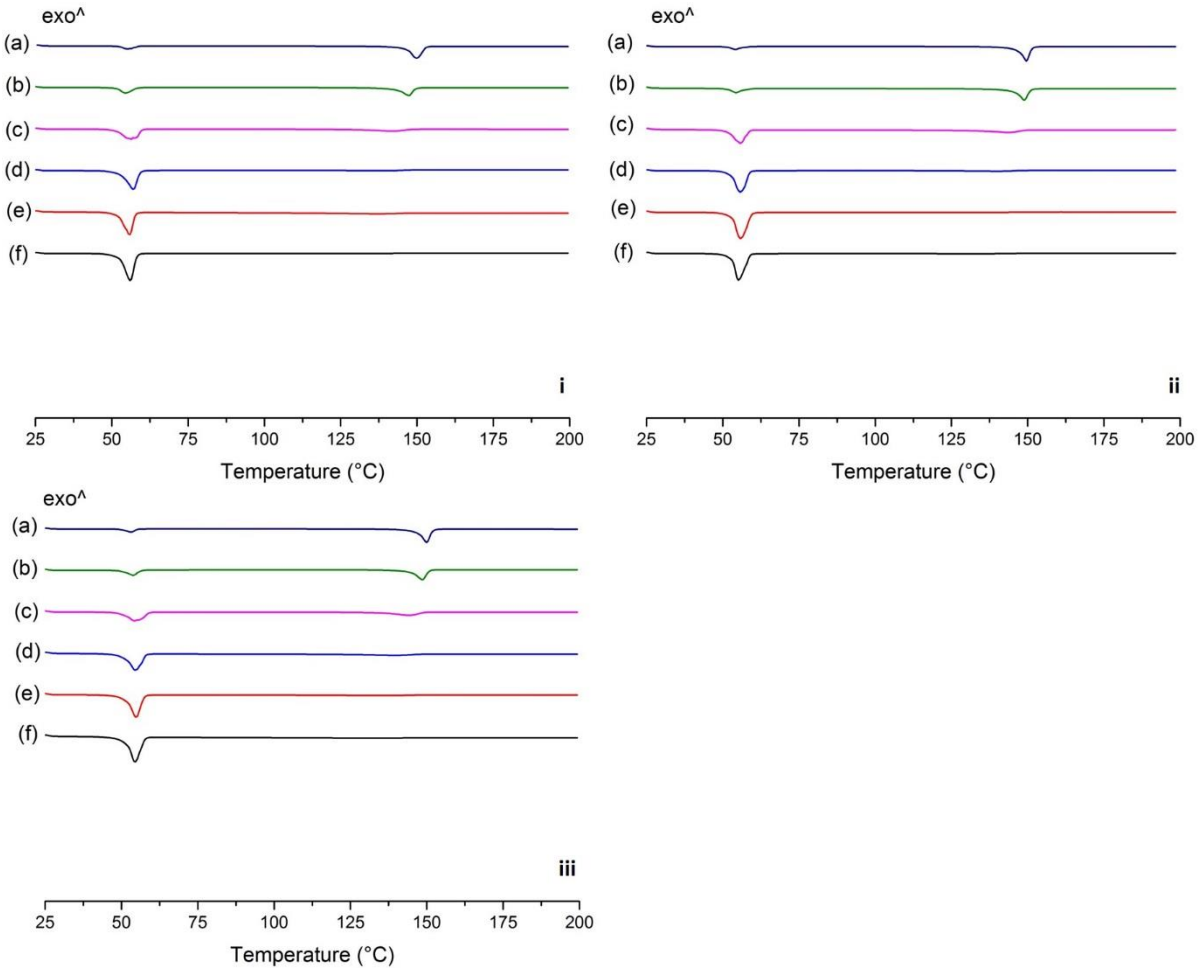

Fig. A.3.2. DSC curves for KETO and (i) PEG (ii) MPEG (iii) DMPEG and (a) 0.95 KETO weight fraction (b) 0.9 KETO weight fraction (c) 0.85 KETO weight fraction (d) 0.8 KETO weight fraction (e) 0.7 KETO weight fraction (f) 0.5 KETO weight fraction.

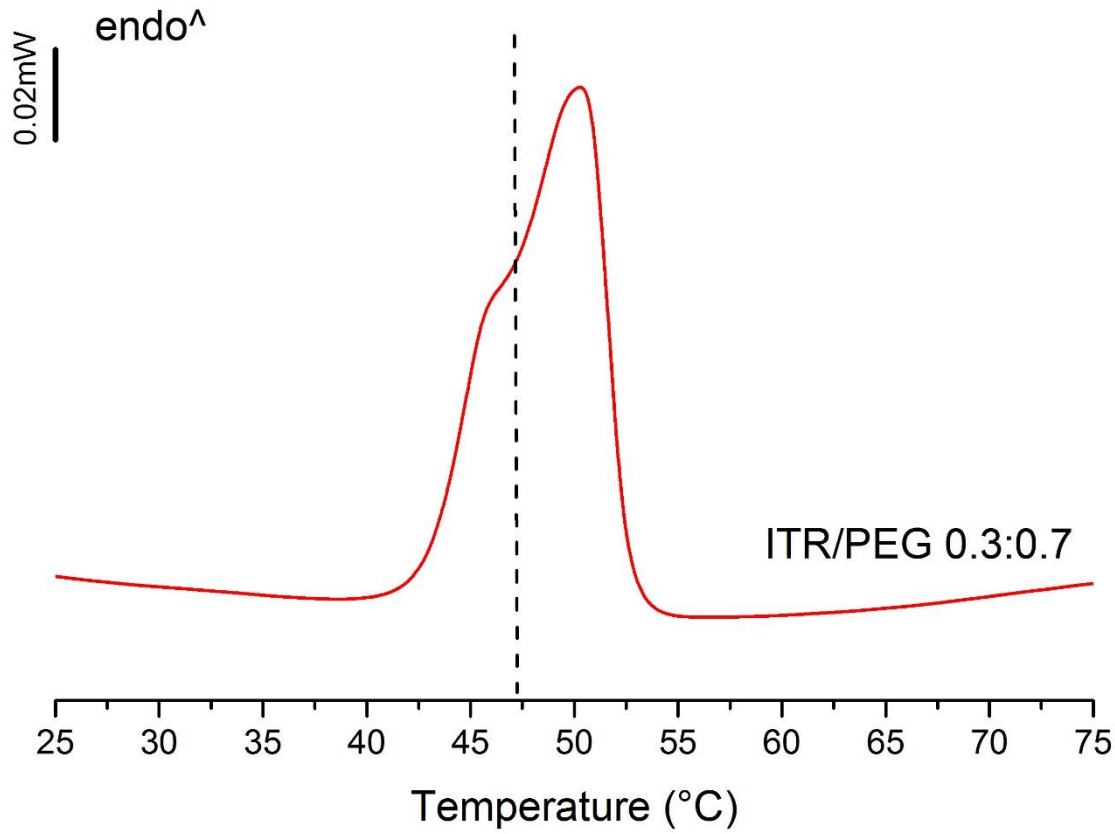

Fig. A.3.3. DSC curve for ITR and PEG 0.3:0.7 weight ratio on second heating using Perkin Elmer DSC. The black dashed line represents possible overlap of two individual melting events.

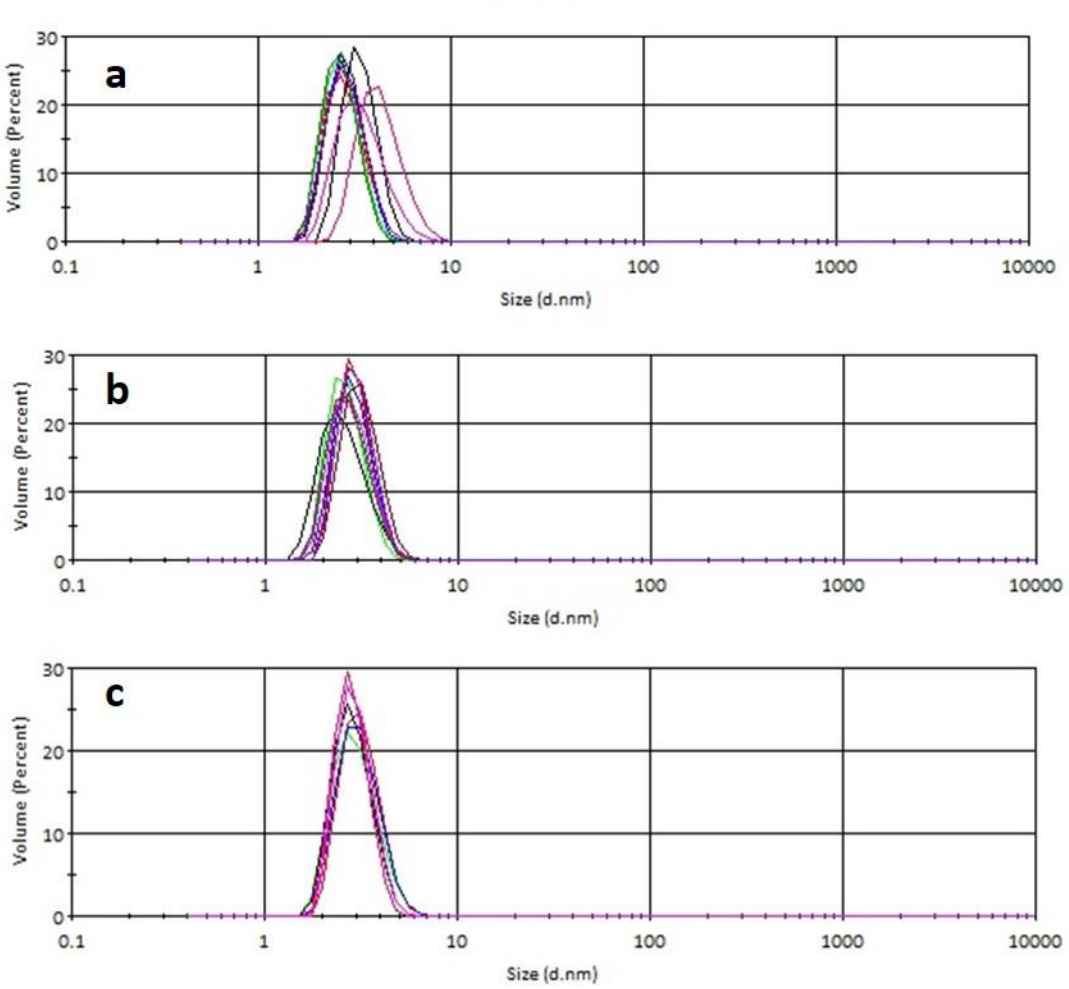

Fig. A.3.4. Volume based size distribution for (a) PEG (b) MPEG (c) DMPEG 5mg/ml solution alone obtained using DLS at 25 °C after gentle shaking for 5 minutes.

APPENDIX 4

Table A.4.1. Properties of sugars investigated as potential matrix formers for ITR NMPs.

Sugar	Melting point (°C)	Glass transition temperature (°C)	Reducing/non-reducing property	Solid state on spray drying
Lactose	213	101[a)]	reducing	amorphous
Trehalose	203	95[b)]	non-reducing	amorphous
Sucrose	187	46[b)]	non-reducing	amorphous
Mannitol	165	13[c)]	non-reducing	crystalline
Maltose	123	87[d)]	reducing	amorphous
Raffinose	82	109[e)]	non-reducing	amorphous

a) (Roos and Karel, 1991)**, b)** (Simperler et al., 2006)**, c)** (Yu et al., 1998)**, d)** (Foster et al., 2006)**, e)** (Ramos et al., 2005)**.**

Table A.4.2. Itraconazole and anhydrous sugar properties including molecular weight, aqueous solubility, hydrogen bond donor and acceptor counts.

Material	Molecular weight (MW)	Aqueous solubility (mg/ml)	Hydrogen bond donor count	Hydrogen bond acceptor count
Itraconazole	706	0.001[a)]	0	9
Lactose	342	195[b)]	8	11
Trehalose	342	68.9[c)]	8	11
Sucrose	342	2100[b)]	8	11
Mannitol	182	216[b)]	6	6
Raffinose	504	203[d)]	11	16
Maltose	342	780[b)]	8	11

[a)] (Matteucci et al., 2009), [b)] (Yalkowsky and Dannenfelser, 1992), [c)] (Jain and Roy, 2009), [d)] (Storey et al., 1998).

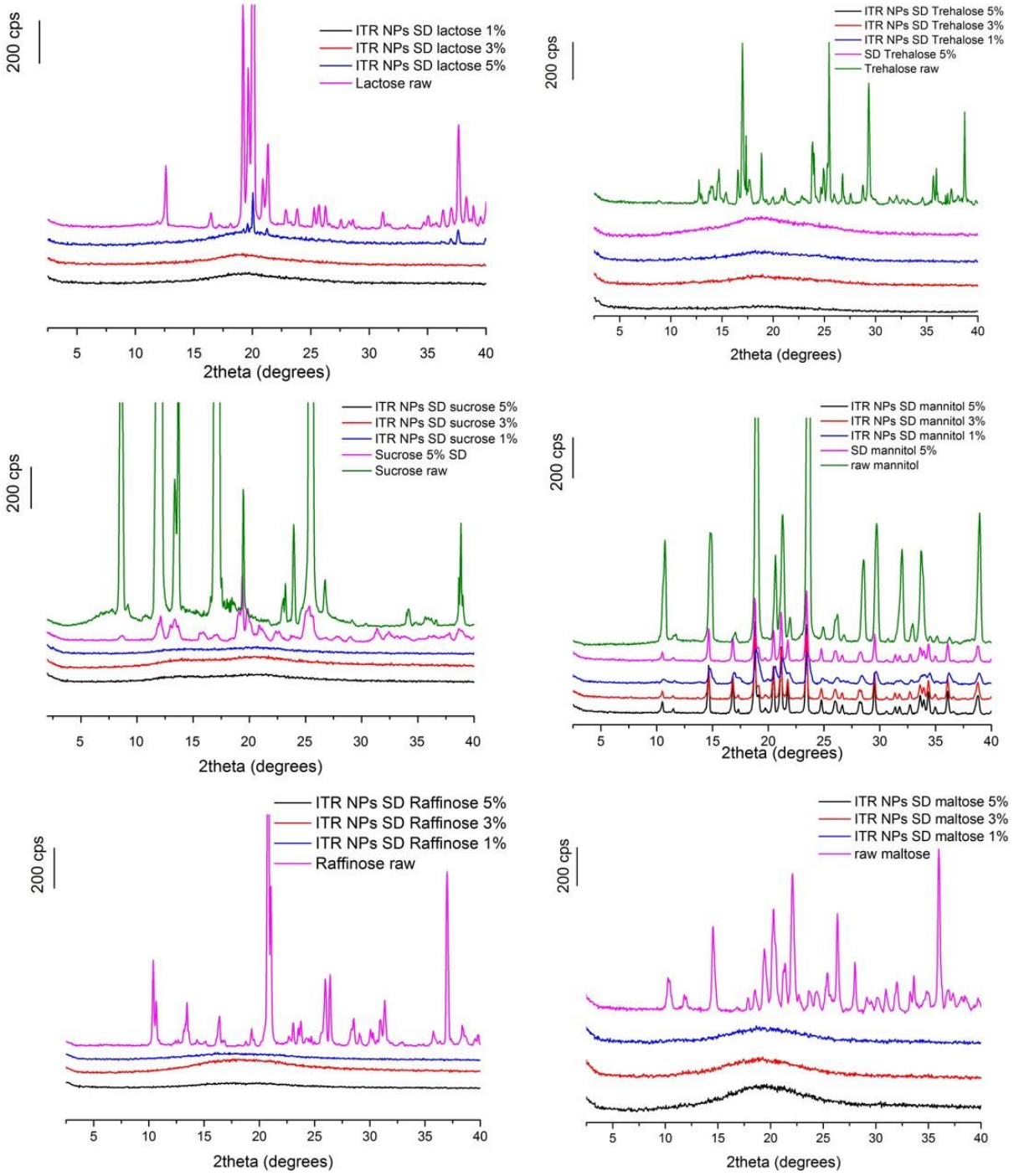

Fig. A.4.1. PXRD diffraction patterns for spray dried ITR NPs with lactose, trehalose, sucrose, mannitol, raffinose and maltose at 1, 3 and 5 % (w/v).

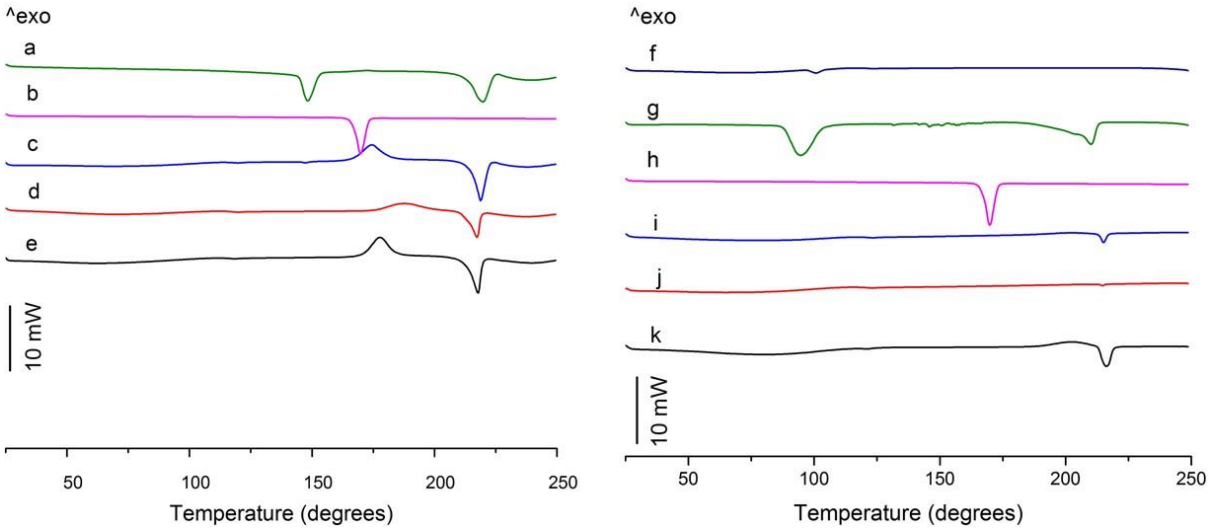

Fig. A.4.2. DSC traces of: (a) lactose raw (b) ITR raw (c) ITR NPs spray dried with 5% lactose (d) ITR NPs spray dried with 3% lactose (e) ITR NPs spray dried with 1% lactose (f) spray dried 5% trehalose (g) trehalose raw (h) ITR raw (i) ITR NPs spray dried with 5% trehalose (j) ITR NPs spray dried with 3% trehalose and (k) ITR NPs spray dried with 1% trehalose.

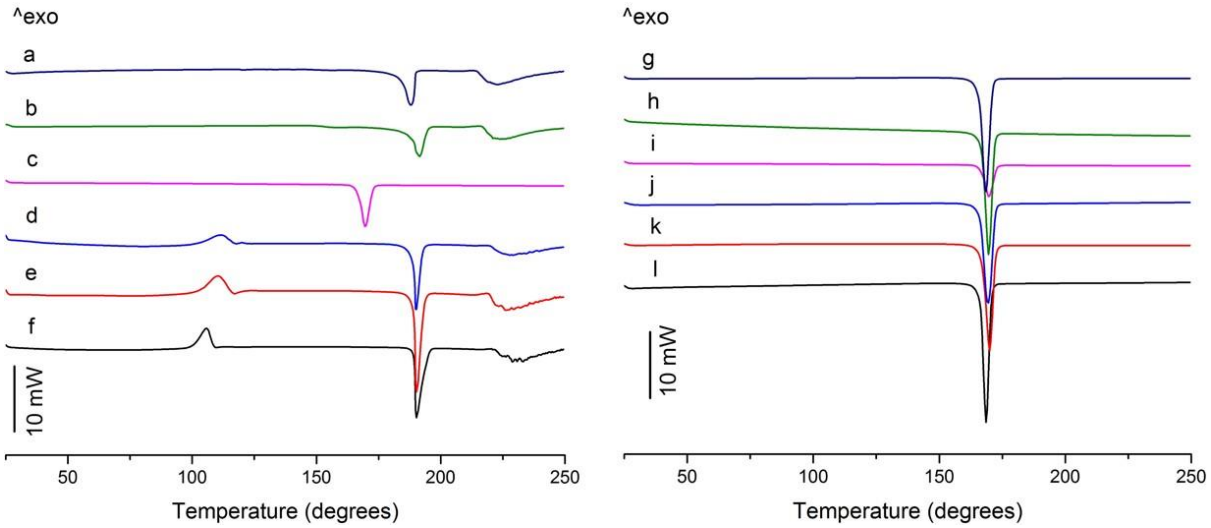

Fig. A.4.3. DSC traces of: (a) spray dried sucrose 5% (b) sucrose raw (c) ITR raw (d) ITR NPs spray dried with 5% sucrose (e) ITR NPs spray dried with 3% sucrose (f) ITR NPs spray dried with 1% sucrose (g) spray dried mannitol 5% (h) mannitol raw (i) ITR raw (j) ITR NPs spray dried with 5% mannitol (k) ITR NPs spray dried with 3% mannitol and (l) ITR NPs spray dried with 1% mannitol.

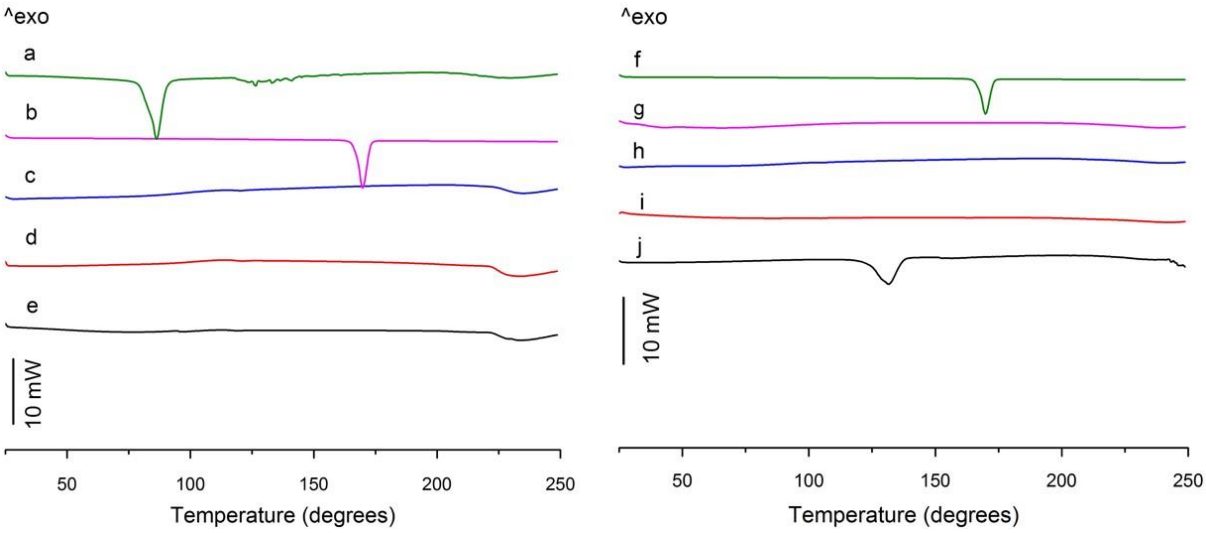

Fig. A.4.4. DSC traces of: (a) raffinose raw (b) ITR raw (c) ITR NPs spray dried with 5% raffinose (d) ITR NPs spray dried with 3% raffinose (e) ITR NPs spray dried with 1% raffinose (f) ITR raw (g) ITR NPs spray dried with maltose 5% (h) ITR NPs spray dried with 3% maltose (i) ITR NPs spray dried with 5% maltose and (j) maltose raw.

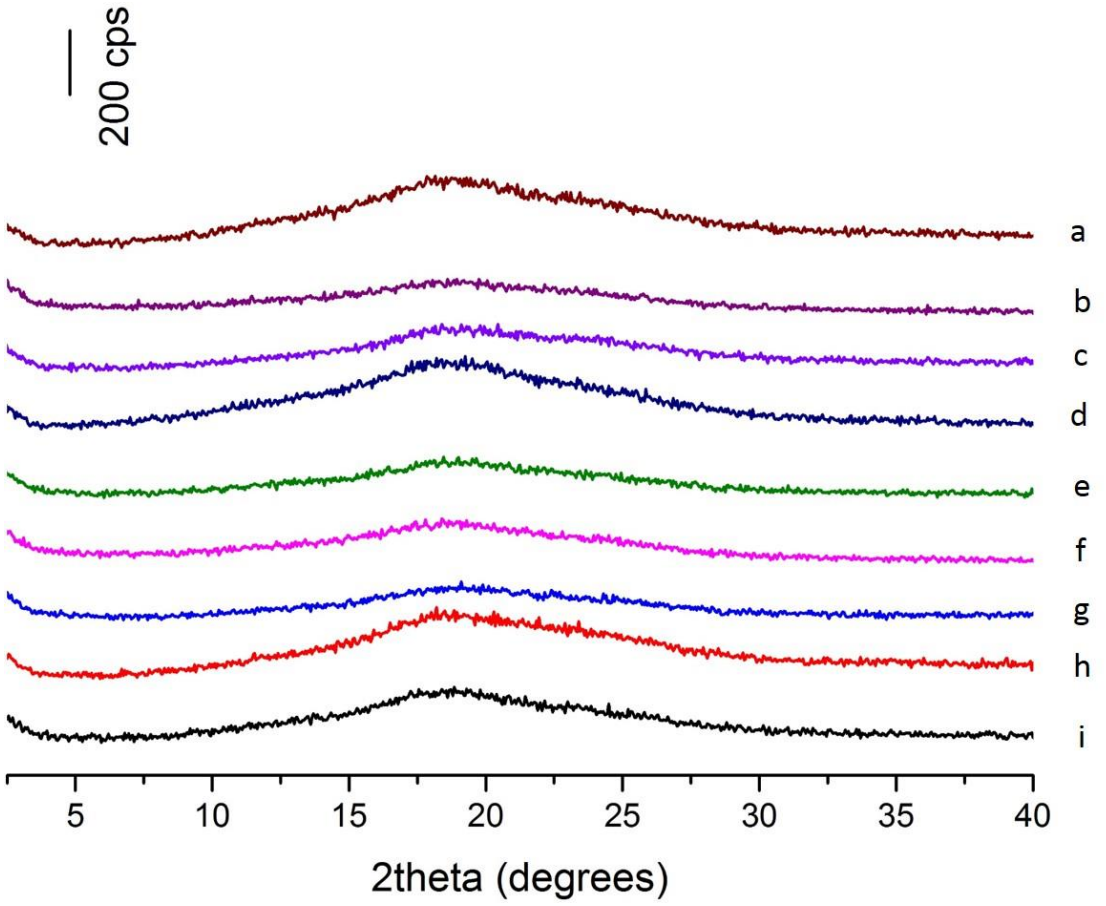

Fig. A.4.5. PXRD diffraction patterns for ITR NPs spray dried with trehalose 5% (w/v) after (a) immediately after collection from the spray dryer and (b) one hour (c) two hours (d) three hours (e) four hours (f) one day (g) two days (h) three days (i) four days after collection from the spray dryer. Samples were stored inside a desiccator at 4 °C.

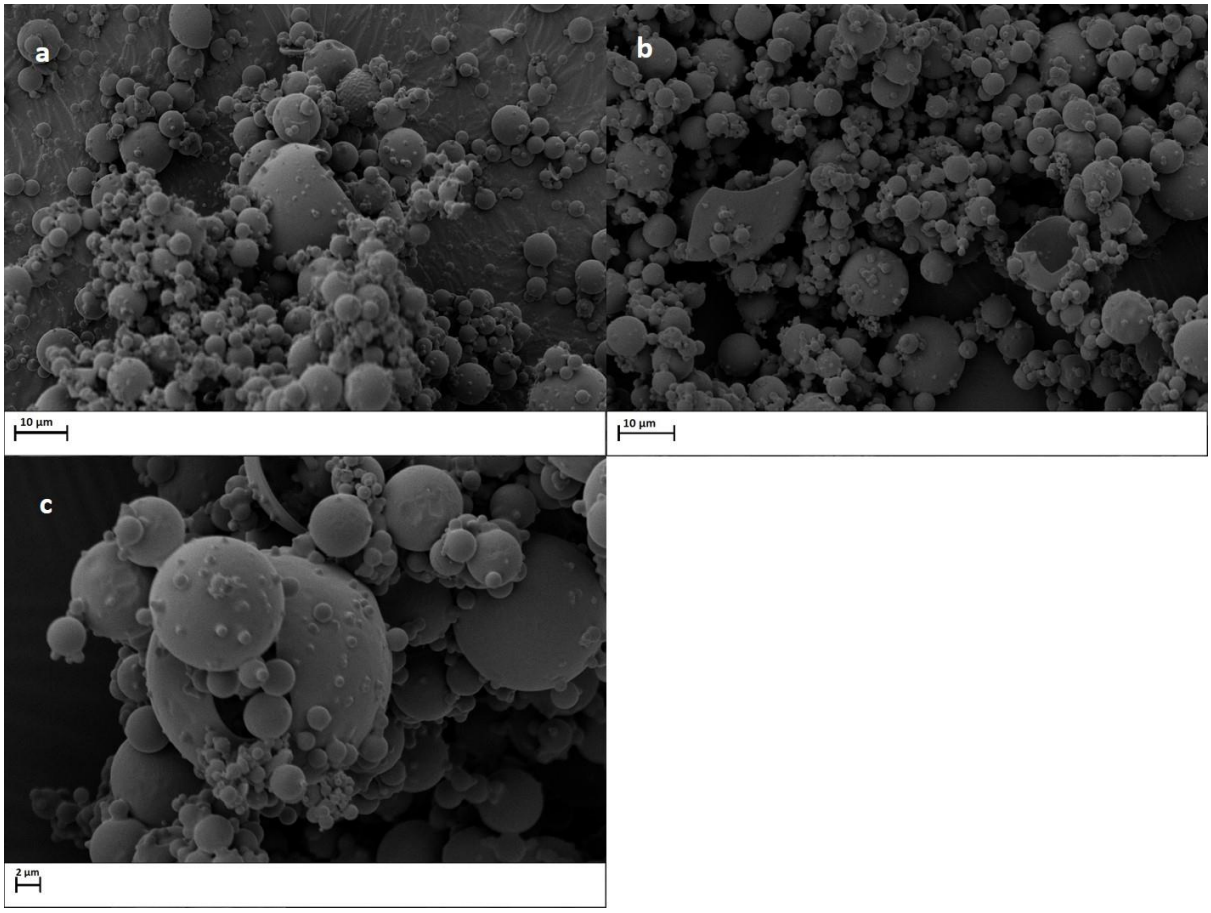

Fig. A.4.6. SEM images of ITR NPs spray dried with raffinose 5% (w/v).

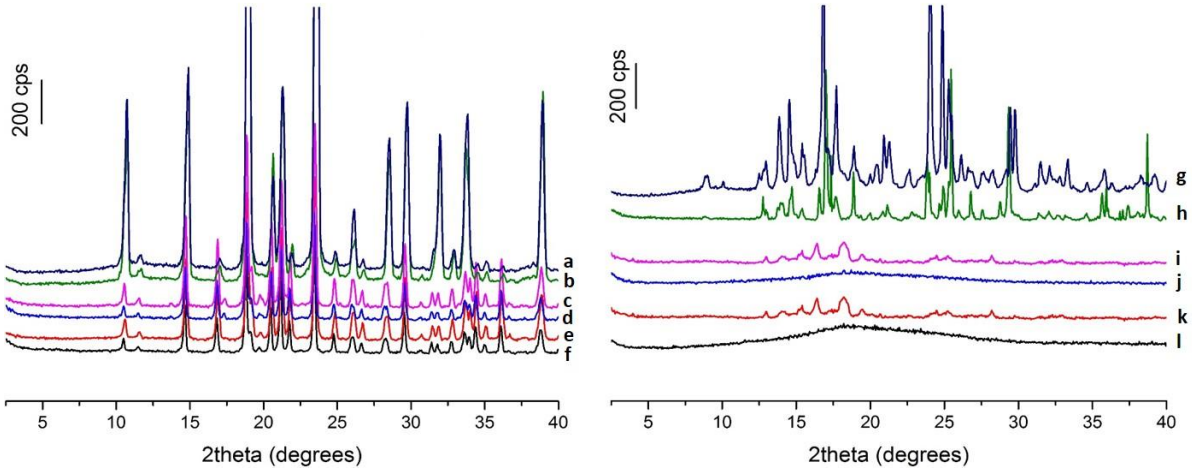

Fig. A.4.7. PXRD diffraction patterns for raw materials and post DVS analysis (a) raw mannitol (b) raw mannitol after DVS (c) ITR NPs SD with mannitol 5% (w/v) (d) ITR NPs SD with mannitol 5% (w/v) after DVS (e) SD mannitol 5% (w/v) (f) SD mannitol 5% (w/v) after DVS (g) raw trehalose after DVS (h) raw trehalose (i) ITR NPs SD with trehalose 5% (w/v) after DVS (j) ITR NPs SD with trehalose 5% (w/v) (k) SD trehalose 5% (w/v) after DVS (l) SD trehalose 5% (w/v).

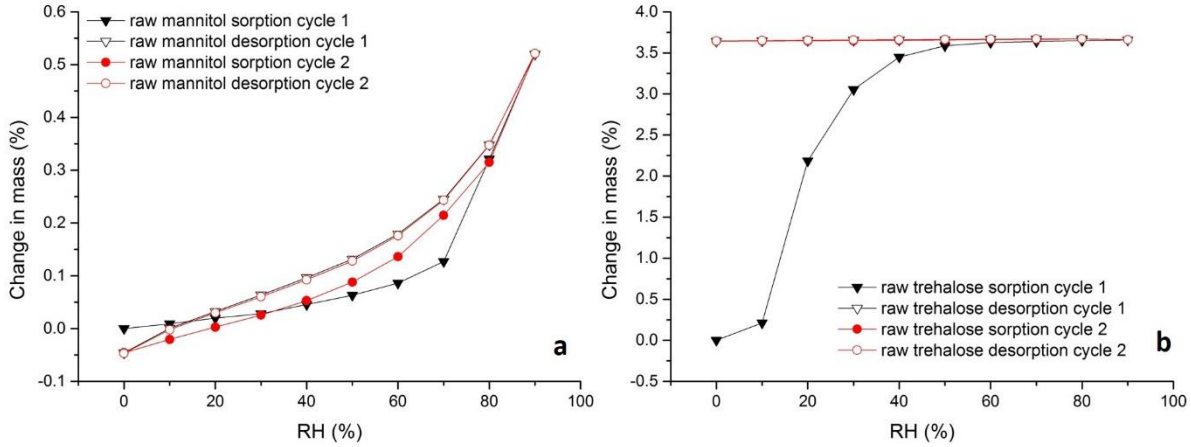

Fig. A.4.8. DVS sorption-desorption isotherm of (a) raw mannitol (b) raw trehalose.

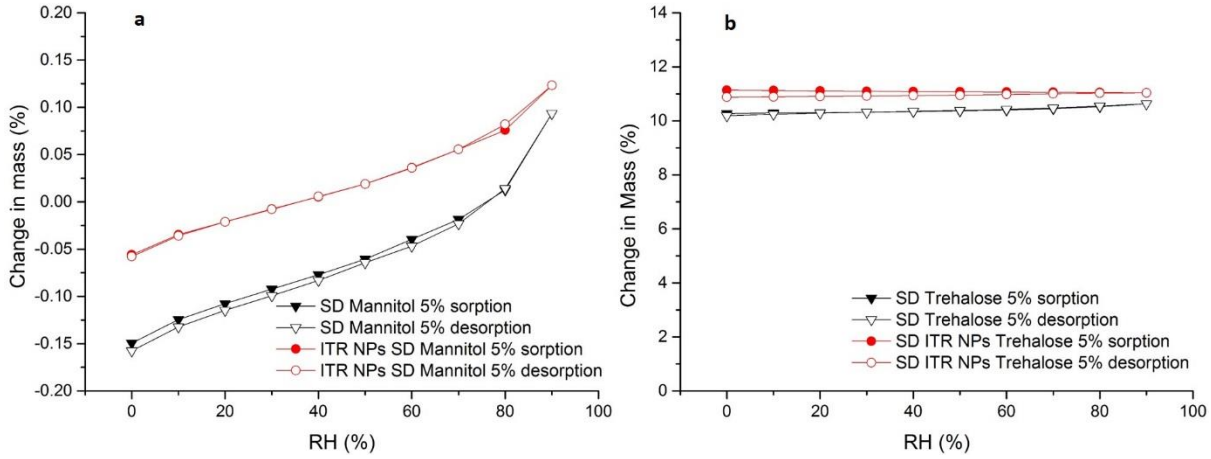

Fig. A.4.9. DVS sorption-desorption isotherm for (a) SD mannitol 5% (w/v) (b) SD trehalose 5% (w/v) and ITR NPs trehalose 5% (w/v).

Table A.4.3. Density measurements of spray dried uncompressed powders performed at ambient temperature in triplicate.

	Average density ± SD (g/cm^3)
Spray dried mannitol 5% (w/v)	1.50 ± 0.007
ITR NPs spray dried with mannitol 5% (w/v)	1.43 ± 0.003
Spray dried trehalose 5% (w/v)	1.55 ± 0.001
ITR NPs spray dried with trehalose 5% (w/v)	1.43 ± 0.01

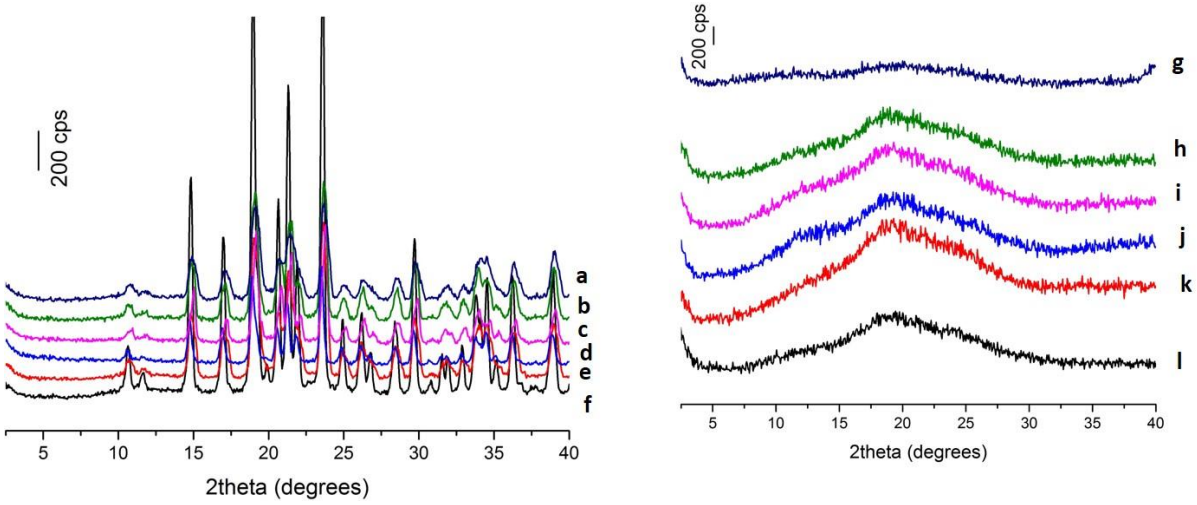

Fig. A.4.10. PXRD diffraction patterns for tablets (a) ITR NPs spray dried with mannitol 5% (w/v) compacted at 149 MPa (b) spray dried mannitol 5% (w/v) compacted at 239 MPa (c) spray dried mannitol 5% (w/v) compacted at 199 MPa (d) spray dried mannitol 5% (w/v) compacted at 149 MPa (e) spray dried mannitol 5% (w/v) compacted at 99 MPa (f) spray dried mannitol 5% (w/v) compacted at 50 MPa (g) ITR NPs spray dried with trehalose 5% (w/v) compacted at 99 MPa (h) spray dried trehalose 5% (w/v) compacted at 239 MPa (i) spray dried trehalose 5% (w/v) compacted at 199 MPa (j) spray dried trehalose 5% (w/v) compacted at 149 MPa (k) spray dried trehalose 5% (w/v) compacted at 99 MPa spray dried trehalose 5% (w/v) compacted at 50 MPa.

Table A.4.4. Disintegration testing for SD mannitol and trehalose 5% (w/v) compacted tablets. Analysis performed on three individual tablets in 900 ml of deionised water at 37 °C.

Type of compact and compaction pressure (MPa)	Time ± SD (s)
Mannitol 239	176 ± 6
Mannitol 199	189 ± 19
Mannitol 99	155 ± 12
Mannitol 50	165 ± 41
Trehalose 239	185 ± 11
Trehalose 199	198 ± 3
Trehalose 149	197 ± 15
Trehalose 50	186 ± 9